

Describing and predicting molecular properties via vibrational spectroscopy in combination with electron density analysis

Dissertation

zur Erlangung des akademischen Grades
doctor rerum naturalium (Dr. rer. nat.)

vorgelegt dem Rat der Chemisch-Geowissenschaftlichen Fakultät
der Friedrich-Schiller-Universität Jena

von

Diplomchemiker Martin Presselt

geboren am 19.12.1979 in Jena

Jena 2009

Gutachter:

1. Prof. Dr. Jürgen Popp

2. Prof. Dr. Gerd Buntkowsky

3. Prof. Dr. Wolfgang Kiefer

Tag der öffentlichen Verteidigung: 10. 06. 2009

Für Katja

Contents

List of Figures	iii
List of Tables	vii
List of Abbreviations	ix
1 Introduction	1
2 Theoretical details	7
2.1 Concepts to describe atomic properties, bonds and reactivities	7
2.2 Calculation and analysis of the electron density distribution	9
2.2.1 Quantum mechanical calculations	9
2.2.2 The quantum theory of atoms in molecules	13
2.3 Vibrational spectroscopy	15
2.3.1 Normal modes and vibrational transition energies	17
2.3.2 IR and Raman intensities	20
2.3.3 Resonance Raman spectroscopy	23
2.4 Relations between reactivities and spectroscopic properties	24
3 Experimental details	27
3.1 UV-vis absorption and remission spectroscopy	27
3.2 Fluorescence spectroscopy	27
3.3 Raman spectroscopy	27
3.4 Processing of Raman spectra	28
4 Characterizing molecules in the electronic ground state	29
4.1 Electron density studies in life sciences	29
4.2 Prediction of electron density features	37
4.2.1 Electron density properties	37
4.2.2 Vibrational and NMR data	41
4.2.3 Prediction of $\rho(r)$ -features utilizing spectroscopic data	42

4.3	The π -conjugation in tpy-ph derivatives and their metal complexes	62
4.3.1	The influence of Zn^{2+}	62
4.3.2	The influence of substituents at the 4-phenyl position	76
4.3.3	Comparison of Zn^{2+} and Ru^{2+} complexes and derivation of new molecular structure with improved properties	85
5	Characterizing the initial step of photoexcitation	101
5.1	Substructures involved in the $^1\text{MLCT}$ of $[(\text{tbut-tpy})\text{Ru}(\text{tpy-ph-R})]^{2+}$	101
5.2	Charge localization at the $^1\text{MLCT}$ of $[(\text{tbut-bpy})_2\text{Ru}(\text{tpphz})\text{PdCl}_2]^{2+}$	105
5.2.1	Assignment of Raman and resonance Raman bands to substructures in $[(\text{tbut-bpy})_2\text{Ru}(\text{tpphz})\text{PdCl}_2]^{2+}$	106
5.2.2	Estimation of $^1\text{MLCT}$ energies in $[(\text{tbut-bpy})_2\text{Ru}(\text{tpphz})\text{PdCl}_2]^{2+}$	107
6	Summary - Zusammenfassung	113
6.1	Summary	113
6.2	Zusammenfassung	116
A	Supporting vibrational data	121
A.1	Vibrational assignment of the Raman spectrum of $[\text{Zn}(\text{L4})_2]^{2+}$	121
A.2	Raman spectra of $[(\text{tbut-bpy})_2\text{Ru}(\text{tpphz})\text{PdCl}_2]^{2+}$, $[(\text{tbut-bpy})_2\text{Ru}(\text{tpphz})]^{2+}$ and $[(\text{tbut-bpy})_2\text{Ru}(\text{dppz})(\text{Br})_2]^{2+}$	126
	Bibliography	127
	Selbstständigkeitserklärung	143
	Acknowledgement - Danksagung	145
	Vita	147

List of Figures

4.1	Structure and ρ^{DFT} -map of dimethyl-3((4-nitro)phenyl)aziridine-2,2-dicarboxylate	30
4.2	Crystal section of a dimethyl-3((4-nitro)phenyl)aziridine-2,2-dicarboxylate single crystal (16 molecules)	32
4.3	Dimers of dimethyl-3((4-nitro)phenyl)aziridine-2,2-dicarboxylate extracted from the crystal structure and respective $\Delta\rho^{DFT}$ -maps of the aziridine ring referring to the isolated molecule. The aziridines referring to the $\Delta\rho^{DFT}$ -maps are labelled with an asterisk.	33
4.4	$\Delta\rho^{DFT}$ -map of dimethyl-3((4-nitro)phenyl)aziridine-2,2-dicarboxylate in a simulated aqueous environment.	36
4.5	Comparison of DFT and MP2 calculated ρ -values.	38
4.6	Comparison of the lowest- ρ - and the <i>cis</i> -convention.	39
4.7	Electron densities (left), respective laplacians (middle) and ellipticities (right) in the BCPs of the CH-bonds in phenyl.	41
4.8	Comparison of calculated $\rho(\text{ph-CH-BCP})$ values with the transition energies of corresponding CD-stretching vibrations.	45
4.9	Data related to the $\rho(\text{WN}, \sigma_{\text{C6H6}}^{1\text{H}})$ fit at the <i>meta2</i> -position	50
4.10	Data related to the $\rho(\text{RA}, \sigma_{\text{C6H6}}^{1\text{H}})$ fit at the <i>ortho1</i> -position	51
4.11	DFT-calculated, fitted and validated ρ -values of the best fits for CH-BCPs on all ph-positions.	54
4.12	DFT-calculated, fitted and validated $\nabla^2\rho$ -values of the best fits for CH-BCPs on all ph-positions.	55
4.13	DFT-calculated, fitted and validated ε -values of the best fits for CH-BCPs on all ph-positions.	57
4.14	DFT-calculated and validated $\rho(\text{r})$ -target values ($\rho, \nabla^2\rho, \varepsilon$) of the best fits for CH-BCPs on all ph-positions applying rel. variables.	61
4.15	UV-vis spectra of L4 and $\text{Zn}(\text{L4})_2^{2+}$	64
4.16	Raman spectra of L4	66
4.17	Bond lengths in L4 and $[\text{Zn}(\text{L4})_2](\text{PF}_6)_2$	68

4.18	Experimental (top) and DFT-calculated (bottom; BP86/RI/def2-TZVP) Raman spectra of $[\text{Zn}(\mathbf{L4})_2]^{2+}$	70
4.19	Top: DFT-calculated structure of $[\text{Zn}(\mathbf{L4})_2]^{2+}$ with atomic labels. Middle and bottom: Trig. ring breathing modes $\delta_{ip}(\text{trig. ring br.})$ ($\tilde{\nu}^{DFT} = 1010 \text{ cm}^{-1}$) and $\nu(\text{ph-py}(\text{trig}))$ ($\tilde{\nu}^{DFT} = 1351 \text{ cm}^{-1}$).	71
4.20	Sketch of the correlation between Raman shift of $\nu(\text{ph-py}(\text{trig}))$ and bond shortening of the ph-py bond upon complexation.	72
4.21	<i>Inter-$\Delta\rho$</i> -plot: $\rho(\text{trans-}\mathbf{L4})-\rho([\text{Zn}(\mathbf{L4})_2]^{2+})$	74
4.22	<i>Inter-$\Delta\rho$</i> -plots of $[\text{Zn}(\mathbf{L2})_2]^{2+}$, $[\text{Zn}(\mathbf{L3})_2]^{2+}$ and $[\text{Zn}(\mathbf{L4})_2]^{2+}$, referring to $[\text{Zn}(\mathbf{L1})_2]^{2+}$	78
4.23	Experimental Raman spectra of $\text{Zn}(\mathbf{L1})_2^{2+}$ - $\text{Zn}(\mathbf{L4})_2^{2+}$	79
4.24	Correlation between ε , geometrical and Raman characteristics.	80
4.25	Raman spectra of $[\text{Zn}(\mathbf{L})_2](\text{PF}_6)_2$ containing vinyl groups (top: $\mathbf{L} = \mathbf{L3}, \mathbf{L5}, \mathbf{L7}$) or ethynyl (down: $\mathbf{L} = \mathbf{L4}, \mathbf{L6}, \mathbf{L9}$) groups at phenylene	82
4.26	HOMO (bottom) and LUMO (top) of $\text{Zn}(\mathbf{L3})_2^{2+}$	84
4.27	Valence formula of tpy-ph, the homoleptic Zn(II) complexes, the heteroleptic Ru(II) as well as substituents at phenylene.	86
4.28	Correlations between ε and r and α of the py-ph bond in tpy-ph-R and related Zn(II) and Ru(II) complexes	88
4.29	Vectors defining the plane studied in the <i>inter-$\Delta\rho$</i> -plots.	90
4.30	<i>Inter-$\Delta\rho$</i> -plots to visualize the influences of the cation and substitution on $\rho(r)$ in the ph-py bond.	91
4.31	HOMO-, LUMO- and gap-energies of Ru(II) and Zn(II) complexes of tpy-ph-R dependent on $\varepsilon(\text{py-ph-BCP})$	93
4.32	Structural representations of complexes $[\text{Zn}(\text{tpy-ph-R})_2]^{2+}$ with the ph moieties substituted with NH_2 - and vinyl-groups.	97
5.1	Normalized absorption spectra of $[\text{Ru}(\text{tbut-tpy})_2]^{2+}$ and $[(\text{tbut-tpy})\text{Ru}(\text{tpy-ph-R})]^{2+}$ dissolved in CH_3CN	102
5.2	RRS of $[(\text{tbut-tpy})\text{Ru}(\text{tpy-ph-R})]^{2+}$ (from top: $\text{R}=\text{Br}, \text{NH}_2, \text{NO}_2$) and $[\text{Ru}(\text{tbut-tpy})_2]^{2+}$ (bottom), dissolved in CH_3CN (*).	103
5.3	Resonance Raman spectrum of $[(\text{tbut-tpy})\text{Ru}(\text{tpy-ph-CN})]^{2+}$ dissolved in dichloromethane (RR-bands labelled with asterisks).	105
5.4	Valence structure of $[(\text{tbut-bpy})_2\text{Ru}(\text{tpphz})\text{PdCl}_2]^{2+}$ ($[\text{RuPd}]^{2+}$, left) and $[(\text{tbut-bpy})_2\text{Ru}(\text{dppz})(\text{Br})_2]^{2+}$ (right).	106
5.5	Comparison of the resonance Raman spectra of $[\text{RuPd}]^{2+}$ (upper graph, different RRS are corresponding to different excitation wavelength, see legend) and $[\text{Ru}(\text{tbut-bpy})_3]^{2+}$ ($\lambda_{ex}=458 \text{ nm}$).	107

5.6	Deconvolution of experimental resonance Raman spectra of $[\text{RuPd}]^{2+}$ dissolved in acetonitrile, excited at 515, 488, 477, 458, 413 nm.	109
5.7	MLCT-absorption band of $[\text{RuPd}]^{2+}$; dots: normalized sums of ν^4 -corrected RR-intensities, star-shaped dots: tp-phz-assigned RR-bands, circle dots: tbut-bpy-assigned RR-bands, dotted and dashed lines: Gauss-fits; upper graph: solvent = CH_3CN , lower graph: solvent = CH_2Cl_2 ; inset: normalized UV-vis spectra of $[\text{RuPd}]^{2+}$ dissolved in CH_3CN (solid line) and CH_2Cl_2 (dotted line). Horizontal lines: $^1\text{MLCT}$ shifts at 10% absorption.	110
5.8	$^1\text{MLCT}$ energy differences ΔE referring to the groundstate energy (set zero). ΔE -values are estimated at 10% of the maximal amplitude of the Gauss profiles. Left: solvent = CH_3CN , right: solvent = CH_2Cl_2	111
A.1	Comparison of the Raman spectra of $[\text{RuPd}]^{2+}$, $[(\text{tbut-bpy})_2\text{Ru}(\text{tp-phz})]^{2+}$ and $[(\text{tbut-bpy})_2\text{Ru}(\text{dppz})(\text{Br})_2]^{2+}$ detected in the solid state.	126

List of Tables

2.1	Overview over the different CPs defined within the QTAIM	14
2.2	ρ -distribution in the CC-bonds, ρ and ε within the respective BCPs of ethane, ethene (ethylene), ethyne (acetylene)	15
4.1	Experimentally and theoretically determined AIM charges of carbons C1 and C2 of the aziridine ring.	34
4.2	Correlation coefficients r between vibrational and $\rho(\mathbf{r})$ data	44
4.3	χ^2 and $val\text{-}\chi^2$ of the fits of the electron densities	48
4.4	Parameters of the best linear fit-functions of the electron densities	53
4.5	Parameters of the best linear fit-functions of the laplacians of the electron densities in the BCPs for each ph-CH bond.	53
4.6	Parameters of the best linear fit-functions of the ellipticities	56
4.7	Parameters of the best linear fit-functions of ρ -, $\nabla^2\rho$ -, ε -values applying relative spectroscopic variables	60
4.8	Investigated Zn(II) <i>bis</i> -terpyridine complexes	63
4.9	Selected parameters indicating variations in the π -electron delocalization due to complexation	69
4.10	Selected parameters indicating variations in the π -electron delocalization due to complexation	77
4.11	LUMO energy (derived from electrochemical investigations) and photochemical properties.	83
4.12	$\varepsilon(\text{py-ph-BCP})$ -values of free all- <i>trans</i> -tpy-ph-R ligands (L), $[\text{Zn}(\text{tpy-ph-R})_2]^{2+}$ (Zn) and $[(\text{tbut-tpy})\text{Ru}(\text{tpy-ph-R})]^{2+}$ (Ru) complexes and $\Delta\varepsilon$ -values between complexes and ligands. In the lower part $\varepsilon(\text{vinyl-ph-BCP})$ -values are presented.	87
4.13	Correlations between ε and r and α of the py-ph bond in tpy-ph-R and related Zn(II) and Ru(II) complexes	89
4.14	HOMO, LUMO and respective gap energies of tpy-ph-R ligands and respective Ru(II) and Zn(II) complexes	95

4.15	Fit-parameter of the data in table 4.14 according equation 4.8.	95
5.1	Wavenumber-positions in cm^{-1} of resonantly enhanced modes, which are assigned to involve the ph-R moiety in $[(\text{tbut-tpy})\text{Ru}(\text{tpy-ph-R})]^{2+}$ with $\text{R}=\text{Br}, \text{NH}_2, \text{NO}_2$	104
A.1	Vibrational assignment of the DFT-calculated RS of $[\text{Zn}(\text{L4})_2]^{2+}$	121

List of Abbreviations

ACP	attractor critical point
AO	atomic orbital
ar-ar bond	bond between two aromatic rings
BCP	bond critical point
bpy	2,2'-bipyridine
CP	critical point
DFT	density functional theory
ε	ellipticity
GGA	generalized gradient approximation
HF	Hartree-Fock
HOMO	highest occupied molecular orbital
ILCT	intra ligand charge transfer
IR	infra red
L	ligand
LASER	light amplification by stimulated emission of radiation
LDA	local density approximation
LUMO	lowest unoccupied molecular orbital
M	metal
marij	multipole accelerated resolution of the identity
³ MC	metal centered triplet state
MLCT	metal to ligand charge transfer
MP2	Møller-Plesset perturbation theory of second order
NAO	natural atomic orbital
NBO	natural bond orbital
NHO	natural hybride orbital
NM	normal mode
NMR	nuclear magnetic resonance
OFET	organic field effect transistor
OLED	organic light-emitting diode

QTAIM	quantum theory of atoms in molecules
$\rho(r)$	electron density distribution
R	substituent
RI	resolution of the identity
RRS	resonance Raman spectroscopy
RS	Raman spectroscopy
SCF	self consistent field
SERS	surface enhanced Raman spectroscopy
τ	lifetime
tbut-bpy	4,4'-di(tert-butyl)-2,2'-bipyridine
TEA	triethylamine
TON	turn over number
tpy	2,2':6',2''-terpyridine
tpy-ph	4'(phenyl)-2,2':6',2''-terpyridine
WN	wavenumber

1 Introduction

One of the most important topics in physical chemistry is the prediction of reactivity properties of molecules. One approach to determine molecular properties is to analyze the molecular electron density distribution $\rho(\mathbf{r})$. According to the Hohenberg-Kohn-Theorem¹ (Nobel prize awarded to Walter Kohn in 1998, together with John Pople) molecular properties, like the reactivity, can be derived from the ρ -distribution. The positions of the nuclei are determined by the maxima in $\rho(\mathbf{r})$ and also the nuclear charges can be derived from the gradient of ρ at the positions of the nuclei. Hence, the external potential can be calculated from the ρ -distribution and the total number of electrons can be calculated by integrating $\rho(\mathbf{r})$ over the molecular space. With it, one can derive the molecular wavefunction based on $\rho(\mathbf{r})$ and can calculate the property of interest.

In the last few years the experimental ρ -determination by means of high-resolution x-ray measurements has drawn much attention, since the technical improvements permit ρ -determinations with justifiable effort and time consumption.²⁻⁷ These experimental investigations of $\rho(\mathbf{r})$ have led to a paradigm shift in describing chemical bonding situations towards characterizing molecular key-regions by means of their electron density features. Recently, $\rho(\mathbf{r})$ -studies have been also successfully applied in the life sciences⁸⁻¹⁰ where the crystal site environments are supposed to represent the intermolecular interactions present under physiological conditions.² However, $\rho(\mathbf{r})$ of macromolecules, such as proteins or polynucleotides, can only be determined experimentally for special cases^{2,11,12} since experimental $\rho(\mathbf{r})$ -studies are generally linked to high-quality single crystals. Experimental $\rho(\mathbf{r})$ -studies cannot be applied for substances which do not tend to form single crystals or of substances in various non-crystalline environments. For example, in life-sciences it would be of high interest to get information about $\rho(\mathbf{r})$ of a pharmaceutically active molecule in a physiological environment just before acting or, even more ambitious, to trace $\rho(\mathbf{r})$ during the mode of action of a molecule. Although there are ongoing efforts to make experimental $\rho(\mathbf{r})$ -studies a routine application in the life sciences^{2,13-20} the latter task necessitates alternative approaches.

$\rho(\mathbf{r})$ can also be studied theoretically by means of quantum mechanics also facilitating the considerations of homogeneous solvents or more complex environments. However, quantum mechanical calculations of large assemblies of reliable quality are usually quite time-consuming for which reason complex environments are not involved in standard cal-

culations. Apart from technical limitations in calculating $\rho(\mathbf{r})$ from experimental diffraction data, differences to quantum mechanically calculated $\rho(\mathbf{r})$ might be caused by the neglect of the crystal site environment in the theoretical calculations to some extent.^{21,22} Within this work an example studied by Grabowsky et al.⁸ is picked up in section 4.1 to unravel the influence of intermolecular interactions on the deviations between DFT-calculated $\rho(\mathbf{r})$ and experimentally determined $\rho(\mathbf{r})$ of a pharmaceutical active aziridine derivative. The study highlights the benefits and limitations of experimental $\rho(\mathbf{r})$ determinations and points on the needs of a method supporting information about $\rho(\mathbf{r})$ of molecules in different environments.

A possible experimental alternative to high-resolution x-ray crystallography to study $\rho(\mathbf{r})$ characteristics, also of substances in various physical states, is the application of spectroscopic techniques to determine quantities related to $\rho(\mathbf{r})$ -features. In the past, vibrational and NMR spectroscopy were applied to estimate reactivity properties.²³⁻²⁶ Analog to these works the direct correlation of spectroscopic parameters with particular $\rho(\mathbf{r})$ -features should be possible. An in this way derived experimental methodology applicable to various physical states and environments, which leads to the desired $\rho(\mathbf{r})$ -characteristics, would be of great impact for natural sciences. Following the work related to the Hammett equation, the correlation between ρ -characteristics and NMR as well as vibrational spectroscopic quantities is studied in section 4.2 for the example of CH-bonds in a series of mono-substituted benzene derivatives.

The electron density distribution of the electronic ground state, unambiguously defining a molecule, also determines corresponding excited state properties. Hence, it is assumed that via particular ρ -characteristics of the electronic ground state even certain properties of the electronic excited state can be estimated. For example photoelectric properties of unsaturated polymers depend on the degree of the π -conjugation. The properties of π -conjugated polymers can be tuned in a wide range so that characteristics of metals and semiconductors can be achieved.²⁷⁻²⁹ The manipulation of electrical and photophysical properties of a huge variety of π -conjugated systems has lead to very exciting applications like e-papers,^{30,31} organic light emitting diodes (OLEDs),³²⁻³⁴ organic field-effect transistors^{35,36} (OFETs) and integrated circuits,³⁷⁻⁴² polymer solar cells^{43,44} and others.⁴⁵⁻⁴⁹ To appreciate the seminal work on electrically conductive polymers, the Nobel prize in chemistry was awarded to Heeger, MacDiarmid and Shirakawa in 2000.⁵⁰⁻⁵²

For the synthesis of polymers to be utilized in OLEDs 4'(phenyl)-2,2':6',2''-terpyridine (tpy) derivatives are currently under investigation since the tpy-moiety enables the coordination to transition metal ions like Zn^{2+} , what is assumed to improve the self organization properties in polymer based devices.⁵³ The ground and excited state properties of those polymers depend on the torsion between pyridine and phenylene, since the torsion strongly influences the π -conjugation between adjacent aromatic rings.⁵⁴⁻⁵⁶ This torsion

is caused by steric repulsions of adjacent hydrogen atoms and can be avoided either by applying heteroaromatic rings or by inserting vinylene or acetylene groups acting as spacers.⁵⁷⁻⁶¹ In condensed aromatic systems the problem of torsion is not present, but these substances can not be polymerized using standard protocols.⁶² Indeed, to optimize and to trim the conducting properties of polymers an adjustable π -character of the bond between aromatic rings instead of a rigid coplanar structure would be beneficial. The variation of the bond-properties of such a bond connecting neighboring aromatic rings can be achieved by attaching substituents on the rings, either pushing or pulling electron density in the rings and in the connecting bond.⁵³

To study the π -character of bonds in general, the quantum theory of atoms in molecules (QTAIM) developed by Bader⁶³ provides the ellipticity ε as a quantity capable to express the fraction of π -binding within a bond. Within the QTAIM the topology of the ρ -distribution is analyzed with the aim of localizing the turning points of $\rho(r)$ (so called critical points CPs). I.e., certain quantities like ρ or ε within the CP assigned to a bond are used to characterize the electron density properties of the respective bond, what is explained in detail in section 2.1.

Applying the QTAIM the effect of the substituents on the ring-connecting bond (ar-ar bond) can be reliably estimated and new target-molecules with a defined electron delocalization can be suggested. For example, it can be studied to which extend the π -character of an ar-ar bond, being the bottleneck for conductivity in related polymers, can be raised due to various substituents or other modifications as discussed in section 4.3. In this context QTAIM is rarely applied but leads to meaningful clear insights in the bond properties with eligible computational effort. High-resolution x-ray measurements to proof the calculated electron density distribution are not possible in polymers possessing a heterogeneous secondary structure. Hence, theoretically determined $\rho(r)$ -features have to be validated via spectroscopic techniques, for example.

When using ruthenium(II) ions instead of Zn^{2+} for complexation, completely new photophysical properties arise due to the accessibility of metal to ligand charge transfers (MLCTs), since Ru^{2+} possesses a non-filled d-shell. Especially ruthenium(II) bipyridine and terpyridine complexes are able to serve as light harvesting antennas⁶⁴⁻⁶⁹ and were therefore extensively investigated in the last decades.⁵⁷⁻⁶¹ The major aim in designing such complexes is to find structures in which the charge, located on a ligand after an ¹MLCT, is further transferred to end up at an catalytic active site and act in redox reactions with certain target molecules. In order to enable efficient charge or energy transfer to the desired site, deactivation of the excited states along competitor channels have to be minimized. The rate constants of the charge transfers and the deactivations depend on the energetic levels of the involved excited states. Hence, regarding the light harvesting complexes, charge separated excited states with prolonged life times are aspired, as

it is the case for $\text{Ru}(2,2'\text{-bipyridine})_3^{2+}$ with $\tau(^3\text{MLCT})=1100$ ns.⁷⁰ Unfortunately, for the creation of larger polynuclear assemblies with increased light absorption probability substitution on the stereogenic $\text{Ru}(\text{bpy})_3^{2+}$ moieties might lead to facial and meridional isomers.⁷¹ Using two terpyridine ligands instead of three bipyridine ligands leads to achiral $\text{Ru}(\text{tpy})_2^{2+}$ motifs facilitating the creation of enantiopure polynuclear complexes. Since in $\text{Ru}(\text{tpy})_2^{2+}$ the octahedral geometry is stronger disturbed than in $\text{Ru}(\text{bpy})_3^{2+}$ the ligand field is weaker, thus leading to an energetically lower dd metal centered triplet state (^3MC). Consequently, the ^3MC state gets thermally accessible from the $^3\text{MLCT}$ enabling radiationless decay to the electronic ground state and significantly reducing the life time of the excited state ($^3\text{MLCT}$) to 250 ps compared to $\text{Ru}(\text{bpy})_3^{2+}$. Several basic attempts have been advanced to increase the lifetime of the charge separated state in $\text{Ru}(\text{tpy})_2^{2+}$ -complexes after photoexcitation, reviewed by Medlycott and Hanan.⁵⁸ In these approaches the tpy-ligands are modified either to increase the energetic distance between the $^3\text{MLCT}$ and the ^3MC state to avoid the deactivation pathway over the ^3MC state or to graft additional chromophoric systems with a non-radiative triplet states, energetically close to the $^3\text{MLCT}$ state, onto tpy to achieve an energetic equilibrium facilitating the repopulation of the $^3\text{MLCT}$ state after emission.

It could be shown that via electron withdrawing or unsaturated substituents in the 4'-position of tpy the luminescence lifetimes could be increased to 50 ns and 580 ns, respectively.⁷²⁻⁷⁶ Unsaturated substituents like acetylene have been shown to stabilize the ligand based LUMO (lowest unoccupied molecular orbital) due to extending the π -electron delocalization going along with an increased $^3\text{MLCT}$ - ^3MC energy gap. In the case of aromatic substituents the ground and $^1\text{MLCT}$ states are significant differently affected, since the phenyl group is tilted against tpy in cause of steric hindrance between hydrogens in the ground state and coplanar in the $^1\text{MLCT}$ excited state. Hence, the π -electron delocalization between tpy and ph is more pronounced in the $^3\text{MLCT}$ state than in the ground state causing a decreased energy gap between these states going along with a reduced excited state lifetime (4 ns).⁷⁷ To overcome this problem different approaches are possible: either avoiding the steric hindrance to reach a coplanar structure in the ground state, i.e. due to introducing a pyrimidyl unit instead of a phenyl group, or modifying the electron density distribution towards a higher π -character of the pyridine-phenylene (py-ph) bond via certain substituents on ph or avoiding the planarization in the excited state due to introducing larger substituents on ph in *ortho* position to the inter-annular bond.⁵⁸

The control of the electron density distribution and the dihedral angle between py and ph in $(\text{L})\text{M}(\text{tpy-ph-R})_2^{2+}$ complexes is discussed in section 4.3. The particular focus within the presented investigations lies on the characterization of the pyridine-phenylene (py-ph) bond. After validating the respective theoretical electron density studies via the correlation of $\rho(r)$ properties of the py-ph bond with Raman data it is shown how ρ properties of

the py-ph bond, in particular the π -character, can be adjusted whereas Bader's Quantum Theory of Atoms in Molecules (QTAIM) and the findings of the benzene-study in section 4.2 are applied. The well-defined adjustments of the π -character of crucial bonds being the bottleneck for π -electron delocalization, as in the case of the py-ph bond or inter-aromatic bonds present in poly-phenylene or related polymers, facilitates the selective control of conductivity properties as well as of photochemical properties. The defined assessment of the influence of various chemical modifications of substances in the research focus via QTAIM offers a feasible method to develop new materials for applications in the field of organic solar cells, organic light emitting diodes, photocatalysis and others.

A further crucial question concerning the photochemistry of (L)Ru(tpy-ph-R)²⁺ complexes is about the nature of the ¹MLCT. It is up to now unsettled, whether the ph-moiety is directly involved in the ¹MLCT which is of high interest to force spatial charge separation. For that purpose differently substituted (tbut-tpy)Ru(tpy-ph-R)²⁺ complexes were investigated applying resonance Raman spectroscopy (RRS) as shown in section 5.1. This vibrational spectroscopic technique is the method of choice to trace the prompt modification of the electron density distribution at the initial step of photoexcitation, i.e. at the Franck-Condon point.⁷⁸⁻⁸⁰ In the resonance Raman spectra bands are the more enhanced (up to a factor of 10⁶) the larger the displacement of the respective normal coordinates potential is. Hence, one can localize the geometrical changes caused by the change in the electron density distribution during the ¹MLCT.

The geometrical changes accompanied with the ¹MLCT depend in heteroleptic complexes inherently on the excitation wavelength, since the different ligands represent different chromophores with different absorption characteristics. If the ¹MLCT absorption maxima of the ligands are overlapping thus leading to just one ¹MLCT absorption band, the latter can be deconvoluted by means of RRS thus estimating the relative energies between the ¹MLCTs towards the different ligands. This procedure enables the energetic optimization of photoexcitation to selectively excite the desired ¹MLCT initializing charge separations and subsequent photocatalytic reactions. In doing so the ¹MLCT absorption band of the dinuclear hydrogen evolving (tbut-bpy)Ru(tpphz)PdCl₂²⁺ catalyzer, developed in the research group of Prof. Rau, was deconvoluted as shown in section 5.2. The (tbut-bpy)Ru(tpphz)PdCl₂²⁺ complex possesses a TON of 56 mol H₂ per mol catalyzer whereas triethylamine (TEA) is used to reduce the oxidized Ru(III) and acts as a donor of protons which are supposed to be reduced at the Pd-site (solvent=acetonitrile).⁸¹

In summary, the impact of experimental electron density determinations and their experimental limitations are introduced at the beginning of the present work (sections 1 and 4.1). In the following alternative approaches to determine electron density properties

experimentally are suggested and studied theoretically for a series of monosubstituted benzene derivatives 4.2. Subsequently, manipulations of electron density distribution between pyridine and phenylene are investigated in conjunction with related photophysical properties 4.3. Herein, zinc(II)-tpy-ph complexes serving as model compounds for polymers with potential applications in OLEDs and ruthenium(II) analogues serving as light harvesting antennas in photocatalytic devices are studied to derive suggestions for structural modifications for improved photophysical properties. A comparable task is examined in chapter 5, where resonance Raman spectroscopy is applied to Ru(II)-complexes to investigate the initial step of photoexcitation. In doing so, molecular substructures are assigned to be involved in the Franck-Condon transition and $^1\text{MLCT}$ -absorption bands are deconvoluted to facilitate optimized photoexcitations.

2 Theoretical details

2.1 Concepts to describe atomic properties, bonds and reactivities

Up to now one of the leading chemical concepts to estimate reactivity properties of molecules is the concept of electronegativity introduced by L. Pauling in 1932. The difference between the electronegativities χ of two atoms A and B according to Pauli depends on bond dissociation energies D according equation 2.1.⁸²

$$D_{AB} - \sqrt{D_{AA}D_{BB}} = 96,48 \frac{kJ}{mol} (\chi_A - \chi_B)^2 \quad (2.1)$$

To calculate electronegativities the D -values are determined experimentally and a reference value for χ of a certain atom has to be defined. Pauling chose the electronegativity of fluorine to be 4 being the reference value. The electronegativities defined by Pauling are up to now implemented in common periodic system tables and his benefits are valued with the Nobel prize in chemistry in 1954.⁸³

In 1934 Mulliken introduced an alternative definition of the electronegativity χ_M , calculated as mean value of the electron affinity E_a and the ionization energy I_e of an atom according equation 2.2.⁸⁴ The Nobel prize was awarded to Mulliken "for his fundamental work concerning chemical bonds and the electronic structure of molecules by the molecular orbital method" in 1966.⁸³

$$\chi_M = \frac{I_e + E_a}{2} \quad (2.2)$$

Allred and Rochow introduced the Coulomb force acting on a bond $F \propto Z/r^2$ in 1958. Z is the nuclear charge and r is the atomic radius. Due to parametrization this quantity was adjusted to the electronegativity values defined by Pauling according to equation 2.3.^{85,86}

$$x = 0,359Z/r^2 + 0,744 \quad (2.3)$$

In the past great efforts have been made to derive atomic properties like the electronegativity of atoms within molecules from molecular wavefunctions or molecular electron density distributions to predict reactivities of molecules or to get insights in bonding situations.⁸⁷⁻⁹¹

Even if the advances in quantum chemistry facilitated the computation of actually large molecules and various of their properties,^{78,92-94} the calculation of atomic properties within molecules is not trivial and still different concepts are applied.⁹¹ The origin of the challenge is that electrons are quantum mechanically treated as influenced by the external potential of the nuclei but not as inherently assigned to particular nuclei within the molecule. Hence, the edges of atoms between nuclei are not obvious. Consequently, the calculation of partial charges is not unambiguous since the atomic volume Ω is not predetermined by quantum mechanics.

To overcome these problems molecular partitioning schemes were developed in the past which are based either on partitioning of the wavefunction or on the real space partitioning of the electron density distribution. By far the most frequently applied wavefunction based partitioning schemes are the one of Mulliken⁸⁷⁻⁹⁰ and the NBO (natural bond orbitals) approach.⁹⁵⁻¹⁰⁰ While Mulliken charges and related are known to be strongly basis set dependent, NBO analysis leads to more reliable results. Furthermore, applying the NBO approach leads to well localized molecular natural orbitals usually being in accordance to traditional chemical concepts. Starting from a given molecular wavefunction, natural orbitals are calculated via an eigenvalue equation, whereas the first-order reduced density operator Γ acts on the natural orbitals Θ as shown in equation 2.4.

$$\Gamma\Theta_k = p_k\Theta_k \tag{2.4}$$

The corresponding eigenvalues p_k are the populations of the eigenfunctions. Within the NBO formalism natural atomic orbitals (NAOs) are localized one-center orbitals which can be transformed in natural hybrid orbitals (NHOs) via optimized linear combination of NAOs. Finally, NHOs are used to compose NBOs.

However, since in contrast to wavefunctions the electron density is an observable real space electron density distribution partitioning schemes are gaining importance in the last years. The different approaches, amongst them Bader's Quantum Theory of Atoms In Molecules (QTAIM, described in detail in section 2.2.2)^{63,101-103} being the most popular one, were comparatively reviewed by Meister and Schwarz.⁹¹

In contrast to properties derived from calculations based on the partitioning schemes of Mulliken and related approaches the QTAIM results are known to be less basis set dependent.^{3,4,91,104} Furthermore, AIM charges were found to be rather independent on the theoretical method used for computation even if they are expected to exaggerate the real atomic charges, since a high density offloads the zero flux surface.^{4,104,105} A study of Gomes et al. shows that the AIM charges give rise to good performances in calculating IR intensities and are consistent with the chemical experience based on the electronegativity concept.¹⁰⁶ Hence, $\rho(\mathbf{r})$ -features determined by using the QTAIM are appropriate for quantum mechanical studies in context with vibrational investigations.

2.2 Calculation and analysis of the electron density distribution

Within the following subsections the methods and theories applied in the present work are briefly introduced. Detailed descriptions and comparisons with alternative methods can be found elsewhere.^{91,93,107-114}

2.2.1 Quantum mechanical calculations

A huge variety of quantum mechanical methods to calculate molecular structures, electron density distributions, spectroscopic parameters and further molecular properties is known. For many applications density functional theory (DFT)^{93,107-109} is the quantum mechanical theory of choice, since reliable results can be obtained with usually justifiable computational effort.^{78,94}

The development of density functional theory started nearly at the same time as the development of the Hartree-Fock (HF) theory. In the origins of DFT the homogeneous electron gas was treated and later on Hohenberg and Kohn showed that the molecular ground state energy E depends on the ground state electron density distribution $\rho(\vec{r})$.¹ Since E is a scalar and depends on a function ($\rho(\vec{r})$) $E[\rho]$ is called an energy functional or density functional (see eq. 2.5) leading to the expression "density functional theory".

$$E = E[\rho] \quad (2.5)$$

In comparison to the Hartree-Fock theory the problem to determine the molecular energy is formally downscaled from $3N$ to 3 variables (cartesian frame \vec{r} of $\rho(\vec{r})$) in DFT whereas N is the number of atoms.

In analogy to the HF-formalism the energy in DFT is a sum of the kinetic energy of the electrons E_T , their potential energy in the field of the nuclei $E_{V_{eK}}$, their Coulomb as well as exchange energy (E_J and E_X) and additionally the contribution of the correlation energy E_C , aimed to compensate the simplification of assuming independent particles as shown in eq. 2.6, and the parametrically included potential energy of the nuclei interactions $E_{V_{KK}}$.

$$E = E_T + E_{V_{eK}} + E_J + E_X + E_C + E_{V_{KK}} \quad (2.6)$$

Herein, the terms E_V and E_J can be easily expressed in terms of density functionals:

$$E_{V_{eK}} = - \sum_{a=1}^K Z_a e \int \frac{\rho(\vec{r})}{|\vec{R}_a - \vec{r}|} dV \quad (2.7)$$

$$E_J = \frac{1}{2} \int \int \frac{\rho(\vec{r}_i)\rho(\vec{r}_j)}{r_{ij}} dV_i dV_j \quad , \quad (2.8)$$

whereas Z represents the atomic number of the K atoms indexed with a , e is the elementary charge and $|\vec{R}_a - \vec{r}|$ is the distance from nucleus a to the point of integration \vec{r} . Unfortunately, comparable expressions are not possible for E_T , E_X and E_C .

The problem was solved by using orbitals as transferred from the HF-theory and solving one-electron eigenvalue equations (see 2.9) via the variation principle.

$$\left\{ -\frac{\hbar^2}{2m_e}\Delta_i - \sum_{a=1}^K \frac{Z_a e^2}{r_{ai}} + \sum_{\substack{l=1 \\ l \neq k}}^N \int \frac{e^2 \psi_l^*(\vec{r}_j) \psi_l(\vec{r}_j)}{r_{ij}} dV_j + U_{XC} \right\} \psi_k(\vec{r}_i) = \epsilon_k \psi_k(\vec{r}_i) \quad (2.9)$$

In contrast to the HF-equations, equation 2.9 contains the electron correlation and exchange term combined in the *exchange-correlation-potential* $U_{XC}[\rho] = \frac{\partial E_{XC}[\rho]}{\partial \rho}$ with $E_{XC} = E_X + E_C$. The one-electron functions $\psi_k(\vec{r}_i)$ are the *Kohn-Sham* orbitals. The effective field acting on the electrons is determined via SCF methods (self-consistent field).

The kinetic energy of the electrons E_T (eq. 2.10), the potential energy of the electron-nuclei interaction E_V (eq. 2.11) and the Coulomb energy of the electrons E_J (eq. 2.12) can be calculated as follows:

$$E_T = \sum_{k=1}^N \int \psi_k^*(\vec{r}) \left[-\frac{\hbar^2}{2m_e}\Delta_i \right] \psi_k(\vec{r}_i) dV_i \quad (2.10)$$

$$E_V = - \sum_{a=1}^K \sum_{k=1}^N \int \psi_k^*(\vec{r}) \frac{Z_a e^2}{r_{ai}} \psi_k(\vec{r}_i) dV_i \quad (2.11)$$

$$E_J = \frac{1}{2} \sum_{k=1}^N \sum_{\substack{l=1 \\ l \neq k}}^N \int \int \psi_k^*(\vec{r}_i) \psi_l^*(\vec{r}_j) \frac{e^2}{r_{ij}} \psi_k(\vec{r}_i) \psi_l(\vec{r}_j) dV_i dV_j \quad (2.12)$$

Unfortunately, similar expressions are not known for the exchange and correlation energies E_X and E_C which were aimed to be expressed in terms of density functionals: $E_X = E_X[\rho]$ and $E_C = E_C[\rho]$. The calculation of ρ is facilitated by the solution of equation 2.9 on the basis of orbitals as shown in equation 2.13.^a

$$\rho(\vec{r}) = \sum_k b_k e \psi_k^*(\vec{r}) \psi_k(\vec{r}) = \sum_k b_k e |\psi_k(\vec{r})|^2 \quad (2.13)$$

If ρ is involved in the E_{XC} functionals just via the value of $\rho(\vec{r})$ at the point \vec{r} , referred to as *local density approximation* (LDA), no reliable energies are obtained. Significant improvements were achieved by applying non-local corrections, in particular *gradient corrections*. The gradient corrected density functionals (also: *generalized gradient approximation* (GGA)) involve the gradient of the density $\nabla \rho = \partial \rho / \partial \vec{r}$ facilitating the treatment

^a e is the elementary charge and b_k is occupation number of the k^{th} orbital.

of inhomogenities in the ρ -distribution. If the exchange energy is calculated by involving the HF-exchange expression, the density GGA-functionals are called *hybrid functionals* and are not local anymore.

One of the most frequently applied density functionals is B3LYP, which is a hybrid functional shown to lead to reliable molecular geometries, energies and various properties in numerous publications.^{115–119} The corresponding exchange-correlation functional is constructed as follows:

$$E_{XC}^{B3LYP} = (1 - A)E_X^{Slater} + AE_X^{HF} + BE_X^{Becke} + CE_C^{LYP} + (1 - C)E_C^{VWN} \quad (2.14)$$

The exchange functionals are the one of Slater, the regular HF and the gradient corrected part of Becke's exchange functional and the correlation functionals are from Lee, Yang, Parr (LYP) and Vosko, Wilk and Nusair (VWN).^{120–122} In common quantum mechanical programs the parameter A is 0.2, B and C amount 0.72 and 0.81, respectively.¹²³

However, the GGA functional BP86^{121,124,125} was also shown to give reliable geometries, energies and in particular Raman spectra.^{7,78,92,94,105,126} The exchange part of BP86 contains Slater and Becke (B88) functionals and the correlation part contains the functionals of Vosko, Wilk and Nusair (VWN) and of Perdew (P86) as shown in eq. 2.15.^{127–131}

$$E_{XC}^{BP86} = E_X^{Slater} + E_X^{Becke} + E_C^{VWN} + E_C^{P86} \quad (2.15)$$

When applying the BP86 functional the density can be treated local (the HF-term is not included in E_{XC}) and the resolution of identity (RI) option can be used which downscales the dependency of the computational effort from N^4 to N^3 , with N being the number of basis functions.^{132–135} For very large systems or for preoptimizations the multipole accelerated resolution of identity (marij) option was used, thus further downscaling the computational effort to $N^{1.5}$.¹³¹ Due to the possibility to use such fast techniques and the high performance in simulating Raman spectra without applying scaling factors, the BP86 functional was used preferentially in the present work.

According to literature MP2-calculations^{93,107,108,136} (Møller-Plesset perturbation theory of order 2) were performed to approve BP86 calculated results to be reasonable.¹⁰⁴ Within MP-calculations the correlation energy is estimated via introducing a perturbation operator \hat{V} :

$$\hat{H} = \hat{H}^{(0)} + \lambda\hat{V} \quad (2.16)$$

The energy is expanded in a series according equation 2.17, whereas $E^{(0)} + E^{(1)}$ corresponds to the SCF energy of a HF-calculation and the higher terms correspond to correlation energies.

$$E_0 = E^{(0)} + E^{(1)} + E^{(2)} + E^{(3)} + \dots \quad (2.17)$$

In MP2-calculations $E^{(2)}$ is the highest considered term and therefore is the term accounting for electron correlation as shown in eq. 2.18.^b

$$E^{(2)} = - \sum_a^{\text{occ}} \sum_{b>a}^{\text{occ}} \sum_r^{\text{virt}} \sum_{s>r}^{\text{virt}} \frac{|\langle \psi_a(i) \psi_b(j), \frac{e^2}{r_{ij}} [\psi_r(i) \psi_s(j) - \psi_s(i) \psi_r(j)] \rangle|^2}{\epsilon_r + \epsilon_s - \epsilon_a - \epsilon_b} \quad (2.18)$$

The quality of the results of DFT as well as of MP2 calculations further depends on the basis sets chosen. In the present work Ahlrich's type basis sets leading to excellent results in combination with the BP86 functional for geometries, energies and Raman spectra as well as the popular Pople basis sets were applied.

Every SCF cycle starts with a certain set of molecular orbitals $\phi_n(i)$ (MOs) which are created via linear combinations of atomic orbitals χ_μ (LCAO method) corresponding to 2.19:

$$\phi_n(i) = \sum_{\mu=1}^M c_{n\mu} \chi_\mu(i) \quad (2.19)$$

The exact functions for hydrogen comparable atoms are very similar to *Slater* functions possessing a negative exponential radial decay $e^{-\zeta r}$, whereas ζ is the so-called *Slater exponent*. Unfortunately, Slater functions are very difficult to integrate efficiently if the functions are ranging over several centers. Alternatively, *Gauß* functions were used to describe AOs which can be treated computationally much more efficiently. The deviation in the decay character due to the squared exponent $e^{\alpha r^2}$ (α : *Gauß exponent*) from the optimal Slater-type behavior is compensated by using many Gauß functions instead of one Slater function, leading to still significantly faster computations. For example, in a STO-3G basis set one Slater function is approximated via one contracted Gauß function constituted from three primitive Gauss functions.

A very successful compromise between reliable results and computational cost was the implementation of *split valence* basis sets where the core atomic orbitals are described by one contracted or primitive Gauß function and the valence orbitals are simulated via multiple (ζ) Gauss functions.

For example, the triple- ζ Pople basis set 6-311+G(3df)¹³⁷⁻¹⁴² used in this work in combination with MP2, which is known to give reliable electron density values,¹⁰⁴ is composed as follows: the core AOs are described via one contracted Gauß function (constituted of six primitives) and the valence AOs are approximated using one contracted (constituted of three primitives) and two primitive Gauß functions, what is indicated by 6-311G (scheme: [6/311]). The term "triple- ζ " results from the usage of three Gauß functions

^bThe summation runs over all occupied (*occ*, *a*, *b*) and virtual (*virt*, *r*, *s*) spin-orbitals, ϵ are the corresponding eigenvalues, e is the elementary charge, and r_{ij} is the distance between electron i and j .

(one contracted and two primitives) for the valence AOs. In 6-311+G(3df) the 6-311G basis set is supplemented by diffuse functions (+) and further by three sets of d and one set of f-functions for heavy atoms.¹⁴³

Within the present work Ahlrich's type triple- ζ basis set TZVP^{144,145} with polarization functions on all atoms was used preferentially, since it was shown to give accurate molecular structures, frequencies and Raman intensities for medium sized molecules^{78,92,126} in combination with - and recommended for - BP86. TZVP consists of 5s1p functions contracted to 3s1p for H (according to scheme [311/1]) and 11s6p1d functions contracted to 5s3p1d according to [62111/411/1] for B to Ne. Preoptimizations were performed using the basis set SVP (Be-Ne:[511/31]).¹⁴⁴ Generally, the program Turbomole (TM)¹⁴⁶ was applied for the DFT calculations presented within this work, except section 4.2 where the program Gaussian03 (g03)¹⁴⁷ was used.

Vibrational spectra were calculated using the program SNF,⁹⁴ TM's module Aoforce or the internal module in g03.¹⁴⁸

2.2.2 The quantum theory of atoms in molecules

As mentioned in section 2.1, Baders quantum theory of atoms in molecules (QTAIM) is a method to characterize the electron density distribution $\rho(\mathbf{r})$ via the properties in turning points of $\rho(\mathbf{r})$ called critical points (CPs). Furthermore, the theory enables the real space partitioning of the molecular $\rho(\mathbf{r})$ to yield uniquely defined atomic regions composing the molecule.

The CPs of the ρ -distribution are classified by the curvatures of $\rho(\mathbf{r})$ at the turning points. The curvatures are expressed by the second derivatives of $\rho(\mathbf{r})$, which are included in the Hesse matrix H (3×3 matrix in the cartesian frame). Diagonalization of H leads to D , including the eigenvectors of H , which are the three principal curvatures of $\rho(\mathbf{r})$ λ_i (equation 2.20).

$$D(\mathbf{r}) = \begin{pmatrix} \frac{\partial^2 \rho}{\partial x^2} & 0 & 0 \\ 0 & \frac{\partial^2 \rho}{\partial y^2} & 0 \\ 0 & 0 & \frac{\partial^2 \rho}{\partial z^2} \end{pmatrix} = \begin{pmatrix} \lambda_1 & & \\ & \lambda_2 & \\ & & \lambda_3 \end{pmatrix} \quad (2.20)$$

If a local maximum in $\rho(\mathbf{r})$ is present (i.e. at the positions of the nuclei) all curvatures, and with it the three hessian eigenvalues λ_i , are negative and the CP is labelled (3,-3) and called an attractor point. The first entry in the latter notation corresponds to the number of hessian eigenvectors and the latter entry is the sum over the algebraic signs of the eigenvectors. Therefore, i.e. a local minimum in $\rho(\mathbf{r})$, like present in cages, is labelled as a (3,+3) CP since the curvatures (the three eigenvalues of the Hessian) are positive. A saddle point with one maximum in $\rho(\mathbf{r})$, hence possessing one negative eigenvalue of the Hessian, and two minima (positive second derivatives of $\rho(\mathbf{r})$) as for the case in the middle

of rings (i.e. benzene), the CP is labelled (3,+1). The other possibility of a saddle point is the presence of two negative and one positive eigenvalue of the Hessian, labelled (3,-1). This is the case for bonds where in two perpendicular directions orthogonal to the bond elongation maxima in $\rho(\mathbf{r})$ and along the bond a minimum in $\rho(\mathbf{r})$ is present. Therefore, the (3,-1) CPs are abbreviated as BCPs (bond critical point). The nomenclature of CPs is summarized in table 2.1.

Table 2.1: Overview over the different CPs defined within the QTAIM

abbreviations	notation $\left(n, \sum_{i=1}^n \frac{\lambda}{ \lambda_i }\right)$	name	signs of Hessian eigenvalues
ACP	(3,-3)	attractor critical point	-, -, -
BCP	(3,-1)	bond critical point	-, -, +
RCP	(3,+1)	ring critical point	-, +, +
CCP	(3,+3)	cage critical point	+, +, +

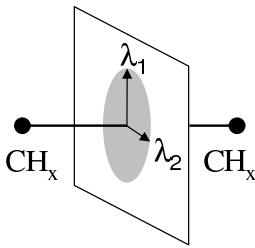
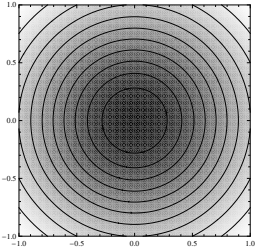
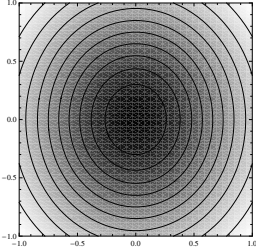
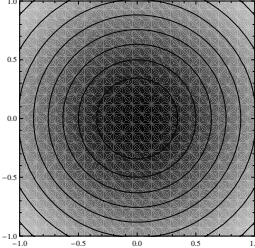
Properties of $\rho(\mathbf{r})$ within a CP which are usually studied are the electron density within the point itself (ρ), the corresponding gradients and the ellipticity ε . The ellipticity is defined according to equation 2.21 and is a measure of the π -character of double bonds. A perfect σ -bond with a rotational symmetric ρ -distribution for example would possess $\varepsilon=0$ within the respective bond critical point, since the magnitudes of the two eigenvalues λ_1 and λ_2 corresponding to the maxima in $\rho(\mathbf{r})$ in the BCP are identical. Also triple bonds with an almost rotational symmetric charge distribution are possessing ε -values close to zero, whereas ε in the CC-BCPs of ethene or benzene amounts ≈ 0.28 and ≈ 0.16 , for example.

$$\varepsilon = \frac{|\lambda_1|}{|\lambda_2|} - 1 \quad (2.21)$$

In table 2.2 properties of the ρ -distribution in the carbon-carbon bonds of ethane, ethene (ethylene) and ethyne (acetylene) are compared. The contour plots show $\rho(\mathbf{r})$ within a plane ($2 \times 2 \text{ \AA}$) perpendicular to the CC-bond, with the origin located in the middle of the CC-bond. The rotational symmetric ρ -distributions in the case of ethane and ethyne, as visualized by the contour plots, are causing the low ε -values, also shown in table 2.2. The deformation of $\rho(\mathbf{r})$ in the case of ethene is pronounced, whereas the ratio between λ_1 and λ_2 is roughly 1.28 as $\varepsilon \approx 0.28$ suggests. The electron density within the BCPs is systematically increased from ethane to ethene to ethyne.

The CPs can be localized by following the trajectories of $\rho(\mathbf{r})$ starting and ending at $\partial\rho/\partial r = 0$. This condition is fulfilled at the outer "edge" of a molecule and in the CPs for which reason each trajectory leads from the "edge" of a molecule to a critical point. In theoretical simulations the positions of the nuclei, and with it the positions of the ACPs,

Table 2.2: ρ -distribution in the CC-bonds, ρ and ε within the respective BCPs of ethane, ethene (ethylene), ethyne (acetylene)

	ethane	ethene	ethyne
			
$\varepsilon(\text{CC-BCP})$:	0.0001	0.2766	$2 \cdot 10^{-6}$
$\rho(\text{CC-BCP}) [e/\text{\AA}^3]$:	0.2272	0.3303	0.3948

are already known and the search for BCPs starts at the average values of the coordinates of neighboring nuclei. If a BCP is found between atom A and B, a bond between A and B is thusly defined within QTAIM. In this case two trajectories are present starting from the BCP and ending up either in atom A or B. This couple of trajectories is called a bond path. All trajectories starting at the molecules "edge" and are ending in a BCP are forming surfaces dividing the molecule into atomic basins. The thusly formed surfaces are called surface of zero flux. Hence, within the QTAIM no particular part of the molecular $\rho(r)$ is assigned to bonds connecting atoms but the atoms share surfaces of zero flux and bonds are defined via bond paths and bond critical points.

Due to the surfaces of zero flux the atomic volumes Ω are well-defined and the atomic charge q can be calculated by subtracting the number of electrons N_Ω within the atomic volume Ω from the nuclear charge $Z \cdot e$ (Z being the atomic number and e the elementary charge) according equation 2.22, whereas N is usually not an integer number. Further properties, like dipole moments or higher, can be calculated accordingly.

$$q_i = e \left(Z_i - \int_{\Omega_i} \rho(r) dr \right) \quad (2.22)$$

In conclusion, the AIM theory facilitates the calculation of certain properties of well-defined atoms in molecules and furthermore offers a possibility to characterize molecular key regions by particular properties of $\rho(r)$ in well-defined points. For example, bonds can be characterized by properties of $\rho(r)$ (i.e. with ρ or ε) within the respective bond critical points.

2.3 Vibrational spectroscopy

Vibrational spectroscopy can be applied to determine molecular structures via reference spectra (experimental or theoretical) or to quantify concentrations via the law of Lambert

and Beer (IR-absorption spectroscopy only) or calibration functions. For structure evaluation vibrational spectroscopy is a powerful tool since even large and complex molecules are possessing unique vibrational spectra which are denoted as molecular fingerprints in the literature.^{25, 80, 149}

If a molecular structure can not be unraveled by means of vibrational spectroscopy, usually still important structural information can be extracted from IR or Raman spectra. For example, the majority of functional groups possesses characteristic IR- or Raman-bands from which one can conclude on their presence. Typically, such characteristic bands correspond to vibrational pictures, called normal modes (see section 2.3.1), which are well located on the respective functional groups ^c. An example of a vibrational picture restricted to just one bond is the stretching vibration between carbon and deuterium $\nu(\text{CD})$ in mono-deuterated substances ^d which are employed in the present work (see section 4.2). In such cases, where the normal mode is restricted to just one bond, the energetic location of the vibrational band is related to the bond character which is defined by the electron density distribution. Hence, vibrational spectroscopy offers a method to investigate the nature of chemical structures if the normal modes are known. The calculation of normal modes and the respective wavenumbers is illustrated in section 2.3.1.

The intensities of bands in IR-spectra depend on the change of the dipole moment during a vibration, whereas the Raman intensity depends on the change of the molecular polarizability upon vibration. In conjunction with the energetic location of the bands both quantities provide the characteristic pattern in IR and Raman spectra, respectively. In general and particularly for molecules possessing a center of inversion Raman and IR spectra contain complementary information. Furthermore, due to applying polarized radiation and linear analyzers symmetry properties of molecules can be derived. Calculation of IR- and Raman-intensities is discussed in section 2.3.2.

The particular focus of the present work lies on Raman spectroscopy, which underwent a renaissance due to the development of LASERs ^e. However, the Raman effect was already observed in 1928 by Raman and Krishnan¹⁵⁰ and independently by Landsberg and Mandelstam^{151, 152} during the investigation of light-scattering on fluids and on crystals, respectively. Theoretical investigations concerning light-scattering on an anharmonic oscillator were already published by Lommel in 1871.¹⁵³ In 1923 studies of Smekal were released.^{25, 80, 154}

Nowadays, Raman spectroscopy is a frequently applied technique in almost all natural science disciplines.^{80, 155, 156} For example, in life sciences Raman microspectroscopy (i.e.

^cusually a couple of normal modes are not related to a defined characteristic group but involve almost the whole molecule

^d $\tilde{\nu}(\text{CD})$ lies in a well separated energy-range around 2300 cm^{-1} ; no coupling to other modes

^eLASER: Light Amplification by Stimulated Emission of Radiation

combination of Raman spectroscopy with a light microscope) facilitates label-free microscopic pictures based on chemical information.^{157–160} Since the Raman process is a very weak one Raman signal enhancing techniques like SERS^{161–165} (Surface Enhanced Raman Scattering) and RRS^{64,79,166–171} (Resonance Raman Scattering) are applied. They permit the detection of ultra-low concentrated substances. Furthermore, RRS is applied to study the initial step in photo-excitation, i.e the Franck-Condon point, the symmetry and even the equilibrium geometry. In the present work RRS is applied to study MLCT transitions in Ru(II)-complexes as described in chapter 5. A basic theory of resonance Raman enhancement is outlined in section 2.3.3.

2.3.1 Normal modes and vibrational transition energies

Normal modes are independent (orthogonal) vibrational coordinates possessing a defined vibrational potential determining vibrational quantum states i and with it vibrational transition energies E_i . In the harmonic approximation^f all vibrational states within a certain potential are equidistant and the respective energy difference depends on the vibrational frequency ν according to equation 2.23. Furthermore, ν is related to the steepness of the potential and is proportional to the root of the force constant f according equation 2.24. Hence, a bond-located vibrational transition energy mirrors the bond strength^{25,80,149,172 g}.

$$E_i = h \cdot \nu(v_i + 1/2) \quad (2.23)$$

$$\nu \propto \sqrt{f/\mu} \quad (2.24)$$

Normal modes can be derived classically by solving the equation of motion according Newtonian mechanics involving all $3N$ degrees of freedom of a molecule constituted of N atoms. Along the calculations mass-weighted cartesian coordinates are introduced, the Hesse-matrix is diagonalized and furthermore 3 translational and 3 rotational (2 for linear molecules) modes are projected out. Hence, a non-linear molecule in the gasphase^h possesses $3N - 6$ normal modes ($3N - 5$ for linear molecules) with their individual potentials, force constants f and reduced masses μ ⁱ.

^fwell suited to describe the bottom of a vibrational potential, i.e. the fundamental transition $v = 1 \leftarrow v = 0$; to account for an anharmonic character and particularly for dissociation processes the Morse potential was derived empirically by fitting a quadratic negative e -function with negative exponent yielding $U = hcD_{eq}(1 - e^{-a(r-r_0)})^2$

^g μ is the reduced mass; $\frac{1}{\mu} = \frac{1}{m_1} + \frac{1}{m_2}$ for a diatomic molecule

^hi.e. in solids the situation is more complicated in cause of lattice vibrations and frustrated translations^{25,80,173,174}

ⁱexcept degenerated modes

The nuclear coordinates of a vibration are defined as follows: $x_\alpha = a_\alpha - a_{\alpha,e}$, $y_\alpha = b_\alpha - b_{\alpha,e}$, $z_\alpha = c_\alpha - c_{\alpha,e}$:

$$\begin{aligned} (x, y, z)_\alpha & \quad \text{atomic oscillation coordinates} \\ (a, b, c)_\alpha & \quad \text{molecule fixed coordinates} \\ (a, b, c)_{\alpha,e} & \quad \text{molecule-fixed equilibrium coordinates} \end{aligned}$$

The kinetic energy of a vibration is expressed classically according equation 2.25:

$$T = \frac{1}{2} \sum_{\alpha=1}^N m_\alpha \left[\left(\frac{dx_\alpha}{dt} \right)^2 + \left(\frac{dy_\alpha}{dt} \right)^2 + \left(\frac{dz_\alpha}{dt} \right)^2 \right] \quad (2.25)$$

The introduction of mass-weighted coordinates $q_{3N} = m_N^{1/2} z_N$ leads to:

$$\begin{aligned} T &= \frac{1}{2} \sum_{\alpha=1}^{3N} \left(\frac{dq_i}{dt} \right)^2 \quad \text{or} \\ T &= \frac{1}{2} \sum_{\alpha=1}^{3N} \dot{q}_i^2 \equiv \frac{1}{2} \dot{\mathbf{q}}^2 = \frac{1}{2} \dot{\mathbf{q}} \cdot \dot{\mathbf{q}} \quad , \end{aligned} \quad (2.26)$$

if matrix notation is applied, whereas the latter term is the dot product of the row and column vector containing the \dot{q}_i .

The potential energy $U(q_1, \dots, q_{3N})$ is approximated via a Taylor series expansion about the equilibrium body-fixed coordinates.

$$\begin{aligned} U &= U_e + \sum_{i=1}^{3N} \left(\frac{\partial U}{\partial q_i} \right)_e q_i + \frac{1}{2} \sum_{i=1}^{3N} \sum_{k=1}^{3N} \left(\frac{\partial^2 U}{\partial q_i \partial q_k} \right)_e q_i q_k \\ &+ \frac{1}{6} \sum_{i=1}^{3N} \sum_{j=1}^{3N} \sum_{k=1}^{3N} \left(\frac{\partial^3 U}{\partial q_i \partial q_j \partial q_k} \right)_e q_i q_j q_k + \dots \end{aligned} \quad (2.27)$$

The reference energy U_e can be set zero by definition, the first derivative of the potential is also zero for an energy-minimum as present in an optimized geometry ($(\partial U / \partial q_i)_e \approx 0$). Furthermore, in the harmonic approximation $(\partial^3 U / \partial q_i \partial q_j \partial q_k)_e$ and higher terms are neglected, hence leading to:

$$U \approx \frac{1}{2} \mathbf{q}' \mathbf{U} \mathbf{q} \quad , \quad (2.28)$$

whereas \mathbf{q}' is the transposed \mathbf{q} and \mathbf{U} the matrix of all second derivatives of U .

$$U_{ik} = \frac{\partial^2 U}{\partial q_i \partial q_k} = (m_i m_k)^{-1/2} (k_i k_k)^{1/2} \quad (2.29)$$

Applying the derived expressions for the kinetic and the potential energy the equation of motion $F = m \cdot a$ can be solved. F can be expressed as follows:

$$F_{x,\alpha} = - \frac{\partial U}{\partial x_\alpha} = - \frac{\partial U}{\partial q_j} \frac{\partial q_j}{\partial x_\alpha} = - m_\alpha^{1/2} \frac{\partial U}{\partial q_j} \quad (2.30)$$

with $q_j = m_\alpha^{1/2} x_\alpha$ and $(\partial q_j / \partial x_\alpha) = m_\alpha^{1/2}$.

Furthermore, $m \cdot a$ can be written according equation 2.31 applying $q_j = m_\alpha^{1/2} x_\alpha \rightarrow x_\alpha = q_j / m_\alpha^{1/2}$.

$$a = \frac{d^2 x_\alpha}{dt^2} = \frac{d^2}{dt^2} \left(\frac{q_i}{m_\alpha^{1/2}} \right) = m_\alpha^{-1/2} \frac{d^2 q_j}{dt^2} \quad (2.31)$$

Inserting equation 2.30 and 2.31 in $F = m \cdot a$ yields:

$$\begin{aligned} -m_\alpha^{1/2} \frac{\partial U}{\partial q_j} &= m_\alpha^{1/2} \frac{d^2 q_j}{dt^2} \\ \frac{d^2 q_j}{dt^2} + \frac{\partial U}{\partial q_j} &= 0 \end{aligned} \quad (2.32)$$

for $j = 1, \dots, 3N$. These $3N$ systems of equations can be simplified, since

$$U \approx \frac{1}{2} \sum_{i=1}^{3N} \sum_{k=1}^{3N} U_{ik} q_i q_k \quad (2.33)$$

(see eq. 2.28ⁱ) and only one of the sums survives the partial derivative, yielding:

$$\frac{d^2 q_j}{dt^2} + \frac{1}{2} \sum_{k=1}^{3N} U_{jk} q_k = 0 \quad j = 1, \dots, 3N \quad (2.34)$$

This set of $3N$ differential equations, each involving $3N$ coordinates, can be simplified since the matrix \mathbf{U} containing all U_{jk} is real and symmetric and \mathbf{U} can be diagonalized applying the matrix \mathbf{L} :

$$\mathbf{UL} = \mathbf{L}\mathbf{\Lambda} \Leftrightarrow \mathbf{L}'\mathbf{UL} = \mathbf{\Lambda} \quad (2.35)$$

The application of the transposed diagonalization matrix \mathbf{L}' on the mass-weighted cartesian coordinates \mathbf{q} gives the normal coordinates \mathbf{Q} , since $\mathbf{q} = \mathbf{LQ}$:

$$\mathbf{Q} = \mathbf{L}'\mathbf{q} \quad \text{or} \quad Q_i = \sum_{k=1}^{3N} l_{ki} q_k \quad (2.36)$$

Substituting eq. 2.36 in 2.28 yields:

$$U = \frac{1}{2} (\mathbf{LQ})' \mathbf{U} (\mathbf{LQ}) = \frac{1}{2} \mathbf{Q}' \mathbf{L}' \mathbf{U} \mathbf{L} \mathbf{Q} = \frac{1}{2} \mathbf{Q}' \mathbf{\Lambda} \mathbf{Q} \quad (2.37)$$

As just outlined, the transformations lead to $U \approx \frac{1}{2} \mathbf{Q}' \mathbf{\Lambda} \mathbf{Q}$ (eq. 2.37) starting from $U \approx \frac{1}{2} \mathbf{q}' \mathbf{U} \mathbf{q}$ (eq. 2.28, whereas U involves the *double sum* as shown in eq. 2.33). Eq. 2.37 is a significant simplification of eq. 2.28 since $\mathbf{\Lambda}$ is a diagonal matrix leading to a *single sum* over the trace of $\mathbf{\Lambda}$ according eq. 2.38.

$$U = \frac{1}{2} \sum_{k=1}^{3N} \lambda_k Q_k^2 = \frac{1}{2} \sum_{k=1}^{3N-6} \lambda_k Q_k^2 \quad (2.38)$$

ⁱ U_{ik} being the force constants between atoms i and k with displacements in q_i and q_k

In the case of translations and rotations no change in the potential is present for which reason the respective $\lambda_k Q_k^2$ are zero, hence reducing the sum from $3N$ to $3N - 6$ or $3N - 5$ for linear molecules.

The kinetic energy T (see eq. 2.26) has to be transformed likewise:

$$T = \frac{1}{2} \dot{\mathbf{q}}' \dot{\mathbf{q}} = \frac{1}{2} (\mathbf{L}\dot{\mathbf{Q}})' \mathbf{L}\dot{\mathbf{Q}} = \frac{1}{2} \dot{\mathbf{Q}}' \mathbf{L}' \mathbf{L} \dot{\mathbf{Q}} = \frac{1}{2} \dot{\mathbf{Q}}' \dot{\mathbf{Q}} \quad (2.39)$$

Thus, expressing the equation of motion in eq. 2.34 in normal coordinates yields (applying eq. 2.39):

$$\frac{\partial^2 Q_k}{\partial t^2} + \frac{\partial U}{\partial Q_k} = 0 \quad k = 1, \dots, 3N \quad (2.40)$$

Applying eq. 2.38 leads to:

$$\frac{\partial^2 Q_k}{\partial t^2} + \lambda_k Q_k = 0 \quad k = 1, \dots, 3N \quad (2.41)$$

The solution of this set of $3N$ differential equations can be derived classically yielding ^k:

$$Q_k = B_k \sin(\lambda_k^{1/2} t + b_k) \quad k = 1, \dots, 3N \quad (2.42)$$

Since eq. 2.42 is a solution of eq. 2.41, the $\lambda_k^{1/2}$ are the vibrational angular velocities which can be easily transformed to frequencies ν_k and to vibrational wavenumbers $\tilde{\nu}_k$:

$$\nu_k = \frac{\lambda_k^{1/2}}{2\pi}, \quad \tilde{\nu}_k = \sqrt{\frac{\lambda_k}{4\pi^2 c^2}} \quad (2.43)$$

With it, the vibrational transition energies $\tilde{\nu}_k$ for every normal mode k and the normal coordinates are calculated. Hence, $\tilde{\nu}_k$ may be assigned to molecular substructures. The λ_k are related to force constants in terms of normal coordinates.

2.3.2 IR and Raman intensities

The disquisition on **IR-intensities** is limited to a basic consideration since this technique was not applied experimentally in the present work. Detailed papers can be found elsewhere.^{80,149}

The most important relation in IR spectroscopy is the dependency of the IR intensity on the change of the dipole moment μ during a vibration along a normal mode Q_k according:

$$I_k^{IR} \propto \left(\frac{\partial \mu}{\partial Q_k} \right)_0^2 \quad (2.44)$$

Hence, also non-polar molecules like CO_2 may exhibit IR-active vibrational transitions if $\frac{\partial \mu}{\partial Q_k} \neq 0$, i.e. as true for the asymmetric stretching vibration in CO_2 .

^ksimplification of eq. 2.42: $Q_k = \sin(\sqrt{\lambda_k} t)$; insertion in eq. 2.41: $(\lambda_k - \lambda_k) \sin(\sqrt{\lambda_k} t) = 0$

In contrast, **Raman intensities** depend on the change of the polarizability α during a vibration along a normal mode Q_k according:

$$I_k^{Raman} \propto \left(\frac{\partial \alpha}{\partial Q_k} \right)_0^2 \quad (2.45)$$

In general, the Raman effect is caused by inelastic light scattering. The intensity of the scattered light in certain directions depends on the induced dipole moment, which is related to the electric field vector of the incident radiation due to the polarizability tensor α :¹⁷⁵

$$\tilde{\mu} = \alpha \tilde{\mathbf{E}} \quad (2.46)$$

I.e., if linear polarized incident light is used (z-direction) eq. 2.46 becomes:

$$\begin{pmatrix} \mu_x \\ \mu_y \\ \mu_z \end{pmatrix} = \begin{pmatrix} \alpha_{xx} & \alpha_{xy} & \alpha_{xz} \\ \alpha_{yx} & \alpha_{yy} & \alpha_{yz} \\ \alpha_{zx} & \alpha_{zy} & \alpha_{zz} \end{pmatrix} \begin{pmatrix} 0 \\ 0 \\ E_z \end{pmatrix} = \begin{pmatrix} \alpha_{xz} E_z \\ \alpha_{yz} E_z \\ \alpha_{zz} E_z \end{pmatrix} \quad (2.47)$$

If an analyzer is applied additionally to detect exclusively x-polarized light eq. 2.46 becomes:

$$\mu_x = \alpha_{xz} E_z. \quad (2.48)$$

If the electric field oscillates with ν , than $\vec{E} = \vec{E}_0 \cdot \cos \nu t$ and the induced dipole moment $\vec{\mu}_{ind}$ oscillates with the same frequency:

$$\vec{\mu}_{ind} = \alpha \vec{E}_0 \cdot \cos \nu t \quad (2.49)$$

Since the molecular polarizability α depends on the molecular geometry and electron density distribution, α is modulated by molecular vibrations. To account for this effect, α can be expanded in a Taylor series at the equilibrium positions, since the molecular distortions are small:

$$\alpha(Q_k) = \alpha_0 + \left(\frac{\partial \alpha}{\partial Q_k} \right)_0 Q_k + \dots \quad (2.50)$$

The oscillation with the frequency ν along a normal mode is assumed to follow equation 2.51:

$$Q_k = Q_{k0} \cos \nu_k t \quad (2.51)$$

Substitution of eq. 2.51 and eq. 2.50 in eq. 2.49 yields:

$$\vec{\mu}_{ind} = \left[\alpha_0 + \left(\frac{\partial \alpha}{\partial Q_k} \right)_0 Q_{k0} \cos \nu_k t \right] \vec{E}_0 \cdot \cos \nu t \quad (2.52)$$

Trigonometric transformation leads to:

$$\begin{aligned} \vec{\mu}_{ind} = \alpha_0 \vec{E}_0 \cdot \cos \nu t + \frac{1}{2} \left(\frac{\partial \alpha}{\partial Q_k} \right)_0 Q_0 \vec{E}_0 \cdot \cos(\nu - \nu_k) t \\ + \frac{1}{2} \left(\frac{\partial \alpha}{\partial Q_k} \right)_0 Q_0 \vec{E}_0 \cdot \cos(\nu + \nu_k) t \quad , \end{aligned} \quad (2.53)$$

in other terms:

$$\vec{\mu}_{ind} = \vec{\mu}_{Rayleigh} + \vec{\mu}_{Stokes} + \vec{\mu}_{Anti-Stokes} \quad , \quad (2.54)$$

whereas Stokes is synonymous for Raman in this case. Hence:

$$\vec{\mu}_{Raman} = \frac{1}{2} \left(\frac{\partial \alpha}{\partial Q_k} \right)_0 Q_0 \vec{E}_0 \cdot \cos(\nu - \nu_k) t \quad (2.55)$$

To calculate the corresponding Raman intensity the equation defining the radiation intensity in the solid angle 4π of an Herzian dipole source is applied:

$$I_0 = \frac{3\bar{P}}{8\pi} = \frac{|\ddot{\mu}|^2}{16\pi^2 \epsilon_0 c^3} = \frac{\nu^4}{32\pi^2 \epsilon_0 c^3} \vec{\mu}_0^2 \quad , \quad (2.56)$$

whereas $\vec{\mu} = \vec{\mu}_0 \cos \nu t$, $\ddot{\mu} = -\vec{\mu}_0 \nu^2 \cos \nu t$ and $\cos^2 \nu t = 1/2$.

Inserting eq. 2.55 into eq. 2.56 and introducing the substitution $\vec{E}_0^2 = \frac{2}{\epsilon_0} I_0$ leads to relation 2.57:

$$I_k^{Raman} \propto \nu^4 I_0 \left(\frac{\partial \alpha}{\partial Q_k} \right)_0^2 \quad (2.57)$$

Schrötter and Klöckner⁸⁰ derived an expression for the absolute differential Raman scattering cross-section, which is proportional to the observed radiant power:¹

$$\left(\frac{d\sigma}{d\Omega} \right)_{k\perp}^- = \frac{\pi^2}{45\epsilon_0^2} \cdot \frac{b_k^2 \cdot (\tilde{\nu}_0 - \tilde{\nu}_k)^4}{1 - e^{-hc\tilde{\nu}_k / kT}} \cdot g_j \cdot (45\bar{\alpha}'_k{}^2 + 7\bar{\gamma}'_k{}^2) \cdot L \quad (2.58)$$

In eq. 2.58 σ is the cross section, Ω is the solid angle, \perp indicates the detected polarization being perpendicular to the incident one, g_j is the degeneracy of a vibration, $\tilde{\nu}_0$ and $\tilde{\nu}_k$ are the frequencies of the incident radiation and the excited vibration, respectively. Furthermore, $b_k^2 = h/8\pi^2 c \tilde{\nu} k$ and $L = (n_R/n_0)(n_R^2 + 2)^2(n_0^2 + 2)^2/3^4$, L being the internal field vector and n_0 and n_R are the refractive indices at the wavelength of the exciting and the Raman radiation, respectively. $\bar{\alpha}'_k$ (mean polarizability, isotropic part of α) and $\bar{\gamma}'_k{}^2$ (anisotropy) are particular combinations of components of the polarizability tensor α ,

¹ $\left(\frac{d\sigma}{d\Omega} \right)_{k\perp}^-$ refers to a Stokes and $\left(\frac{d\sigma}{d\Omega} \right)_{k\perp}^+$ to an anti-Stokes Raman band. h is the Planck constant, c the speed of light, k is the Boltzmann constant, T is the temperature.

which are invariant to coordinate transformations:

$$\bar{\alpha}' = \frac{1}{3} (\alpha'_{xx} + \alpha'_{yy} + \alpha'_{zz}) \quad (2.59)$$

$$2 \cdot \gamma'^2 = (\alpha'_{xx} - \alpha'_{yy})^2 + (\alpha'_{yy} - \alpha'_{zz})^2 + (\alpha'_{zz} - \alpha'_{xx})^2 + 6 (a'_{xy}{}^2 + a'_{yz}{}^2 + a'_{zx}{}^2) \quad (2.60)$$

$$\rho = \frac{I_{\parallel}}{I_{\perp}} = \frac{3\gamma'^2}{45\bar{\alpha}'^2 + 4\gamma'^2} \quad (2.61)$$

Eq. 2.61 shows the expression for the depolarization ratio ρ which is related to the symmetry of a vibrational transition and hence to the symmetry of the molecule.

Symmetry is an important molecular property determining **selection rules** and therefore facilitating the prediction of IR- or Raman-activity of a vibrational transition. In terms of quantum mechanics the transition probability $A_{vv'}$ is proportional to the square of the induced dipole moment $\vec{M}_{vv'}$ between two states of energies E_v and $E_{v'}$:

$$M_{vv'} = \int_{-\infty}^{+\infty} \psi^*(v) \hat{o} \psi(v') d\tau \quad , \quad (2.62)$$

whereas \hat{o} is the transition operator (IR: \hat{r} , Raman: $\hat{\alpha}$). Consequently, transitions can be observed if $\int_{-\infty}^{+\infty} \psi^*(v) \hat{o} \psi(v') d\tau \neq 0$, what is true if the direct product of the irreducible representations $\Gamma_{\psi(v)} \Gamma_{\hat{o}} \Gamma_{\psi(v')}$ yields the total symmetric irreducible representation. Since $\psi(0)$ transforms totally symmetric and $\Gamma_{\psi(1)} = \Gamma_Q$ the transition probability depends on the symmetry of the normal mode Q and on the availability of a component of \hat{o} fitting the condition $\int_{-\infty}^{+\infty} \psi^*(v) \hat{o} \psi(v') d\tau \neq 0$.¹⁷⁶

2.3.3 Resonance Raman spectroscopy

Utilizing the resonance Raman (RR) effect, Raman bands can be enhanced up to a factor of 10^6 . Furthermore, analyzing the enhancement pattern and assigning RR-bands to the respective normal modes facilitates the description of an electronic transition at the Franck-Condon point as demonstrated in chapter 5 of the present work.

Currently, two theories to explain the RR-effect are applied: the traditional Kramers-Heisenberg-Dirac and the Lee-Heller theory, also called sum-over-state and time-dependent theory, respectively.^{80,149} To illustrate the reason for the outstanding enhancement due to the RR-effect the basic equation of the sum-over-state picture is outlined:

$$(\alpha_{\rho\sigma})_{fi} = \sum_r \left(\frac{\langle f | \mu_{\rho} | r \rangle \langle r | \mu_{\sigma} | i \rangle}{\hbar\omega_{ri} - \hbar\omega_0 - i\Gamma_r} + \frac{\langle f | \mu_{\sigma} | r \rangle \langle r | \mu_{\rho} | i \rangle}{\hbar\omega_{rf} + \hbar\omega_0 - i\Gamma_r} \right) \quad (2.63)$$

In eq. 2.63 ρ and σ indicate dipole components in the cartesian frame and Γ_r is a damping factor which is related to the lifetime of the state r . i, f and r are the initial, the final and

any state of the unperturbed molecule, respectively. I.e., $\langle f|\mu_\rho|r\rangle$ is the ρ th component of the transition dipole moment for the transition $f \leftarrow r$ with the operator in the ρ direction. Furthermore, ω_0 and ω_{ri} are the angular frequencies of the incident radiation and of the transition $r \leftarrow i$, respectively. If the Raman excitation energy lies in the range of an electronic absorption ω_{ri} roughly equals ω_0 (resonance condition), wherefore the denominator of the first term in equation 2.63 gets extremely small. Consequently, this first term gets very large and raises $(\alpha_{\rho\sigma})_{fi}$ dramatically so that one may write if $\omega_0 \approx \omega_{ri}$:

$$(\alpha_{\rho\sigma})_{fi} = \sum_r \left(\frac{\langle f|\mu_\rho|r\rangle\langle r|\mu_\sigma|i\rangle}{\hbar\omega_{ri} - \hbar\omega_0 - i\Gamma_r} \right) \quad (2.64)$$

2.4 Relations between reactivities and spectroscopic properties

Between the forties and the nineties of the past century extensive studies were performed to predict reactivities from spectroscopic data. Since the reactivity is a direct consequence of a present electron density distribution, comparable predictions might be possible for $\rho(r)$ -features by means of spectroscopic data which are broadly applicable and not limited to a particular physical state. Based on thusly derived $\rho(r)$ -features various related properties might be calculated subsequently.

In the past the most popular spectroscopic methods to conclude on $\rho(r)$ -dependent molecular properties were vibrational and NMR spectroscopy which are applicable to molecules in various physical states.⁹¹ Kagiya et al.¹⁷⁷ for example derived a simple relation between the relative electron-donating or -accepting nature of organic compounds and the IR-wavenumber positions of O-D or the C=O stretching bands of deuterated methanol or acetophenone. A frequently used approach to characterize reactivities, being a direct consequence of the respective ρ -distribution, is by means of the Hammett parameter which is based on reaction rate constants.²³⁻²⁵ The Hammett parameter σ quantifies the influence of a substituent X on the reactivity of a substituent or side-chain of benzene derivatives and is related to the reaction rate constant K of the X and Y substituted derivative according the Hammett equation:

$$\lg K - \lg K_0 = \rho\sigma \quad (2.65)$$

K_0 is the reaction rate constant of the exclusively Y substituted reference substance and ρ is a constant accounting for the type and the conditions of the reaction and the properties of Y .

Hansch et al. summarized the extensive work dealing with the application and refinement of the Hammett equation.²⁶ Several studies dealt with the electronic effects of substituents on the ρ -distribution of benzene-derivatives via Hammett parameters based on

NMR-data.^{178,179} Dailey et al. found a linear correlation between ρ in the *para*-position of differently substituted benzenes and the corresponding ^1H -NMR-shift compared to unsubstituted benzene.¹⁸⁰ In further studies also the influence of neighboring atoms was taken into account.¹⁸¹ Another possibility to calculate particular Hammett parameters describing the substituent effects on $\rho(r)$ is by using vibrational data. For example Brownlee and co-workers correlated the squared resonance substituent constant σ_R^0 with the IR-absorption of certain normal modes.^{182–185} Schmid et al. discovered the IR absorption of aromatic C-H stretching modes to be directly related to the Taft substitution constant σ_I .^{186–191} Furthermore, a comparison between NMR- and IR-derived substituent resonance effect constants was performed by Palat et al.¹⁹² Bobowitsch et al. pointed out how Raman intensities correlate with the Hammett parameter.^{25,193–196}

3 Experimental details

3.1 UV-vis absorption and remission spectroscopy

UV-vis absorption measurements were predominantly used to identify spectral regions with no electronic absorption, thus suited for excitation in non-resonant Raman measurements, or to locate absorption bands assigned to a desired electronic transition to be investigated via resonant Raman measurements.

Dissolved as well as solid samples were investigated using the spectrometer Cary 5000 (Varian). Dissolved substances were measured in 10 mm cells using standard conditions and solid samples were measured as powders applying a praying mantis accessory.^{197,198}

3.2 Fluorescence spectroscopy

Fluorescence and fluorescence excitation spectra were recorded for dissolved substances before and after resonance Raman measurements (RR) to investigate if a substance was photochemically destroyed during the RR-measurements. The spectra were detected using the spectrometer Fluorolog-3 from ISA.

3.3 Raman spectroscopy

The majority of non-resonant Raman spectra was detected in 180° back-scattering geometry using the inverse micro-Raman setup LabRam HR (Jobin Yvon Horiba), equipped with an Olympus IX70 inverse microscope. The 532 nm output of a frequency doubled Nd:YAG laser (Coherent), the 633 nm line of a HeNe laser (Coherent) and the 830 nm of a cavity semiconductor laser (TEC100 Raman, Sacher Lasertechnik) were used for excitation. The spectrometer provides gratings with 300 or 1800 grooves/mm, has a focal length of 800 mm and is equipped with a CCD camera (1024×512 pixels). The setup is described in detail in the literature.^{80,149,199,200}

Further Raman measurements were performed at the Julius-Maximilian University (JMU) of Würzburg in the group of Prof. Kiefer. Fourier transform off-resonance FT-Raman spectra were recorded with a Bruker IFS 120 HR spectrometer with an integrated FRA

160 Raman module and a liquid nitrogen cooled germanium detector. The 1064 nm radiation of a Nd:YAG laser was employed for excitation.

Various non-resonant and in particular resonant Raman spectra were detected at setups with 90° scattering geometry. Partially, a setup in a laboratory of Prof. Kiefer (JMU Würzburg), a Raman-difference²⁰¹ and a further customized setup as well as an accordingly designed (without difference option) setup at IPHT Jena were used. In the different laboratories Argon ion^(a) 300C Motofred, Coherent), mixed gas ion (ILM 120, Carl Zeiss Jena), Krypton ion (Innova 302C, Coherent) or HeNe (Coherent) laser were available for excitation. The laser beam was usually dispersed via a Pellin-Broca prism, if necessary polarized via a Glan-Laser polarizer and the plane of the polarized light is turned applying a Fresnel rhomb. In the case of dissolved substances^b the vertical beam is focussed at the inner edge of a cell which rotates to avoid heating and destruction of the sample. The scattered light is collected via convex lenses or photo objectives, if necessary polarized, and analyzed in a spectrometer^c equipped with a CCD detector.

3.4 Processing of Raman spectra

Baseline-corrections, for example to subtract fluorescence backgrounds, were performed either by manually selecting data points^d to approximate the background^e or by fitting Gaussian, pseudo-Voigt or inverse polyoma to the background.

Apart from background corrections, wavenumber positions were checked by comparison with Raman bands of standard substances (TiO₂, cyclohexane) or of the solvent serving as internal standard in solutions. If necessary, the wavenumber axis was adjusted so that the solvent bands fit the positions given by Schrader.²⁰²

To determine relative Raman intensities, Raman bands were fitted with pseudo-Voigt profiles. In the program Origin7G the Gaussian amplitude is defined in an elegant way, so that integration of the Gaussian profile²⁰³ equals the fit-parameter A .^f Since also $l(x)$ can be defined accordingly, the parameter A of the pseudo-Voigt profile equals the area of a Raman band in case of the definition given in Origin7G:

$$y = y_0 + A \left[\mu \frac{2}{\pi} \frac{w}{4(x - x_c)^2 + w^2} + (1 - \mu) \frac{\sqrt{4 \ln 2}}{\sqrt{\pi} w} e^{-\frac{4 \ln 2}{w^2} (x - x_c)^2} \right] \quad (3.1)$$

^a λ_{ex} =515, 488, 477, 458 nm

^bConcentration was optimized to obtain an optimal signal-to-noise ratio (millimolar range).

^cLab. IPC/IPHT: Spectra Pro 2750, $f = 0.750$ (Acton); Lab. IPC2: triple monochromator T6400 (Jobin Yvon); Lab. Kiefer: Photometrics model RDS 200CCD Raman detector system

^dstandard baseline correction in programs Origin7G and Labspec

^eselected points are linearly connected

^f $a = \frac{A}{w\sqrt{\frac{\pi}{2}}}$ and $\int_0^\infty e^{-a^2 x^2} = \frac{\sqrt{\pi}}{2a}$, hence: $\frac{A}{w\sqrt{\frac{\pi}{2}}} \int e^{-2\frac{x^2}{w^2}} = \frac{A}{w\sqrt{\frac{\pi}{2}}} \int_{-\infty}^{+\infty} e^{-2\left(\frac{\sqrt{2}}{w}\right)^2 x^2} = 2 \cdot \frac{A}{w\sqrt{\frac{\pi}{2}}} \cdot \frac{\sqrt{\pi}}{2\sqrt{2}} \cdot w = A$

4 Characterizing molecules in the electronic ground state

4.1 Electron density studies in life sciences: The influence of intermolecular interactions on the electron density distribution of a protease inhibitor

In this section the application of electron density studies in life sciences is demonstrated. The following example continues a study about elucidating the reactivity and the mode of action of the protease inhibitor dimethyl-3[(4-nitro)phenyl]aziridine-2,2-dicarboxylate.^{8,204} The key step in the mode of action of this aziridine derivative, shown in figure 4.1, is the cleavage of the CC bond in the NCC-ring due to a nucleophilic attack at either of the carbon atoms. Grabowsky et al. studied the electron density distribution $\rho(\mathbf{r})$ within the aziridine ring by means of static deformation density plots^a. The plot arising from experimental determination of $\rho(\mathbf{r})$ revealed a significantly higher electrophilic character of the ph-NO₂-substituted carbon in the aziridine ring compared to the other aziridine-ring-carbon.⁸ In contrast, the plot of the static deformation density obtained from DFT calculations of the isolated aziridine derivative possesses only minor differences between the two carbon atoms within the aziridine ring. Apart from technical difficulties of deriving $\rho(\mathbf{r})$ from experimental data,^{21,22} the question arises to which extent the neglect of the crystal site environment in the DFT-calculations contributes to the $\rho(\mathbf{r})$ -differences between theoretical and experimental results. This question is of particular interest since it determines the validity of experimental $\rho(\mathbf{r})$ -studies in life sciences. For such a study the example of Schirmeister and Grabowsky is well suited, since $\rho(\mathbf{r})$ -differences between the investigated carbons are small.

In case of a single crystal, the intermolecular interactions are expected to compensate each other in a large part, since crystallization occurs according to thermodynamical con-

^aIn a deformation density plot an artificial $\rho(\mathbf{r})$, referring to free non-bonded atoms arranged to match a defined molecular geometry, is subtracted from the respective realistic molecular $\rho(\mathbf{r})$. Thus, the change in $\rho(\mathbf{r})$ due to bond forming is visualized, whereas positive regions in the ρ -deformation plot are assigned to bond regions.

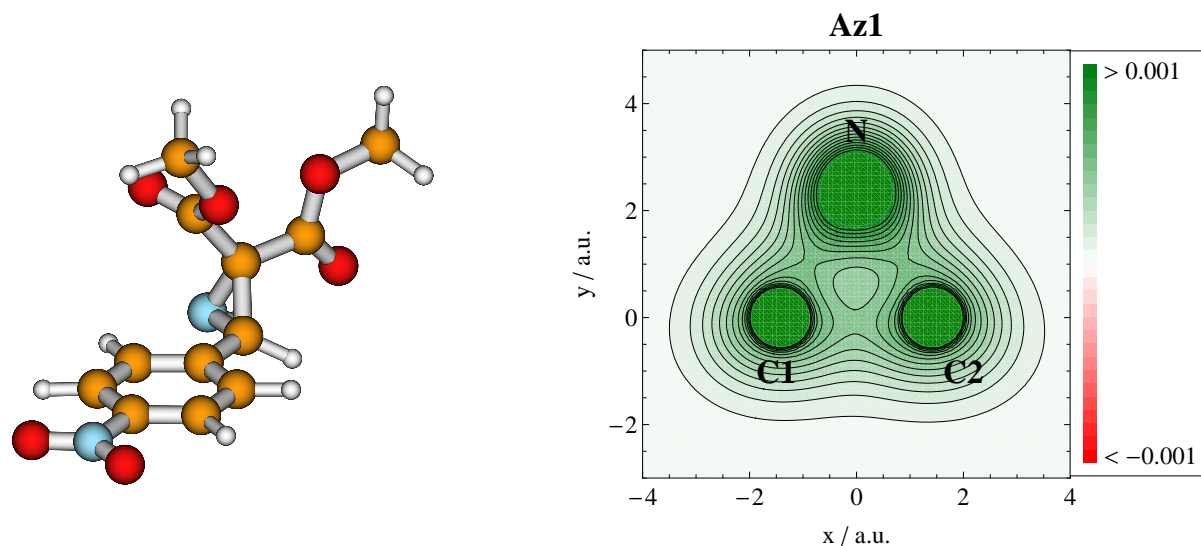


Figure 4.1: **Left:** Structure of dimethyl-3[(4-nitro)phenyl]aziridine-2,2-dicarboxylate. Red balls illustrate oxygen atoms, blue, brownish and white balls represent nitrogen, carbon and hydrogen atoms. **Right:** BP86/marij/TZVP calculated map of the electron density distribution within the plane of the aziridine ring applying the x-ray determined geometry.

ditions. Therefore, $\rho(r)$ of a molecule in a single crystal is expected to be comparable to $\rho(r)$ of an isolated molecule to some degree. However, in many molecular single crystals, especially if particular intermolecular interactions like hydrogen bridges are present, the crystal site environment is not spherically symmetric or homogeneous. Consequently, the object of the present investigation is to assess the sensitivity of $\rho(r)$ in the aziridine towards intermolecular interactions which is a crucial topic concerning pharmacologic applications of the studied aziridine derivative. In doing so, $\rho(r)$ of an aziridine in an artificial crystal section is compared to $\rho(r)$ of an isolated aziridine to unravel possible differences. Furthermore, aziridine dimers according to the experimental crystal structure are investigated, thus identifying the fundamental interactions. Subsequently, $\rho(r)$ of the aziridine monomer in a simulated solvent environment is studied and compared to the one referring to the single crystal since both environments are supposed to be related to the physiological case.²

The influence of intermolecular interactions on the electrophilicity of the two carbon atoms within the aziridine unit of dimethyl-3[(4-nitro)phenyl]aziridine-2,2-dicarboxylate (see figure 4.1) is studied by means of DFT-calculations and Raman spectroscopy. The difference in the electrophilicity between the aziridine-carbons is estimated via the respective $\rho(r)$ -values and atomic charges.

Following Grabowsky et al.,⁸ DFT-single-point calculations were performed at the ex-

perimentally determined geometry of the aziridine derivative ^b to obtain $\rho(r)$ data. In contrast to Grabowsky et al., who used the hybrid functional B3LYP and the Pople basis set 6-311++D(d,p), the GGA functional BP86 and the Ahlrichs-type TZVP basis set in combination with the multipole accelerated resolution of identity method (marij)¹³¹ (see section 2.2.1) were applied in the present work to account for the huge number of basis functions in larger crystal sections.

To visualize $\rho(r)$ or changes in $\rho(r)$ within the aziridine ring, $\rho(r)$ - or $\Delta\rho(r)$ -plots within the plane of the aziridine ring are generated using Turbomoles \$pointval option and the program Mathematica.²⁰⁵ The plane in the $\rho(r)$ -plot shown in figure 4.1 is defined by two vectors \vec{v}_1 ^c and \vec{v}_2 ^d which provide a perpendicular coordinate system and the origin is set at the center between atoms C1 (adjacent to ph-NO₂) and C2 (belonging to dimethyl malonate) ^{e, f}

In accordance to the work of Grabowsky et al.,⁸ the isolated molecule exhibits an almost symmetrical charge distribution between the carbons within the aziridine ring (see figure 4.1) what is in contrast to the experimental results obtained for the single crystal. To unravel differences between the isolated aziridine derivative and a respective molecule in the single crystal site, a crystal section involving all 15 next neighbors of an aziridine according the experimental crystal structure was constructed to simulate the single crystal. As shown in figure 4.2 the molecules are arranged in layers, stacked via interactions of the ph-NO₂ moieties and also via interactions of the dimethyl malonate moieties to some extent. Such sequences are connected due to hydrogen bonds as illustrated by the red dashed lines.

To extract the interactions with the highest impact on $\rho(r)$, the crystal model constituted of 16 aziridine derivatives (abbreviated as Az16 in the following) is fragmented in dimers, which are depicted in figure 4.3. The dimer involving a hydrogen bond is abbreviated Az2a and the respective $\Delta\rho$ -plot^g is labelled Az2a-Az1. As visualized in the respective plot in figure 4.3, the hydrogen bond strongly affects the $\Delta\rho$ -pattern in the aziridine ring. Around the nitrogen atom $\rho(r)$ is strongly decreased (about $0.005 e/\text{\AA}^3$), since $\rho(r)$ is shifted along the NH bond into the NH \cdots N hydrogen bond. Within the NC bonds of the ring, $\rho(r)$ is increased with the maxima close to the carbons (≈ 0.003

^bCoordinates from the atoms in the unit cell were kindly supplied by Simon Grabowsky (research group Prof. Dr. P. Luger, Freie Universität Berlin, Institut für Chemie und Biochemie / Kristallographie)

^c $\vec{v}_1 = \vec{C}_2 - \vec{C}_1$

^d $\vec{v}_2 = \vec{v}_1 \times \vec{v}_3$; $\vec{v}_3 = \vec{v}_1 \times (\vec{N}_{aziridine} - \vec{C}_1)$

^eOrigin: $1/2 \cdot (\vec{C}_1 + \vec{C}_2)$

^fData points in each dimension: $\approx 100 \Rightarrow 10^4 \rho$ -values constituting the ρ -plot in figure 4.1

^gconsidered aziridine is labelled with an asterisk in figure 4.3; the $\Delta\rho$ -plots are calculated by subtracting the ρ -plot of the isolated aziridine from the ρ -plot referring to a dimer.

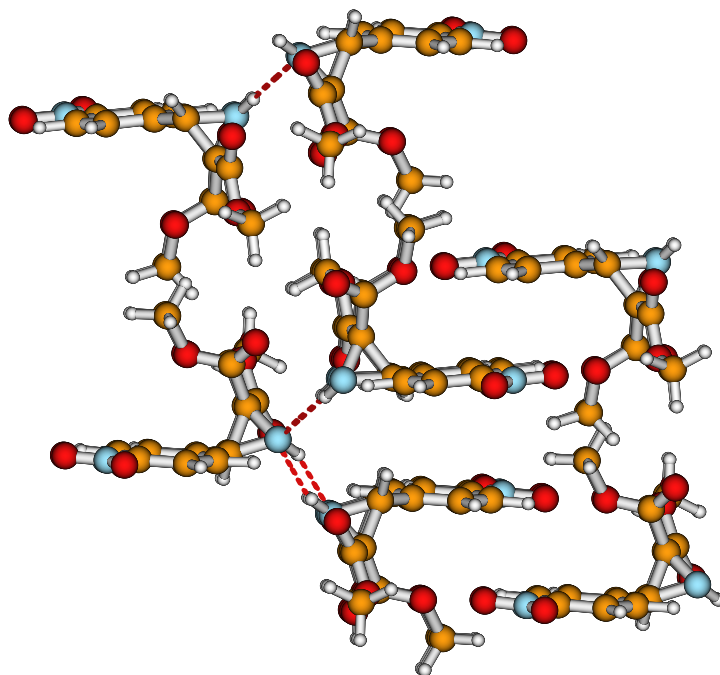


Figure 4.2: Crystal section of a dimethyl-3[(4-nitro)phenyl]aziridine-2,2-dicarboxylate single crystal. Red balls illustrate oxygen atoms, blue, brownish and white balls are nitrogen, carbon and hydrogen atoms. Red dashed lines are H-bonds.

$e/\text{\AA}^3$), but lower at C2. Furthermore, the hydrogen bond leads to a decreased $\rho(r)$ within the C1-C2 bond with the $\Delta\rho(r)$ -minimum at C2 ($\approx 0.002 e/\text{\AA}^3$). In conclusion, the intermolecular interaction via a $\text{NH}\cdots\text{H}$ hydrogen bond strongly influences $\rho(r)$ at C1 and C2, whereas $\rho^{C2}(r)$ is stronger decreased than $\rho^{C1}(r)$ along the C1-C2 bond.

Since the $\Delta\rho$ -plots in figure 4.3 just illustrate the relative changes in $\rho^{C1}(r)$ and $\rho^{C2}(r)$ due to intermolecular interactions with respect to the isolated molecule, the examination of the nucleophilic character of C1 and C2 has to be extended to the respective atomic charges (see table 4.1)^h. In accordance to the literature,¹⁰⁴ theoretically derived QTAIM-charges (Q_{AIM}^{DFT}) exceed experimentally obtained ones (Q_{AIM}^{exp}), i.e. the calculated charges amount more than twice the experimental ones determined by Grabowsky et al. (see table 4.1). Although $Q_{AIM}^{exp}(C2)$ is slightly higher than $Q_{AIM}^{exp}(C1)$, Grabowsky et al. conclude from chemical investigations and the deformation density plots that C1 is more electrophilic than C2. However, the charges calculated in the present work are in contrast to these experimentally derived charges but in accordance to the conclusions of Grabowsky et al., since $Q_{AIM}^{DFT}(C1) > Q_{AIM}^{DFT}(C2)$ for the monomer as shown in table 4.1. If the charges are averaged across the considered molecules in the various dimers depicted in figure 4.3, $\Delta Q_{AIM}^{DFT} (= Q_{AIM}^{DFT}(C1) - Q_{AIM}^{DFT}(C2))$ remains roughly unaffected, but $Q_{AIM}^{DFT}(C1)$ and $Q_{AIM}^{DFT}(C2)$ are generally increased due to the neighboring molecules (see

^hAtomic charges were calculated using the programm AIM2000.^{206,207}

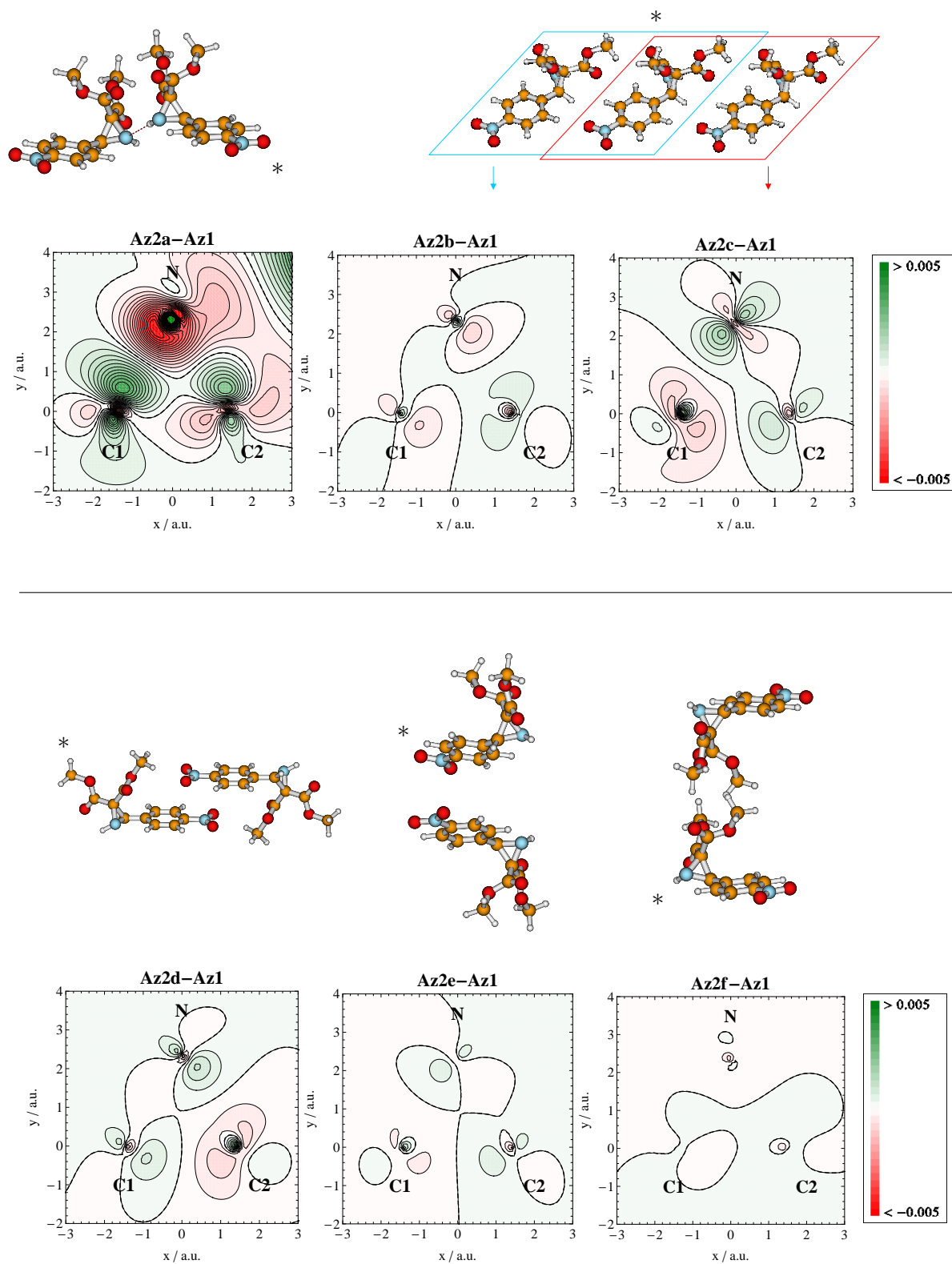


Figure 4.3: Dimers of dimethyl-3((4-nitro)phenyl)aziridine-2,2-dicarboxylate extracted from the crystal structure and respective $\Delta\rho^{DFT}$ -maps of the aziridine ring referring to the isolated molecule. The aziridines referring to the $\Delta\rho^{DFT}$ -maps are labelled with an asterisk.

Table 4.1: Experimentally^a and theoretically determined AIM charges of carbons C1 and C2 of the aziridine ring.

Ensemble	Determination	$Q(\text{C1})$ [e]	$Q(\text{C2})$ [e]	ΔQ [e]
Single crystal ^a	exp.	0.100	0.110	-0.010
Aziridine monomer	BP86/marij/TZVP	0.253	0.251	0.002
Dimers: mean	BP86/marij/TZVP	0.276	0.273	0.003
Dimer a	BP86/marij/TZVP	0.259	0.270	-0.011
Dimer b	BP86/marij/TZVP	0.282	0.300	-0.017
Dimer c	BP86/marij/TZVP	0.282	0.278	0.004
Dimer d	BP86/marij/TZVP	0.270	0.266	0.004
Dimer e	BP86/marij/TZVP	0.282	0.266	0.016
Dimer f	BP86/marij/TZVP	0.279	0.257	0.022

^a Grabowsky et al., *European Journal of Organic Chemistry*, **2007**, 2759-2768.⁸

table 4.1). The minor difference between ΔQ_{AIM}^{DFT} of the isolated aziridine and ΔQ_{AIM}^{DFT} averaged across the dimers suggest the choice of dimers which represent compensating intermolecular interactions. In conclusion, the total crystal site environment minor influences the difference between the charges of C1 and C2 within aziridine-ring, even if the electron density distribution is modified (see figure 4.2). This result can be explained by slightly shifted electron densities which are accompanied with respective changes of the atomic boundaries and volumes (see section 2.2.2 for calculation of AIM-charges).

As already indicated by the $\Delta\rho$ -plot of dimer Az2a (see figure 4.3) the NHN-hydrogen bond significantly influences $\rho(r)$ in the aziridine-plane, thus leading to a stronger decrease in electron density on C2 as compared to C1. This $\rho(r)$ -shift apparently applies for the atomic volumes, since due to the hydrogen bonding $Q(\text{C2})$ exceeds $Q(\text{C1})$ about $0.011e$, hence roughly matching the experimentally derived ΔQ value. The different change in $\rho(r)$ at the aziridine ring carbons originates from the asymmetric influence of the hydrogen bonding on the nitrogen as visualized by the $\Delta\rho$ -plot of dimer Az2a.

The interactions within a layer of the single crystal influence $\rho(r)$ within the aziridine plane significantly less than the previously discussed hydrogen bonding as can be concluded from the $\Delta\rho$ -plots of dimer Az2b and Az2c. In both cases $\rho(\text{C2})$ is increased, whereas $\rho(\text{C1})$ is slightly decreased. This $\Delta\rho$ -pattern is more pronounced in Az2c than in Az2b, since in Az2c the NO_2 -group of the adjacent molecules is close to the hydrogen of aziridine carbon C1, thus shifting ρ into the respective $(\text{C1})\text{H}\cdots\text{O}(\text{NO})$ -interaction. The electron depletion at C1 is mirrored in the increased $Q(\text{C1})$ charges of both dimers. However, the differences between $\rho(\text{C1})$ of Az2b and Az2c indicated by the $\Delta\rho$ -plots is not present for the $Q(\text{C1})$ charges. According to the $\Delta\rho$ -plot of Az2c, $Q(\text{C2})$ is lower than $Q(\text{C1})$

in this dimer. In contrast, $Q(C2)$ is even higher than $Q(C1)$ in Az2b (see table 4.1). Consequently, the ΔQ -value induced by the neighboring molecule in Az2b is comparable to the change due to the NHN-hydrogen bond.

The layers each including the dimers Az2b and Az2c are stacked by ph-NO₂ interactions within the single crystal. Hence, dimers with ph-NO₂-groups "above" and "under" the ph-NO₂-moiety of the central aziridine derivative are studied (dimers Az2d and Az2e). In case of the anti-parallel orientation in Az2d, the $\Delta\rho$ -plot suggests a ρ -rise at C1 and ρ -depletion at C2, while the intermolecular interaction in Az2e affects $\rho(r)$ to minor extends, but with slightly raised ρ at C1 and slightly decreased ρ at C2. However, even if ρ -depletion at C2 is stronger than at C1 in the aziridine plane of Az2d, the ph-NO₂ interactions in Az2d and Az2e lead to a higher positive atomic charge of C1 than of C2 (see table 4.1). Consequently, the interactions in the dimers Az2d and Az2e are leading to a more electrophilic character of C1 as compared to C2, which is in accordance to the assumption of Grabowsky et al.. In dimer Az2f interactions between dimethyl-malonate moieties are considered. Even if negligible $\Delta\rho$ values are present, $\Delta Q=0.022 e$ is the highest value of all investigated dimers. The charge on C1 ($=0.279e$) is comparable to most of the remaining dimers possessing $Q(C1)=0.282 e$, except Az2a ($Q(C1)=0.259 e$) and Az2d ($Q(C1)=0.270 e$). In contrast, $Q(C2)=0.257 e$ in Az2f is the lowest value of all considered dimers which are possessing values between $0.266 e$ for the ph-NO₂ interactions and $0.300 e$ for the *intra*-layer interactions in Az2b.

In conclusion, the NHN hydrogen bond in Az2a and the *intra*- and the *inter*-layer interactions in Az2b and Az2d, respectively, and the interactions between the dimethyl-malonate moieties are leading to the most pronounced differences between the Q_{AIM}^{DFT} charges of C1 and C2 (table 4.1). Consequently, it is possible to switch the order of leading electrophilic characters between C1 and C2 by targeted manipulation of the functional groups in dimethyl-3[(4-nitro)phenyl]aziridine-2,2-dicarboxylate via intermolecular interactions.

The interactions leading to $Q(C1) < Q(C2)$ are the NHN hydrogen bond (Az2a, in accordance to the $\Delta\rho$ -plot) and the *inter*-layer interaction (Az2b), in which the former (Az2a) particularly decreases $Q(C1)$ and the latter (Az2b) especially increases $Q(C2)$. Therefore, the exclusive action of these interactions would lead to a more electrophilic character for C2 than for C1, thus changing the selectivity of the inhibition reaction.

The interactions leading to $Q(C1) > Q(C2)$ are the *inter*-layer and the *inter*-dimethyl-malonate interactions (Az2e, Az2f). In Az2e no exceptionally high or low charges are present, as also indicated by the $\Delta\rho$ -plot, whereas in Az2f primarily $Q(C2)$ is decreased, in particular if compared to the other dimers. Surprisingly, the resulting large ΔQ value is in contrast to the respective $\Delta\rho$ -plot possessing considerably less pronounced features than the remaining $\Delta\rho$ -plots. From the results of Schirmeister and Grabowsky^{8,204} who

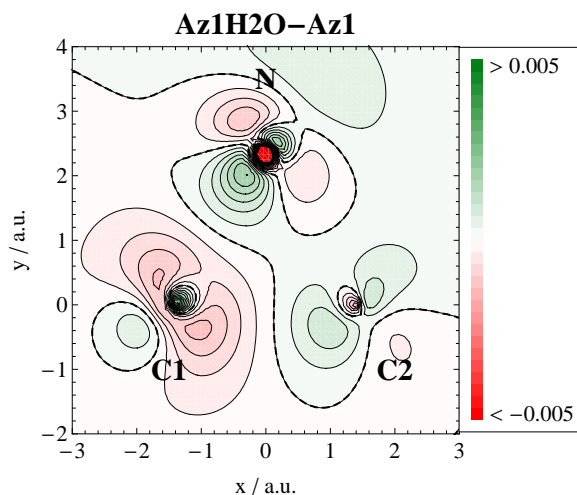


Figure 4.4: BP86/marij/TZVP calculated map of the electron density distribution within the plane of the aziridine ring, influenced by an aqueous solvent environment simulated applying the polarizable continuum model.

reported C1 being more electrophilic than C2, particularly in wet chemical reactions, one has to conclude, that especially dimethyl-malonate interactions and those comparable to the ones in Az2e are the dominant interactions ruling the reactivities.

Since the investigated dimers are based on the crystal structure and are isolated it has to be researched, if the derived results can be transferred to dimethyl-3[(4-nitro)phenyl]aziridine-2,2-dicarboxylate in an aqueous physiological environment being relevant for the mode of action of this aziridine. Hence, the ρ -distribution in an homogeneous aqueous medium using the polarizable continuum model was calculated, again applying the x-ray determined coordinates for the isolated aziridine derivative. The resulting $\Delta\rho$ -plot is visualized in figure 4.4 and reveals a significant electron density depletion on C1 in the directions of the C1-N and the C1-C2 bond and a ρ -increase in the remaining quadrants as shown in figure 4.4. For carbon atom C2 the opposite is true, but with less pronounced electron depletion due to the simulation of the aqueous medium as compared to the isolated molecule. Hence, one might expect that in contrast to the Q_{AIM} charges derived experimentally C1 is more electrophilic than C2. However, the latter assumption is to handle with care, since a crucial question is which of the electrophilic regions of the carbon atoms is better accessible for the nucleophilic reactant. In conclusion, reliable predictions of reactivities of molecules via experimental x-ray investigations are promising but also challenging and require sophisticated quantum mechanical studies of the reaction path including environmental effects. An alternative experimental technique to conclude on electron density properties of target molecules in various environments would be of great impact for natural sciences.

4.2 Prediction of electron density features in BCPs of phenyl-CH-bonds via vibrational spectroscopic and NMR parameters

As already summarized in section 2.4, great efforts were made in the past to unravel the relation between spectroscopic quantities and reactivity-related properties. In particular, vibrational and NMR spectroscopy were applied to conclude on $\rho(\mathbf{r})$ -dependent molecular reactivities usually derived from kinetic data.⁹¹ Alternatively, since reactivities are determined by $\rho(\mathbf{r})$, Bader and Chang studied the reactivity properties of substituted benzenes on the basis of the Quantum Theory of Atoms in Molecules (QTAIM) via analysing the topology of $\rho(\mathbf{r})$.^{63,101–103} These studies revealed that the π -populations, the quadrupole moments of the ring carbon atoms, the ellipticities of the phenyl C-H bonds and the respective laplacians are responsible for the reactivity in electrophilic aromatic substitution reactions.^{208,209}

Consequently, it appears to be a promising approach to study the relations between spectroscopic quantities and crucial $\rho(\mathbf{r})$ -features (according to Bader properties in CPs as also motivated in section 2.1) aiming to express $\rho(\mathbf{r})$ -characteristics and related properties in terms of spectroscopic data. That would offer a methodology facilitating the prediction of $\rho(\mathbf{r})$ -key-characteristics by means of spectroscopic investigations without limitation to a particular physical state.ⁱ To research this issue, the relations between DFT-calculated ρ -, $\nabla^2\rho$ - and ε -values and DFT-calculated vibrational and ¹H-NMR spectroscopic quantities were studied for a set of 18 mono-substituted benzene derivatives. The following sections report about the calculations of $\rho(\mathbf{r})$ -properties within BCPs and vibrational as well as ¹H-NMR quantities. Subsequently, it is described how $\rho(\mathbf{r})$ -target values are fitted against corresponding spectroscopic variables by means of linear as well as quadratic multi-dimensional functions. Finally, the parameters of the functions best suited to predict ρ , $\nabla^2\rho$ and ε in the certain CH-BCPs of the phenyl-ring are presented.²¹⁰

4.2.1 Electron density properties

The geometry optimizations, the computations of vibrational and NMR data were performed using the program GAUSSIAN03 (g03),¹⁴⁷ applying two different theoretical levels. On the one hand the pure density functional of Becke and Perdew BP86^{121,124} and the triple- ζ basis set TZVP^{144,145} (polarization function on all atoms), known to give accurate molecular structures, frequencies and Raman intensities for medium sized molecules, were applied.^{78,92} On the other hand the MP2¹³⁶ method in combination with the triple- ζ

ⁱcompare x-ray studies which are limited to high-quality single-crystals but are the only experimental access to $\rho(\mathbf{r})$

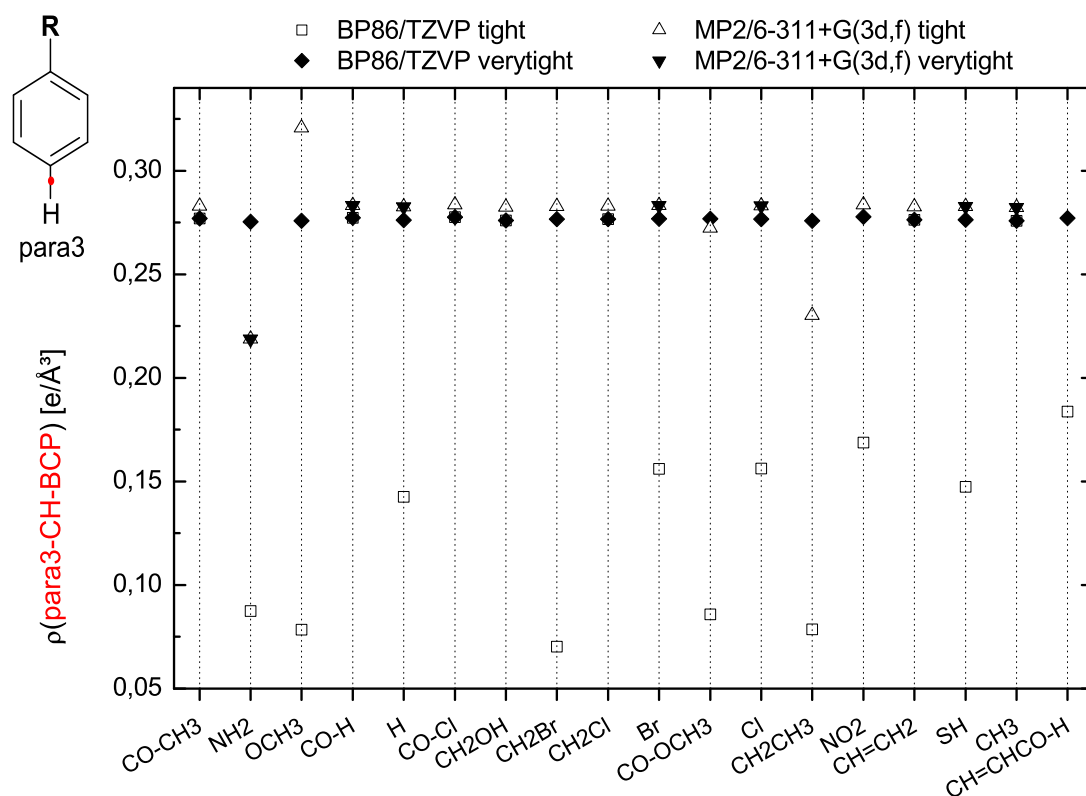


Figure 4.5: ρ in the BCPs of the *para*-CH-bonds of all calculated benzene derivatives. Empty and filled dots: results obtained under *tight* and *verytight* optimization conditions, respectively. Squares and triangles correspond to BP86/TZVP and MP2/6-311+G(3df) calculations, respectively.

basis set 6-311+G(3df)^{137–142} which is known to give reliable electron density values for bond critical points (BCPs) was used.¹⁰⁴ The geometry optimization procedures in g03 were performed under *tight* and partially *verytight* (in conjunction with an *ultrafine* grid) optimization conditions, to get reliable electron density characteristics, subsequently calculated with the program AIM2000.^{206, 207}

Figure 4.5 compares the BP86/TZVP and MP2/6-311+G(3df) calculated ρ -values in the BCPs of the *para*-CH-positions of a set of mono-substituted benzene derivatives, thus proving the ρ -data used in this study being reliable. The *tight* optimization condition (default grid) leads for the BP86/TZVP calculations to strongly divergent results while for the *verytight* optimization condition (ultrafine grid) the results are consistent. This behavior cannot be found for the MP2/6-311+G(3df) calculations. It can be seen in figure 4.5 that for aniline, benzaldehyde, benzene, bromo- and chloro-benzene, thiophenole and toluole ρ does not differ noteworthy between the MP2/6-311+G(3df) calculations under

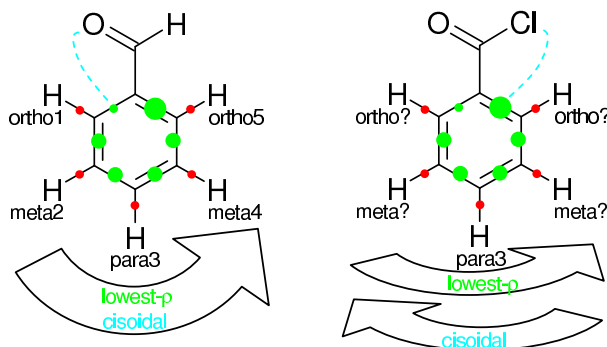


Figure 4.6: Illustration of the lowest- ρ - and the *cis*-convention illustrated for the example of benzaldehyd (both conventions are leading to identical data-sets) and benzoyl chloride (conventions are leading to inverse data-sets). Magnitudes of ρ in the CC-BCPs are indicated by the size of the green dots. Red dots indicate CH-BCPs. The cyan dashed line points up the determination of the start-CC-bond according to the *cis*-convention.

tight and *verytight* conditions (default and ultrafine grids, respectively). Hence, the *tight* optimization condition is sufficient to get reliable ρ -values for the MP2/6-311+G(3df) approach. The corresponding densities are usually about $0.006 \text{ e}/\text{\AA}^3$ higher than for the BP86/TZVP calculated ones with the exception of $\text{R}=\text{OCH}_3$ (anisole) with an about $0.45 \text{ e}/\text{\AA}^3$ higher $\rho(\textit{para}\text{-CH-BCP})$ and $\text{R} = \text{NH}_2, = \text{COOCH}_3, = \text{CH}_2\text{CH}_3$ (aniline, benzoic-acid-methylester, ethyl-benzene) with a lower $\rho(\textit{para}\text{-CH-BCP})$. Generally, the values calculated using MP2/6-311+G(3df) (*tight*) are spread over a wider range than the ones calculated applying BP86/TZVP (*verytight*). The MP2-calculations were performed in the default mode, i.e. using "frozen cores" whereas the inner shells are not involved in the correlation calculation. Some MP2 geometry optimizations necessitated the use of GDIIS- instead of the default Berny-optimization to achieve convergence.

For a comparison of ρ of the four remaining ph-CH-BCPs one has to account for the computational limitation to fixed structures, for which reason the two sides of the phenylene group (*ortho*1/5, *meta*2/4) are differently affected by asymmetric substituents like CO-Cl (see fig. 4.6 and 4.7). Consequently, different ρ -values are obtained for the different *ortho*- and *meta*-positions and for the CC-bonds on the different ph-sides, respectively. Hence, to decide which sides of different benzene derivatives to compare, conventions are needed.

One possibility is to apply a *cis*-convention (see figure 4.6) where the data are collected starting at the ph-CC-bond or ph-CH-bond cisoidal to the β -substituent atom with the highest atomic number, going away from the substituent and ending up at the ph-CC-bond transoidal to the substituent atom with the highest atomic number. Alternatively, the lowest- ρ -convention (see figure 4.6) was applied, where the name indicates the starting point of the data collection, which is the only difference to the *cis*-convention. The

starting point is defined by the ph-CC-bond with the lowest ρ in the BCP adjacent to the ph-R bond. The properties of the CH-bonds are collected according to the direction defined by ρ of the ph-CC-bonds, regardless of ρ in the BCPs of the ph-CH-bonds. The two conventions are compared in figure 4.6. In the left graph the example benzaldehyde is given, where the two conventions lead to equivalent data-sets, since the start-CC-bonds are identical. In benzaldehyde the substituent atom with the highest atomic number is oxygen and therewith the neighboring ph-CC-bond is the starting point in the *cis*-convention. The same ph-CC-bond also possesses a lower $\rho(\text{ph-CC-BCP})$ (visualized by a green dot) than the ph-CC-bond transoidal to the carbonyl group, for which reason it is also the start-CC-position in the lowest- ρ -convention. In the case of benzoyl chloride, shown on the right side of figure 4.6, the two conventions are leading to different orders of the ph-CH-properties. The lowest- ρ -convention collects the data in the same direction like in the example of benzaldehyd, but in benzoyl chloride the substituent atom with the highest atomic number is not oxygen anymore but the chlorine atom. For that reason, the collection of data is performed in the opposite direction applying the *cis*-convention compared to the lowest- ρ -convention. The sequences obtained from either convention, based on the ph-CC-bonds, provide the basis for all data sets used in this work. The two conventions lead to equivalent assignments of *ortho*- and *meta*-positions with the exception of acetophenone and benzoyl chloride.

In figure 4.7 ρ , $\nabla^2\rho$ and ε in the BCPs of all phenyl-CH-positions are compared. The electron densities shown were calculated under *verytight* geometry-optimization conditions using BP86/TZVP and applying the lowest- ρ -convention. As expected, the *ortho*-CH-BCPs are most affected by the inductive substituent-effects as visualized by the large data range of ρ , $\nabla^2\rho$ and ε for the *ortho*-CH-BCPs in figure 4.7. The fact, that for example in benzoyl chloride, anisole and aniline ρ in the BCP of the *para*-CH-bond is stronger influenced by the substituent than ρ in the BCP of the *meta*-CH-bond can be explained by mesomeric effects. That the latter play an important role is suggested by the large influence of the substituents on the ellipticities in the BCPs of the *para*-CH-bonds. The $\varepsilon(\textit{para-CH-BCP})$ are differing by the same amount as the ellipticities within the *ortho*-CH-bonds, whereas the ellipticities in the BCPs of the *meta*-CH-bonds are less affected. The largest decrease of the ρ - and $\nabla^2\rho$ -values in the CH-BCPs is observed for aniline while the largest increase of ρ and $\nabla^2\rho$ of the CH-BCPs can be found for nitrobenzole and benzoyl chloride. The NH_2 -group (aniline) and the methoxy-group (anisole) are leading to the highest ellipticities in the *ortho*- and *para*-CH-BCPs. Furthermore, the different ρ -, $\nabla^2\rho$ - as well as ε -values in the two *ortho*-CH-BCPs of anisole highlight the different influence of asymmetric substituents on different phenyl-sides, as shown in figure 4.7. The lowest ε -values for the CH-BCPs can be found for nitrobenzole, benzoylchloride and benzaldehyde. Therefore, to manipulate phenyl-CH-bond properties, the most

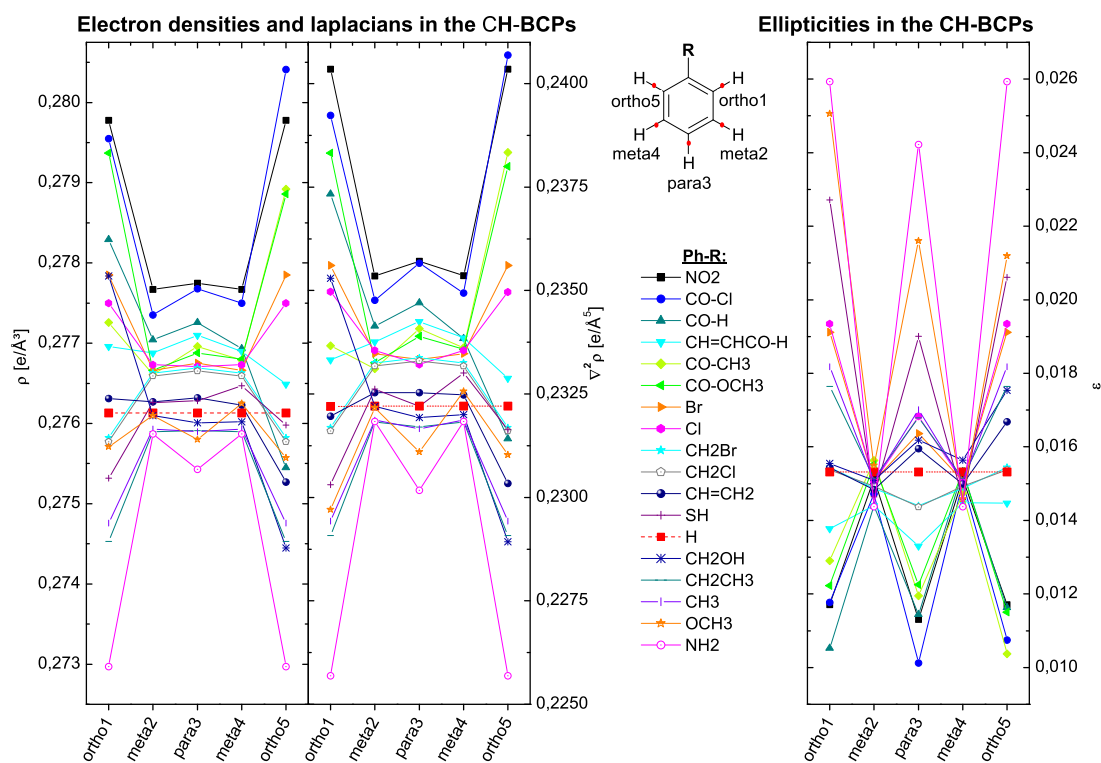


Figure 4.7: Electron densities (left), respective laplacians (middle) and ellipticities (right) in the BCPs of the CH-bonds of the phenyl-group, according to the lowest- ρ -convention.

effective way is to place NO₂, COCl or NH₂ substituents in the *ortho*-positions or, if the *ortho*-positions are not accessible, in the *para*-positions.

4.2.2 Vibrational and NMR data

As described in the previous section, ρ -values in BCPs were calculated, which are unambiguously related to the respective bonds. Since one aim of this study is the connection of these localized target-quantities with vibrational data it is necessary to use vibrational data which are likewise localized. Usually, this is not the case for normal modes (NM). Even if certain phenyl-NMs like the trigonal ring breathing vibration of mono- or *meta*-substituted benzenes are known to be substituent-independent (since substituent motions are not involved in the vibrational mode) neither of these NMs are strictly located to a single bond.

One way to overcome this problem is to consider mono-deuterated benzene derivatives. The substitution of a single phenyl-hydrogen leads to a strong localized carbon-deuterium

stretching vibration $\nu(\text{CD})$ which can be found in a well separated wavenumber region of about 2300 cm^{-1} . Consequently, the stretching vibration of a given CD-bond does not mix with other vibrations and is thus well located. The chemical properties of the CD-bond are expected to be equal to the ones of a CH-bond. Hence, vibrational characteristics of $\nu(\text{CD})$ for a correlation with the ρ -properties of the CH-bonds were used. For the case of symmetric substituents (Br, Cl, NH_2 , NO_2 , CH_2Br , CH_2Cl , H, CH_2CH_3 , CH_3) and ρ -distributions, three Raman as well as IR spectra were calculated for *ortho*-, *meta*- and *para*-deuteration, respectively. In the case of asymmetric substituents (CO-Cl , CO-H , CH=CHCO-H , CO-CH_3 , CO-OCH_3 , CH=CH_2 , SH, CH_2OH , OCH_3) and consequently asymmetric ρ -distributions, five Raman and IR spectra were calculated for every mono-substituted benzene derivative, respectively.

To be consistent with the calculations of the density properties and following the work of Reiher et al.⁹² the vibrational data were calculated applying BP86/TZVP and g03 simply by involving the key-word *freq=raman* (see previous section). As a starting point pure Raman activities, as computed in the standard procedure of g03,¹⁴⁸ are used for the correlations. To relate the study to experimental investigations the combinations of spectroscopic variables leading to the best fit results were reinvestigated by applying *relative* wavenumbers, IR intensities and Raman intensities using benzene as standard. The relative wavenumbers were calculated as differences to the one of the CD-stretching vibration of benzene; relative IR and Raman intensities were normalized to the vibration of benzene. Raman intensities were calculated from Raman activities according to Schrötter and Klöckner assuming 293.15 K and an excitation wavelength of 752.488 nm.^{80,211}

The chemical shifts of the phenyl- ^1H ($\sigma_{\text{C}_6\text{H}_6}^{1\text{H}}$) were calculated using the Gauge Independent Atomic Orbital (GIAO) method²¹²⁻²¹⁶ and subtracting the resulting isotropic shielding value of ^1H of the various benzene derivatives from the respective value of benzene. The NMR-calculations are based on the ones of the Raman data, i.e. employing DFT^{217,218} (BP86/TZVP), performing single point computations (involving the checkpointfile of the geometry optimization and Raman calculations).

4.2.3 Prediction of electron density features utilizing spectroscopic data

In a first attempt linear correlation coefficients were calculated to test for linear relationships between spectroscopic variables (vibrational wavenumbers, IR absorptions, Raman activities and ^1H -NMR shifts) and properties of the ρ -distributions in the CH-bonds (ρ , $\nabla^2\rho$ and ε within the CH-BCPs). Furthermore, the different dataset generation conventions (lowest- ρ - and *cis*-convention) were applied to decide which convention is to be preferred. In a next step, linear and quadratic fit functions were tested for their ability

to predict ρ -, $\nabla^2\rho$ - and ε -values in the CH-BCPs of unknown benzene derivatives.

4.2.3.1 Linear correlation coefficients

The linear correlation coefficients r were calculated according to equation 4.1 involving differences between spectroscopic data x as well as between $\rho(\text{r})$ -data f and their respective mean-values (\bar{x}, \bar{f}) .^{203,219} The quantity n is the number of substances studied within this work.

$$r_{x,f} = \frac{1/n \sum_{i=1}^n (x_i - \bar{x})(f_i - \bar{f})}{\sqrt{1/n \sum_{i=1}^n (x_i - \bar{x})^2} \sqrt{1/n \sum_{i=1}^n (f_i - \bar{f})^2}} \quad (4.1)$$

For the spectroscopic variable x the chemical shifts ($\sigma_{\text{C}_6\text{H}_6}^{1\text{H}}$, described in the last section) of the phenyl protons, the wavenumber-values of $\nu(\text{CD})$ (WN) and the associated IR absorptions (IR) and Raman activities (RA) were used. For the $\rho(\text{r})$ -data f (ρ , $\nabla^2\rho$ as well as ε) in the BCP of the phenyl-CH-bond were chosen. The calculated correlation coefficients r are plotted in table 4.2 for all combinations of spectroscopic quantities and $\rho(\text{r})$ -target-quantities corresponding to the respective positions of the phenyl-ring and to both data-conventions (except for $\nabla^2\rho$, ε) described above.

Regarding the data in table 4.2 it can be concluded, that there are no significant differences in the correlation performances between both conventions. We decided to use the lowest- ρ -convention because of easier data-handling in the following.

Furthermore, the data in table 4.2 suggest that the spectroscopic data, especially wavenumber-values and IR absorptions of highly localized $\nu(\text{CD})$ and $\sigma_{\text{C}_6\text{H}_6}^{1\text{H}}$, are very strong linearly correlated to the electron density in the BCP of the CH-bonds for certain positions of the mono-substituted benzene rings. The pairs of variables (i.e. spectroscopic variable and ρ , $\nabla^2\rho$ or ε) leading to absolute values of linear correlation coefficients higher than 0.75, indicating a very strong linear correlation, are highlighted bold in table 4.2. The *para*-position is the only CH-position possessing weak linear correlations between the vibrational variables and ρ . In contrast, the linear correlation between ρ and $\sigma_{\text{C}_6\text{H}_6}^{1\text{H}}$ in the *para*-CH-BCP is very strong. Comparable high linear correlations are present between ρ and $\sigma_{\text{C}_6\text{H}_6}^{1\text{H}}$ at the *ortho*-CH-positions. In summary, at the *para*-position $\rho(\text{ph-CH-BCP})$ correlates well with $^1\text{H-NMR}$ shifts, at the *meta*-positions $\rho(\text{ph-CH-BCP})$ correlates well with vibrational data and at the *ortho*-positions $\rho(\text{ph-CH-BCP})$ correlates well with both spectroscopic data ($\sigma_{\text{C}_6\text{H}_6}^{1\text{H}}$ and vibrational data). Generally, the vibrational variables WN and IR as well as $\sigma_{\text{C}_6\text{H}_6}^{1\text{H}}$ exhibit the highest correlation coefficients to $\rho(\text{ph-CH-BCP})$. In conclusion, vibrational and $^1\text{H-NMR}$ data complement one another and are perfectly suited to predict electron densities from easily determinable spectroscopic data. Equivalent correlations were obtained for $\nabla^2\rho$.

For a better visualization of e.g. the correlation between WN and ρ for a certain phenyl-

Table 4.2: Correlation coefficients r between vibrational and $\rho(\mathbf{r})$ data (upper, middle, lower part: ρ , $\nabla^2\rho$, ϵ in ph-CH-BCPs, respectively). Bold and italic values indicate strong to full and medium to strong correlations, respectively.

ph-pos.		NMR σ_{C6H6}^{1H}	Vibrational data		
			WN	IR	RA
$\rho(\text{BCP})$					
<i>ortho1</i>	lowest- ρ -conv.	0.83	0.88	-0.88	<i>-0.58</i>
	cis-conv.	0.86	0.88	-0.89	<i>-0.64</i>
<i>meta2</i>	lowest- ρ -conv.	<i>0.64</i>	0.98	-0.90	<i>0.50</i>
	cis-conv.	<i>0.65</i>	0.98	-0.88	0.27
<i>para3</i>	lowest- ρ -conv.	0.81	0.14	0.07	0.27
<i>meta4</i>	lowest- ρ -conv.	<i>0.69</i>	0.99	-0.85	0.21
	cis-conv.	<i>0.69</i>	1.00	-0.86	0.40
<i>ortho5</i>	lowest- ρ -conv.	0.90	0.90	-0.86	-0.82
	cis-conv.	0.88	0.89	-0.84	-0.77
$\nabla^2\rho(\text{BCP})$					
<i>ortho1</i>	lowest- ρ -conv.	0.85	0.84	-0.85	<i>-0.52</i>
<i>meta2</i>	lowest- ρ -conv.	<i>0.61</i>	0.98	-0.90	<i>0.52</i>
<i>para3</i>	lowest- ρ -conv.	0.86	0.05	0.15	0.33
<i>meta4</i>	lowest- ρ -conv.	<i>0.66</i>	0.99	-0.85	0.23
<i>ortho5</i>	lowest- ρ -conv.	0.92	0.89	-0.85	-0.83
$\epsilon(\text{BCP})$					
<i>ortho1</i>	lowest- ρ -conv.	-0.95	-0.34	0.47	0.44
<i>meta2</i>	lowest- ρ -conv.	0.10	-0.05	-0.01	-0.44
<i>para3</i>	lowest- ρ -conv.	-0.98	0.35	<i>-0.52</i>	<i>-0.56</i>
<i>meta4</i>	lowest- ρ -conv.	0.39	0.11	-0.30	-0.37
<i>ortho5</i>	lowest- ρ -conv.	-0.90	-0.35	0.43	<i>0.68</i>

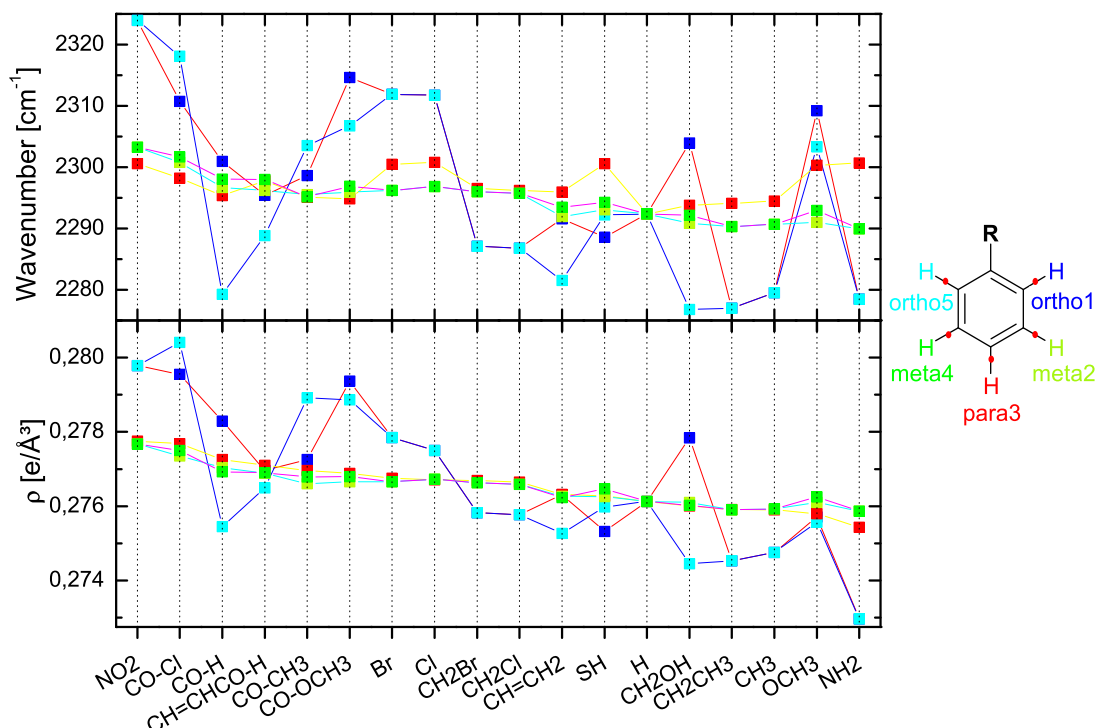


Figure 4.8: Comparison of the calculated ρ in the phenyl-CH-BCPs and the corresponding CD-stretching vibrations for different ph-positions of all benzene derivatives studied within this work. The upper graph shows the wavenumbers of $\nu(\text{CD})$ and the lower ones the corresponding ρ in the BCP(CH). The x-axis is build with respect to a decreasing ρ in *para*-CH-BCP from the left to the right.

CH-BCP and for a comparison of the substituent influence on the CH-BCPs for the different phenyl-positions, the devolutions of the ρ - and the WN-values of all phenyl-CH-positions are plotted against the different substituents in figure 4.8. The high correlation coefficients between ρ and WN for the *meta*-CH/CD-positions are well reflected in figure 4.8, since the characteristics of the WN-graphs are fitting well to the characteristics of the corresponding ρ -graphs. However, slight differences between the curve progression of the ρ - and the WN-graphs of the *ortho*-positions (figure 4.8) are present, even if the correlation coefficients $r(\text{WN}, \rho)$ for the *ortho*-positions indicate a strong linear correlation. The curve progressions of the WN-graphs for the *para*-position do not correspond to the ones of the respective ρ -graphs, causing the low correlation coefficient between the vibrational wavenumber and the electron density in the BCP of the *para*-CH-bonds.

Comparing the correlation coefficients r between the spectroscopic quantities and the

ellipticities in the different ph-CH-BCPs, shown in table 4.2, the only quantity yielding high absolute values of r , indicating a strong linear correlation to ε , is $\sigma_{C_6H_6}^{1H}$ for the protons in the *ortho*- and *para*-positions. In the *meta2*- and *meta4*-positions $r(\sigma_{C_6H_6}^{1H}, \varepsilon)$ is very-weak to weak (see table 4.2). In the case of the *meta2*-position the best but moderate linear correlation to ε can be found for the Raman activity. For the *meta4*-position the weak linear correlation between $\sigma_{C_6H_6}^{1H}$ and ε is nevertheless the highest for this position ($r(\sigma_{C_6H_6}^{1H}, \varepsilon)=0.39$), followed by $r(\text{RA}, \varepsilon)=-0.37$ and $r(\text{IR}, \varepsilon)=-0.30$. Since $\sigma_{C_6H_6}^{1H}$ and RA complement each other in the linear relation to ε , these spectroscopic quantities are expected to be the most important variables to predict ε in the BCPs of phenyl-CH-bonds via linear fits.

4.2.3.2 Fit-procedures

In the former section it was shown that ρ -, $\nabla^2\rho$ - as well as ε -values for the different ph-CH-BCPs can be described by certain spectroscopic variables via linear fit-relations. For a quantitative conclusion from one or more spectroscopic variables to the ρ -, $\nabla^2\rho$ - as well as to the ε -values, it is necessary to find appropriate functions fitting the ρ -, $\nabla^2\rho$ - or ε -values. In a first step, ρ , $\nabla^2\rho$ and ε were fitted to be linear dependent on one of the spectroscopic variables $\sigma_{C_6H_6}^{1H}$, WN, IR, RA, respectively. In a next step, the dimension of the linear function was extended stepwise to the fifth dimension by involving additional spectroscopic variables. In doing so, all possible permutations in each dimension were considered. Finally, the same procedure for quadratic functions was performed and the best methods to calculate ρ -, $\nabla^2\rho$ - and ε -values were identified.

All fits were performed with data-sets build up according the lowest- ρ -convention and are based on either equation 4.2 or 4.3. The target quantities ρ , $\nabla^2\rho$ and ε are denoted as f while the different spectroscopic values WN, IR, RA of the CD-bond stretching vibrations and $\sigma_{C_6H_6}^{1H}$ were chosen as variables (α , β , γ , δ) in the fit-functions; i.e. equations 4.2 and 4.3. The latin characters $a - p$ (except f) are the corresponding fit-parameters. Equation 4.2 represents the linear fit-function of the highest dimension. The quadratic fit-function with the highest dimension (equation 4.3) includes linear, quadratic and mixing terms.

$$f^{lin}(\alpha, \beta, \gamma, \delta) = a + b\alpha + c\beta + d\gamma + e\delta \quad (4.2)$$

$$\begin{aligned} f^{quad}(\alpha, \beta, \gamma, \delta) = & f^{lin}(\alpha, \beta, \gamma, \delta) + g\alpha^2 + h\beta^2 + i\gamma^2 + j\delta^2 \\ & + k\alpha\beta + l\alpha\gamma + m\alpha\delta + n\beta\gamma + o\beta\delta + p\gamma\delta \end{aligned} \quad (4.3)$$

The fit performance is evaluated by the sum of the squared errors χ^2 (equation 4.4) and by the validated sum of squared errors $val\text{-}\chi^2$ (equation 4.5). In these equations n is the number of substances studied within this work (see also equation 4.1), f_i are the DFT-calculated ρ -, $\nabla^2\rho$ - or ε -values, f_{fit} are the corresponding fit-function values and f_{refit} is

explained in the following.

$$\chi^2 = \sum_{i=1}^n (f_i - f_{fit})^2 \quad (4.4)$$

$$val-\chi^2 = \sum_{i=1}^n (f_i - f_{refit})^2 \quad (4.5)$$

$val-\chi^2$ was calculated to estimate the capability of a fit-function to predict ρ -, $\nabla^2\rho$ - or ε -values of new substances which were not considered in the fit. Therefore, each point within a fit is treated as unknown once by omitting the point from the fit. Subsequently, the f -value of the particular omitted point was predicted by using the respective spectroscopic data as input, thus yielding f_{refit} . The sum of the squared differences between all in this way predicted values f_{refit} and the corresponding DFT calculated values f_i is $val-\chi^2$. Since the final goal is to predict electron density properties of new substances with unknown electron density distributions the focus is on the $val-\chi^2$ -values when comparing different fits in the following.

Linear fit-results of electron densities in ph-CH-BCPs. The χ^2 - and the $val-\chi^2$ -values of the linear fits of electron densities depending on spectroscopic variables are compared in the upper part of table 4.3. For *ortho*- and *para*-positions extension of the fit-dimensionality from the second to the third dimension results in a significant decrease of $val-\chi^2$ of about one magnitude. Further enhancement of the dimensionality of fit-functions leads only to minor changes in $val-\chi^2$. Since for the *meta*-positions an almost perfect linear correlation between WN and the ρ -values can be found, the consideration of additional spectroscopic variables does not lead to significant improvements in the fit-performance. In the following, different linear fits of the ρ -values are compared for each position to identify the best fit procedure.

The highest $val-\chi^2$ -values were found for the linear fit dependent on one variable for the *ortho*-positions. The best linear fits of ρ (*ortho*-CH-BCP) dependent on one variable are achieved by using IR-absorption in case of the *ortho1*-position and by using σ_{C6H6}^{1H} in case of the *ortho5*-position. For both *ortho*-positions a fit-dimensionality enhancement by using a further spectroscopic variable leads to a decrease of $val-\chi^2$ of roughly one magnitude. Surprisingly, $\rho(WN, \sigma_{C6H6}^{1H})$ leads to a significant lower $val-\chi^2$ -value than $\rho(WN, IR)$ even if the correlation coefficient $r(\rho, IR)$ is slightly higher than $r(\rho, \sigma_{C6H6}^{1H})$. A further extension of the dimensionality of the linear fit of ρ in *ortho1*-CH-BCPs by including the IR-absorption leads only to a slight lowering of $val-\chi^2$, whereas a subsequent extension by additionally using the Raman activity lowers the $val-\chi^2$ -value about one-fifth. Equivalent results are obtained for ρ in the *ortho5*-positions with the exception of the lowest and the highest dimensional linear fit. The linear fit of ρ (*ortho5*-BCP) with the lowest $val-\chi^2$ depends on WN, IR and σ_{C6H6}^{1H} .

Table 4.3: Sums of squared errors χ^2 and validated sums of squared errors $val\text{-}\chi^2$ of the fits of the electron densities in the BCPs of all ph-CH-bonds, depending on the spectroscopic parameters WN, IR, RA, σ^{1H} . Bold values are the lowest within each fit-dimension, underlined values are the lowest $val\text{-}\chi^2$ -values at the respective position taking all fits into account.

χ^2 [e/Å ³] and $val\text{-}\chi^2$ [e/Å ³] for ρ (BCP)-prediction, based on lowest ρ -convention										
variables	<i>ortho1</i>		<i>meta2</i>		<i>para3</i>		<i>meta4</i>		<i>ortho5</i>	
linear ^a	χ^2	$val\text{-}\chi^2$	χ^2	$val\text{-}\chi^2$	χ^2	$val\text{-}\chi^2$	χ^2	$val\text{-}\chi^2$	χ^2	$val\text{-}\chi^2$
WN ^b	1.35E-05	1.70E-05	1.48E-07	1.75E-07	6.99E-06	8.98E-06	9.68E-08	1.13E-07	1.34E-05	1.68E-05
IR ^b	1.31E-05	1.65E-05	8.52E-07	1.06E-06	7.10E-06	8.92E-06	1.28E-06	1.62E-06	1.80E-05	2.26E-05
RA ^b	3.88E-05	5.29E-05	3.24E-06	3.91E-06	6.62E-06	8.58E-06	4.32E-06	5.19E-06	2.21E-05	3.21E-05
σ^{1H} ^c	1.80E-05	2.37E-05	2.52E-06	3.17E-06	2.42E-06	2.96E-06	2.40E-06	2.97E-06	1.28E-05	1.54E-05
WN, IR	9.92E-06	1.52E-05	1.08E-07	1.36E-07	4.90E-06	6.92E-06	9.63E-08	1.27E-07	1.18E-05	1.63E-05
WN, RA	1.19E-05	1.62E-05	1.36E-07	1.83E-07	5.77E-06	8.29E-06	9.64E-08	1.33E-07	5.31E-06	1.00E-05
WN, σ^{1H}	1.68E-06	2.58E-06	1.08E-07	1.51E-07	2.00E-07	3.35E-07	8.99E-08	1.41E-07	1.65E-06	2.59E-06
IR, RA	1.30E-05	1.92E-05	7.21E-07	1.27E-06	6.45E-06	8.80E-06	7.29E-07	1.11E-06	1.27E-05	2.10E-05
IR, σ^{1H}	5.72E-06	7.88E-06	5.24E-07	7.42E-07	2.59E-07	3.96E-07	8.71E-07	1.19E-06	4.50E-06	6.17E-06
RA, σ^{1H}	1.73E-05	2.72E-05	1.90E-06	2.60E-06	2.07E-06	2.84E-06	2.34E-06	3.27E-06	1.14E-05	1.83E-05
WN, IR, RA	9.87E-06	1.79E-05	1.03E-07	1.31E-07	4.71E-06	8.02E-06	9.65E-08	1.44E-07	5.23E-06	1.15E-05
WN, IR, σ^{1H}	1.53E-06	2.53E-06	8.93E-08	1.40E-07	1.51E-07	2.93E-07	8.99E-08	1.55E-07	1.44E-06	2.57E-06
WN, RA, σ^{1H}	1.55E-06	2.58E-06	9.13E-08	1.68E-07	2.00E-07	3.87E-07	8.98E-08	1.65E-07	1.28E-06	3.26E-06
IR, RA, σ^{1H}	4.75E-06	8.78E-06	4.08E-07	9.47E-07	2.34E-07	4.32E-07	5.17E-07	1.02E-06	4.47E-06	9.31E-06
WN, IR, RA, σ^{1H}	1.17E-06	2.02E-06	7.97E-08	1.37E-07	1.40E-07	3.14E-07	8.97E-08	1.82E-07	1.25E-06	3.93E-06
quadratic^d										
WN	1.29E-05	1.87E-05	1.49E-07	1.90E-07	5.66E-06	9.00E-06	9.62E-08	1.22E-07	1.34E-05	1.88E-05
IR	1.27E-05	2.03E-05	8.38E-07	1.20E-06	4.84E-06	6.99E-06	1.24E-06	1.70E-06	1.64E-05	2.68E-05
RA	3.81E-05	8.17E-05	3.20E-06	4.05E-06	6.20E-06	9.10E-06	4.31E-06	6.63E-06	1.51E-05	3.80E-05
σ^{1H}	1.68E-05	2.97E-05	2.13E-06	3.31E-06	2.10E-06	4.20E-06	2.33E-06	3.46E-06	1.28E-05	1.95E-05
WN, IR	9.32E-06	3.57E-05	1.03E-07	1.90E-07	2.87E-06	6.90E-06	7.94E-08	1.31E-07	1.09E-05	3.00E-05
WN, RA	1.18E-05	3.05E-05	1.05E-06	1.05E-06	4.53E-06	1.41E-05	8.99E-08	3.51E-07	3.77E-06	1.58E-05
WN, σ^{1H}	1.23E-06	4.71E-06	7.12E-08	1.25E-07	1.40E-07	4.86E-07	5.05E-08	1.59E-07	1.22E-06	3.57E-06
IR, RA	6.95E-06	4.08E-05	2.71E-06	2.71E-06	4.58E-06	1.04E-05	4.49E-07	2.00E-06	5.35E-06	2.97E-05
IR, σ^{1H}	3.89E-06	1.20E-05	3.89E-07	7.00E-07	2.02E-07	3.94E-07	6.85E-07	1.25E-06	2.61E-06	5.97E-06
RA, σ^{1H}	1.09E-05	4.10E-05	1.59E-06	4.98E-06	1.92E-06	6.20E-06	1.59E-06	1.05E-05	8.76E-06	3.91E-05
WN, IR, RA	2.93E-06	6.76E-05	9.07E-08	1.13E-05	1.63E-06	2.71E-05	5.78E-08	6.98E-07	1.66E-06	1.68E-05
WN, IR, σ^{1H}	1.13E-06	3.77E-05	2.34E-08	3.36E-07	2.17E-08	1.81E-07	2.94E-08	2.98E-07	6.70E-07	8.63E-06
WN, RA, σ^{1H}	7.41E-07	1.24E-05	4.10E-08	1.39E-06	7.86E-08	6.81E-07	3.37E-08	3.40E-07	4.93E-07	6.60E-06
IR, RA, σ^{1H}	1.29E-06	7.63E-06	1.19E-07	2.15E-06	1.13E-07	4.82E-07	8.63E-08	6.65E-07	1.44E-06	2.57E-05
WN, IR, RA, σ^{1H}	2.02E-07	1.01E-04	6.50E-09	6.24E-06	1.32E-08	2.43E-05	3.63E-09	1.01E-06	3.68E-07	6.14E-05

For the *meta2* and the *meta4*-positions, where correlation coefficients of roughly one were calculated for the linear relation between WN of $\nu(\textit{meta}\text{-CD})$ and ρ in the corresponding BCPs, very good two-dimensional linear fits of $\rho(\text{BCP})$ dependent on WN are of course possible. Only slight improvements of the performance of the linear fits are observed by using additional variables, where the lowest *val*- χ^2 -value for the *meta2*-position can be found if all three vibrational variables are included. For the *meta4*-position the linear fit of ρ depending just on WN leads to the lowest *val*- χ^2 . Furthermore, in each dimension the same combinations of variables are leading to the best linear fits of ρ in both *meta*-positions, respectively.

Considering the bad correlations between $\rho(\text{CH-BCP})$ and vibrational spectroscopic variables in the *para*-position poor linear fits are expected. However, in contrast to vibrational spectroscopic quantities a strong linear relation between $\rho(\textit{para3}\text{-CH-BCP})$ and $\sigma_{\text{C6H6}}^{1\text{H}}$ is present as indicated by the correlation coefficient of 0.81. Comparable results were obtained by Dailey et al., who found $^1\text{H-NMR}$ -spectra of substituted benzenes to correlate reasonably well with π -electron densities in the *para*-position.¹⁸⁰ Nevertheless, the application of WN and IR of $\nu(\textit{para3}\text{-CD})$ as additional variables to $\sigma_{\text{C6H6}}^{1\text{H}}$ leads to a significant lowering of *val*- χ^2 as compared to the linear two-dimensional fit of ρ in the *para3*-CH-BCP just depending on $\sigma_{\text{C6H6}}^{1\text{H}}$.

Quadratic fit results of the electron densities in ph-CH-BCPs. Because of the additional degrees of freedom, the quadratic fit-functions (equation 4.3) lead to lower χ^2 -values than the linear fit-functions as shown in table 4.3. Nevertheless, quadratic functions are not automatically better suited to predict unknown ρ -values than linear functions as indicated by the *val*- χ^2 -values. There are only two cases (see table 4.3), where the quadratic fit yields a slightly lower *val*- χ^2 than the respective linear fit. These are the three- and four-dimensional quadratic fits of ρ in the *meta2*- and the *para3*-CH-BCPs, respectively, labelled as bold underlined *val*- χ^2 -values in table 4.3. Thereby, $\rho(\textit{meta2}\text{-CH-BCP})$ in the quadratic fit depends on WN and $\sigma_{\text{C6H6}}^{1\text{H}}$ and $\rho(\textit{para3}\text{-CH-BCP})$ depends on WN, IR and $\sigma_{\text{C6H6}}^{1\text{H}}$.

Figure 4.9 provides a graphical illustration of the fit results. The red dots display the input data for the fit derived from our DFT calculations, i.e. ρ in *meta2*-CH-BCP plotted against WN, $\sigma_{\text{C6H6}}^{1\text{H}}$. The blue surface displays the fit function and the blue dots represent the fitted ρ -values. For a perfect fit the red and blue dots would match. The green dots display ρ -values predicted via validated functions. The quadratic fit function (blue surface; lower part of fig. 4.9) reveals that the quadratic terms contribute minor to the fit-surfaces within the region the data-points are spread over.

For most of the cases studied within this work (see table 4.3) the quadratic functions lead to higher *val*- χ^2 -values than the linear functions. The reason for that is the stronger de-

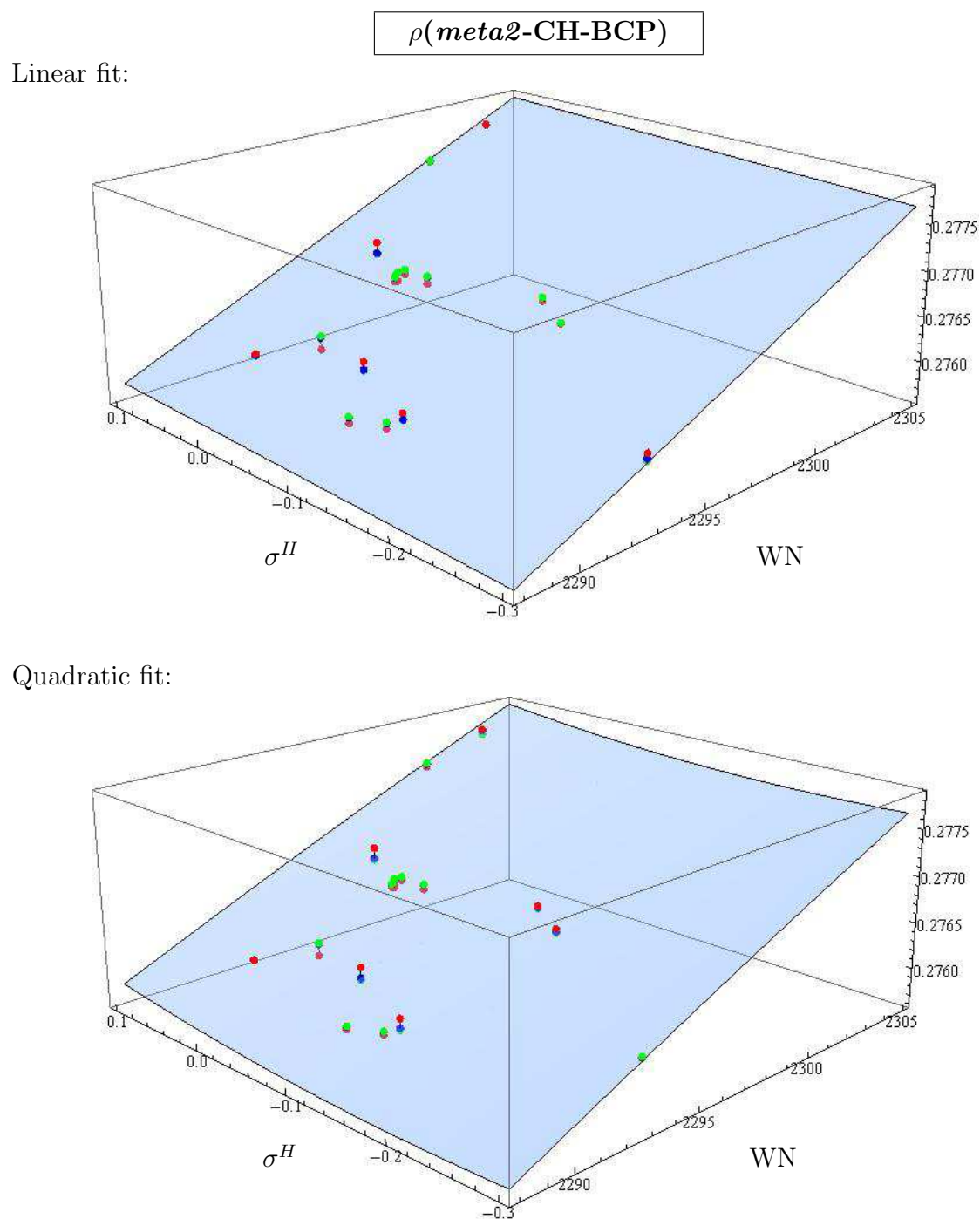


Figure 4.9: Graphical illustration of $\rho(\text{WN}, \sigma_{\text{C6H6}}^{\text{H}})$ of the *meta2*-position: top: linear fit, bottom: quadratic fit; dots: red: DFT calculated, blue: fitted, green: predicted due to refitting; surface: fitted function based on all DFT-calculated data points.

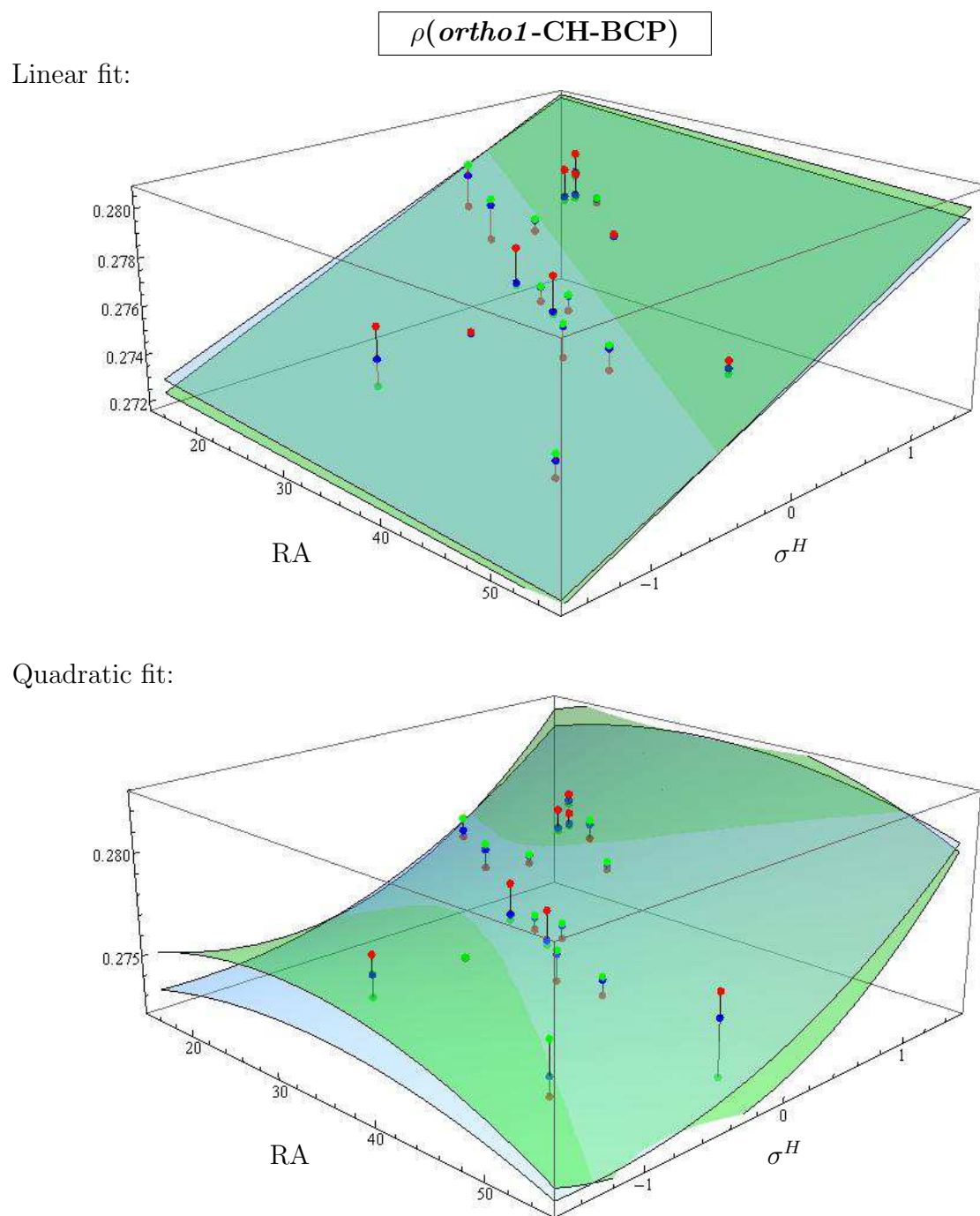


Figure 4.10: Graphical illustration of $\rho(\text{RA}, \sigma_{\text{C6H6}}^{\text{1H}})$ of the *ortho1*-position: top: linear fit, bottom: quadratic fit; dots: red: DFT calculated, blue: fitted, green: predicted due to refitting; surfaces: blue: fitted function based on all DFT-calculated data points, green: fitted function based on all predicted/refitted data.

scent or ascent of the quadratic function away from the center of the data-volume, which is illustrated in figure 4.10 where the surface of the fit function (blue surface) is compared to a surface based on a fit of the validated ρ -values (equivalent function with recalculated parameters; green surface). The larger vertical distance of the $val\text{-}\chi^2$ -surface (green) to the DFT-fit-surface (blue) at the edges of the plot (lower graph in figure 4.10) highlights the strong dependency of fit-parameters of quadratic functions on the data-distribution. In particular, predicting data-points in the peripheral regions via quadratic functions leads to poor results in many cases, since the validation functions derived without knowing the target value usually differ significantly in the slope from the fit-functions involving all data-points. Such difficulties are less pronounced for linear functions (see figure 4.10), for which reason they lead to somewhat more robust results as shown in table 4.3.

The globally best fit concerning the prediction of unknown $\rho(\text{CH-BCP})$, i.e. the fit with the lowest $val\text{-}\chi^2$, was found to be the linear fit dependent on WN at the *meta4*-position ($val\text{-}\chi^2 = 1.1 \cdot 10^{-7} \text{ e}/\text{\AA}^3$). The values for the slope and the intercept are $1.392 \cdot 10^{-4} \text{ e}/\text{\AA}^3$ and $-0.043 \text{ cm}\cdot\text{e}/\text{\AA}^3$, respectively. Generally, $\sigma_{C_6H_6}^{1H}$ and WN are the most important variables to predict ρ in the BCPs of phenyl-CH-bonds, applying linear functions. This combination gives relatively low $val\text{-}\chi^2$ -values for all five phenyl-CH-positions. The additional consideration of IR leads to slight improvements in the ρ -prediction performance, as the lower $val\text{-}\chi^2$ -values summed over all CH-positions ($5.65 \cdot 10^{-6} \text{ e}/\text{\AA}^3$) compared to the application of WN and $\sigma_{C_6H_6}^{1H}$ in the three-dimensional fit ($5.82 \cdot 10^{-6} \text{ e}/\text{\AA}^3$) reveals. The parameters of the globally best linear fit-function and of the linear functions $\rho(\text{WN}, \sigma_{C_6H_6}^{1H})$ and $\rho(\text{WN}, \sigma_{C_6H_6}^{1H}, \text{IR})$ to predict the ρ -values in the BCPs of each phenyl-CH-position are summarized in table 4.4.

To further assess the performance of predicting ρ -values in ph-CH-bonds on the basis of the fit-functions presented in table 4.4 the DFT-calculated, the fitted and the validated ρ -values corresponding to the best linear ρ -fits (see table 4.4) are depicted in figure 4.11. The upper graph shows ρ in the *ortho*-CH-BCPs, the middle and the lower graph show ρ in the *meta*- and *para*-CH-BCPs, respectively. For the *ortho*- and *meta*-graphs, the left and the right side of each column corresponds to the *ortho1*-, *ortho5*-, *meta2*-, and the *meta4*-positions, respectively. As illustrated by figure 4.11 the application of fitted functions corresponding to equation 4.2 and table 4.4 enable a quite accurate prediction of electron densities in BCPs of phenyl-CH-bonds, what facilitates a classification of unknown ρ on the basis of spectroscopic data.

Linear and quadratic fit results of laplacians $\nabla^2\rho$ in ph-CH-BCPs. Since especially laplacians are sensitive to reactivities the relations derived for ρ were translated onto the laplacians. As can be seen in figure 4.7 the laplacian-values are distributed in a similar way as the electron density values in the CH-BCPs. Consequently, a similar prediction

Table 4.4: Parameters of the best linear fit-functions of the electron densities in the BCPs for each ph-CH bond. In the first, second and third row of each position the parameters of the globally best linear fit and of the generally good fits of $\rho(\text{WN}, \sigma_{\text{C6H6}}^{1\text{H}})$ and $\rho(\text{WN}, \sigma_{\text{C6H6}}^{1\text{H}}, \text{IR})$ are presented, respectively.

Fits of $\rho(\text{BCP})$ based on lowest ρ -convention and according to equation 4.2							
Variables Parameter	1 a	$\sigma^{1\text{H}}$ b	WN c	IR d	RA e	χ^2 [e/Å ³]	val- χ^2 [e/Å ³]
<i>Ortho1</i>	0.1221	1.80E-03	6.71E-05	-1.40E-04	2.44E-05	1.17E-06	2.02E-06
	0.1131	1.69E-03	7.12E-05	-7.97E-05	0	1.53E-06	2.53E-06
	0.0876	1.80E-03	8.22E-05	0	0	1.68E-06	2.58E-06
<i>Meta2</i>	-0.1079	0	1.67E-04	1.06E-04	4.88E-06	1.03E-07	1.31E-07
	-0.0806	3.42E-04	1.55E-04	8.34E-05	0	8.98E-08	1.40E-07
	-0.0107	4.69E-04	1.25E-04	0	0	1.08E-07	1.52E-07
<i>Para3</i>	0.0783	2.73E-03	8.68E-05	-1.63E-04	0	1.51E-07	2.92E-07
	0.0783	2.73E-03	8.68E-05	-1.63E-04	0	1.51E-07	2.92E-07
	-0.0482	2.56E-03	1.42E-04	0	0	2.00E-07	3.35E-07
<i>Meta4</i>	-0.0429	0	1.39E-04	0	0	9.68E-08	1.13E-07
	-0.0323	2.02E-04	1.35E-04	7.29E-07	0	8.99E-08	1.55E-07
	-0.0318	2.03E-04	1.34E-04	0	0	8.99E-08	1.41E-07
<i>Ortho5</i>	0.1422	2.01E-03	5.86E-05	-8.15E-05	0	1.44E-06	2.57E-06
	0.1422	2.01E-03	5.86E-05	-8.15E-05	0	1.44E-06	2.57E-06
	0.1148	2.07E-03	7.04E-05	0	0	1.65E-06	2.59E-06

Table 4.5: Parameters of the best linear fit-functions of the laplacians of the electron densities in the BCPs for each ph-CH bond.

Fits of $\nabla^2\rho(\text{BCP})$ based on lowest ρ -convention and according to equation 4.2							
Variables Parameter	1 a	$\sigma^{1\text{H}}$ b	WN c	IR d	RA e	χ^2 [e/Å ⁵]	val- χ^2 [e/Å ⁵]
<i>Ortho1</i>	-0.042	4.37E-03	1.19E-04	-3.92E-04	1.01E-04	7.76E-06	1.30E-05
	-0.155	4.65E-03	1.68E-04	0	6.98E-05	1.07E-05	1.90E-05
	-0.126	4.15E-03	1.56E-04	0	0	1.43E-05	2.33E-05
<i>Meta2</i>	-0.463	0	3.03E-04	1.24E-04	1.83E-05	4.99E-07	6.43E-07
	-0.363	5.51E-04	2.60E-04	0	0.00E+00	5.93E-07	8.37E-07
	-0.388	0.00E+00	2.71E-04	0	0	6.48E-07	7.62E-07
<i>Para3</i>	-0.132	6.33E-03	1.59E-04	-4.15E-04	3.98E-05	7.58E-07	1.62E-06
	-0.162	6.39E-03	1.73E-04	-3.35E-04	0	8.46E-07	1.59E-06
	-0.422	6.03E-03	2.86E-04	0	0	1.06E-06	1.74E-06
<i>Meta4</i>	-0.361	0.00E+00	2.59E-04	-4.65E-05	9.38E-06	4.59E-07	6.82E-07
	-0.399	2.56E-05	2.75E-04	0	0	4.82E-07	7.47E-07
	-0.4	0	2.76E-04	0	0	4.82E-07	5.62E-07
<i>Ortho5</i>	-0.071	4.00E-03	1.33E-04	0	-5.18E-05	3.38E-06	7.81E-06
	-0.032	4.47E-03	1.16E-04	-1.47E-04	0	3.68E-06	6.07E-06
	-0.082	4.59E-03	1.37E-04	0	0	4.35E-06	6.65E-06

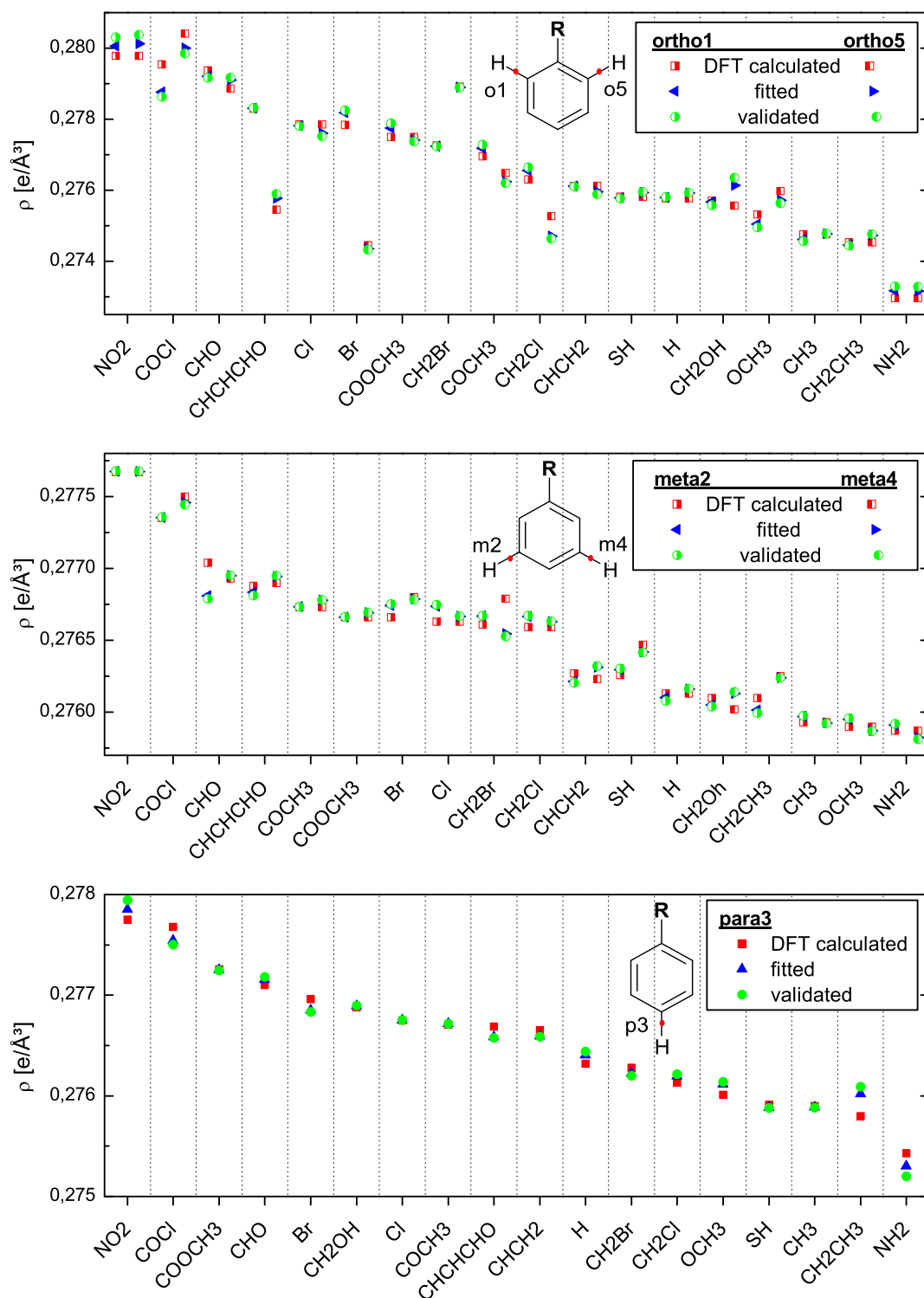


Figure 4.11: DFT-calculated (red), fitted (blue) and validated (green) ρ -values of the best fits for CH-BCPs on all ph-positions. In the two upper graphs, the values left and right in each column correspond to *ortho1/meta2* and *meta4/ortho5* positions, respectively. The fit-functions are linear and the parameters are the ones leading to the lowest *val*- χ^2 shown in table 4.4.

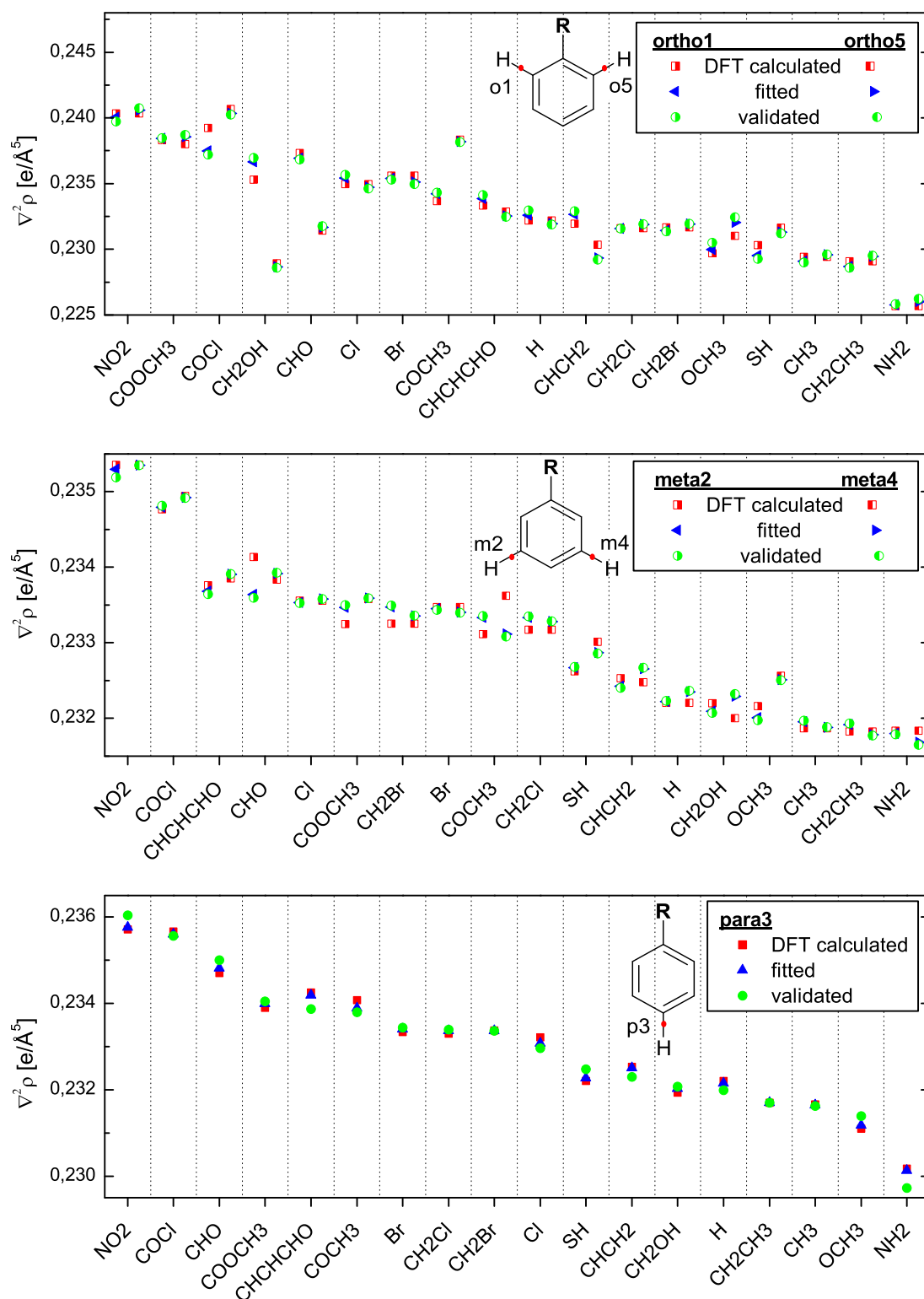


Figure 4.12: DFT-calculated, fitted and validated $\nabla^2\rho$ -values in the BCP of the CH-bonds (compare figure 4.11). The fit-functions are linear and the parameters are the ones leading to the lowest $val-\chi^2$ in table 4.5.

performance is expected. In table 4.5 χ^2 - and $val\text{-}\chi^2$ -values and parameters of the best fits are presented. Table 4.5 reveals that the $val\text{-}\chi^2$ -values are roughly half a magnitude higher than the best fits of ρ , since the $\nabla^2\rho$ -values are covering a significant larger data range. To visualize the excellent fit results, the DFT-calculated, the fitted and the validated laplacians are plotted in figure 4.12.

Linear and quadratic fit results of ellipticities ε in ph-CH-BCPs. The same procedure as described above for the prediction of electron density values was applied to study the relation between the spectroscopic variables and ε . As already suggested by the correlation coefficients shown in table 4.2, the most important variables to predict ε in BCPs of phenyl-CH-bonds in a two-dimensional linear fit are $\sigma_{C_6H_6}^{1H}$ and RA, leading to the lowest $val\text{-}\chi^2$ -values in the *ortho/para*- and *meta*-positions, respectively. The low $val\text{-}\chi^2$ -values for the *meta*-positions compared to the other CH-positions are simply due to the small changes of ε between all benzene-derivatives at the *meta*-positions as visualized in figure 4.13 where the DFT-calculated ε values and the ones corresponding to the best fit (lowest $val\text{-}\chi^2$) for each phenyl-position are depicted. The respective parameters of the best fits are presented in table 4.6.

Table 4.6: Parameters of the best linear fit-functions of the ellipticities in the BCPs for each ph-CH bond. In the first, second and third row of each position the parameters of the globally best linear fit and of the generally good fits $\rho(\text{WN}, \sigma_{C_6H_6}^{1H})$ and $\rho(\text{WN}, \sigma_{C_6H_6}^{1H}, \text{IR})$ are presented, respectively.

Fits of $\varepsilon(\text{BCP})$ based on lowest ρ -convention and according to equation 4.2							
Variables	1	σ^{1H}	WN	IR	RA		
Parameter	a	b	c	d	e	χ^2 [e/Å ³]	$val\text{-}\chi^2$ [e/Å ³]
<i>Ortho1</i>	-0.1181	-8.71E-03	5.92E-05	0	0	2.70E-05	3.58E-05
	-0.0512	-8.98E-03	3.04E-05	-2.09E-04	0	2.60E-05	4.24E-05
<i>Meta2</i>	0.0174	0	0	0	-4.01E-05	1.99E-06	2.41E-06
	0.054	5.73E-04	-1.70E-05	0	0	2.39E-06	3.52E-06
<i>Para3</i>	0.2569	9.40E-04	-1.05E-04	-2.42E-04	0	2.24E-06	3.64E-06
	0.0187	-1.38E-02	0	5.89E-04	-1.50E-04	4.65E-06	7.47E-06
<i>Meta4</i>	0.313	-1.36E-02	-1.30E-04	0	0	6.60E-06	1.05E-05
	-0.1843	-1.43E-02	8.49E-05	6.39E-04	0	5.85E-06	1.02E-05
<i>Ortho5</i>	0.2624	1.74E-03	-1.07E-04	-2.48E-04	0	1.08E-06	1.71E-06
	0.0705	1.44E-03	-2.42E-05	0	0	1.53E-06	2.17E-06
<i>Ortho5</i>	0.2624	1.74E-03	-1.07E-04	-2.48E-04	0	1.08E-06	1.71E-06
	-0.2531	-9.31E-03	1.18E-04	0	0	2.51E-05	3.71E-05
	-0.3105	-9.17E-03	1.43E-04	1.71E-04	0	2.42E-05	4.42E-05

For the *ortho1*-position the linear function $\varepsilon(\sigma_{C_6H_6}^{1H}, \text{WN})$ possesses the lowest $val\text{-}\chi^2$. The respective fit for the *ortho5*-position is of comparable performance, even if the application of the IR-absorption instead of the WN ($\varepsilon(\sigma_{C_6H_6}^{1H}, \text{IR})$) leads to a somewhat lower $val\text{-}\chi^2$ for a quadratic fit-function. In general, ε can be well predicted by means of WN

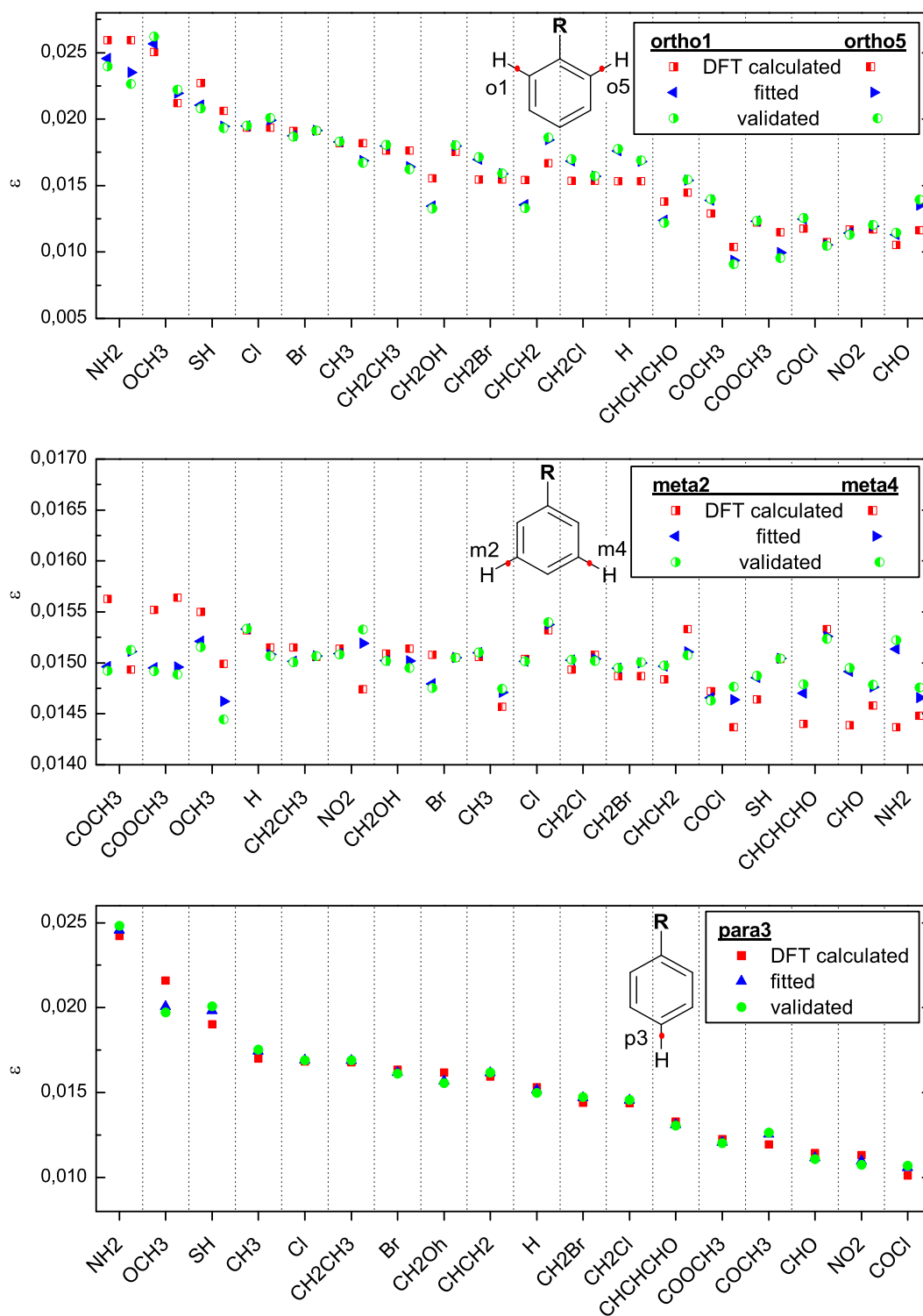


Figure 4.13: DFT-calculated (red), fitted (blue) and validated (green) ϵ -values of the best fits for CH-BCPs on all ph-positions. In the two upper graphs, the values left and right in each column correspond to *ortho1/meta2* and *meta4/ortho5* positions, respectively. The fit-functions are linear and the parameters are the ones leading to the lowest *val*- χ^2 shown in table 4.6.

and $\sigma_{C_6H_6}^{1H}$ as can be seen in figure 4.13. For ε in the *meta*2-CH-BCPs the best results are obtained by involving Raman activities in the case of linear fits, as suggested by the correlation coefficients summarized in table 4.2. The inclusion of additional variables does not improve the fit. Nevertheless, for ε in the *meta*2-CH-BCPs, the lowest *val*- χ^2 is found for the quadratic dependence of ε on $\sigma_{C_6H_6}^{1H}$. For ε in the *meta*4-CH-BCPs the best fit is obtained for a linear function using all spectroscopic variables except the Raman activity. The precision in predicting ε in the *meta*-positions is higher than for all other positions. However, classifying predicted ε (*meta*-CH-BCP)-values is quite challenging due to the low differences between ε (*meta*-CH-BCP) of the benzene-derivatives, as shown in figure 4.13. In contrast, in case of the *para*-position the best fit-function allows a precise classification of new ε (*para*-CH-BCP)-values in a set of known ε , since the ε (*para*-CH-BCP)-values are covering a much larger range than e.g. ε (*meta*-CH-BCP), as visualized in figure 4.13. The three variables with the highest correlation coefficients concerning ε ($\sigma_{C_6H_6}^{1H}$, IR, RA) are also the ones leading to the lowest *val*- χ^2 -values of linear fits.

Hence, one can conclude that on the basis of spectroscopic variables ε in CH-BCPs of mono-substituted benzene derivatives can be well predicted. A constraint is only present for the *meta*-positions, where the prediction accuracy is high, but is not sufficient to classify ε of comparable CH-BCPs of new substances into a set of already studied benzene derivatives. This constraint is caused by the low differences between ε in the BCPs at the *meta*-positions of the studied molecules (see figure 4.7).

Application of relative values. Relative values can be used to enhance the accuracy of the deployed quantities (even experimental) to predict the target values ρ , $\nabla^2\rho$ or ε . In case of the ^1H -NMR-shifts, relative values are already employed in the preceding sections. Additionally, the validity of the fits when using exclusively relative spectroscopic quantities, as relative wavenumbers (difference to the respective value of benzene), IR intensities and Raman intensities (normalized to the benzene signals) was investigated, whereas the latter were calculated from Raman activities as described in the section 4.2.2. As can be seen in table 4.7, the fit-results are almost identical to the ones discussed previously (see tables 4.4, 4.5, 4.6). Nevertheless, the application of relative values is very promising with regard to the employment of accurate experimental spectroscopic data. In this context the precision of the experimentally determined spectroscopic variables is of crucial importance. Since the accuracy of such measures usually depends on the investigated system and the utilized setup a minimal and a common error were estimated. The resulting total experimental error ΔF_{rel} is compared to the standard deviation of the fits SD_{rel} calculated from *val*- χ_{rel}^2 as shown in table 4.7. SD_{rel} and ΔF_{rel} were calculated according to equations 4.6 and 4.7.

$$SD_{rel} = \sqrt{\frac{val-\chi^2}{n-1}} \quad (4.6)$$

$$\Delta F = b\Delta\alpha + c\Delta\beta + d\Delta\gamma + e\Delta\delta \quad (4.7)$$

In equation 4.7 the quantities $\Delta\alpha$, $\Delta\beta$, $\Delta\gamma$, $\Delta\delta$ correspond to the measurement errors of the $^1\text{H-NMR}$ shift, the wavenumber shift, the relative IR intensities and Raman intensities, each with respect to benzene, and are weighted by the parameters of the fit-model (see table 4.7). For the detection of $^1\text{H-NMR}$ shifts a minimal error of 0.001 ppm and a usual error of 0.01 ppm were assumed. In the case of vibrational spectroscopy, wavenumber shifts with an accuracy of about 1 cm^{-1} can be detected, whereas the sensitivity can be even enhanced to shifts of roughly 0.02 cm^{-1} by applying sophisticated difference setups.²⁰¹ The ratios of IR²²⁰ as well as Raman bands are assumed to possess a minimal error of 0.001 for optimal conditions and a usual error of about 0.05.

As revealed by table 4.7 and visualized in figure 4.14 the estimated minimal uncertainties are 1 - 2 magnitudes lower than the standard deviations of the validated fits. Even the estimated uncertainties obtainable via standard measurements are of comparable scale as SD_{rel} or are even one magnitude lower. Hence, the application of the herein derived methodology can be reliably transferred to experimental values, whereas high performance measurements should be applied if accessible. In particular, the exact determination of $^1\text{H-NMR}$ - and wavenumber-shifts is a crucial task, since even the exclusive application of these quantities leads to excellent $val-\chi_{rel}^2$ values (see tables 4.3, 4.4, 4.5, 4.6, 4.7).

Table 4.7: Parameters of the best fit-functions of ρ , $\nabla^2\rho$ or ρ in the BCPs of each ph-CH bond applying relative values for each spectroscopic variable. The corresponding fit-performance is estimated via the $val-\chi^2_{rel}$ - or SD_{rel} -values ($val-\chi^2_{abs}$ listed for comparison). The minimal and common uncertainties of the measures were regarded to estimate the errors of the predicted values due to imperfect input data for the fits ΔF_{rel} .

Var. Param.	Fits of ρ(BCP) - relative values					$val-\chi^2_{rel}$ [e/Å ³]	$val-\chi^2_{abs}$ [e/Å ³]	SD_{rel} [e/Å ³]	ΔF_{rel}	
	1 a	σ^{1H} b	WN c	IR d	RA e				Min. [e/Å ³]	Common [e/Å ³]
$o1$	0.276	1.79E-03	6.75E-05	-9.51E-04	1.24E-03	2.02E-06	2.02E-06	3.45E-04	2.21E-06	8.58E-05
$m2$	0.275	0	1.67E-04	7.14E-04	2.46E-04	1.31E-07	1.31E-07	8.78E-05	4.06E-06	1.68E-04
$p3$	0.277	2.73E-03	8.68E-05	-1.10E-03	0	2.92E-07	2.92E-07	1.31E-04	3.37E-06	1.13E-04
$m4$	0.276	0	1.39E-04	0	0	1.13E-07	1.13E-07	8.14E-05	2.78E-06	1.39E-04
$o5$	0.277	2.01E-03	5.86E-05	-5.51E-04	0	2.57E-06	2.57E-06	3.89E-04	2.63E-06	7.81E-05
Fits of $\nabla^2\rho$(BCP) - relative values						[e/Å ⁵]	[e/Å ⁵]	[e/Å ⁵]	[e/Å ⁵]	[e/Å ⁵]
$o1$	0.23	4.37E-03	1.21E-04	-2.68E-03	5.10E-03	1.28E-05	1.30E-05	8.69E-04	4.15E-06	1.67E-04
$m2$	0.23	0	3.03E-04	8.39E-04	9.23E-04	6.42E-07	6.43E-07	1.94E-04	6.92E-06	3.05E-04
$p3$	0.235	6.39E-03	1.73E-04	-2.26E-03	0	1.59E-06	1.59E-06	3.06E-04	7.58E-06	2.34E-04
$m4$	0.232	0	2.76E-04	0	0	5.62E-07	5.62E-07	1.82E-04	5.52E-06	2.76E-04
$o5$	0.233	4.47E-03	1.16E-04	-9.95E-04	0	6.07E-06	6.07E-06	5.98E-04	5.78E-06	1.59E-04
Fits of ε(BCP) - relative values										
$o1$	0.018	-8.71E-03	5.92E-05	0	0	3.58E-05	3.58E-05	1.45E-03	-7.53E-06	-2.80E-05
$m2$	0.017	0	0	0	-2.09E-03	2.39E-06	2.41E-06	3.75E-04	-2.09E-08	-2.09E-06
$p3$	0.019	-1.38E-02	0	4.11E-03	-7.70E-03	7.41E-06	7.47E-06	6.60E-04	-9.73E-06	-1.41E-04
$m4$	0.017	1.73E-03	-1.07E-04	-1.67E-03	0	1.71E-06	1.71E-06	3.17E-04	-2.08E-06	-9.14E-05
$o5$	0.017	-9.31E-03	1.18E-04	0	0	3.71E-05	3.71E-05	1.48E-03	-6.95E-06	2.46E-05

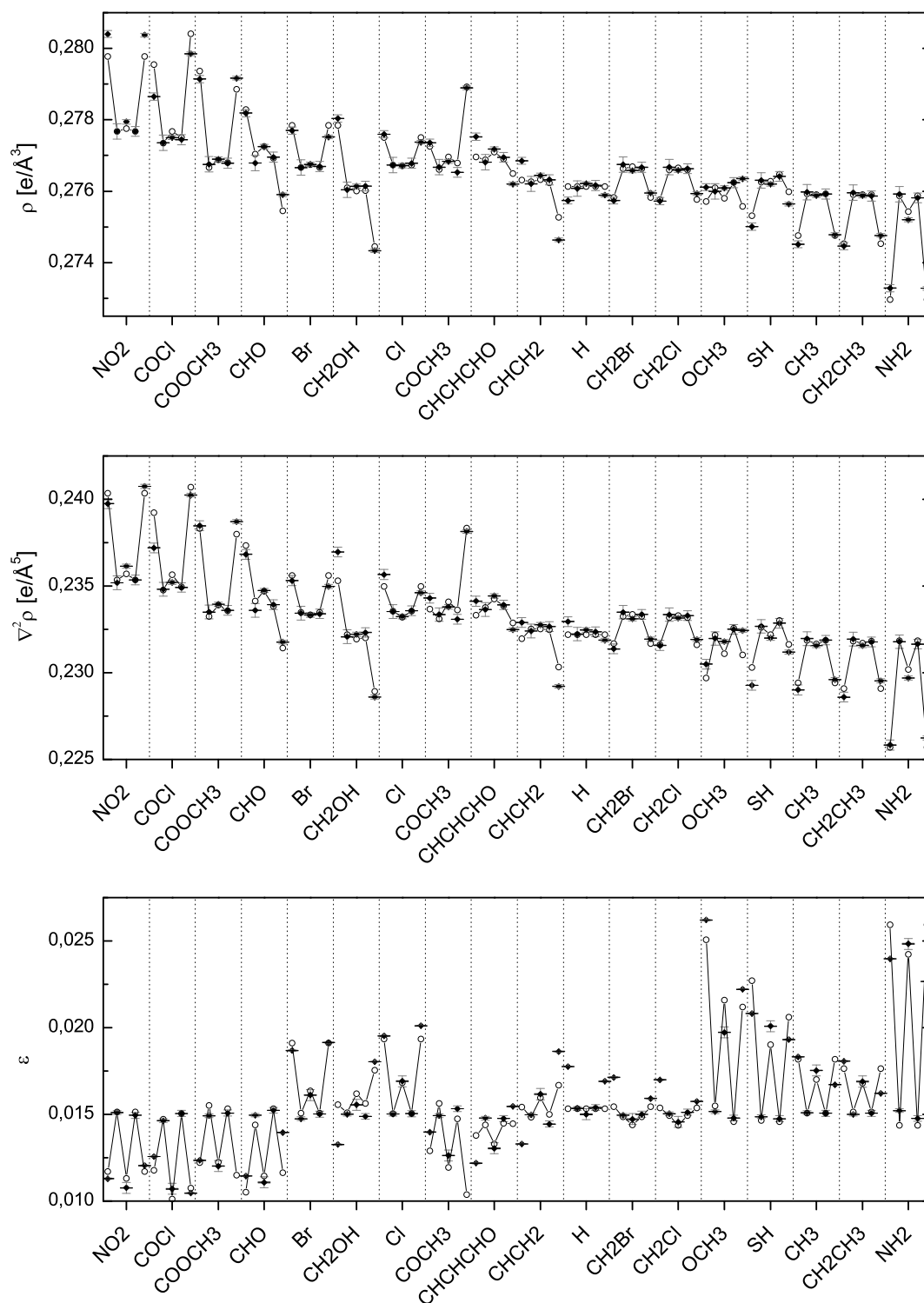


Figure 4.14: DFT-calculated (connected circles) and validated (diamonds) target values (ρ , $\nabla^2 \rho$, ϵ) in all CH-BCPs (left to right in each column), applying relative measures and linear fit-functions (parameters: see table 4.7). Minimal and common estimated experimental uncertainties are added as error bars (black broad; gray slender).

4.3 The π -conjugation in 4'(phenyl)-2,2':6',2''-terpyridine derivatives and their complexes

The π -conjugation, in particular in conjunction with aromatic structures,⁶² is one of the crucial research topics in chemistry since it determines conductivity as well as photovoltaic properties of organic molecules as already pointed out in chapter 1. The substances studied in the actual section are based on 4'-(phenyl)-2,2':6',2''-terpyridine (tpy-ph) and were designed for applications either in OLEDs or in photocatalytic active devices. For both applications the π -conjugation between pyridine and phenylene influences important properties like absorption and emission energies, conductivity properties, band gaps, quantum yields, charge distributions of excited states and so on.

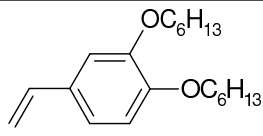
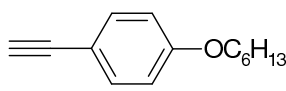
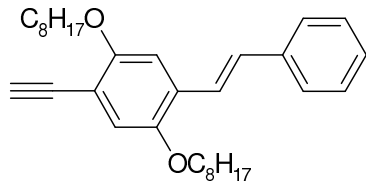
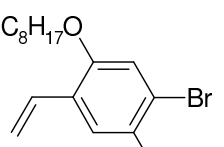
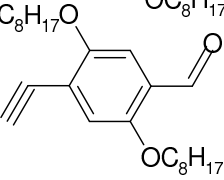
The coordination of Zn(II) to tpy is expected to improve self-organization properties, but to minor change photophysical properties of tpy-ph related oligomers or polymers. Nevertheless, Zn(II) might influence molecular properties among which the π -character of the py-ph bond is in the research-focus of the studies presented in section 4.3.1.²²¹ A further possibility to influence the π -character of the py-ph bond is to modify the skeletal tpy-ph structure due to variation of substituents in the *para*-ph position. The respective changes in the $\rho(r)$ -properties, molecular geometries, Raman spectra and photophysical properties are described in section 4.3.2.⁵³

A series of further substituted tpy-ph-R derivatives and the influences of transition metals with different coordination properties (Zn(II) compared to Ru(II)) on the py-ph bond are studied in section 4.3.3. Hence, a broad spectrum of possibilities to actuate the π -character of the py-ph bond is presented. The derived findings facilitate the design of new structures with defined π -systems. Exemplarily, new structures with extended π -systems and maximized π -delocalization are suggested and the respective properties of the π -systems are predicted by means of QTAIM. Furthermore, the impact of ε (py-ph-BCP) on selected photophysical properties is studied exemplarily.²²²

4.3.1 The influence of Zn²⁺ on the py-ph bond

The high affinity of terpyridine towards most transition metal ions, because of $d\pi \rightarrow p\pi^*$ bonds and the good chelating properties, enables self-organization and highly-ordered architectures and is widely applied in modern supramolecular chemistry.^{61, 223–225} In contrast to frequently used Ru²⁺, Os²⁺ or Ir³⁺ ions for coordination,^{226, 227} Zn²⁺ possesses a full d-shell for which reason MLCT transitions are not observed in related complexes.²²⁸ Therefore, the absorption properties in Zn(II)-complexes are dominated by intraligand (IL) charge transfer between terpyridin and the adjacent chromophores, even in metallo-polymers.^{229, 230}

Table 4.8: Investigated Zn(II) bis-terpyridine complexes

Entry	R:	Entry	R:
Zn(L1) ₂ ²⁺	H	Zn(L7) ₂ ²⁺	
Zn(L2) ₂ ²⁺	Br	Zn(L8) ₂ ²⁺	
Zn(L3) ₂ ²⁺	CH=CH ₂	Zn(L9) ₂ ²⁺	
Zn(L4) ₂ ²⁺	C≡CH		
Zn(L5) ₂ ²⁺			
Zn(L6) ₂ ²⁺			

A series of Zn(II) complexes was synthesized by Winter and coworkers as model compounds for highly ordered self-assembling metallopolymers (see table 4.8). The photophysical properties of the polymers are adjusted by the chromophore design or by π -conjugated spacers facilitating the development of high-performance emissive host materials in OLED applications.²³¹ To investigate the influence of Zn(II) on the π -character of the py-ph bond, the ethynyl substituted tpy-ph derivative 4'(4-p-ethynylphenyl)-2,2'6',2''-terpyridine, abbreviated as **L4**, was chosen as representative example of the derivatives shown in table 4.8.

4.3.1.1 Changes in the UV-vis absorption spectra of L4 due to complexation

As shown in figure 4.15 the coordination of Zn(II) to **L4** leads to a significant change in the absorption spectrum, which exhibits two major absorption regions. In both absorption spectra (**L4** and Zn(II)-complex) the band between 280 and 295 nm is assigned to the terpyridine unit,²³² while the bands between 310 and 350 nm belong to phenylene local-

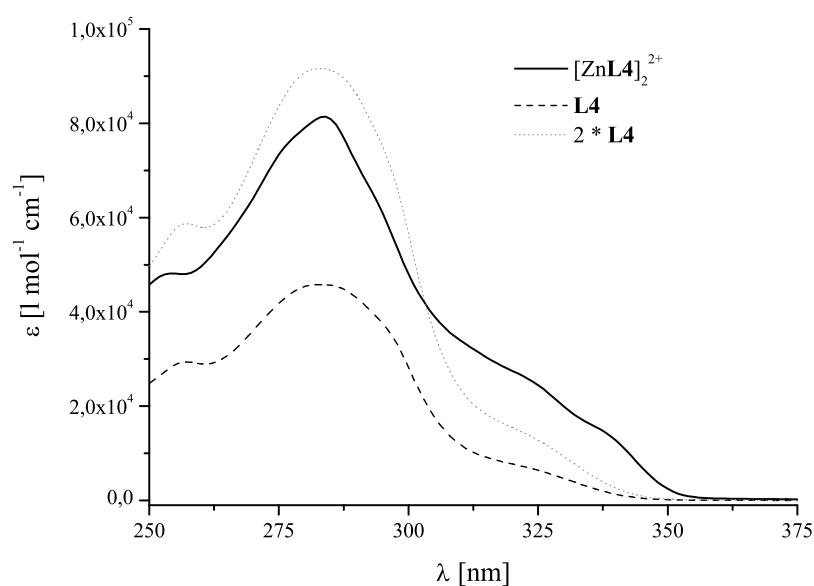


Figure 4.15: UV-vis spectra of **L4** (dashed) and the corresponding zinc(II) complex $[\text{Zn}(\text{L4})_2](\text{PF}_6)_2$ (solid). In addition, the UV-vis spectrum of **L4** multiplied with a factor of 2 (dotted graph), to allow the comparison between the UV-vis spectra of **L4** and $[\text{Zn}(\text{L4})_2](\text{PF}_6)_2$, is included (data determined by Winter and coworkers²²¹).

ized transitions. Generally, the UV-vis spectrum of $[\text{ZnL4}_2](\text{PF}_6)_2$ shows nearly twice the extinction of the **L4**-UV-vis spectrum, since $[\text{ZnL4}_2](\text{PF}_6)_2$ possesses two of the ligands **L4** with the respective chromophore systems.

In the UV-vis spectrum of $[\text{ZnL4}_2](\text{PF}_6)_2$, the region between 310 and 350 nm shows two bands at 325 and 340 nm, whereas the latter is not visible in the UV-vis spectrum of **L4** (figure 4.15). The UV-vis spectrum of **L4** has been multiplied with a factor of 2 to highlight the shift of the bathochromic absorption edge of $[\text{ZnL4}_2](\text{PF}_6)_2$ to lower energies compared to the respective band of **L4**. This bathochromic shift might be due to a shift of a phenylene-based transition to lower energies or the absorption-increase of a low-energetic phenylene transition due to complexation. In both cases, the shift is attributed to a change in the π -system of the phenylene moiety. This change is expected to be rather a slight extension of the ph- π system along the ph-py bond than along the ethynyl group, since the latter should remain unaffected by complex formation.

Even if the supposed slight change of the ph-py- π character is located close to the tpy-chromophore system, a significant bathochromic shift of the low-energy tpy-absorption edge is neither expected nor observed in figure 4.15. This is due to the assignment of the low-energy tpy-absorption (bathochromic edge of the absorption band around 280 nm) to the

tpy-long-axis transition with a transition moment perpendicular to the ph-py bond. The tpy-long-axis transition is expected to be of lower energy and of lower oscillator strength than the transition corresponding to the short tpy-axis.²³² Since the transition dipole moment of the tpy-short-axis transition is parallel to the ph-py bond it should be influenced somewhat more by the higher π -character in the ph-py bond. However, a significant corresponding bathochromic shift is not observable in the hypsochromic edge of the tpy-assigned absorption band (280 - 295 nm) of $[\text{ZnL4}_2]^{2+}$ compared to **L4** (figure 4.15). That means, that even if the π -character of the ph-py bond is somehow increased due to complexation neither of the energies of the tpy located electronic transitions is significantly lowered.

After assuming a change in the electron-density distribution $\rho(r)$ within **L4** upon complexation to be responsible for the bathochromic shift in the phenylene-absorption band around 340 nm, it was studied if this change in $\rho(r)$ can be correlated with changes in the DFT-calculated geometries. To experimentally corroborate the structural changes and the changes in the π -electron delocalization due to complexation Raman spectroscopic experiments were performed.

4.3.1.2 Characterizing the ligand **L4** via DFT-optimized geometries and Raman spectra

Before being able to compare DFT-calculated geometrical differences and differences in the Raman spectra between **L4** and $[\text{ZnL4}_2]^{2+}$, the structure and Raman spectrum of **L4** has to be discussed. The geometry optimizations with subsequent calculations of the Raman spectra of various conformers of the free ligand and of the Zinc complex were performed using the BP86 functional and the TZVP basis set (see section 2.2.1).

While calculating the Raman spectrum of **L4**, one has to account for the different conformers of **L4**. The two most important conformers are the all-*cis* and the all-*trans* structures with respect to the terpyridine moiety. This is because the orientation of the terminal pyridines in the all-*cis* conformer is somehow comparable to the situation in the zinc complex, while the all-*trans* conformer is expected to correspond to the global energetic minimum of the free ligand. The electronic energy of the all-*trans* conformer was calculated to be -1050.065 h and the Gibbs enthalpy is 670.78 kJ/mol. The electronic energy of the all-*cis* conformer is about 0.02 h higher (-1050.045 h) and the corresponding Gibbs enthalpy is about 3 kJ/mol lower (667.94 kJ/mol) than for the all-*trans* conformer. Errors of these DFT energies have been estimated to be below 0.1 mh/atom.^{233,234} This allows the estimation of the accuracy of the computed energies of the **L4** conformers (83 atoms) to be about 0.008 h. The most obvious differences in the geometry of the two conformers are the dihedral angles between the aromatic rings. Geometry optimization of the all-*trans* conformer confirmed the expected planar structure in the terpyridine unit

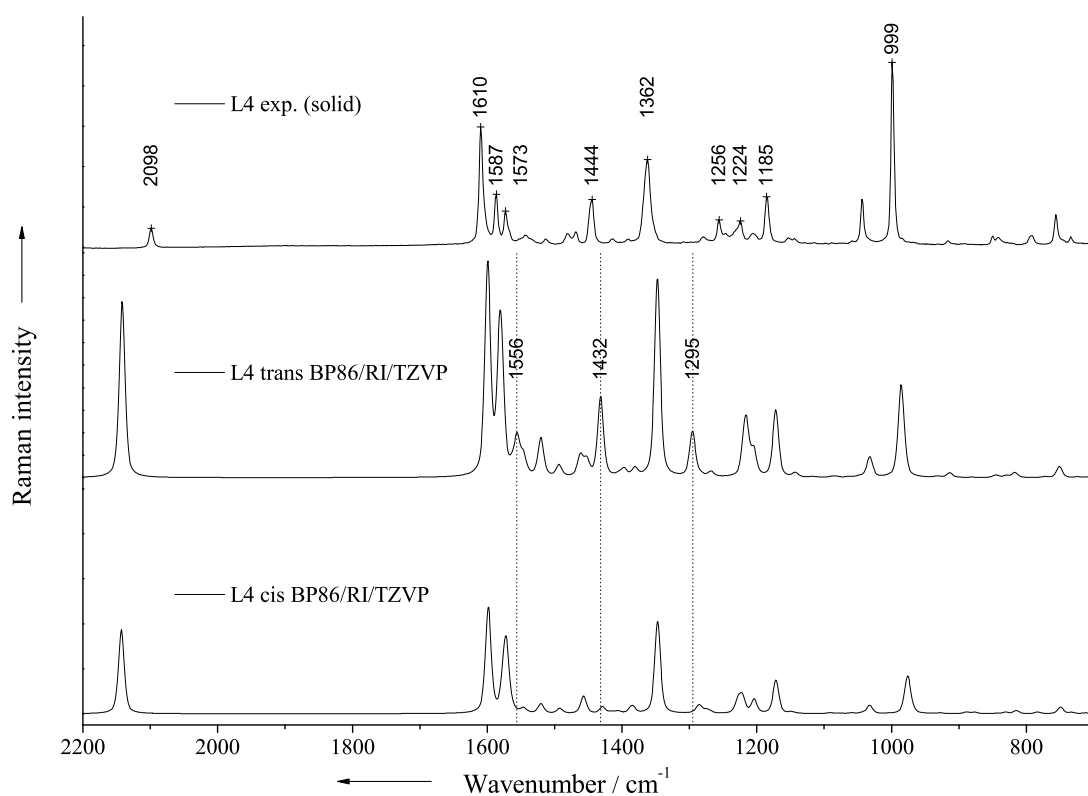


Figure 4.16: Raman spectra of **L4**. Top: Experimental RS ($\lambda_{ex}=830$ nm, grating: 300 gr/mm, solid sample). Middle and bottom: DFT-calculated RS of all-*trans*-**L4** and all-*cis*-**L4** (functional: BP86, basis-set: TZVP, RI-approximation).

with the phenylene group being tilted about 33.2° out-of-plane. This dihedral angle was calculated to be about 3° larger (36.5°) in the case of the all-*cis* conformer, while the angle between the pyridine rings is about 41° . The bondlength of the ph-py bond differs negligible between the all-*cis* and the all-*trans* conformer which is shown in figure 4.17 in the next section in context with the influence of the complexation.

In figure 4.16 the experimental Raman spectrum of **L4** is compared to the DFT-calculated Raman spectra of the all-*cis* and the all-*trans* conformer of **L4**. The most intense bands are at comparable wavenumber positions with an equivalent intensity pattern. In the DFT-calculated Raman spectra of **L4** the intense band at 980 cm^{-1} can be assigned to trigonal ring breathing vibrations located in the terpyridine moiety with quasi-stationary carbon atoms forming the interaromatic ring bonds. The band at 1347 cm^{-1} is assigned to a trigonal ring breathing vibration basically located on the central pyridine ring and the phenylene unit. It involves strong movements of the interaromatic-ring bond

carbon atoms which are accompanied by a pronounced stretch vibration of the phenylene and pyridine connecting bond (C-(H) and N in the central py quasistationary). The bands at 1575 and 1600 cm^{-1} are assigned to aromatic in-plane vibrations corresponding to Wilson No. 8a, located either in the terpyridine unit (1575 cm^{-1}) or in the phenylene group (1600 cm^{-1}).²³⁵ Finally, the Raman band at 2142 cm^{-1} corresponds to the well-separated stretching vibration of the ethynyl group. These modes can be easily identified in the experimental Raman spectrum (RS) of the free ligand **L4** (Figure 4.16). The DFT-calculated modes at 980, 1347, 1575, 1600, 2142 cm^{-1} correspond to bands at 999, 1362, 1587, 1610 and 2098 cm^{-1} in the experimental RS. The somewhat modified intensity pattern in the experimental RS compared to the DFT-calculated one is due to a lower spectrometer sensitivity at higher wavenumbers applying a 830 nm laser line for excitation. The good agreement between experimental and DFT-calculated Raman spectra suggests that the structural features obtained from the DFT calculations are reasonable.

The differences between the DFT-calculated Raman spectra of all-*cis*- and all-*trans*-**L4** allows the determination which of the conformers, primary differing in dihedral angles between the pyridine rings, is present in the experiment. Monitoring the differences in the dihedral angles directly by Raman spectroscopy appears rather challenging because the corresponding torsional modes are expected to occur in the low wavenumber region with strongly reduced Raman intensities. However, differences of the dihedral angles between the aromatic rings influence the aromatic in-plane vibrational modes that dominate the Raman spectrum in the region between 900 and 1700 cm^{-1} . In particular, the rather less intense Raman bands calculated to occur at 1296, 1433 and 1556 cm^{-1} in the spectrum of the all-*trans* conformer are not clearly identifiable in the corresponding Raman spectrum of the all-*cis* conformer. Hence, they appear to be appropriate marker bands for the *trans* conformation. Experimentally, these marker bands are observed at 1444 and 1573 cm^{-1} . Though, the calculated marker band of the *trans*-**L4** at 1296 cm^{-1} cannot be clearly identified in the experimental data, the strong presence of the other *trans*-characteristic bands in the experimental spectrum of **L4** suggest that the latter spectrum is mainly dominated by the *trans* conformer.

4.3.1.3 Investigation of the changes in geometry upon complexation and discussion of the Raman spectrum of $[\text{Zn}(\text{L4})_2]^{2+}$.

According to the DFT calculations the terpyridine moiety in $[\text{Zn}(\text{L4})_2](\text{PF}_6)_2$ is planar in contrast to the free *cis*-**L4**. Consequently, the larger overlap of the free electron pairs of the nitrogen atoms with the d-orbitals of the zinc(II) ion in combination with a higher degree of π -delocalization in the planar terpyridine moiety compensates the steric hindrance of the neighboring hydrogen atoms on the respective pyridines. Furthermore, the dihedral angle between phenylene and pyridine is with 30.0° slightly but distinctly lower than in

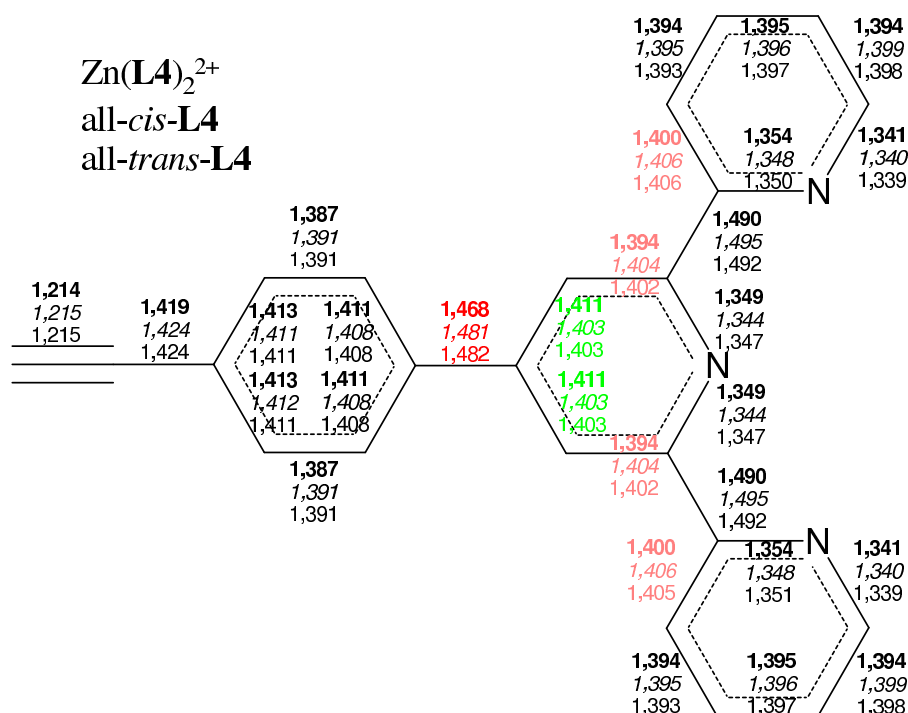


Figure 4.17: Bond lengths in the ligand $\mathbf{L4}$ and the corresponding complex $[\text{Zn}(\mathbf{L4})_2](\text{PF}_6)_2$ as derived from DFT calculations. Significant changes upon complexation. Pale red: 0.006 - 0.01 Å shortened bonds; red: > 0.01 Å shortened bond; green: > 0.006 Å elongated bonds.

both conformers of the uncomplexed ligand as shown in table 4.9 (*cis*- $\mathbf{L4}$: 36.5°, *trans*- $\mathbf{L4}$: 33.2°).

The DFT calculations reveal that most of the carbon-carbon bond lengths differ less than 0.005 Å between uncomplexed $\mathbf{L4}$ and $[\text{Zn}(\mathbf{L4})_2](\text{PF}_6)_2$ (figure 4.17). However, bonds that are shortened due to complexation are the pyridine-carbon-carbon bonds adjacent to the pyridine connecting bonds. The respective bond lengths differ from 0.006 to 0.01 Å (0.4-0.7%) between $[\text{Zn}(\mathbf{L4})_2](\text{PF}_6)_2$ and any of the conformers of $\mathbf{L4}$ and are colored pale red in figure 4.17. The most significant shortened bond due to complexation is the ph-py bond with a length of 1.468 Å in $[\text{Zn}(\mathbf{L4})_2](\text{PF}_6)_2$ compared to 1.481 and 1.482 Å in all-*cis*-L and all-*trans*-L, respectively (figure 4.17, red labels). Besides the bond shortening, significant bond elongations of 0.008 Å (0.6%) are observed for pyridine-carbon-carbon bonds adjacent to the ph-py bond (figure 4.17, green labels).

The value of the dihedral angle between phenyl and pyridine is lowered upon complexation. Concertedly, the ph-py bond is shortened indicating a higher degree of π -delocalization between ph and py in $[\text{Zn}(\mathbf{L4})_2](\text{PF}_6)_2$ compared to free $\mathbf{L4}$. The lower dihedral angle goes along with a larger overlap of the π -orbitals of the carbon atoms of the ph-py bond. Additionally, the shortening of the ph-py bond indicates a higher bond order and with it

Table 4.9: Selected parameters indicating variations in the π -electron delocalization due to complexation

Comp.	$\alpha^{\circ a}$	$r(\text{py-ph})^b$	wavenumber		Raman ^{c,d}		BCP(py-ph)	
	theor.	theor.	theor.	exp.	activity	i. r.	ρ	ε
	[$^{\circ}$]	[\AA]	[cm^{-1}]	[cm^{-1}]	[$\text{\AA}^4/\text{amu}$]		[$e/\text{\AA}^3$]	
<i>cis</i> - L4	36.5	1.481	1347.2	1362	1400	0.772	0.255	0.069
<i>trans</i> - L4	33.2	1.482	1347.5		1692		0.260	0.058
$\text{Zn}(\mathbf{L4})_2^{2+}$	30.0	1.468	1351.4	1370	6171	1.345	0.255	0.081

^a Dihedral angle between the central pyridine ring and the phenyl substituent (py-ph).

^b Bond length between the central pyridine ring and the phenyl substituent. ^c $\nu(\text{ph-py}(\text{trig}))$ (see text). ^d Raman activity: DFT-calculated; Raman intensity ratio (i.r.): experimentally determined, $\nu(\text{ph-py}(\text{trig}))/\delta_{ip}(\text{trig. ring br.})$.

also a higher π -character of the ph-py bond.

By comparing the Raman spectra of **L4** and $[\text{Zn}(\mathbf{L4})_2]^{2+}$ it can be seen that the most intense Raman bands appear at comparable wavenumbers and with comparable relative Raman intensities (figure 4.16 and 4.18). Hence, the vibrational pictures of $[\text{Zn}(\mathbf{L4})_2]^{2+}$ underlying these intense bands, e.g. the aromatic in plane vibrations, are comparable to those of **L4**, described in the previous section. Identical or energetically closely spaced vibrations on both ligands in $[\text{Zn}(\mathbf{L4})_2]^{2+}$ are coupled. This coupling leads to a splitting of **L4**-modes giving rise to symmetrical and 180° phase shifted modes in $[\text{Zn}(\mathbf{L4})_2]^{2+}$, slightly shifted to higher or lower wavenumbers. Hence, differences in the Raman spectra, e.g. the vibration corresponding to the band at 1362 cm^{-1} in the Raman spectrum of **L4** (see figure 4.16) is assigned to the band at 1370 cm^{-1} in the Raman spectrum of $[\text{Zn}(\mathbf{L4})_2]^{2+}$ (figure 4.18, table 4.9), are due to geometrical changes upon complexation and slight shifts caused by mode-coupling in $[\text{Zn}(\mathbf{L4})_2]^{2+}$ to some extent (see appendix A.1 (table A.1) for complete vibrational assignment, supported by a DFT-calculated Raman spectrum). The DFT-calculated Raman spectrum is in good agreement with the experimental Raman spectrum (see figure 4.18) and is based on the fully optimized geometry of $[\text{Zn}(\mathbf{L4})_2]^{2+}$ which is depicted in figure 4.19 with respective atomic labels.

4.3.1.4 Tracing the change of the electron density distribution in the ph-py bond due to complexation by means of Raman spectroscopy

As previously discussed, changes in the geometry due to complexation, manifested by shortening of the ph-py bond and lowering of the dihedral angle between ph and py, indicate a higher bond order and with it a higher π -character of the ph-py bond. It is possible to monitor these changes by means of Raman spectroscopy since a marker

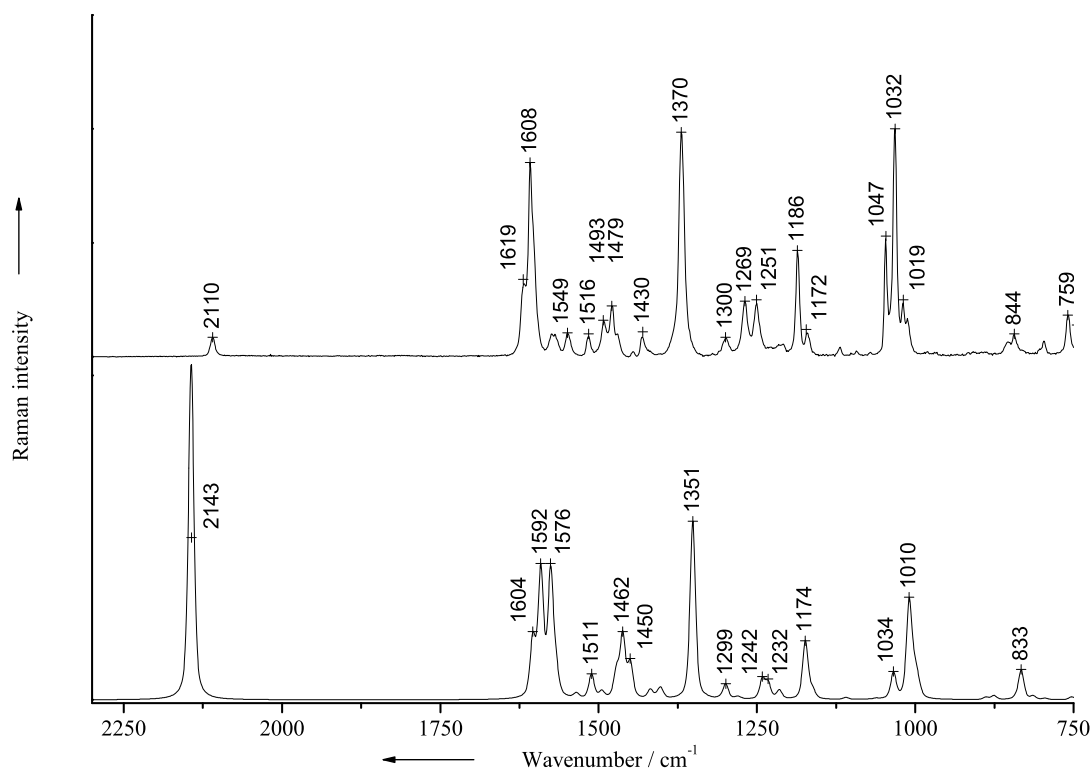


Figure 4.18: Experimental (top) and DFT-calculated (bottom; BP86/RI/def2-TZVP) Raman spectra of $[\text{Zn}(\mathbf{L4})_2]^{2+}$.

band is present, which involves significant ph-py bond stretchings. This marker band is the trigonal ring breathing mode $\nu(\text{ph-py}(\text{trig}))$ involving strong ph-py bond stretchings and appearing around 1365 cm^{-1} in the experimental RS (see table 4.9). It is basically located on the central pyridine ring with strong movements of the substituted carbon atoms. Thus, strong stretchings of the ph-py bond and inter-pyridine bonds are involved, as shown in the lower graph of figure 4.19. An increased bond order due to complexation in the ph-py bond goes along with a higher force constant and is expected to give rise to a shift to higher wavenumbers of $\nu(\text{ph-py}(\text{trig}))$.

When comparing $\nu(\text{ph-py}(\text{trig}))$ between $\mathbf{L4}$ and $[\text{Zn}(\mathbf{L4})_2]^{2+}$, one has to account for the 2-fold existence of $\mathbf{L4}$ in the complex $[\text{Zn}(\mathbf{L4})_2]^{2+}$. The observed mode coupling leads to a splitting into a symmetric ($\nu(\text{ph-py}(\text{trig}))_s$) and an asymmetric mode ($\nu(\text{ph-py}(\text{trig}))_{as}$ 180° phase-shifted $\mathbf{L4}$ -vibrations). The symmetric vibration is shifted to higher wavenumbers ($\nu(\text{ph-py}(\text{trig}))_s$: 1351 cm^{-1} , Raman activity $6171 \text{ \AA}^4/\text{amu}$) and the asymmetric vibration is shifted to lower wavenumbers ($\nu(\text{ph-py}(\text{trig}))_{as}$: 1349 cm^{-1} , Raman activity $243 \text{ \AA}^4/\text{amu}$) following the DFT calculations.

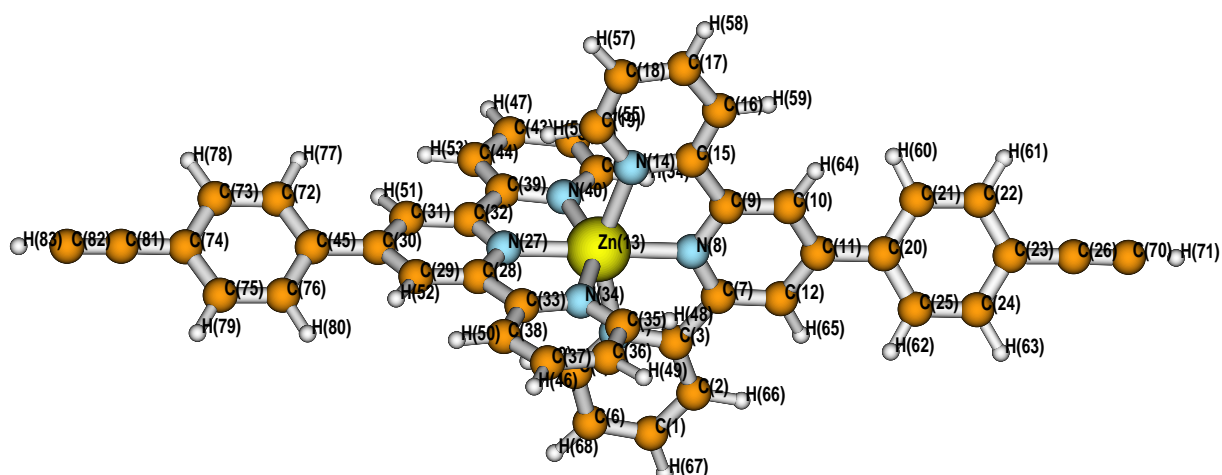
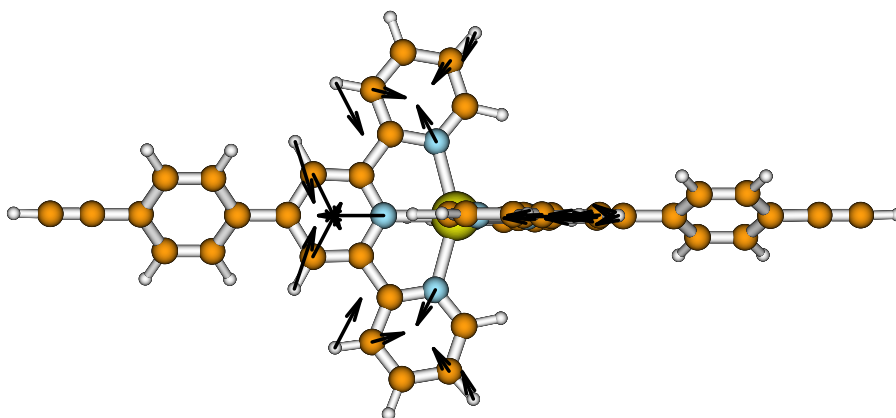
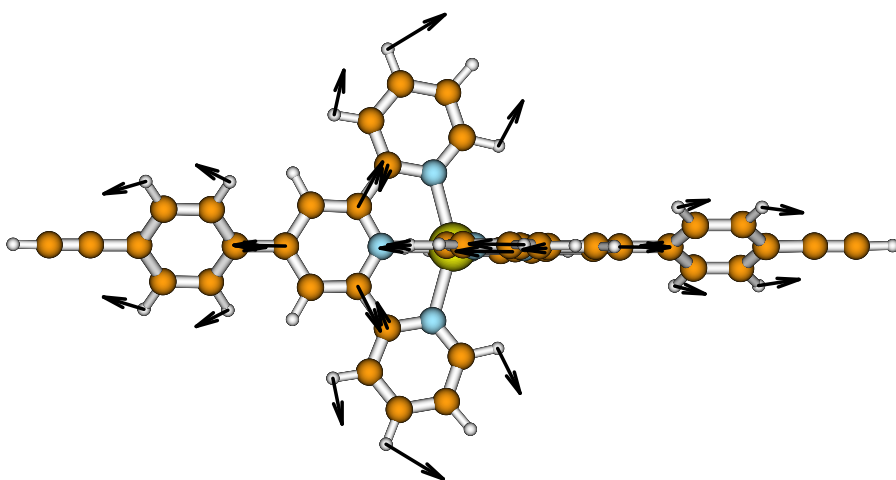
Atomic labels for $[\text{Zn}(\text{L4})_2]^{2+}$:Trigonal ring breathing vibration $\delta_{ip}(\text{trig. ring br.})$ ($\tilde{\nu}^{DFT} = 1010 \text{ cm}^{-1}$):Trigonal ring breathing vibration $\nu(\text{ph-py}(\text{trig}))$ ($\tilde{\nu}^{DFT} = 1351 \text{ cm}^{-1}$):

Figure 4.19: Top: DFT-calculated structure of $[\text{Zn}(\text{L4})_2]^{2+}$ with atomic labels. Middle and bottom: Trig. ring breathing modes $\delta_{ip}(\text{trig. ring br.})$ ($\tilde{\nu}^{DFT} = 1010 \text{ cm}^{-1}$) and $\nu(\text{ph-py}(\text{trig}))$ ($\tilde{\nu}^{DFT} = 1351 \text{ cm}^{-1}$.)

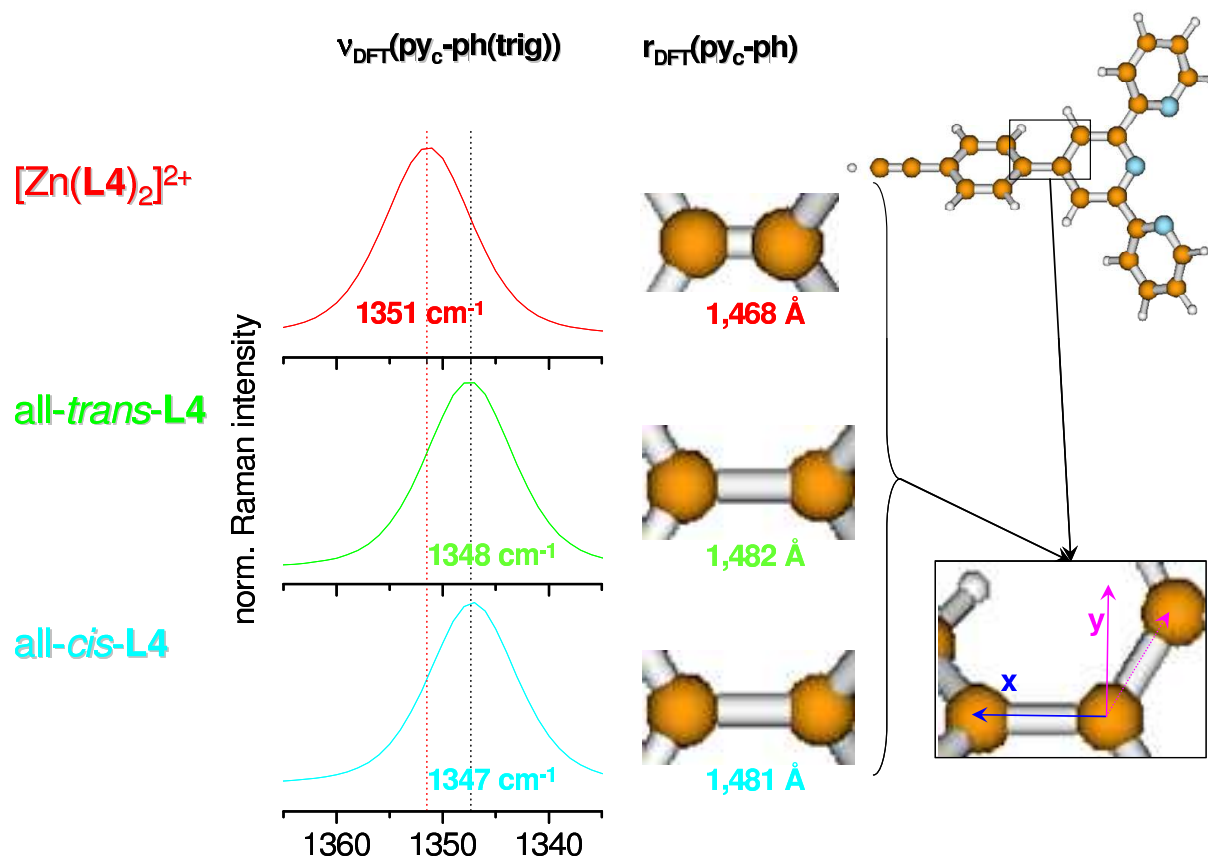


Figure 4.20: Sketch of the correlation between Raman shift of $\nu(\text{ph-py}(\text{trig}))$ and bond shortening of the ph-py bond upon complexation. Definition of the central pyridine plane: magenta and blue arrows.

In the experimental Raman spectrum of $[\text{Zn}(\text{L4})_2]^{2+}$ the band at 1370 cm^{-1} has been assigned to $\nu(\text{ph-py}(\text{trig}))_s$ whereas $\nu(\text{ph-py}(\text{trig}))_{as}$ exhibits too low intensity to be seen experimentally. The $\nu(\text{ph-py}(\text{trig}))_s$ mode is correlated with the corresponding vibration in **L4** $\nu(\text{ph-py}(\text{trig}))$ at 1362 cm^{-1} . So, a total shift of the $\nu(\text{ph-py}(\text{trig}))$ mode of roughly 8 cm^{-1} was observed when comparing $\nu(\text{ph-py}(\text{trig}))$ of **L4** and $[\text{Zn}(\text{L4})_2]^{2+}$. This difference exceeds the expected wavenumber shift of 1 cm^{-1} due to splitting of this mode in a symmetric and an antisymmetric mode. Hence, the difference follows from the higher bond order in the ph-py bond and with it from the increased π -electron delocalization between phenylene and pyridine upon complexation (see table 4.9). The correlation between bond length of the ph-py bond and shift of the $\nu(\text{ph-py}(\text{trig}))$ vibration to higher wavenumbers is schematically illustrated in figure 4.20.

The higher π -delocalization is further corroborated by the higher calculated Raman activity of $\nu(\text{ph-py}(\text{trig}))_s$ in $[\text{Zn}(\text{L4})_2]^{2+}$. This is due to a higher π -character of the ph-py bond, which causes a higher electronic polarizability α and, consequently, a higher Raman activity of $\nu(\text{ph-py}(\text{trig}))$. Together with the Raman activity of $\nu(\text{ph-py}(\text{trig}))_{as}$, the summed Raman activity is with $6413 \text{ \AA}^4/\text{amu}$ roughly four times higher than for *cis*- and

trans-**L4** (1400 and 1692 $\text{\AA}^4/\text{amu}$, respectively). This finding cannot be explained simply by invoking the 2-fold existence of **L4** in $[\text{Zn}(\mathbf{L4})_2]^{2+}$ ($2 \times 1692 \text{\AA}^4/\text{amu} = 3384 \text{\AA}^4/\text{amu}$) and hence points to an increase of the π -character of the ph-py bond due to complexation. The calculated increase in Raman activity of $\nu(\text{ph-py}(\text{trig}))$ due to complex formation is difficult to confirm experimentally since the two substances exhibit different scattering cross sections. Therefore, the $\nu(\text{ph-py}(\text{trig}))$ Raman band has been normalized to the band of the trigonal ring breathing mode ($\delta_{ip}(\text{trig. ring br.})$). The vibrational picture of $\nu(\text{ph-py}(\text{trig}))$ as well as of $\delta_{ip}(\text{trig. ring br.})$ is shown in figure 4.19. The $\delta_{ip}(\text{trig. ring br.})$ mode is mainly located at the terpyridine moiety and thus is assumed to be almost independent of the binding situation in ph-py since it does not involve $\nu(\text{ph-py})$ vibrations.

The quotient of the integrated Raman bands corresponding to $\nu(\text{ph-py}(\text{trig}))$ and to $\delta_{ip}(\text{trig. ring br.})$ is listed in table 4.9. As can be seen, the value corresponding to the Raman data of $[\text{Zn}(\mathbf{L4})_2]^{2+}$ (1.35) is roughly twice the value of **L4** (0.77) confirming the theoretical results ($\text{RA}\{[\text{Zn}(\mathbf{L4})_2]^{2+}-\nu(\text{ph-py}(\text{trig}))\}_{s+as} = 6413 \text{\AA}^4/\text{amu}$, $2 \times \text{RA}\{\textit{trans-L4}-\nu(\text{ph-py}(\text{trig}))\} = 3384 \text{\AA}^4/\text{amu}$). Thus, the theoretically predicted increase of the Raman activity of $\nu(\text{ph-py}(\text{trig}))$ of $[\text{Zn}(\mathbf{L4})_2]^{2+}$ compared to **L4** is confirmed experimentally and further evidences the increase of π -character of the ph-py bond in **L4** due to complexation. The changes of geometrical parameters upon complexation as well as the Raman shifts and Raman intensity changes are summarized in table 4.9. In addition, results of the analysis of the topological properties of the electron density distribution, presented in the next section, are included in table 4.9.

4.3.1.5 Discussing the change of the electron density distribution in the ph-py bond due to complexation based on a topological analysis and an intermolecular electron-density-difference plot

To obtain a more quantitative picture of changes in the degree of π -electron delocalization between phenylene and pyridine due to complexation, an analysis of the DFT-calculated topology of electron density distribution ($\rho(\mathbf{r})$) according to Baders AIM theory is performed (see sec. 2.2.2). In doing so, the investigation focusses on ρ - and ε -values in the ph-py bond critical points (BCP(ph-py)) which are compared in table 4.9. Remarkably, ρ differs less between free ligand **L4** and the respective complex $[\text{Zn}(\mathbf{L4})_2]^{2+}$ in contrast to the ellipticity ε . Since ε in the ph-py-BCP is significantly raised in $[\text{Zn}(\mathbf{L4})_2]^{2+}$ to 0.081 as compared to *cis*-**L4** (0.069), the assumption of a higher bond order and a higher π -character of the ph-py bond in $[\text{Zn}(\mathbf{L4})_2]^{2+}$, based on the geometries and Raman spectra, is supported. As shown in table 4.9, ellipticities correlate well with the Raman intensities (RI). However, this behavior cannot be observed for ρ and RI. Unfortunately, the punctiform characterization of the bonding situation in the ph-py bond according to Bader's

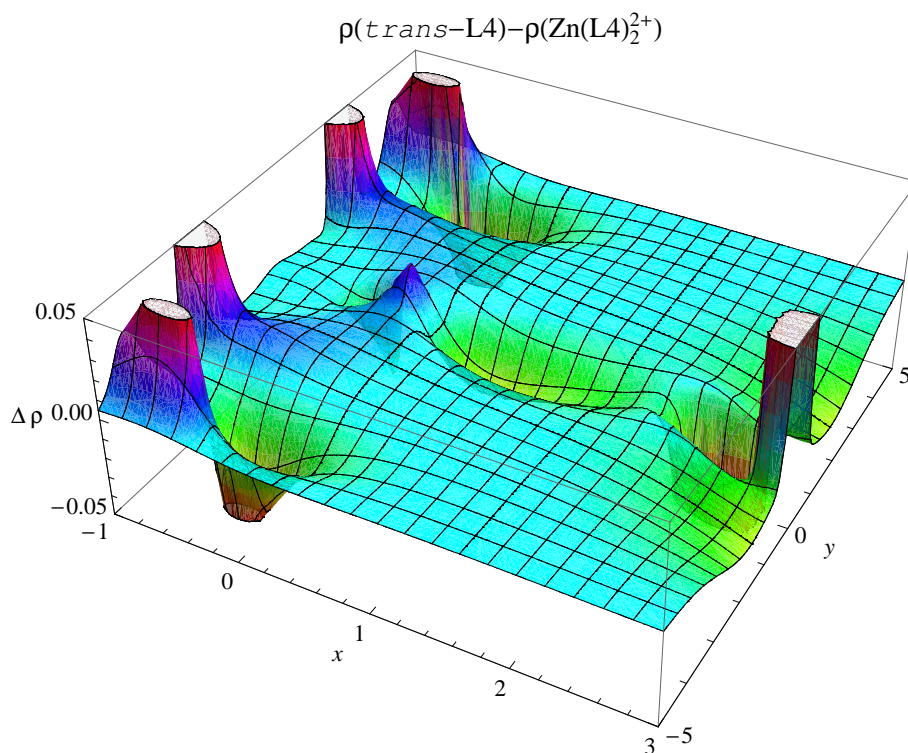


Figure 4.21: *Inter- $\Delta\rho$ -plot*: $\rho(\text{trans-L4}) - \rho([\text{Zn}(\text{L4})_2]^{2+})$. In the middle of the graph, the ρ -difference in the ph-py bond is visible. The origin is the carbon atom belonging to the pyridine ring of the ph-py bond. The vectors defining the drawing plane are depicted in figure 4.20. The z -axis corresponds to $\Delta\rho/\text{e}/\text{\AA}^3$, x - and y -axis are distances in a.u.. For details, see text.

QTAIM neither is pictorial nor describes the ph-py bond comprehensively. Hence, an intermolecular electron-density-difference plot was generated (*inter- $\Delta\rho$ -plot*) to highlight the changes in the ph-py bond due to complexation (figure 4.21).

In this *inter- $\Delta\rho$ -plot* the ρ -distribution corresponding to the central pyridine plane of $[\text{Zn}(\text{L4})_2]^{2+}$ is subtracted from the ρ -distribution of the central pyridine plane in *trans-L4*. The plane of the central pyridine rings is defined by the normalized vector corresponding to the ph-py bond and a normalized perpendicular vector lying in the plane of the central pyridine unit and coincides with the drawing plane in figure 4.21. These vectors defining the pyridine plane are visualized on the molecular structure graph of **L4** in figure 4.20, in which the ph-py vector is blue and the second vector defining the py plane is colored magenta. The latter is defined by rotating the vector corresponding to a pyridine carbon-carbon bond (magenta, dotted vector in figure 4.20). The atom common to the vectors (C11 in figure 4.19) is the origin of the coordinate system. In figure 4.21, the molecular section close to the ph-py bond is depicted.

This visualization illustrates changes in the electron density distribution not clearly emerg-

ing from ρ -values in BCP(ph-py). The higher ρ within the ph-py bond of $[\text{Zn}(\mathbf{L4})_2]^{2+}$ as compared to $\mathbf{L4}$ is visualized by the valley in the middle of figure 4.21. Even the slight electron density fluxes from the central pyridine ring to the ph-py bond upon complexation is revealed by the $\Delta\rho$ -plot due to the blue colored positive values along the pyridine-carbon-carbon bonds in figure 4.21. The cusps arise from slightly shifted maxima of ρ at positions of the nuclei. In this way, i.e. invoking unscaled atomic distances, also differences in the geometry between $[\text{Zn}(\mathbf{L4})_2]^{2+}$ and $\mathbf{L4}$ are visualized. The truncated negative cusp close to the position of the ph-carbon atom in the ph-py bond corresponds to the shortening of the ph-py bond upon complexation.

Therefore, this visualization technique facilitates the interpretation of differences in electron density distribution in connection with the geometries of molecular key structures of two different molecules. To compare ρ -distributions of different molecules, it is also possible to plot $\rho(x,y)$ separately for each molecule, but this is not appropriate to study very small ρ -differences. On the other hand, punctiform tabular comparisons, for example on the basis of Baders QTAIM, are neither comprehensive nor illustrative. $\Delta\rho$ -plots are predominantly used to study the ρ -distribution of a single molecule as this is the case in deformation density plots.¹⁰⁴ In other works, the effect of different orbital constructions or different environments is studied applying $\Delta\rho$ -plots.²³⁶⁻²³⁹ However, the *inter*- $\Delta\rho$ -plot exhibits a great potential to study ρ - and geometry differences in narrow key regions of two different molecules, as presented in this work and shown by others.²⁴⁰⁻²⁴²

Of course *inter*- $\Delta\rho$ -plots are not applicable to compare larger molecular sections of different molecules since *inter*- $\Delta\rho$ -plots strongly depend on the respective geometries. To enlarge the molecular section of interest, it is possible to generate the *inter*- $\Delta\rho$ -plot applying locally equalized geometries to reduce the influence of different nuclear positions. For example, the usage of equalized ph-py bonds is possible by suppressing the normalization of the ph-py corresponding vectors of both molecules and using an equal number of plotting points along the ph-py vector. The (x,y) frame of one of the compared molecules serves as reference, and corresponding ρ -values can be subtracted, which equates to a geometrical adjustment. This technique of matching bond length leads to an improved comparison of electron densities regarding spatially more expanded regions. Disadvantageously, this procedure obviously will go along with losing the illustration of changes in the bond lengths between different molecules.

Finally, the investigations of the properties of the electron density distribution, based on Baders QTAIM and visualized by the *inter*- $\Delta\rho$ -plot, confirm the assumption of an increased π -character in the ph-py bond due to complexation as already suggested by changes in the geometry and Raman spectra.

4.3.2 The influence of substituents at the 4-phenyl position on the py-ph bond

Apart from complexation, shown to increase the π -character in the py-ph bond in the last section, a frequently used strategy to modify or extend π -systems is introducing substituents in a given structure. With the aim of highly ordered supramolecular assemblies, the ph moiety was substituted in the *para*-position to achieve roughly linear structures. The resulting derivatives were already introduced in table 4.8 of section 4.3.1.

4.3.2.1 Structural Characterization and Electron Density

According to the preceding section, the π -character of the py-ph bond was quantified by calculating the ellipticity ε within the py-ph BCP according QTAIM. Variations of ε should be accompanied with changes in the py-ph bond distance $r(\text{py-ph})$ and the dihedral angle between py and ph $\alpha(\text{py-ph})$ which have been obtained from DFT-geometry-optimizations. The theoretically derived py-ph-characteristics are verified by experimental Raman spectra.

The subsequent introduction of further aromatic rings and lateral substituents (i.e. solubilizing alkoxy side chains) into the terpyridine-ligands results in a disproportional rise in computational effort. Consequently, the analysis of the electron density according to QTAIM has not been performed for the complexes containing ligands **L5-L9**. Additionally, a vibrational spectroscopic analysis becomes increasingly complex, as the nuclear motions of the additional but structurally related groups are expected to mix with vibrational modes of the basic py-ph structure being the objects of investigation. Therefore, the investigations and discussions are focussed on the Zn(II) complexes with smaller ligands (**L1-L4**).

The highest value for $\varepsilon(\text{py-ph-BCP})$ and also the highest value for $\rho(\text{py-ph-BCP})$ within the series features $[\text{Zn}(\mathbf{L3})_2]^{2+}$, followed by $[\text{Zn}(\mathbf{L4})_2]^{2+}$, $[\text{Zn}(\mathbf{L2})_2]^{2+}$, $[\text{Zn}(\mathbf{L1})_2]^{2+}$ (table 4.10), whereas the differences in $\rho(\text{py-ph-BCP})$ are small. However, the introduction of unsaturated substituents in the *para*-position of the phenyl moiety leads to a significant increase of the π -character of the py-ph bond, while the effect of vinyl slightly exceeds the one of ethynyl. This order is mirrored by the py-ph bond length $r(\text{py-ph})$ and the dihedral angle $\alpha(\text{py-ph})$ between pyridine and phenyl, both decreasing with higher $\varepsilon(\text{py-ph-BCP})$, as shown in table 4.10 and figure 4.22. Remarkably, the differences in $r(\text{py-ph})$ and $\alpha(\text{py-ph})$, only arising from variation of the lateral substituents, are approximately one order of magnitude lower compared to the corresponding geometrical parameters previously obtained for **L4** and $[\text{Zn}(\mathbf{L4})_2]^{2+}$. This indicates a minor change in π -character of the py-ph bond due to the nature of the lateral substituent compared to the change induced upon complexation of the free ligand.

Table 4.10: Selected parameters indicating variations in the π -electron delocalization due to complexation

Comp.	α^{oa}	r^b	$\tilde{\nu}^c$	Raman intensity ratio ^d		BCP(py-ph) ^e	
	[°]	[Å]	[cm ⁻¹]	$\frac{\nu(\text{ph-py}(\text{trig}))}{\delta(\text{tpy}(\text{trig}))}$	$\frac{\nu(\text{ph-py}(\text{W8a}))}{\delta(\text{tpy}(\text{trig}))}$	ρ [e/Å ³]	ε
Zn(L1) ₂ ²⁺	31.5	1.472	1367	1.138	0.647	0.253	0.073
Zn(L2) ₂ ²⁺	30.9	1.469	1368	1.418	0.477	0.254	0.078
Zn(L3) ₂ ²⁺	28.7	1.466	1368	1.160	0.672	0.256	0.083
Zn(L4) ₂ ²⁺	29.6	1.468	1369	1.371	0.585	0.255	0.080

^{a,b} DFT-calculated dihedral angle and bond length between the central pyridine ring and the phenyl substituent (py-ph). ^c experimentally determined wavenumber value of $\nu(\text{ph-py}(\text{trig}))$ (see text). ^d experimentally determined. ^e based on DFT calculations.

The bonding situation in the phenyl-pyridine bond has been visualized by the recently introduced electron-density-difference ($\Delta\rho$) plots (figure 4.22).²²¹ For this purpose, complex $[\text{Zn}(\mathbf{L1})_2]^{2+}$ has been chosen as a reference system and $\rho(\mathbf{r})$ in the plane of the central pyridine of the complexes $[\text{Zn}(\mathbf{L2})_2]^{2+}$, $[\text{Zn}(\mathbf{L3})_2]^{2+}$ and $[\text{Zn}(\mathbf{L4})_2]^{2+}$ has been subtracted from the one corresponding to $[\text{Zn}(\mathbf{L1})_2]^{2+}$, respectively. In general, the calculated changes between the different Zn(II) complexes with ligands **L1**, **L2**, **L3** and **L4**, illustrated by the valleys in the middle of the graphs in figure 4.22, are small compared to the changes induced by complexation (valley-depth roughly one magnitude deeper) presented in section 4.3.1. Figure 4.22 illustrates that any *para*-substituent on the phenyl moiety (Br, vinyl, ethynyl) affects a higher π -electron density in the phenyl-pyridine bond compared to $[\text{Zn}(\mathbf{L1})_2]^{2+}$. The highest electron density is observed for $[\text{Zn}(\mathbf{L3})_2]^{2+}$ (figure 4.22, middle) as visualized by the magnitude of negative electron densities in the region of the phenyl-pyridine bond.

As described in section 4.3.1,²²¹ the properties of the py-ph bond are inter alia reflected by a particular normal mode involving a strong py-ph bond stretching vibration due to trigonal ring breathing vibrations on the tpy and lower on ph, denominated $\nu(\text{ph-py}(\text{trig}))$. This normal mode is well suited to compare the changes in py-ph by forming a homoleptic complex, since the normal modes differ marginally between complex and free ligand. Following this approach one has to stress that comparing $\nu(\text{ph-py}(\text{trig}))$ of differently substituted complexes is significantly more challenging than comparing the Raman spectra of **L4** and the corresponding complex $[\text{Zn}(\mathbf{L4})_2](\text{PF}_6)_2$. This additional complication arises from slight in-plane vibrations of ph, which contribute to $\nu(\text{ph-py}(\text{trig}))$ and are influenced somehow differently by different substituents. The well separated band at about 1368 cm⁻¹, in the Raman spectra of $[\text{Zn}(\mathbf{L1})_2](\text{PF}_6)_2$ to $[\text{Zn}(\mathbf{L4})_2](\text{PF}_6)_2$, as depicted in figure 4.23, is assigned to $\nu(\text{ph-py}(\text{trig}))$. The increase of $\varepsilon(\text{py-ph-BCP})$ goes along with

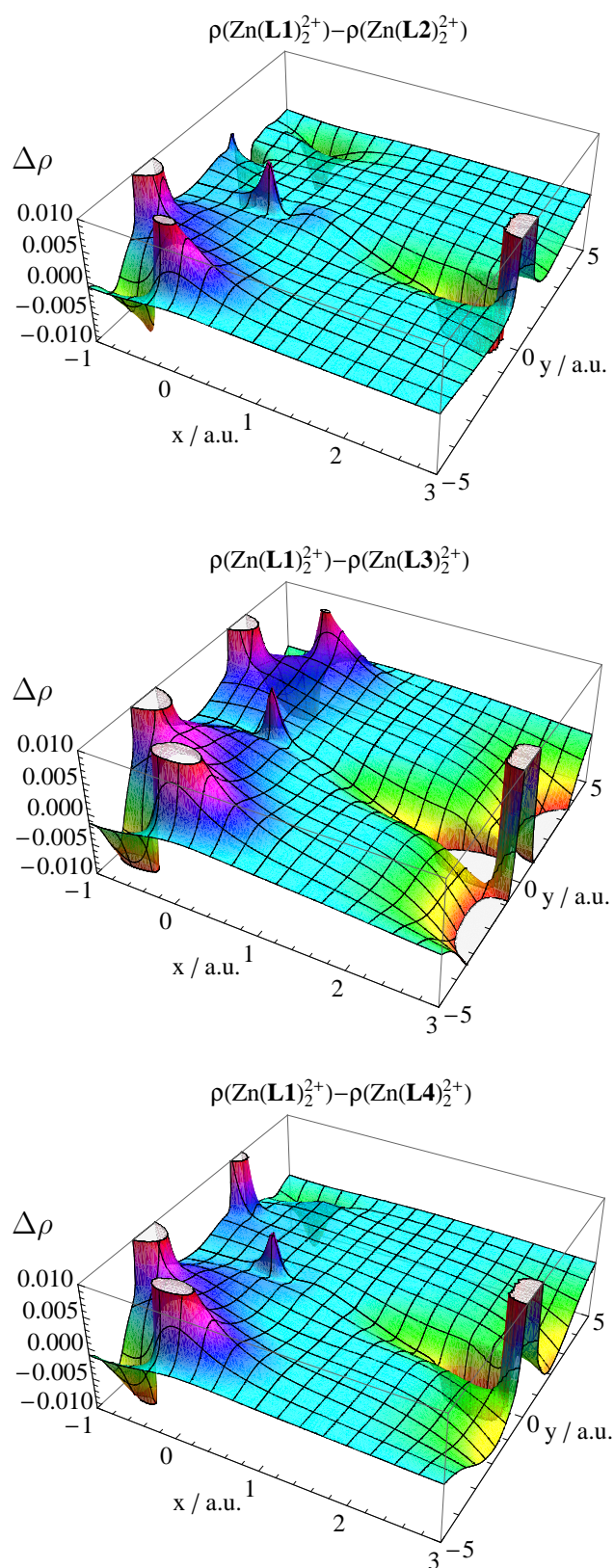


Figure 4.22: *Inter- $\Delta\rho$* -plots of $[\text{Zn}(\mathbf{L2})_2]^{2+}$, $[\text{Zn}(\mathbf{L3})_2]^{2+}$, $[\text{Zn}(\mathbf{L4})_2]^{2+}$ referring to $[\text{Zn}(\mathbf{L1})_2]^{2+}$. Each plot visualizes the change in $\rho(\mathbf{r})$ in the py-ph bond (within the py-plane) which is located in the middle of each graph parallel to the x -axis (C(py): $x=0$ a.u., $y=0$ a.u.; C(ph): $x\approx 3$ a.u., $y=0$ a.u.).

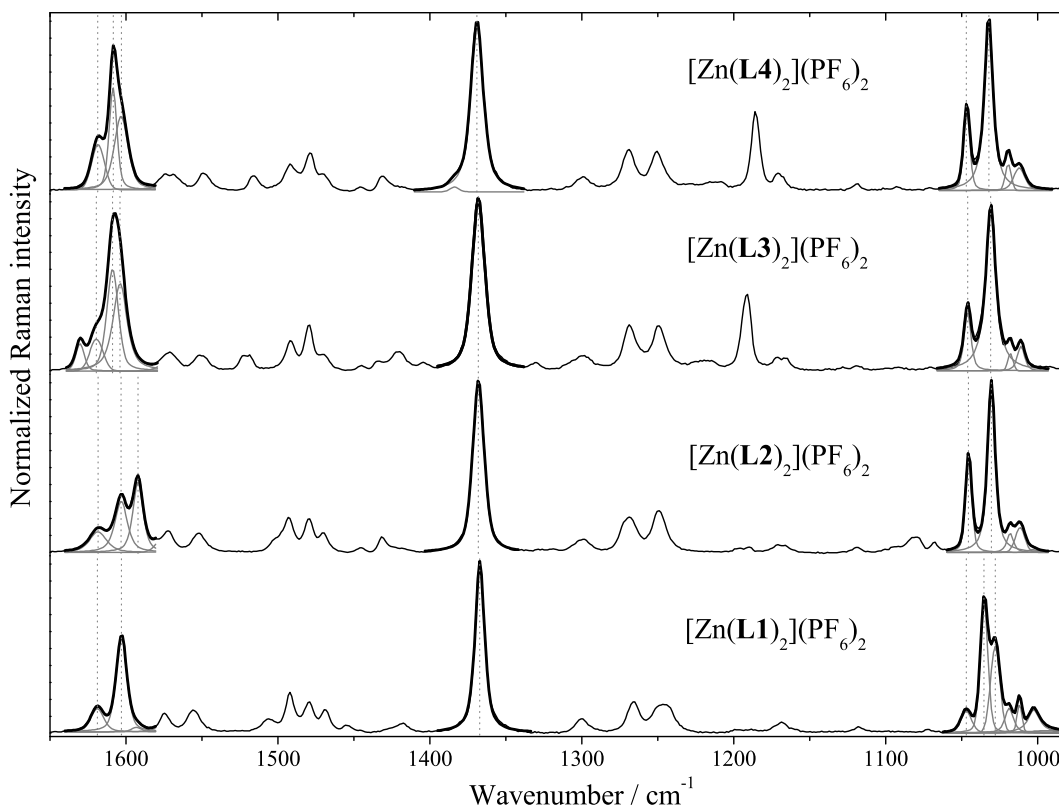


Figure 4.23: Experimental Raman spectra of $\text{Zn}(\mathbf{L1})_2^{2+}$ - $\text{Zn}(\mathbf{L4})_2^{2+}$.

a stronger py-ph bond, what is assumed to affect the tentative trend to higher wavenumber values of $\nu(\text{ph-py}(\text{trig}))$ with increasing $\varepsilon(\text{py-ph-BCP})$ (figure 4.24). However, the observed wavenumber shifts are very small and are close to the error margins, even if the Raman spectra are corrected relatively to the Raman spectrum of TiO_2 , used as a standard. Nevertheless, the experimentally determined wavenumbers of $\nu(\text{ph-py}(\text{trig}))$ corroborate the theoretically derived result of highest π -character of the py-ph bond in $[\text{Zn}(\mathbf{L3})_2](\text{PF}_6)_2$ and $[\text{Zn}(\mathbf{L4})_2](\text{PF}_6)_2$.

Apart from wavenumber shifts the Raman intensity of $\nu(\text{ph-py}(\text{trig}))$ was shown to be a valuable quantity to conclude on changes in the electron density distribution (see section 4.3.1). However, as discussed above, $\nu(\text{ph-py}(\text{trig}))$ involves slight in-plane phenyl vibrations. Since even aromatic in-plane vibrations contribute significantly to the Raman intensity of $\nu(\text{ph-py}(\text{trig}))$, the latter is notably sensitive to a variation of *para*-phenyl substituents. Therefore, all modes involving significant py-ph-stretching fractions, thus leading to ph-vibrations, inherently differ somehow by varying the substituents on phenyl. Hence, in the various complexes $[\text{Zn}(\mathbf{L})_2](\text{PF}_6)_2$ the Raman intensities are also dependent

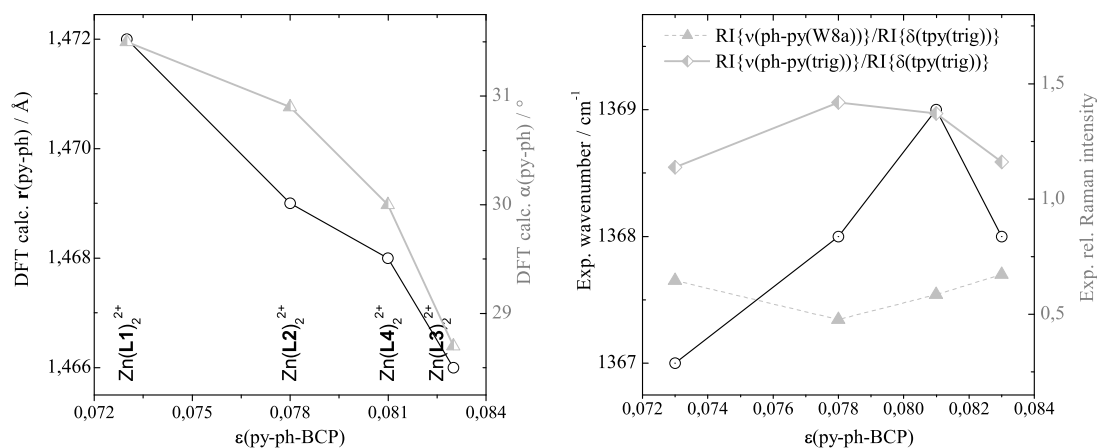


Figure 4.24: Correlation between $\varepsilon(\text{ph-py})$, geometrical and Raman characteristics.

on the π -delocalization of the ph-R moiety and are not necessarily correlated with $\varepsilon(\text{py-ph-BCP})$. For example, both $\nu(\text{ph-py}(\text{trig}))$ (1370 cm^{-1}) and a mode assigned to Wilson No. 8a (on ph and py, $\nu(\text{py-ph}(\text{W8a}))$, 1603 cm^{-1}),²³⁵ involve strong py-ph-stretchings and their Raman intensities show opposite correlations with $\varepsilon(\text{py-ph-BCP})$ (see figures 4.23 and 4.24).

The vibrational assignments are performed in accordance to the one for $\text{Zn}(\text{L4})_2^{2+}$ presented in section 4.3.1.²²¹ The Raman intensities shown in figure 4.24 have been determined via pseudo-Voigt fits and the Raman intensities of $\nu(\text{ph-py}(\text{trig}))$ as well as $\nu(\text{py-ph}(\text{W8a}))$ have been normalized to the Raman band at about 1030 cm^{-1} . The latter is assigned to a trigonal ring-breathing vibration of the pyridine rings $\delta(\text{tpy}(\text{trig}))$ and was suggested as an appropriate reference mode in cause of negligibly involving the substituted phenyl ring and which is hence less dependent on the lateral substituent compared to $\nu(\text{ph-py}(\text{trig}))$ and $\nu(\text{py-ph}(\text{W8a}))$.²²¹ This band cannot be clearly assigned in the RS of $[\text{Zn}(\text{L1})_2](\text{PF}_6)_2$ and therefore, the data points associated to $[\text{Zn}(\text{L1})_2](\text{PF}_6)_2$ in figure 4.24 do not correspond to the trend of the points related to $[\text{Zn}(\text{L2})_2](\text{PF}_6)_2$ until $[\text{Zn}(\text{L4})_2](\text{PF}_6)_2$. However, the Raman bands between 1590 and 1640 cm^{-1} , assigned to in-plane vibrations involving phenyl, are most pronounced in $[\text{Zn}(\text{L3})_2](\text{PF}_6)_2$ and $[\text{Zn}(\text{L4})_2](\text{PF}_6)_2$, what is predominately a consequence of the π -conjugation between the phenyl moiety and the unsaturated substituents. Therefore, this finding does not allow for conclusions on the π -conjugation between pyridine and phenyl. Further extension of the π -system by additional phenyl-based substituents on the vinyl- or the ethynyl-group (complexes $[\text{Zn}(\text{L5})_2](\text{PF}_6)_2$ - $[\text{Zn}(\text{L9})_2](\text{PF}_6)_2$) leads to an increase of the Raman intensity of the bands between 1590 and 1640 cm^{-1} in comparison to $\delta(\text{tpy}(\text{trig}))$ (at

1030 cm^{-1}) as shown in figure 4.25. In contrast, the ratios between the Raman intensities of $\nu(\text{ph-py}(\text{trig}))$ (1370 cm^{-1}) and $\delta(\text{tpy}(\text{trig}))$ are comparable for $[\text{Zn}(\mathbf{L4})_2](\text{PF}_6)_2$, $[\text{Zn}(\mathbf{L6})_2](\text{PF}_6)_2$ and $[\text{Zn}(\mathbf{L9})_2](\text{PF}_6)_2$ (figure 4.25) as well as between $[\text{Zn}(\mathbf{L3})_2](\text{PF}_6)_2$, $[\text{Zn}(\mathbf{L5})_2](\text{PF}_6)_2$ and $[\text{Zn}(\mathbf{L7})_2](\text{PF}_6)_2$ (figure 4.25, top). Therefore, one might conclude that the terminal phenyl-substituents do not influence the tpy-ph bond significantly. However, the different substitution patterns on the terminal phenyl moiety influence the normal modes differently, further complicating a comparison of single Raman bands. Hence, without a reliable normal coordinate analysis it appears not to be suggestive to conclude from the Raman spectra in figure 4.25 on $\varepsilon(\text{py-ph-BCP})$ of such complex systems based on ligands $\mathbf{L5}$ - $\mathbf{L9}$. Nevertheless, the *para*-ph substituents were found to influence the π -conjugation between the tpy- and the ph-moiety, whereas the vinyl-substituted derivatives offer the highest degree of tpy-ph π -conjugation according to our DFT-, AIM- and Raman-investigations. It is assumed, that the additional phenyl-substituents are less affecting the π -character of the py-ph bond, but nevertheless they significantly contribute to the electrochemical and photophysical properties of the respective zinc complexes.

The latter were determined by Winter and coworkers and are summed up in the following section.⁵³ The focus of the discussion is to figure out if the relations of π -conjugations between tpy- and ph-moieties in $[\text{Zn}(\mathbf{L})_2](\text{PF}_6)_2$ with $\mathbf{L}=\mathbf{L1}, \mathbf{L2}, \mathbf{L3}, \mathbf{L4}$, determined by theoretical calculations and Raman spectra, can be verified by the results of the electrochemical and photophysical studies.

4.3.2.2 Electrochemical and photophysical properties

To investigate electrochemical properties Winter and coworkers applied cyclic voltammetry.⁵³ In doing so, the $E_{1/2}^{\text{red}}$ values in the range between -1.13 V and -1.22 V are assigned to the reduction of the tpy moiety. Applying Ferrocen as reference the LUMO energies were calculated and are summarized in table 4.11. To unravel at which molecular structures HOMO and LUMO orbitals are predominantly located, these orbitals are plotted exemplarily for $\text{Zn}(\mathbf{L3})_2^{2+}$ in figure 4.26^j. As can be seen, the HOMO is predominantly located on the ph-vinyl moiety while the LUMO is located at tpy. Even if the py-ph bond is influenced by the different ph-substituents (see section 4.3.1), the tpy-moiety and with it E_{LUMO} is almost unaffected, hence leading to comparable E_{LUMO} values. Oxidation processes were not observed for anodic scans up to 1.75 V and E_{HOMO} values were not determined.

The absorption spectra of $[\text{Zn}(\mathbf{L1})_2](\text{PF}_6)_2$ to $[\text{Zn}(\mathbf{L4})_2](\text{PF}_6)_2$ determined by Winter and coworkers are characterized by a strong absorption band at 280 nm. The respective electronic transition is assigned to a $\pi^* \leftarrow \pi$ transition located at tpy which is roughly

^jHOMO/LUMO-graphs are generated using the program gOpenMol and the results of the DFT calculations. Contours are plotted at values of ± 0.04 .

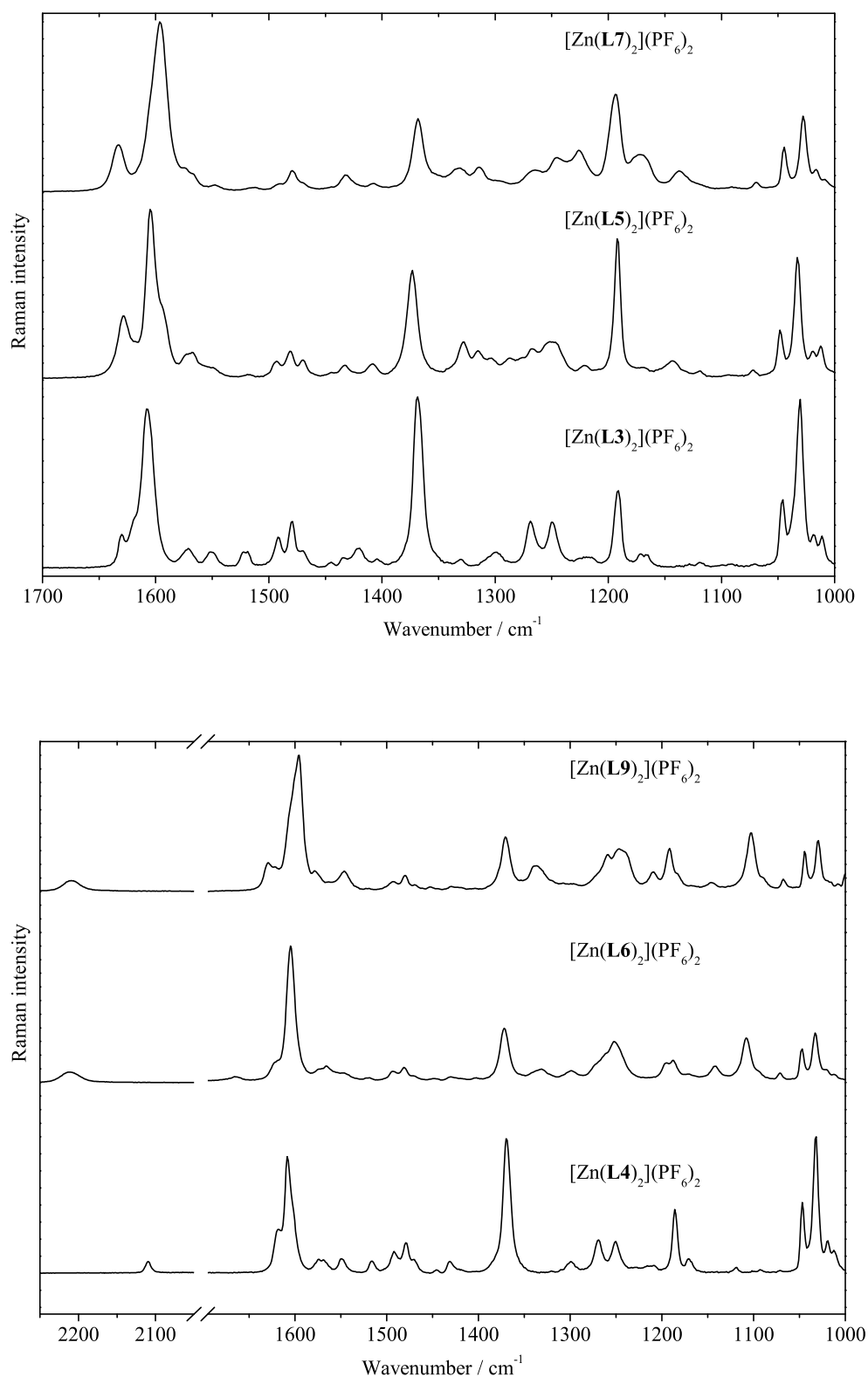


Figure 4.25: Raman spectra of $[\text{Zn}(\text{L})_2](\text{PF}_6)_2$ containing vinyl (top: $\text{L} = \text{L3}, \text{L5}, \text{L7}$) or ethynyl (bottom: $\text{L} = \text{L4}, \text{L6}, \text{L9}$) groups in the *para*-ph position.

Table 4.11: LUMO energy (derived from electrochemical investigations) and photochemical properties:⁵³ absorption and luminescence maxima λ_{abs} , λ_{PL} , energy gaps E_{gap}^{opt} (estimated from absorption spectra), Stokes shifts Δ_S and photo luminescence quantum yields Φ_{PL} .

Substance	E_{LUMO} [eV]	λ_{abs} [nm]	E_{gap}^{opt} [eV]	λ_{PL} [nm]	Δ_S [cm ⁻¹]	Φ_{PL}
[Zn(tpy) ₂](PF ₆) ₂	-3.22	232, 281, 320, 333	3.63	425	6.5	0.35
[Zn(L1) ₂](PF ₆) ₂	-3.23	252, 282, 323	3.59	425	11.93	0.37
[Zn(L2) ₂](PF ₆) ₂	-3.28	252, 276	3.57	427	12.81	0.14
[Zn(L3) ₂](PF ₆) ₂	-3.27	230, 285	3.54	438	12.26	0.59
[Zn(L4) ₂](PF ₆) ₂	-3.26	230, 284	3.58	427	11.79	0.34
[Zn(L5) ₂](PF ₆) ₂	-3.25	254, 282, 326	3.44	454	8.65	0.06
[Zn(L6) ₂](PF ₆) ₂	-3.28	233, 281, 326, 384	2.90	449	3.77	0.20
[Zn(L7) ₂](PF ₆) ₂	-3.23	234, 285, 323, 392	2.69	487	4.98	0.35
[Zn(L8) ₂](PF ₆) ₂	-3.25	234, 285, 323	3.27	447	8.59	0.64
[Zn(L9) ₂](PF ₆) ₂	-3.26	233, 286, 326, 398	2.70	477	4.16	0.53

independent from complexation^k even if the latter affects an increase in the π -character of the py-ph bond.⁵³

For complexes with ligands **L5-L9** absorption bands at 325 and 400 nm which are also assigned to $\pi^* \leftarrow \pi$ transitions become more pronounced. Since they are supposed to be related to the π -system involving ph, these transitions are expected to be more affected by complexation than the tpy located transitions, what is confirmed by significant bathochrome shifts of the low-energetic absorption bands. In particular, for ligands **L7** (red shift ≈ 3260 cm⁻¹) and **L9** (red shift ≈ 1190 cm⁻¹) the strong red shift due to complexation can be explained by ILCT processes.

Since the study of the π -character of the py-ph bond reveals a maximum for [Zn(**L3**)₂](PF₆)₂ in the series of complexes with ligands **L1-L4**, the lowest HOMO-LUMO energy gap is expected for [Zn(**L3**)₂](PF₆)₂ which is in accordance to the estimations made from the absorption spectra^l. The respective E_{gap}^{opt} -values are listed in table 4.11. In agreement to the low E_{gap}^{opt} -value, [Zn(**L3**)₂](PF₆)₂ also shows a significant red shifted maximum of the luminescence spectrum, compared to [Zn(**L**)₂](PF₆)₂ with **L=L1, L2, L4** (see table 4.11). Furthermore, the photo luminescence quantum yield Φ_{PL} of [Zn(**L3**)₂](PF₆)₂ is roughly twice the one of [Zn(**L4**)₂](PF₆)₂.

^k λ_{abs} of ligand and respective Zn(II) complex are almost identical for **L1-L4**.

^lEnergy at 10% of the intensity of the bathochrome absorption edge

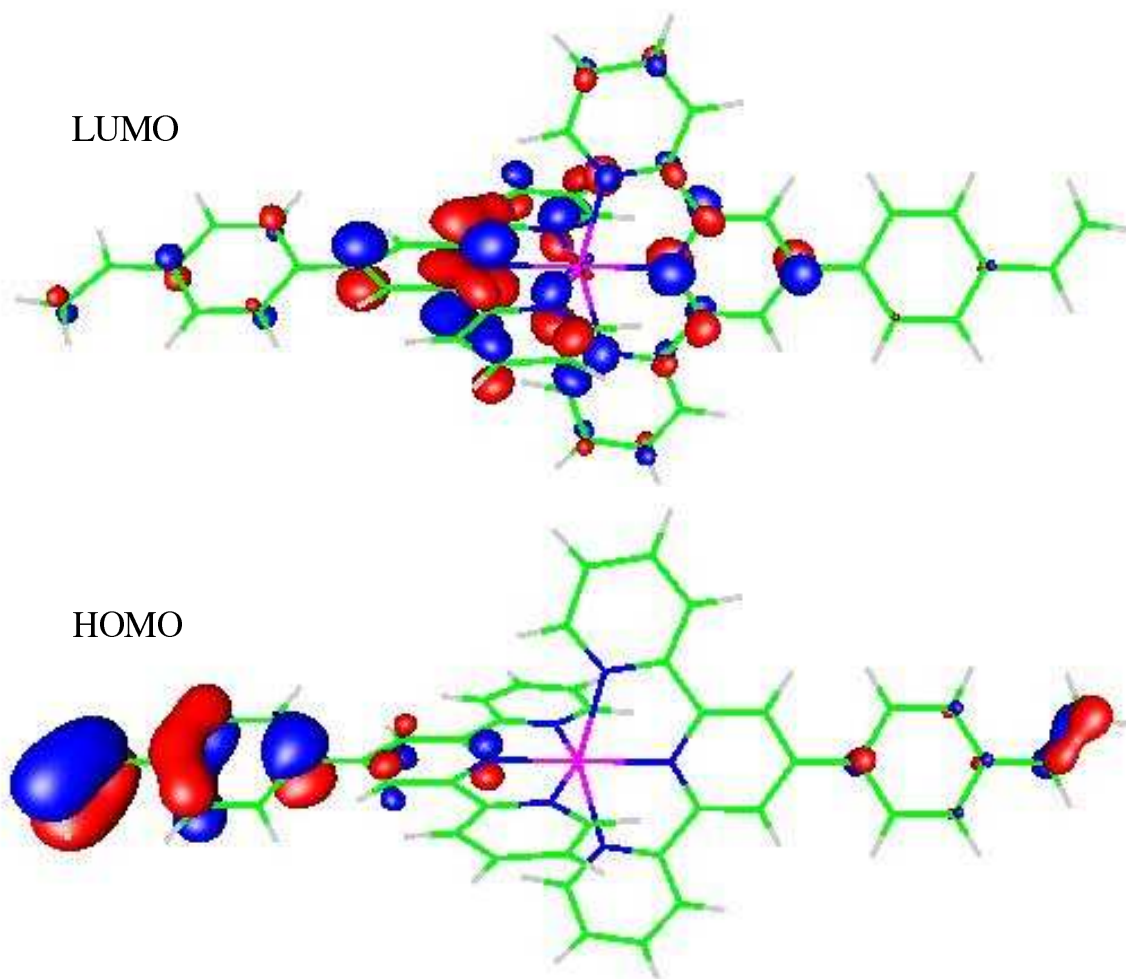


Figure 4.26: HOMO (bottom) and LUMO (top) of $\text{Zn}(\mathbf{L3})_2^{2+}$.

4.3.2.3 Conclusion

The tuning of the opto-electronic properties has been realized by a subsequent extension of the π -conjugated system on the coordinated terpyridine ligand. The investigations of the ground state properties have been supported by Raman spectroscopy, DFT-calculations and analysis of the electron densities according to QTAIM. As visualized by ρ -difference plots, the presence of a vinyl group generally leads to a much higher degree of π -conjugation compared to an ethynyl moiety. Therefore, the tuning of the emission properties is enabled. Intense violet emission is observed for the smaller complexes and the photoluminescence maximum is strongly shifted resulting in bright cyan photoluminescence for the complexes based on terpyridines **L7** and **L9** with the highest degree of π -conjugation. Along with this, also the HOMO energy level is significantly influenced, whereas the energy of the LUMO appears independent from the electronic nature of the terpyridine ligand.

In continuation of the study the materials have been incorporated into PMMA^m matrices resulting in homogeneous thin solid films. The bright emission also in the solid state indicates that the herein described Zn(II) bis-terpyridine complexes are highly promising candidates with respect to potential LED applications.

4.3.3 Comparison of Zn²⁺ and Ru²⁺ complexes and derivation of new molecular structure with improved properties

In analogy to the preceding sections the common structure of all investigated substances is 4'-phenyl-2,2':6',2''-terpyridine which is substituted in the *para*-ph-position (tpy-ph-R) and coordinated with different transition metals to vary the ellipticities within the BCPs of the py-ph bonds ($\varepsilon(\text{py-ph-BCPs})$). In contrast to section 4.3.2, the substituents were chosen to affect the py-ph bond over a wide range. According to the results presented in section 4.2, tpy-ph-R derivatives with R=H, Br, CN, NH₂, NO₂, vinyl, ethynyl are studied. A significant increase in $\varepsilon(\text{py-ph-BCP})$ is expected by introducing a NH₂-group, whereas the NO₂-group is expected to decrease $\varepsilon(\text{py-ph-BCP})$.²¹⁰ An $\varepsilon(\text{py-ph-BCP})$ -increasing effect was also reported for coordinating the tpy-moiety to Zn(II) ions.²²¹ However, previously it was not investigated if coordination with transition metals generally increases $\varepsilon(\text{py-ph-BCP})$ or if this effect is typically only for Zn(II) and related metal ions. To evaluate the influences of transition metal ions which induce totally different photophysical properties, Ru(II) was used to coordinate on tpy-ph-R and was compared to related Zn(II) complexes. In particular, due to different electron configurations of the metal ions Ru(II) complexes show MLCT transitions which are not observed for related Zn(II) complexes. The Ru(II) complexes were synthesized in the group of Prof. Rau with the aim to be used in light driven catalytic systems. The Ru(II) complexes are heterolepticⁿ (see figure 4.27), whereas the Zn(II) complexes are homoleptic since they were designed as model compounds for polymers to be applied in OLEDs or other photoelectric devices.

The $\varepsilon(\text{py-ph-BCP})$ -values of the free ligands and the respective metal complexes are presented in the upper part of table 4.12 in the order of increasing $\varepsilon(\text{py-ph-BCP})$ -values. The influence of complexation on each ligand is quantified via respective $\Delta\varepsilon(\text{M-L})$ -values while $\Delta\varepsilon(\text{M-L}^{R=H})$ -values refer to the unsubstituted tpy-ph-H ligand. The data in table 4.12 reveal, that $\varepsilon(\text{py-ph-BCP})$ is strongly affected due to ph-R substituents as well as due to coordination of the tpy moiety. The NO₂-substituted derivatives possess the lowest $\varepsilon(\text{py-ph-BCP})$ -values while NH₂-substituted derivatives exhibit the highest $\varepsilon(\text{py-ph-BCP})$ -values, which is consistent with electron density studies of benzene derivatives (see section 4.2).²¹⁰ However, $\varepsilon(\text{py-ph-BCP})$ is less influenced by the particular nature

^mPoly(methyl methacrylate)

ⁿsecond ligand is tbut-tpy

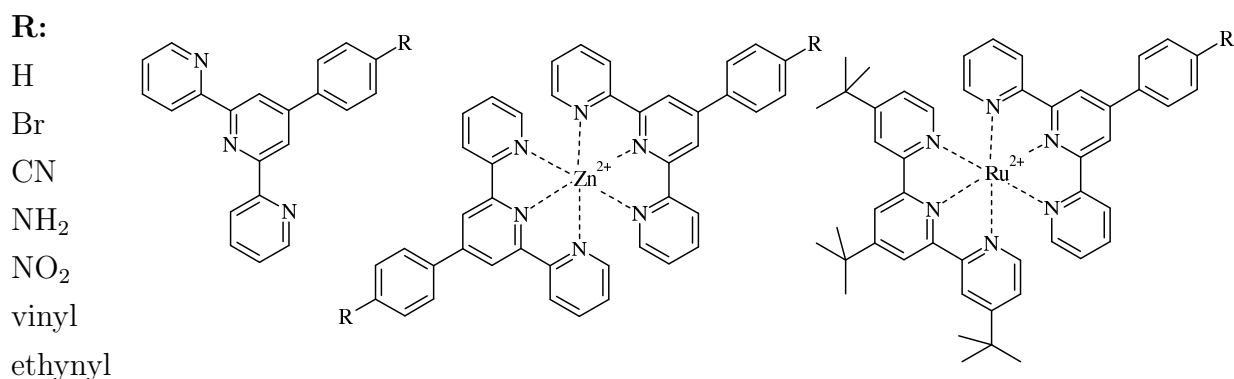


Figure 4.27: Valence formula of tpy-ph, the homoleptic Zn(II) complexes, the heteroleptic Ru(II) as well as the various substituents in the 4-ph-position

of the transition metal ion, since the $\varepsilon(\text{py-ph-BCP})$ -values between Ru(II) and Zn(II) complexes are comparable. The fact that $\varepsilon(\text{py-ph-BCP})$ is increased differently upon complexation ($\Delta\varepsilon(\text{M-L})$ -values) for various *para*-ph substituents is remarkably. In case of NO₂- and NH₂-substituted ligands, which exhibit minimal and maximal $\varepsilon(\text{py-ph-BCP})$ values, complexation with Zn(II) induces minimal (NO₂: $\Delta\varepsilon(\text{M-L})=0.010$) and maximal (NH₂: $\Delta\varepsilon(\text{M-L})=0.034$) increase in $\varepsilon(\text{py-ph-BCP})$. Hence, the higher $\varepsilon(\text{py-ph-BCP})$ in the free ligand, the higher is the increase in $\varepsilon(\text{py-ph-BCP})$ due to complexation (see table 4.12).

Therefore, starting from a given free tpy-ph-H ligand a slight decrease in the π -character of the bond connecting the tpy and the ph moieties can be induced by introducing a NO₂-group in the *para*-position of the ph-moiety ($\Delta\varepsilon(\text{py-ph-BCP})=-0.003$). In contrast, substitution with NH₂ increases the π -character of the py-ph bond ($\Delta\varepsilon(\text{py-ph-BCP})=0.015$) and can further be raised by coordinating the tpy-moiety to either Zn(II) or Ru(II) ($\Delta\varepsilon(\text{py-ph-BCP})=0.034$). This approach yields a total increase of $\Delta\varepsilon(\text{M}^{R=\text{NH}_2}\text{-L}^{R=\text{H}})=0.049$ compared to tpy-ph-H. Roughly 60% of the $\varepsilon(\text{py-ph-BCP})$ -increase are caused by the coordination to a transition metal ion, whereas the different coordination properties of Ru(II) and Zn(II) apparently don't affect $\Delta\varepsilon$. Since ε is zero for perfect σ -bonds and ≈ 0.16 in ph-CC-BCPs of tpy-ph-H, the increased ε in the py-ph bond in $[\text{Zn}(\text{tpy-ph-NH}_2)_2]^{2+}$ (≈ 0.11) indicates the formation of considerable π -conjugation between the tpy and the ph moiety. Hence, due to substitution and complexation (irrespective of using Ru(II) or Zn(II)) the π -character of the py-ph bond could be roughly doubled.

4.3.3.1 Steric effects and correlation between key geometrical structures and $\varepsilon(\text{py-ph-BCP})$

The sterical repulsion between adjacent hydrogen atoms at py and ph causes a significant torsion between py and ph of about 20°-35°. Since an increased torsion lowers the overlap of p-orbitals in the py-ph bond, the π -conjugation between py and ph and consequently

Table 4.12: ε (py-ph-BCP)-values of free all-*trans*-tpy-ph-R ligands (L), $[\text{Zn}(\text{tpy-ph-R})_2]^{2+}$ (Zn) and $[(\text{tbut-tpy})\text{Ru}(\text{tpy-ph-R})]^{2+}$ (Ru) complexes and $\Delta\varepsilon$ -values between complexes and ligands. In the lower part ε (vinyl-ph-BCP)-values are presented.

R	ε (py-ph-BCP)			$\Delta\varepsilon$ (py-ph-BCP)			
	L	Zn	Ru	Zn-L	Ru-L	Zn-L ^{R=H}	Ru-L ^{R=H}
NO ₂	0.055	0.065	0.068	0.010	0.013	0.007	0.010
CN	0.057	0.070	0.071	0.013	0.014	0.012	0.013
H	0.058	0.072	0.074	0.014	0.016	0.015	0.016
Br	0.060	0.079	0.079	0.019	0.019	0.021	0.021
ethynyl	0.060	0.080	0.080	0.020	0.020	0.022	0.022
vinyl	0.061	0.083	0.083	0.022	0.022	0.026	0.026
NH ₂	0.073	0.107	0.107	0.034	0.034	0.049	0.049
Pattern A ^a	0.068	0.111	0.103	0.043	0.035	0.053	0.045
Pattern B ^a	0.082	0.121	0.118	0.039	0.036	0.063	0.060
	ε (vinyl-ph-BCP)			$\Delta\varepsilon$ (vinyl-ph-BCP)			
vinyl	0.072	0.073	0.073	0.001	0.001	0.015	0.015
Pattern A ^a	0.068	0.068	0.067	0.000	-0.001	0.010	0.009
Pattern B ^a	0.095	0.083	0.083	-0.012	-0.012	0.026	0.026

^aPattern A, B are referring to more complex substitutions which are discussed in the following sections.

ε (py-ph-BCP) is lowered. Hence, the torsional angle between adjacent aromatic rings α (py-ph) as well as the respective bond length r (py-ph) are considered to be good measures for the degree of π -conjugation between aromatic systems.⁵⁴⁻⁵⁶ If considering the free ligands and the Zn(II) as well as Ru(II) complexes separately, α (py-ph) and r (py-ph) decrease roughly linear with increasing ε (py-ph-BCP), as shown in figure 4.28. The assignment of the data in figure 4.28 is supported by table 4.13, where the ε -, r -, and α -data of all substances are compared and the parameters of the linear fits are listed. In conclusion, within groups of related substances ε (BCP) and hence the π -character of the py-ph bond can be reliably predicted via the respective bond length or the respective dihedral angle. Both quantities can be experimentally determined by means of x-ray diffraction measurements.

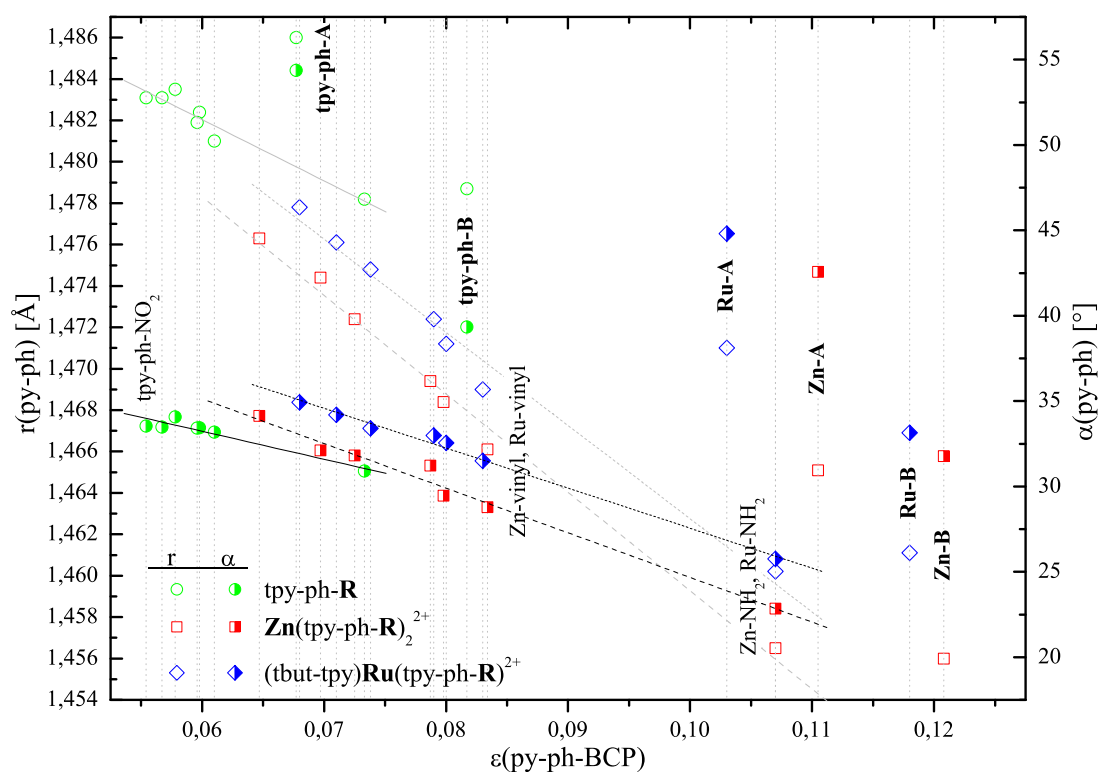


Figure 4.28: Correlations of ε in the BCP of the py-ph bond with the corresponding geometry parameters bond length r (semi-filled symbols) and dihedral angle α (open symbols). The assignment of certain points to the respective structures is facilitated by table 4.13. Bold labeled points are referring to more complex substitution pattern (A, B) which are introduced in the following sections.

4.3.3.2 Influences of coordination and substitution on the tpy-ph π -system

As shown in the preceding sections, the π -character of a bond within a BCP can be described by the ellipticity $\varepsilon(\text{BCP})$. However, the different coordination properties of Zn(II) and Ru(II) are not mirrored in the corresponding $\Delta\varepsilon$ -values. Hence, it is suggestive to extend the analysis of the electron density from a BCP to a plane giving more insights into the nature of the π -systems, as done in sections 4.3.1 and 4.3.2. Such planes can be defined consistently in all investigated substances by choosing one vector being the py-ph bond (C(ph)-C(py), blue in figure 4.29) and the second vector oriented perpendicular to the py-plane (green in figure 4.29) and the origin of both vectors being the common py-carbon atom. The change in $\rho(r)$ in this plane due to coordinating Zn(II) or Ru(II) to the various tpy-ph-R ligands can be studied by subtracting $\rho(r)^{\text{ligand}}$ from $\rho(r)^{\text{complex}}$, thus yielding *inter- $\Delta\rho$* -plots.^{53,221}

Since the dihedral angles between py and ph are differing between the complexes and

Table 4.13: Comparison of py-ph bond lengths (r), dihedral angles between py and ph (α) and ellipticities in the py-ph-BCP (ε) between differently substituted ligands *trans*-tpy-ph-R (L) and related $[\text{Zn}(\text{tpy-ph-R})_2]^{2+}$ (Zn) and $[(\text{tbut-tpy})\text{Ru}(\text{tpy-ph-R})]^{2+}$ (Ru) complexes. The parameters of the linear fits of r and α dependent on ε are also included. These data facilitate the assignment of the points in figure 4.28.

R	L			Zn			Ru		
	r	α	ε	r	α	ε	r	α	ε
NO ₂	1.483	33.5	0.055	1.476	34.1	0.065	1.478	34.9	0.068
CN	1.483	33.5	0.057	1.474	32.1	0.070	1.476	34.2	0.071
H	1.483	34.1	0.058	1.472	31.8	0.072	1.475	33.4	0.074
Br	1.482	33.4	0.060	1.469	31.2	0.079	1.472	33.0	0.079
ethynyl	1.482	33.4	0.060	1.468	29.5	0.080	1.471	32.5	0.080
vinyl	1.481	33.2	0.061	1.466	28.8	0.083	1.469	31.5	0.083
NH ₂	1.478	30.9	0.073	1.456	22.9	0.107	1.460	25.8	0.107
lin. fits:									
slope	-0.30	-164.0		-0.48	-261.3		-0.45	-234.4	
const.	1.500	43.08		1.507	50.81		1.51	51.00	
Pattern A ^a	1.486	54.4	0.068	1.465	42.6	0.111	1.471	44.8	0.103
Pattern B ^a	1.479	39.3	0.082	1.456	31.8	0.121	1.461	33.1	0.118

^aPattern A, B are referring to more complex substitutions which are discussed in the following sections.

also between the free ligands (see table 4.13), the plane perpendicular to py (defined by the green and the blue vector in figure 4.29) cuts ph in different angles with respect to the plane of the ph-R moiety. To minimize $\Delta\rho$ -values arising from geometry differences the *inter*- $\Delta\rho$ -plots are divided in two parts (see figure 4.29): the left part represents the change in electron density at the py-ph bond which is close to py and the right part shows the respective $\Delta\rho$ -values at the ph-side of the py-ph bond. In both parts the plotting planes are perpendicular to the aromatic rings. Hence, in the left part the plane is perpendicular to py and in the right part the plane is perpendicular to ph (plane defined in the same way as the py-plane).

In column "L" of figure 4.30 *inter*- $\Delta\rho$ -plots of the py-ph bond in the free ligands L (tpy-ph-R with R = NO₂, vinyl, NH₂ and a complex substitution pattern "B" introduced in the following sections) relative to the tpy-ph-H ligand are depicted. From these *inter*- $\Delta\rho$ -plots it can be concluded that the NO₂-substituent leads to a decreased $\rho(r)$ at the p-orbitals of C(ph) accompanied with a shift of electron density into the py-ph bond. Also a slight ρ -increase can be found at the π -system of py. According to the QTAIM study,

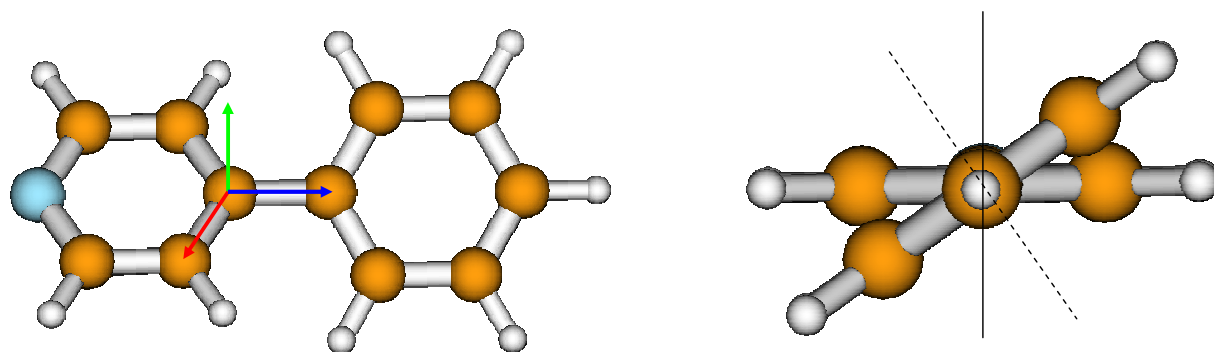


Figure 4.29: Left: vectors defining the plane studied in the *inter*- $\Delta\rho$ -plots: the blue ($\vec{v}_1 = \vec{C}^{ph} - \vec{C}^{py}$) and the green ($\vec{v}_2 = \vec{v}_3 \times \vec{v}_1$ with \vec{v}_3 being the red vector) vectors are defining the plane perpendicular to py. Right: Planes perpendicular to py (solid) and to ph (dashed).

the NH_2 -substituent leads to a considerable increase of $\rho(\mathbf{r})$ at the p-orbitals of C(ph) and therewith to opposite changes in $\rho(\mathbf{r})$ as compared to the NO_2 -group. The vinyl-substituent has nearly no influence on the py-ph bond as shown by the *inter*- $\Delta\rho$ -plot in column "L" of figure 4.30.

Columns "Ru" and "Zn" in figure 4.30 are showing *inter*- $\Delta\rho$ -plots of the py-ph bond in Ru(II) and Zn(II) complexes of tpy-ph-R relative to the free ligands L, to visualize $\rho(\mathbf{r})$ -changes due to complexation. Comparing the plots in column "Ru" reveals that $\rho(\mathbf{r})$ is generally increased in the py-ph bond upon complexation. In accordance to the QTAIM study, $\rho(\mathbf{r})$ in the py-ph bond is increased from the NO_2 - to the NH_2 -derivative, since an increased bond order goes along with a higher electron density within the bond. Adjacent to the region with increased $\rho(\mathbf{r})$ a small region with decreased $\rho(\mathbf{r})$ is visible at the sp^2 -orbital of C(ph) which is getting smaller from NO_2 to NH_2 . Furthermore, complexation leads to a region with increased $\rho(\mathbf{r})$ at a p(C(ph))-orbital which is also getting smaller from NO_2 to NH_2 . That means, that the changes at C(ph) are getting smaller with higher $\rho(\mathbf{r})$ in the py-ph bond. In contrast to the free ligand, where for example the NH_2 -group leads to a $\rho(\mathbf{r})$ -increase predominantly at C(ph), coordination of tpy-ph- NH_2 leads to a $\rho(\mathbf{r})$ -increase in the py-ph bond (row "NH₂" in figure 4.30). Generally, complexation leads to a decreased $\rho(\mathbf{r})$ at the π -systems of py and ph. For the case of the Ru(II) complexes the decrease of $\rho(\mathbf{r})$ at py is almost independent on the *para*-ph-substituent and also the $\rho(\mathbf{r})$ -changes at the π -system of ph induced by complexation are almost identical for R = NO_2 , vinyl and NH_2 .

For the Zn(II) complexes the situation at ph is similar to the one of the Ru(II) complexes. However, the decrease in $\rho(\mathbf{r})$ at py due to complexation gets lower with higher electron density differences in the py-ph bond as shown in column "Zn" of figure 4.30). Consequently, the $\rho(\mathbf{r})$ -decrease at py for the free ligands in the order R= NO_2 , vinyl, NH_2

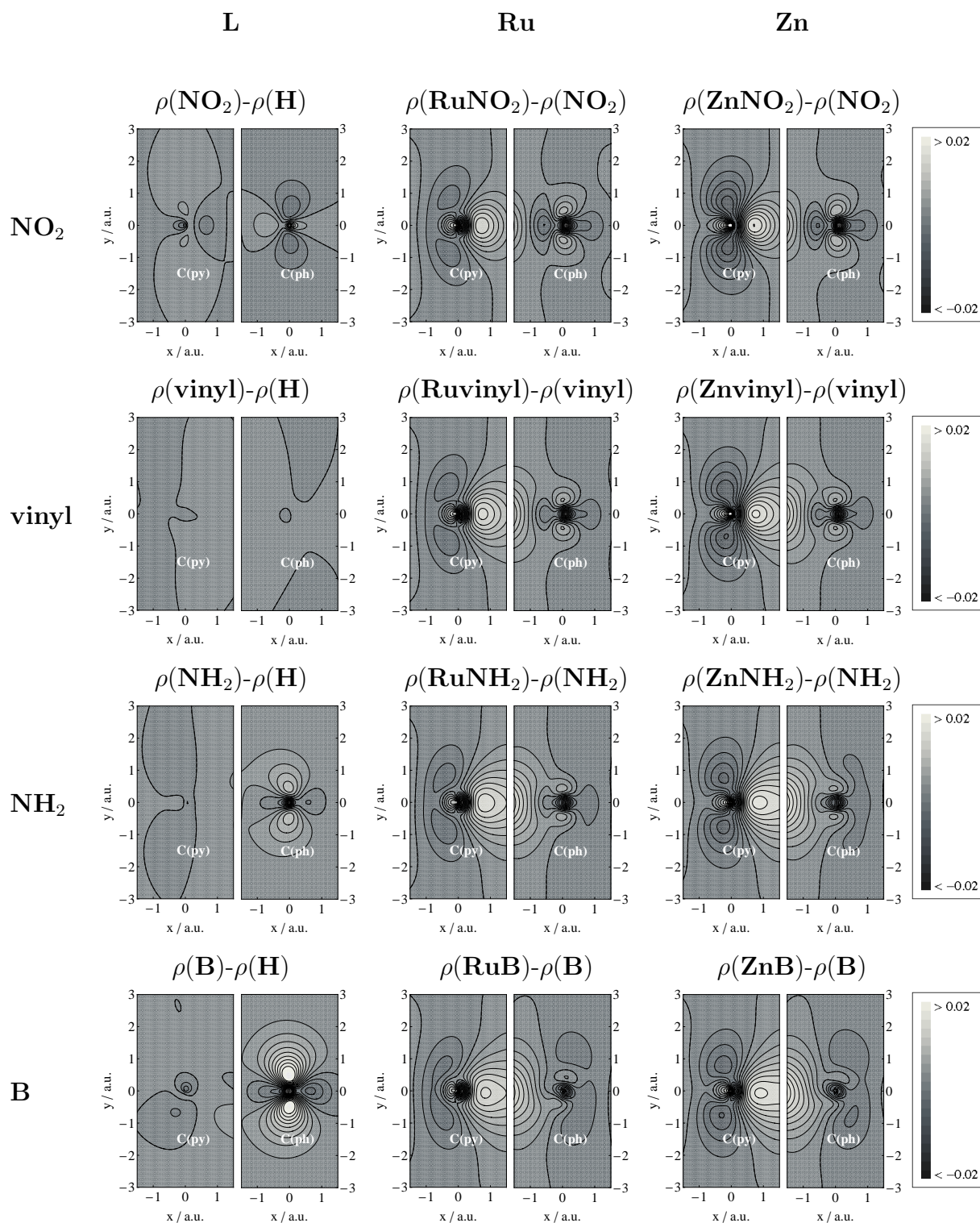


Figure 4.30: *Inter- $\Delta\rho$* -plots to visualize the influences of the cation and substitution on $\rho(r)$ in the ph-py bond: $\rho(\text{tpy-ph-H})$ subtracted from $\rho(\text{tpy-ph-R})$ (column L), $\rho(\text{tpy-ph-R})$ subtracted from $\rho([\text{(tbut-tpy)Ru(tpy-ph-R)}]^{2+})$ (column Ru) and subtracted from $\rho([\text{Zn(tpy-ph-R)}_2]^{2+})$ (column Zn). Top down: NO_2 -, vinyl-, NH_2 -substituted ligands and related complexes and the ones with substitution pattern B (see section 4.3.3.4).

is attenuated due to the coordination with Zn(II). In conclusion, the $\Delta\rho$ -pattern induced by Ru(II) is comparable to the one induced by Zn(II), but Zn(II) leads to a stronger $\rho(r)$ -decrease at py which is more dependent on the *para*-ph substituent than for the case of coordination with Ru(II).

In summary, the increase of $\rho(r)$ in the py-ph bond due to complexation depends on the substituent in the *para*-ph-position. This $\Delta\rho(\text{M-L})$ -increase gets stronger with higher electron density at the p-orbitals of C(ph), e.g. due to the introduction of NH_2 -groups. Furthermore, the *inter*- $\Delta\rho$ -plots reveal differences in the $\Delta\rho(\text{M-L})$ -pattern of related Ru(II) and Zn(II) complexes which are not mirrored in the respective ellipticities of the py-ph-BCP. I.e., in the Ru(II) complexes $\Delta\rho(\text{Ru-L})$ at py is almost independent from R, but $\Delta\rho(\text{Zn-L})$ at py is slightly decreasing with increasing $\Delta\rho$ in the py-ph bond. Furthermore, $\Delta\rho(\text{M-L})$ at py shows considerably lower values for Zn(II) than for Ru(II) complexes. Finally, findings derived from the concise and less complex QTAIM results are confirmed and extended applying *inter*- $\Delta\rho$ -plots, whereas the latter facilitate a comprehensive elucidation of $\rho(r)$ -changes and their origin.

4.3.3.3 Relation between ellipticities and photophysical properties

Since $\varepsilon(\text{py-ph-BCP})$ is related to the π -conjugation between py and ph, variation of $\varepsilon(\text{py-ph-BCP})$ influences photophysical properties. Hence, the impact of $\varepsilon(\text{py-ph-BCP})$ on DFT-calculated HOMO and LUMO energies of the substances introduced in the preceding sections, possessing systematically varied $\varepsilon(\text{py-ph-BCP})$ -values, is studied to search for relations between ground-state- $\rho(r)$ and photochemical properties.

In figure 4.31 the HOMO as well as LUMO energies are plotted against the respective ellipticities (see also table 4.14 for substance assignment). Generally, the HOMO as well as the LUMO energies are increasing with higher $\varepsilon(\text{py-ph-BCP})$ -values, whereas E_{HOMO} increases faster than E_{LUMO} . Hence, the HOMO-LUMO energy gap decreases with increasing $\varepsilon(\text{py-ph-BCP})$ -values, i.e. larger π -systems absorb at lower energies (see figure 4.31). Indeed, the energies of the MOs are significantly decreased due to complexation. Consequently, two groups of HOMO and LUMO energies are present in figure 4.31 which are either referring to the free ligands or the complexes. The devolution of $E_{\text{HOMO,LUMO}}(\varepsilon)$ of the complexes in figure 4.31 is almost uniform for Ru(II) and for Zn(II) complexes, whereas most of the Ru(II) complexes are possessing lower HOMO-energies than the Zn(II) complexes. Only the $\varepsilon(\text{py-ph-BCP})$ -value of the NO_2 -substituted Ru(II) complex rather fits to the E_{HOMO} -devolution of the Zn(II) complexes than to the one of the Ru(II) complexes. One reason for the different HOMO energies of related Zn(II) and Ru(II) complexes is the different localization of the HOMOs in Zn(II) and Ru(II) complexes. As shown in figure 4.26, the HOMO in $[\text{Zn}(\text{tpy-ph-vinyl})_2]^{2+}$ is predominantly located on ph-vinyl without contribution of Zn(II), while the HOMO in the respective

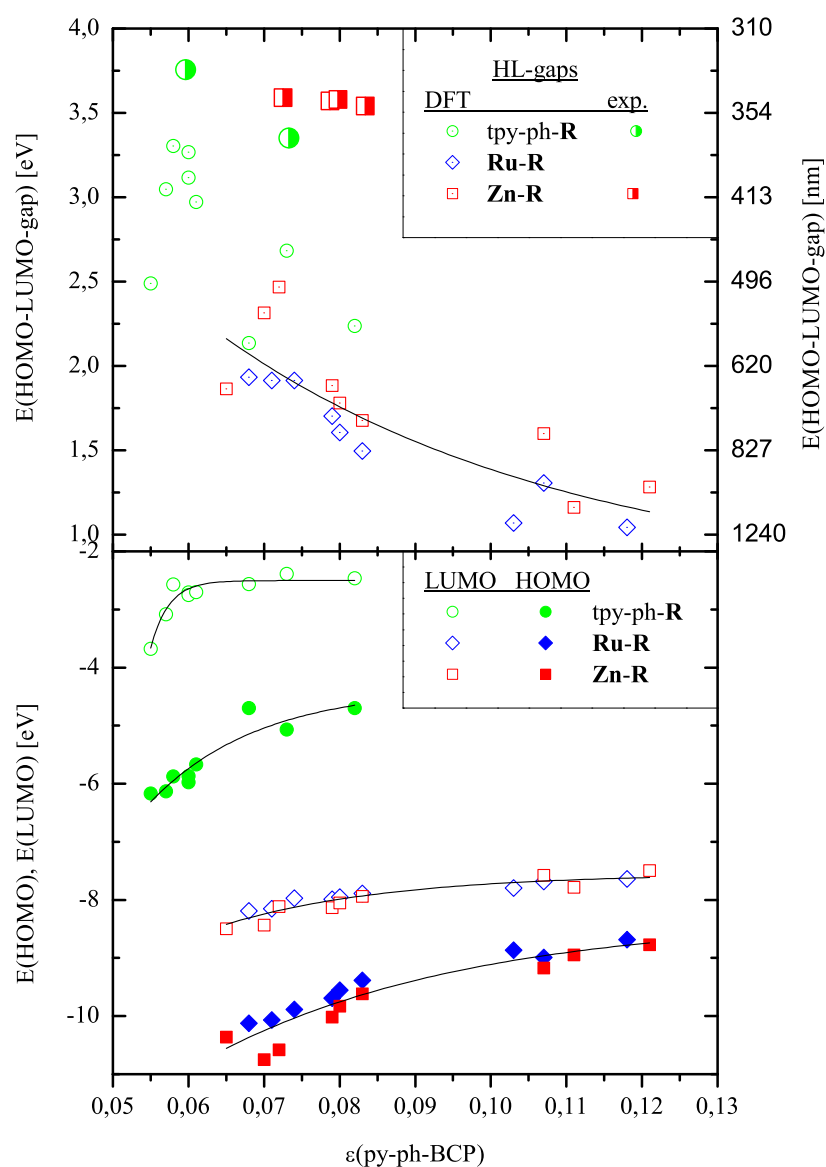


Figure 4.31: DFT-calculated energies of HOMOs, LUMOs (bottom) and the respective gaps (top) of free ligands (circles) and respective Ru(II) and Zn(II) complexes (diamonds, squares). In the upper graph, also energy gaps (semi-filled large symbols) estimated from experimental absorption spectra are included for comparison (see text). For substance assignments see table 4.14. The functions fitting the HOMO and LUMO energies in the lower graph (solid lines) are in accordance to equation 4.8. The corresponding fit-parameters are presented in table 4.15. The function in the upper graph (solid line) corresponds to the energy differences between fitted (according eq. 4.8) HOMO and LUMO energies.

Ru(II) complex ($[(\text{tbut-tpy})\text{Ru}(\text{tpy-ph-vinyl})]^{2+}$) has a significant contribution of Ru(II). However, the substituent dependent HOMO and LUMO energies are clearly related to the ε -values in the BCPs of the py-ph bonds. In case of the free ligands E_{LUMO} is roughly constant for ε -values higher than 0.07, while E_{LUMO} of Zn(II) or Ru(II) complexes changes negligible for ε -values higher than 0.11. In figure 4.31 the separation of the points possessing $\varepsilon(\text{py-ph-BCP}) > 0.1$ is caused by the introduction of NH_2 -groups. However, these points correspond to the devolution of the remaining points as discussed above.

The $E_{HOMO,LUMO}(\varepsilon)$ -values of the free ligands as well as of the complexes were fitted to equation 4.8, whereas a, b, c, d are parameters (see table 4.15) and ε is the variable $\varepsilon(\text{py-ph-BCP})$.

$$E_{HOMO,LUMO}^{fit} = a + be^{-\frac{(\varepsilon-c)}{d}} \quad (4.8)$$

As shown in figure 4.31, the HOMO as well as LUMO energies are fitting well to the graphs determined by equation 4.8. Consequently, the corresponding HOMO-LUMO energy gaps are also correlated to $\varepsilon(\text{py-ph-BCP})$, but the dependency is less clearly pronounced as in the case of the HOMO and LUMO energies. However, the gaps are decreasing for higher $\varepsilon(\text{py-ph-BCP})$ -values (see figure 4.31). Alternatively, the gaps can be calculated via subtracting the fitted HOMO energies from the fitted LUMO energies. The resulting E_{gap}^{fit} -values ($=E_{LUMO}^{fit}-E_{HOMO}^{fit}$) correspond to the function shown in the upper part of figure 4.31. These DFT-calculated energy gaps are assumed to represent trends of electronic absorption energies dependent on the ellipticity, even if these gaps are properties derived from the molecular ground state. To evaluate the proposed dependency of HOMO-LUMO gaps on the ellipticity in the py-ph bond, optical energy gaps derived from experimental absorption spectra are compared to the DFT-calculated HOMO-LUMO gaps in figure 4.31. The optical energy gaps are determined at the wavelength at 10 % of the maximal absorption of the low-energetic absorption edge. In cause of the given simplifications the presented DFT-calculated HOMO-LUMO-gaps are significantly smaller than the estimated experimental optical energy gaps. However, the experimentally derived energy gaps exhibit also a decreasing trend for higher $\varepsilon(\text{py-ph-BCP})$ -values, thus supporting the theoretical results (upper part of figure 4.31, semi-filled symbols).

Finally, one can conclude that the HOMO- and the LUMO-energies of a series of differently substituted tpy-ph-R complexes correlate surprisingly well with the ellipticity in the py-ph bond, even if the substituents are unsaturated and extend the ph- π -system.

4.3.3.4 Suggestion of new structures with tailored π -character of the py-ph bond.

If the basic tpy-ph-R structures presented in the preceding sections should be incorporated in more sophisticated or even macromolecular assemblies the question arises, at which position the tpy-ph-R structure should be extended preferably. Furthermore, applying the

Table 4.14: DFT-calculated HOMO and LUMO energies and the respective energy gap as well as experimentally derived optical energy gaps and experimentally derived energies of bathochrome absorption bands of free ligands and their Ru(II) and Zn(II) complexes.

R:	NO ₂	CN	H	Br	ethynyl	vinyl	NH ₂	A ^a	B ^a	
<i>trans</i> -tpy-ph-R										
ϵ^{DFT}		0.055	0.057	0.058	0.060	0.060	0.061	0.073	0.068	0.082
E_{gap}^{DFT}	[eV]	2.488	3.047	3.303	3.268	3.116	2.971	2.682	2.136	2.236
E_{HOMO}^{DFT}	[eV]	-6.166	-6.130	-5.873	-5.974	-5.869	-5.669	-5.068	-4.700	-4.700
E_{LUMO}^{DFT}	[eV]	-3.678	-3.083	-2.570	-2.706	-2.752	-2.698	-2.386	-2.564	-2.464
E_{gap}^{exp}	[eV]	n.a.	n.a.	n.a.	n.a.	3.757	n.a.	3.351	n.a.	n.a.
λ_{max}^{exp}	[eV]	4.311	4.476	4.460	4.460	4.366	4.335	4.305	n.a.	n.a.
λ_{max}^{exp}	[nm]	283	277	278	278	284	286	288	n.a.	n.a.
[Zn(tpy-ph-R) ₂] ²⁺										
ϵ^{DFT}		0.065	0.070	0.072	0.079	0.080	0.083	0.107	0.111	0.121
E_{gap}^{DFT}	[eV]	1.863	2.315	2.467	1.883	1.780	1.676	1.598	1.161	1.281
E_{HOMO}^{DFT}	[eV]	-10.361	-10.752	-10.582	-10.016	-9.832	-9.617	-9.172	-8.947	-8.774
E_{LUMO}^{DFT}	[eV]	-8.499	-8.436	-8.115	-8.133	-8.053	-7.941	-7.574	-7.786	-7.493
E_{gap}^{exp}	[eV]	n.a.	n.a.	3.590	3.570	3.580	3.540	n.a.	n.a.	n.a.
λ_{max}^{exp}	[eV]	n.a.	n.a.	4.920	4.920	5.391	5.391	5.267	n.a.	n.a.
λ_{max}^{exp}	[nm]	n.a.	n.a.	252	252	230	230	235	n.a.	n.a.
[(tbut-tpy)Ru(tpy-ph-R)] ²⁺										
ϵ^{DFT}		0.068	0.071	0.074	0.079	0.080	0.084	0.107	0.103	0.118
E_{gap}^{DFT}	[eV]	1.932	1.913	1.914	1.702	1.605	1.494	1.306	1.068	1.043
E_{HOMO}^{DFT}	[eV]	-10.122	-10.068	-9.885	-9.694	-9.554	-9.383	-8.988	-8.864	-8.683
E_{LUMO}^{DFT}	[eV]	-8.190	-8.155	-7.971	-7.992	-7.950	-7.889	-7.683	-7.796	-7.641
E_{gap}^{exp}	[eV]	n.a.	n.a.	n.a.	n.a.	n.a.	n.a.	n.a.	n.a.	n.a.
λ_{max}^{exp}	[eV]	2.520	n.a.	n.a.	2.546	n.a.	n.a.	2.515	n.a.	n.a.
λ_{max}^{exp}	[nm]	492	n.a.	n.a.	487	n.a.	n.a.	493	n.a.	n.a.

Data are partially kindly supplied by Dr. Winter and Prof. Rau.

Table 4.15: Parameters of the fits of the data in table 4.14 according equation 4.8.

	a	b	c	d
E_{LUMO}^{ligand}	-2.503	0.04831	-19.466	0.00237
E_{HOMO}^{ligand}	-4.349	0.00521	-62.423	0.01440
$E_{LUMO}^{complex}$	-7.547	-0.02040	-42.627	0.02197
$E_{HOMO}^{complex}$	-8.305	-0.02661	-33.193	0.03405

results discussed above it is demonstrated in the following how to tune the π -character of bottle-neck-bonds for the example of aiming for maximal ε -values. Tpy-ph-R derivatives with large π -systems are under investigation for the usage in electro-optical devices whereas the coordination to Zn(II) is expected to improve self-assembling properties.^{53,221} In this context the adjustment of π -delocalization facilitates the targeted modification of conduction properties. In case of Ru(II) an extension of the ligand structure can be used to tune e.g. absorption and emission properties or to introduce further coordination spheres functioning as a bridge facilitating electron transfer to a reaction center. Furthermore, modified π -delocalizations in ligands with subtle substitution patterns might prolong $^3\text{MLCT}$ lifetimes, which is discussed in the following.

Apart from complexation, the considerations are focussed on the substitution pattern at the aromatic rings adjacent to the py-ph bond. Particularly, the ph-moiety is modified since additional substitutions on the central py-ring are not meaningful because of sterical limitations. As demonstrated in section 4.2 a NH_2 -group should be introduced in the *para*-ph position to maximize $\varepsilon(\text{py-ph-BCP})$. A similar enlargement of $\varepsilon(\text{py-ph-BCP})$ is expected due to introducing NH_2 -groups in *ortho*-position to the py-ph bond as compared to *para*-substitution, while substitution in the *meta*-position has a minor effect (see sec. 4.2).²¹⁰ Consequently, a structure with NH_2 -groups in both *ortho*-positions (substitution pattern R=A) was investigated to achieve even higher $\varepsilon(\text{py-ph-BCP})$ -values as an illustrative example of actuating $\varepsilon(\text{py-ph-BCP})$. Alternatively, a structure with one NH_2 -group in an *ortho*- and one in the *para*-position (substitution pattern R=B) was considered. Furthermore, a structure without *ortho*-substitution, but with one NH_2 -group in the *para*-ph position was investigated (substitution pattern R=C). All three kinds of tpy-ph-R ligands (R=A,B,C) contain a vinyl-group on ph to extend the π -system as shown in figure 4.32. Therefore, aiming for a large π -system the ph-vinyl bond and in particular $\varepsilon(\mathbf{vinyl-ph-BCP})$ is a second key-characteristic besides $\varepsilon(\mathbf{py-ph-BCP})$.

In structure A the vinyl-group was placed in *para*-position to the py-ph bond expected to cause a stronger mutual influence on $\rho(\mathbf{r})$ in the corresponding bonds than substitution in the respective *meta*-position.²¹⁰ Therefore, in structure A the NH_2 -groups are located in *meta*-position with respect to the vinyl-group. Consequently, $\varepsilon(\text{py-ph-BCP})$ is expected to be significantly increased due to the NH_2 -substituents, while $\varepsilon(\text{vinyl-ph-BCP})$ should be influenced negligibly in structure A. In contrast, in structure B py as well as vinyl are located each in *para*- and in *ortho*-position to a NH_2 -group, respectively. Hence, for structure B high $\varepsilon(\text{py-ph-BCP})$ - and high $\varepsilon(\text{vinyl-ph-BCP})$ -values are expected. Since in substance B as well as in substance A two NH_2 -groups are influencing the py-ph bond, but substance A should possess a higher dihedral angle between py and ph, the $\varepsilon(\text{py-ph-BCP})$ -value of structure B is expected to be higher than the one in substance A. To evaluate if the steric effect of substituents in *ortho*-positions exceeds the electronic substituent-effect,

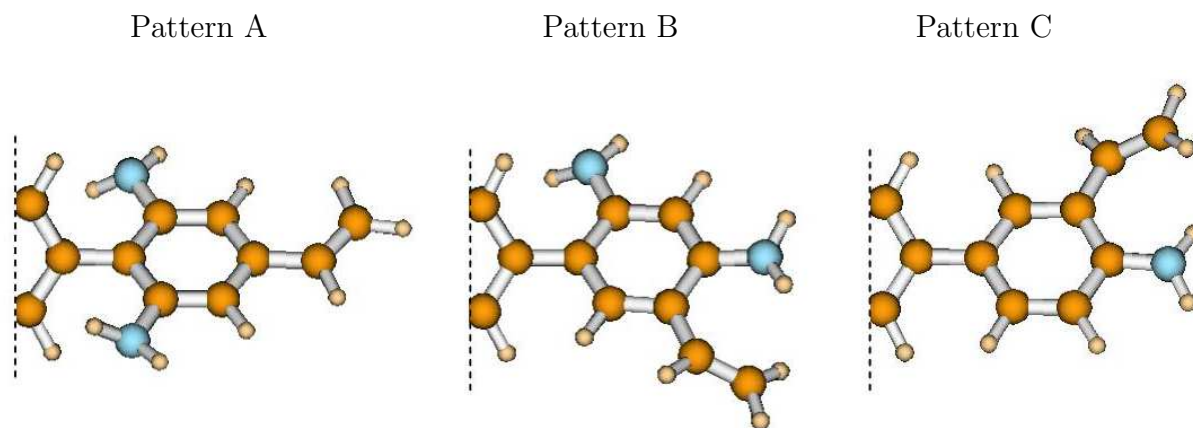


Figure 4.32: Structural representations of complexes $[\text{Zn}(\text{tpy-ph-R})_2]^{2+}$ with the ph moieties substituted with NH_2 - and vinyl-groups.

structure C contains no *ortho*-substituents but a *para*-ph NH_2 -group.

The results of the QTAIM analysis of $\rho(r)$ of structures A and B (ligands and complexes) shown in table 4.12 reveal a further increase in $\varepsilon(\text{py-ph-BCP})$ due to the twofold introduction of NH_2 -groups. However, this trend is not observed for the free ligand with substitution pattern A. In $\text{Zn}(\text{II})$ and $\text{Ru}(\text{II})$ complexes of tpy-ph-A and tpy-ph-B $\varepsilon(\text{py-ph-BCP})$ is further raised to values of 0.111 and 0.121. The highest ε -values are present in molecules possessing substitution pattern B, i.e. $\varepsilon(\mathbf{py-ph-BCP})$: $\varepsilon(\text{L})=0.082$, $\varepsilon(\text{Zn})=0.121$ and also $\varepsilon(\mathbf{vinyl-ph-BCP})$: $\varepsilon(\text{L})=0.095$, $\varepsilon(\text{Zn})=0.083$ (see table 4.12). Indeed, $\varepsilon(\text{vinyl-ph-BCP})$ is either not affected by complexation ($\text{R}=\text{vinyl}$, $\text{R}=\text{A}$) or even reduced ($\text{R}=\text{B}$). Finally, in $[\text{Zn}(\text{tpy-ph-B})_2]^{2+}$ the π -system is further extended and the ε -values of the two bottle-neck bonds py-ph and ph-vinyl are significantly raised (0.121 and 0.083) compared to tpy-ph-vinyl, thus almost reaching values typical for completely delocalized π -systems. For comparison, $\varepsilon(\text{CC}(\text{ph}))$ in tpy-ph-H amounts to 0.15-0.17 and $\varepsilon(\text{CC-single bond})$ in deca-1,3,5,7,9-pentaen amounts to 0.11.^o

The NH_2 -substituents in *ortho*-position to py-ph might also improve material properties, since the *ortho*-substituents lead to a distinctly increased curvature of the rotational potential as the rotational barrier is dramatically increased for coplanar py-ph geometries. Thus, substituents *ortho* to the py-ph bond constrain the torsional degree of freedom and are expected to reduce rotational disorder and to increase supramolecular order.

Since the electronic and the steric effect of the *ortho*- NH_2 -substituents are competing and $\alpha(\text{py-ph})$ in tpy-ph-A (54.4° , see table 4.13) is significantly raised compared to tpy-ph-B ($\alpha=39.3^\circ$)^p, $\varepsilon(\text{py-ph-BCP})$ in tpy-ph-A is lower than in tpy-ph-B. However, the electronic effect of the NH_2 -groups clearly exceeds the competing steric effect for the $\text{Ru}(\text{II})$ and $\text{Zn}(\text{II})$ complexes of tpy-ph-A/B. This finding is proven by the further in-

^ocalculated within the present study for comparison

^pDue to the second NH_2 -group in tpy-ph-A *ortho* to the py-ph bond

creased $\varepsilon(\text{py-ph-BCP})$ -value for the tpy-ph-A/B complexes as compared to the complexes of tpy-ph-NH₂. That the electronic substituent effects are dominating the steric influences is further corroborated by regarding the $\varepsilon(\text{py-ph-BCP})$ -value of structure C (0.106). Consequently, omitting *ortho*-NH₂-groups to lower $\alpha(\text{py-ph})$ does not compensate the missing ε -increasing influence of the omitted substituent.

Since the torsion in structures A and B is raised but $\varepsilon(\text{py-ph-BCP})$ is increased, $\alpha(\text{py-ph})$ is not suited to predict the respective $\varepsilon(\text{py-ph-BCP})$ -values. Therefore, the $\alpha(\text{py-ph})$ -values of *ortho*-substituted tpy-ph derivatives do not fit the linear relations derived for *para*-ph substituted structures (figure 4.28). Consequently, $\varepsilon(\text{py-ph-BCP})$ can not be derived by means of experimentally accessible geometry parameters for such cases and has to be calculated via analyzing theoretically or experimentally determined $\rho(r)$.

The change in $\rho(r)$ due to complexation of the ligand with substitution pattern B is visualized in row "B" of figure 4.30 (columns "Ru" and "Zn"). According to the increasing $\varepsilon(\text{py-ph-BCP})$ -values, the $\Delta\rho$ -pattern of the plots in row "B" fit the trends defined by the plots from row "NO₂" to row "NH₂": the electron density within the py-ph bond is generally further enhanced due to complexation, while the $\rho(r)$ -decrease is lowered at the π -system of py and increased at the π -system of ph if considering complexation via Zn(II). Furthermore, the substitution pattern B leads to significantly increased $\rho(r)$ -values at the p-orbitals of C(ph) with respect to tpy-ph-H (figure 4.30 "L/B").

The increased π -conjugation between py and ph leads to a smaller HOMO-LUMO-gap which fits the relation to $\varepsilon(\text{py-ph-BCP})$ shown in equation 4.8 perfectly. The energy-gap values of Ru(II) and of Zn(II) complexes as well as of the respective free ligands with substitution pattern A and B are included in figure 4.31.

Even if the present study shows that HOMO as well as the LUMO energies are increasing with higher $\varepsilon(\text{py-ph-BCP})$ -values, a higher electron delocalization leads to a stabilized ground state according to Hanan.⁵⁸ Since in Ru(II)-(tpy-ph) complexes without *ortho*-substituents a coplanar structure is present in the excited states, the ³MLCT state is more stabilized than the ground state, thus leading to a lower energy gap and a faster depopulation of the ³MLCT state.⁵⁸ In contrast, the substances suggested in the present work (A, B) are expected to be not planarized in the excited state because of the substituents *ortho* to the py-ph bond. Therefore, the ³MLCT state is not as stabilized as for non-*ortho* substituted structures. Additionally, the electron delocalization in the ground state is increased due to *ortho*-NH₂ groups, thus stabilizing the groundstate. Consequently, the energy gap between the ³MLCT and the ground state is expected to be increased via NH₂-substituents *ortho* to the py-ph bond. Hence, also the ³MLCT lifetime might be increased if other deactivation processes (i.e. via the ³MC state) are not promoted due to *ortho*-substitution. Therefore, *ortho*-substitution, in particular the introduced structures A and B, is a promising approach to improve photophysical properties of tpy-ph

compounds.

4.3.3.5 Conclusion

In summary, the influence of *para*-ph-substituents with electronic properties spanned over a wide range on the π -delocalization between pyridine and phenylene in 4'-(phenyl)-2,2':6',2''-terpyridine derivatives was investigated. Furthermore, it was shown that coordination of Ru(II) and Zn(II) to the tpy-moiety significantly enhances the π -delocalization. The degree of the ε -increase in the py-ph bond due to complexation depends on the ph-substituents. This dependency is more pronounced for complexation via Zn(II) than via Ru(II) as revealed by the *inter*- $\Delta\rho$ -plots.

The influences of coordination and substitution on the π -character of the py-ph bond can be concisely specified by the respective ellipticity values $\varepsilon(\text{py-ph-BCP})$. Therefore, the investigation of the dependency of defined photochemical quantities on $\varepsilon(\text{py-ph-BCP})$ is enabled. Exemplarily, the relation between HOMO and LUMO energies and $\varepsilon(\text{py-ph-BCP})$ was investigated. Despite strongly varying substituents on the ph-moiety, the HOMO and LUMO energies of Ru(II) as well as of Zn(II) complexes are showing a uniform dependency on $\varepsilon(\text{py-ph-BCP})$, respectively. To further corroborate the derived relations between ε -values and photophysical properties, time-dependent DFT calculations are suggested to describe excited states more reliably and further experimental data for comparison are necessary.

Finally, the investigated possibilities to influence ε -values facilitate the targeted design of molecular structures with tailored π -systems. In combination with the results of section 4.2 a kind of modular design system for organic molecules is provided which is supposed to exhibit potential for molecular electronics or photo-electronic issues. In particular, substitutions in *ortho*-position to the py-ph bonds are suggested despite the increased torsion, since for example in the case of NH₂-substituents the electronic influence on the py-ph bond is expected to exceed the steric one.

Furthermore, one might expect prolonged lifetimes of charge separated states in case of the Ru(II) complexes possessing the suggested substitution pattern. Hence, the herein presented study facilitates the design of new complexes with improved abilities in photocatalysis.

5 Characterizing the initial step of photoexcitation

5.1 Assignment of ligand-substructures in

$[(\text{tbut-tpy})\text{Ru}(\text{tpy-ph-R})]^{2+}$ involved in the $^1\text{MLCT}$ at the Franck-Condon-point.

As discussed in chapter 1, Ru(II) terpyridine compounds are under investigation concerning their ability for photocatalysis. In this context, long-lived excited states with spatially distant charge separations are aspired. In particular, the question arises to which extent the ph-moiety is involved in the MLCT of $[(\text{tbut-tpy})\text{Ru}(\text{tpy-ph-R})]^{2+}$ introduced in section 4.3.3. This problem is of importance, since the phenylene moiety can serve as a bridge to further coordination spheres in oligonuclear complexes. A direct excitation of the ph-moiety via a $\text{tpy-ph} \leftarrow \text{Ru}^{2+}$ transition would support the ability of such ligands to serve as bridging ligands despite the torsion between the aromatic rings of phenylene and the adjacent pyridine, which lowers the π -conjugation between tpy and ph.

To study if the $\text{tpy-ph} \leftarrow \text{Ru}^{2+}$ transition involves the phenylene moiety, resonance Raman spectra (RRS) of the homoleptic complex $[\text{Ru}(\text{tbut-tpy})_2]^{2+}$ and of a series of differently substituted heteroleptic complexes $[(\text{tbut-tpy})\text{Ru}(\text{tpy-ph-R})]^{2+}$ were compared. As excitation wavelength the 514 nm output of an argon-ion laser was used. This wavelength is located in the red edge of the MLCT absorption band (see figure 5.1), where the transition to the tpy-ph-R ligand is expected to be dominant, as compared to the transition to the tbut-tpy ligand. The assumption that the $\text{tbut-tpy} \leftarrow \text{Ru}^{2+}$ transition is of a higher energy than the $\text{tpy-ph} \leftarrow \text{Ru}^{2+}$ transition is founded on the extended π -system of tpy-ph-R ligand compared to tbut-tpy (see previous sections). Generally, the MLCT absorption bands of the $[(\text{tbut-tpy})\text{Ru}(\text{tpy-ph-R})]^{2+}$ complexes are located between 425 and 625 nm ($\lambda_{\text{max}}(\text{R}=\text{Br}, \text{NO}_2, \text{NH}_2)=487, 492, 493$ nm), whereas the one of $[\text{Ru}(\text{tbut-tpy})_2]^{2+}$ is located at $\lambda_{\text{max}}=479$ nm.

Since the MLCT transition is assigned to the absorption band with the lowest energy, the MLCT state is expected to involve significant contribution of the LUMO. Following the DFT-calculations, the LUMO is assumed to be predominantly located on the tpy-

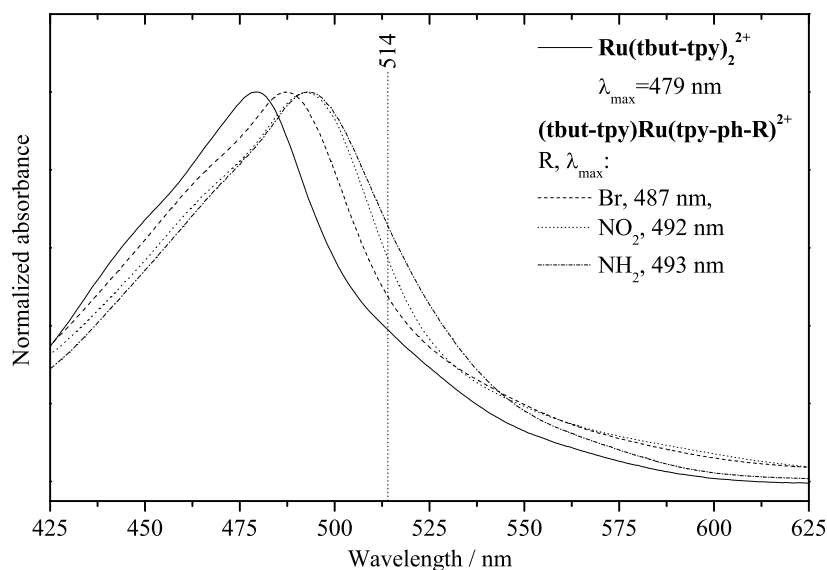


Figure 5.1: Normalized absorption spectra of $[\text{Ru}(\text{tbut-tpy})_2]^{2+}$ and $[(\text{tbut-tpy})\text{Ru}(\text{tpy-ph-R})]^{2+}$ dissolved in CH_3CN . The resonance Raman excitation wavelength is marked by a vertical dotted line at 514 nm.

moiety. Consequently, the largest geometrical changes and therefore strongly resonantly enhanced Raman bands are assumed for tpy if the excitation wavelength is chosen to match the respective MLCT.

Even if a transition to tbut-tpy is slightly hypsochrome to a transition to tpy-ph-R, Raman excitation at 514 nm involves both MLCTs in $[(\text{tbut-tpy})\text{Ru}(\text{tpy-ph-R})]^{2+}$. This is also mirrored by the respective RRS (see figure 5.2) which exhibit bands assigned to the tbut-tpy moiety as well as resonance Raman bands of tpy-ph-R.

In the lowest graph in figure 5.2 the RRS of the homoleptic reference complex $[\text{Ru}(\text{tbut-tpy})_2]^{2+}$ is depicted, which inherently exhibits resonantly enhanced Raman bands of tbut-tpy. The other graphs show RRS of $[(\text{tbut-tpy})\text{Ru}(\text{tpy-ph-R})]^{2+}$ with $\text{R}=\text{Br}, \text{NH}_2, \text{NO}_2$ featuring shifted and additional RR bands. Vibrational modes differing between the RRS of $[\text{Ru}(\text{tbut-tpy})_2]^{2+}$ and $[(\text{tbut-tpy})\text{Ru}(\text{tpy-ph-R})]^{2+}$ are located at the tpy-ph-R moiety. Wavenumber-shifts can be caused by the different substitution pattern between tbut-tpy and tpy-ph-R leading to different reduced masses if motions of the substituted carbons are involved. Furthermore, the altered or missing substituents on tpy in the tpy-ph-R ligand compared to the tbut-tpy ligand are causing an altered electron density distribution of the tpy-moiety and therefore varied force constants and RR-band positions. If the shifted bands are at comparable wavenumber-values for the different $[(\text{tbut-tpy})\text{Ru}(\text{tpy-ph-R})]^{2+}$ complexes, the respective resonantly enhanced modes are predominantly located on tpy,

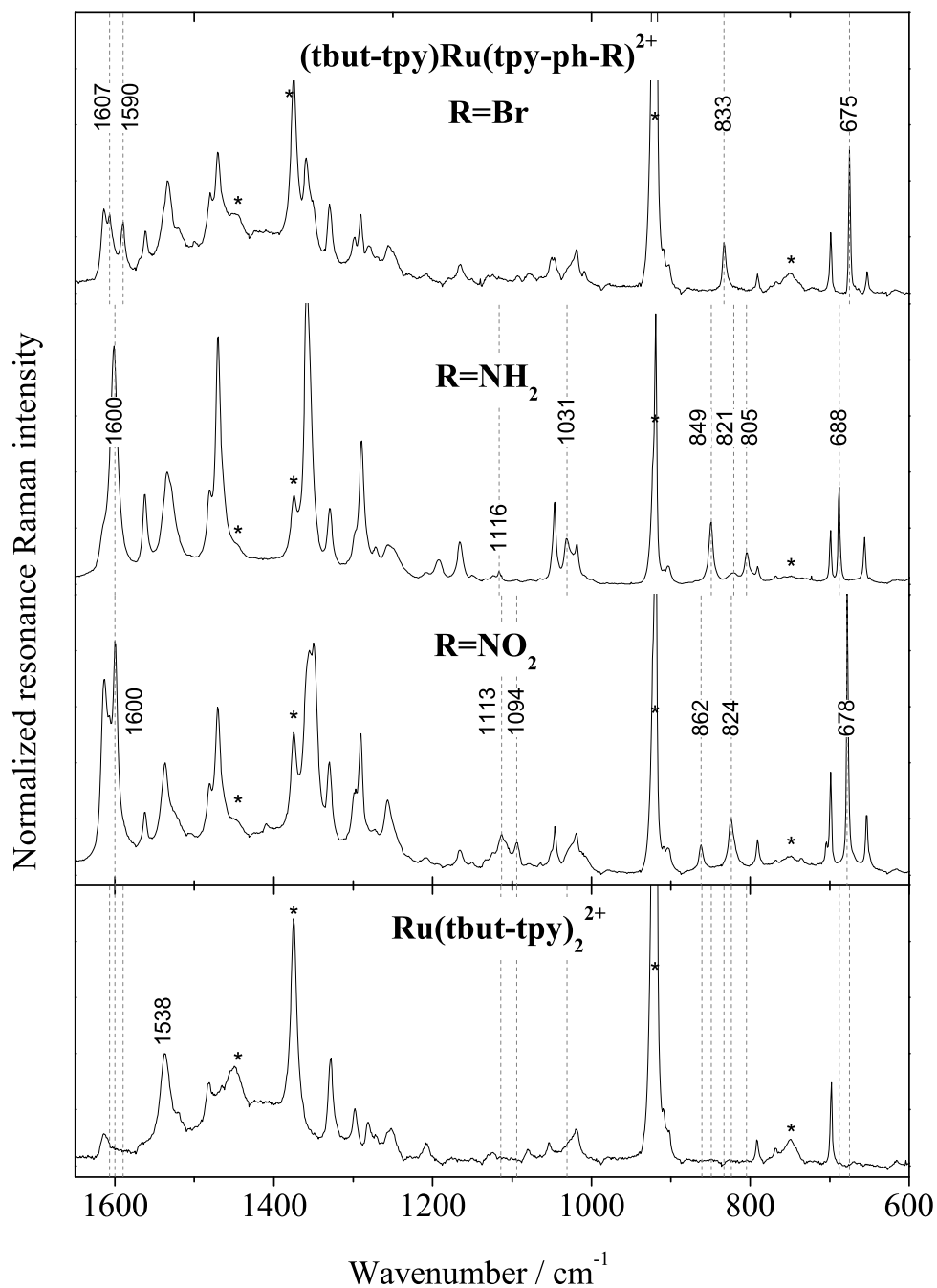


Figure 5.2: RRS of $[(\text{tbut-tpy})\text{Ru}(\text{tpy-ph-R})]^{2+}$ (from top: $\text{R}=\text{Br}$, NH_2 , NO_2) and $[\text{Ru}(\text{tbut-tpy})_2]^{2+}$ (bottom), dissolved in CH_3CN (*). RRS are excited at 514 nm and are normalized to the tbut-tpy-RR band at 1538 cm^{-1} . The dashed lines label RR-bands which are exclusively present in the heteroleptic $[(\text{tbut-tpy})\text{Ru}(\text{tpy-ph-R})]^{2+}$ complexes.

	[(tbut-tpy)Ru(tpy-ph-R)] ²⁺		
	R=Br	R=NH ₂	R=NO ₂
Table 5.1: Wavenumber-positions in cm ⁻¹ of resonantly enhanced modes, which are assigned to involve the ph-R moiety in [(tbut-tpy)Ru(tpy-ph-R)] ²⁺ with R=Br, NH ₂ , NO ₂ .	1607		
	1590	1600	1600
		1116	1113
			1094
		1031	
		849	861
		833	823
		805	
		675	677
		688	

less involving ph-R.

However, in figure 5.2 few RR-bands are present, that are neither present in the RRS of [Ru(tbut-tpy)₂]²⁺ nor are at identical wavenumber-positions in the RRS of the different [(tbut-tpy)Ru(tpy-ph-R)]²⁺ derivatives. These bands are labelled with dashed lines in figure 5.2 and are summarized in table 5.1. The RR-band-shifts between the RRS of [(tbut-tpy)Ru(tpy-ph-R)]²⁺ can only be explained if the corresponding vibrational modes are significantly linked to ph-vibrations, since only ph is considerably affected by the different electronic influences and the different masses of the varied substituents in the *para*-phenylene position. That means, that vibrational coordinates involving phenylene motions are coupled to the electronic transition at the Franck-Condon point. Hence, tpy-ph-R has the potential to serve as appropriate bridging ligand in sophisticated oligonuclear complexes with novel photophysical properties.

To study, if the MLCT is even extended beyond the phenylene ring, i.e. involving unsaturated *para*-ph-substituents, the RRS of [(tbut-tpy)Ru(tpy-ph-CN)]²⁺ was investigated. If the unsaturated CN-group is involved in the MLCT at the Franck-Condon-point, a well separated RR-band in the region between 2000 and 2400 cm⁻¹ is expected. To avoid superpositions with the Raman signal of the CN-stretching mode of the solvent, [(tbut-tpy)Ru(tpy-ph-CN)]²⁺ was dissolved in dichloromethane instead of acetonitrile. However, no RR-band can be detected in the region between 2000 and 2400 cm⁻¹ as shown in figure 5.3. Consequently, the CN-group is not involved in the MLCT transition of (tbut-tpy)Ru(tpy-ph-CN)²⁺ at the Franck-Condon-Point.

In conclusion, it was proven via the differences between the RRS of [(tbut-tpy)Ru(tpy-ph-R)]²⁺ with R=Br, NH₂, NO₂, that the MLCT instantaneously involves the phenylene moiety of the tpy-ph-R ligand, but leaving the substituent R unaffected. Consequently, the design of new aromatic substituents to be introduced in the 4'-position of tpy is of increasing impact for the achievement of improved photophysical properties of related

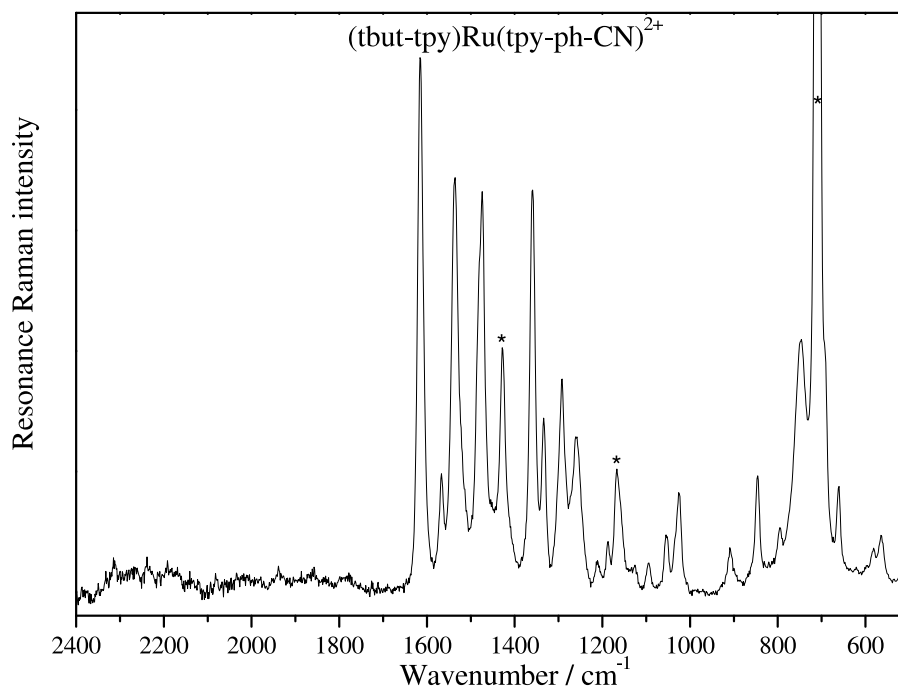
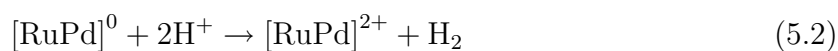
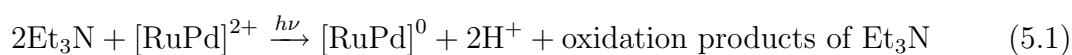


Figure 5.3: Resonance Raman spectrum of [(tbut-tpy)Ru(tpy-ph-CN)]²⁺ dissolved in dichloromethane (RR-bands labelled with asterisks); λ_{ex} =514 nm.

Ru(II) complexes, regardless of a torsion between tpy and the 4'-substituent.

5.2 Initial charge localization in the light driven catalyst [(tbut-bpy)₂Ru(tpphz)PdCl₂]²⁺

As discussed in chapter 1, Ruthenium polypyridine complexes attained a huge interest since they are able to operate as artificial light harvesting antennas.⁶⁵⁻⁶⁷ Particularly, the complex [(tbut-bpy)₂Ru(tpphz)PdCl₂]^{2+a} (see figure 5.4; abbreviated as [RuPd]²⁺) was shown to generate molecular hydrogen upon light irradiation and the presence of triethylamine (TEA; functioning as proton donator and reducing agent) by Rau et al.^{81,243} The supposed reaction pathway starts with a photoinduced electron transfer from ruthenium to phenazine (¹MLCT) yielding a Ru^{III}-phenazine⁽⁻⁾-Pd^{II} moiety. After dissociation of chloride, Pd(II) is assumed to be reduced to Pd(I) via the electron stored at the tpphz moiety. The reduced palladium is expected to be the catalytic active redox-center in the hydrogen generation process, which is summarized in equations 5.1 and 5.2.



^atpphz: Tetrapyrrodo[3,2-a:2,3-c:3,2-h:2,3-j]phenazin

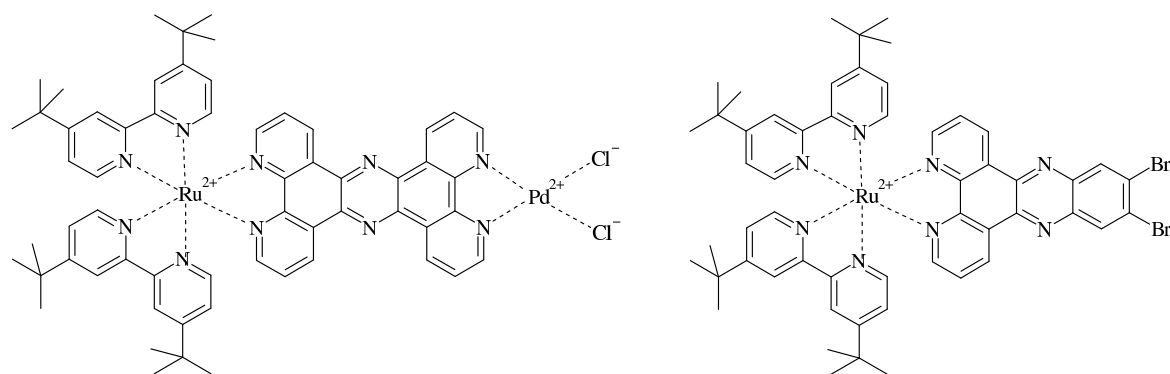


Figure 5.4: Valence structure of $[(\text{tbut-bpy})_2\text{Ru}(\text{tpphz})\text{PdCl}_2]^{2+}$ ($[\text{RuPd}]^{2+}$, left) and $[(\text{tbut-bpy})_2\text{Ru}(\text{dppz})(\text{Br})_2]^{2+}$ (right).

To further improve such catalytic active complexes, a comprehensive understanding of the photophysical processes underlying such reactions is necessary. Since the first step in the outlined photoreactions of $[\text{RuPd}]^{2+}$ is the charge transition from Ru(II) to the tpphz ligand, the nature of this transition determines all following processes. To study the initial steps in such a $^1\text{MLCT}$ transition, resonance Raman spectroscopy (RRS) is the method of choice, because it characterizes the Franck-Condon-Region. The following investigation focusses on the determination of the particular ligand the $^1\text{MLCT}$ ends up, dependent on the incident wavelength. For this aim five different excitation wavelengths were applied.^b

5.2.1 Assignment of Raman and resonance Raman bands to substructures in $[(\text{tbut-bpy})_2\text{Ru}(\text{tpphz})\text{PdCl}_2]^{2+}$

The resonance Raman spectrum (RRS) of $[\text{RuPd}]^{2+}$ is dominated by heavily resonantly enhanced bands in the region of the aromatic in-plane vibrations between 1000 and 1650 cm^{-1} . The respective region is plotted in the upper graph of figure 5.5. To assign the resonantly enhanced Raman bands of $[\text{RuPd}]^{2+}$ to the tbut-bpy or the tpphz ligand, the RRS of $[\text{RuPd}]^{2+}$ is compared to the RRS of $[\text{Ru}(\text{tbut-bpy})_3]^{2+}$ (lower graph in figure 5.5). Since the latter exhibits exclusively RR-bands assigned to tbut-bpy, the corresponding RR-bands at 1617, 1540, 1484, 1321, 1285, 1265 and 1256 cm^{-1} in the

^bResonance Raman spectra were recorded in a 90° scattering geometry utilizing a rotating cell to avoid heating. No changes in the absorption spectra of the complexes could be observed after exposure to the resonant laser light. Excitation lines at 514.5, 488, 476.5 and 458 nm provided by an argon ion laser (Innova300-MotoFreD, Coherent Inc.) and the 413 nm line of a krypton laser (Coherent, Inc.) served for resonant excitation in the range of the $^1\text{MLCT}$ absorption band. The scattered light was analyzed with a Princeton Instruments Acton SpectraPro 2750 spectrograph with a focal length of 750 mm equipped with a 600 lines/mm grating.

RRS of $[\text{RuPd}]^{2+}$ are referring to tbut-bpy modes. Consequently, the intense RR-bands at 1609, 1595, 1582, 1573, 1491, 1460, 1447, 1198 and 1181 cm^{-1} are assigned to the tpphz ligand. The RRS assignment is fully supported by the comparison of non-resonant RS of $[\text{RuPd}]^{2+}$ with the related Ru(II) complexes $[(\text{tbut-bpy})_2\text{Ru}(\text{tpphz})]^{2+}$ and $[(\text{tbut-bpy})_2\text{Ru}(\text{dppz})(\text{Br})_2]^{2+}$ (structure is illustrated in figure 5.4^c) shown in figure A.1 in appendix A.2.

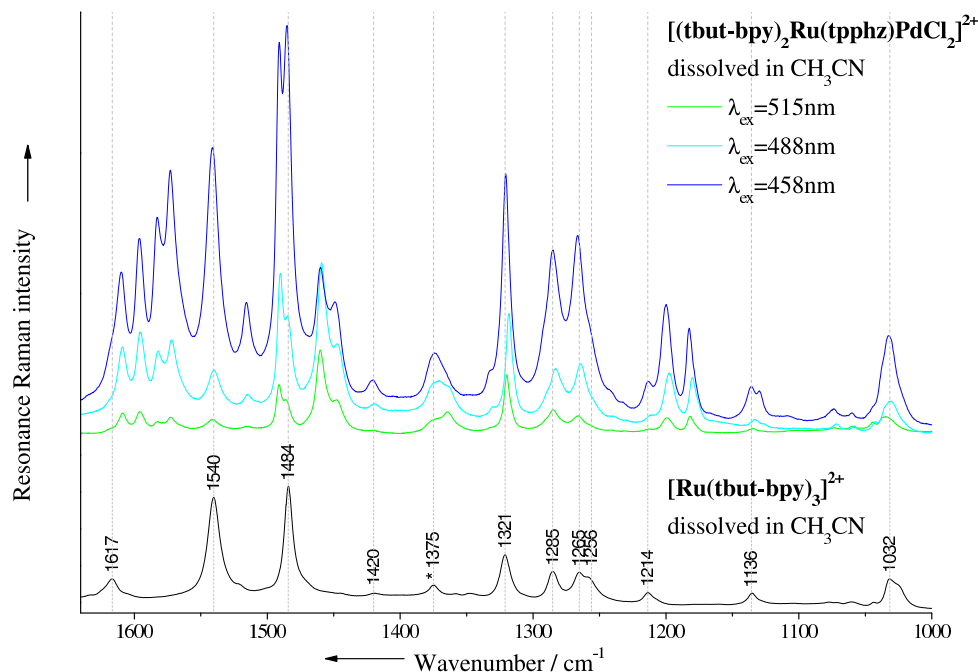


Figure 5.5: Comparison of the resonance Raman spectra of $[\text{RuPd}]^{2+}$ (upper graph, different RRS are corresponding to different excitation wavelength, see legend) and $[\text{Ru}(\text{tbut-bpy})_3]^{2+}$ ($\lambda_{ex}=458$ nm).

5.2.2 Estimation of the $^1\text{MLCT}$ energies of $(\text{tbut-bpy})\leftarrow\text{Ru}^{2+}$ and $(\text{tpphz})\leftarrow\text{Ru}^{2+}$

If the photochemical processes in $[\text{RuPd}]^{2+}$ should be optimized towards an higher efficiency of the charge separating $^1\text{MLCT}$ process, evaluation of the energetic relations between $^1\text{MLCT}$ s ending up at tbut-bpy or tpphz is necessary. The energies of the $(\text{tbut-bpy})\leftarrow\text{Ru}^{2+}$ $^1\text{MLCT}$ and the $(\text{tpphz})\leftarrow\text{Ru}^{2+}$ $^1\text{MLCT}$ can be determined by analyzing the RRS of $[\text{RuPd}]^{2+}$ which are excited at different wavelengths covering the $^1\text{MLCT}$ absorption band. If the ν^4 dependency of the RR-intensities is taken into account the maximal enhancement of a RR-band corresponds to the absorption maximum of the corresponding

^cdppz: Dipyrido[3,2-a:2,3-c]-phenazin

electronic transition. Consequently, the $^1\text{MLCT}$ absorption band can be deconvoluted into the $(\text{tbut-bpy})\leftarrow\text{Ru}^{2+}$ $^1\text{MLCT}$ and the $(\text{tpphz})\leftarrow\text{Ru}^{2+}$ $^1\text{MLCT}$.

Since the most intense resonance Raman bands of $[\text{RuPd}]^{2+}$ are assigned to the tbut-bpy or the tpphz ligand, the corresponding intensities at the excitation wavelength 515, 488, 477, 458, 413 nm were determined by fitting the bands in the region 1150 - 1350 cm^{-1} and 1400 - 1650 cm^{-1} with pseudo-Voigt profiles. Prior to the fitting, the fluorescence background was thoroughly subtracted via either pseudo-Voigt-profiles or inverse polynoma (see section 3.4).^d The intensities of the RR-bands were normalized to a solvent band and the normalized RR-intensities of the tpphz and tbut-bpy assigned bands were summed up, respectively. The summation compensates possible errors evolving from background corrections. The fitted RRS of $[\text{RuPd}]^{2+}$, dissolved in acetonitrile, are shown in figure 5.6. Regarding the RR-enhancement of the tbut-bpy (cyan colored) and tpphz (green colored) assigned RR-bands for increasing excitation energies in figure 5.6, a stronger amplification is present for the tbut-bpy assigned RR-bands as compared to the tpphz-assigned RR-bands.

The summed RR-intensities dependent on the excitation energies are shown in figure 5.7. The star-shaped dots are referring to summed RR-intensities of all green labelled tpphz located RR-bands in figure 5.6. The semi-filled dots are illustrating the RR-intensities of the cyan labelled tbut-bpy assigned RR-bands in figure 5.6. To highlight the shift between the devolutions of the tpphz and tbut-bpy assigned dots, the points were fitted by means of Gauss-profiles (compare section 3.4). Subsequently, the Gauss-profiles were normalized, since the number of RR-bands underlying the summation is different. The shift of the Gauss-profiles corresponds to the energetic difference between the $(\text{tpphz})\leftarrow\text{Ru}^{2+}$ $^1\text{MLCT}$ and the $(\text{tbut-bpy})\leftarrow\text{Ru}^{2+}$ $^1\text{MLCT}$.

Because the solvent significantly influences the hydrogen generation, the RRS of $[\text{RuPd}]^{2+}$ dissolved in CH_3CN is compared to the corresponding CH_2Cl_2 solution. When using CH_3CN as solvent a turn-over-number of 56 was published (generation of 56 H_2 molecules by one $[\text{RuPd}]^{2+}$ molecule), while for the respective CH_2Cl_2 solution no hydrogen generation was observed.^{81,243}

The data corresponding to $[\text{RuPd}]^{2+}$ dissolved in acetonitrile are shown in the upper graph of figure 5.7. In the lower graph the data referring to the respective dichloromethane solution are presented. The maxima in the wavelength dependent development of $\sum I_{RR}(\text{tpphz})$ and $\sum I_{RR}(\text{tbut-bpy})$ (estimated via the Gaussian profiles) differ about 9 nm. For both

^dProgram used for deconvolution: Origin7G. Fluorescence background simulation and subtraction: points of the spectra lying on the baseline were chosen and fitted with pseudo-Voigt profiles or inverse polynoma. RRS-deconvolution via pseudo-Voigt profiles: subsequent fitting of RRS-sections containing about 10 bands, followed by reassembling and global fitting. Minimal χ^2 -values were determined using Levenberg-Marquardt and simplex-iterations.

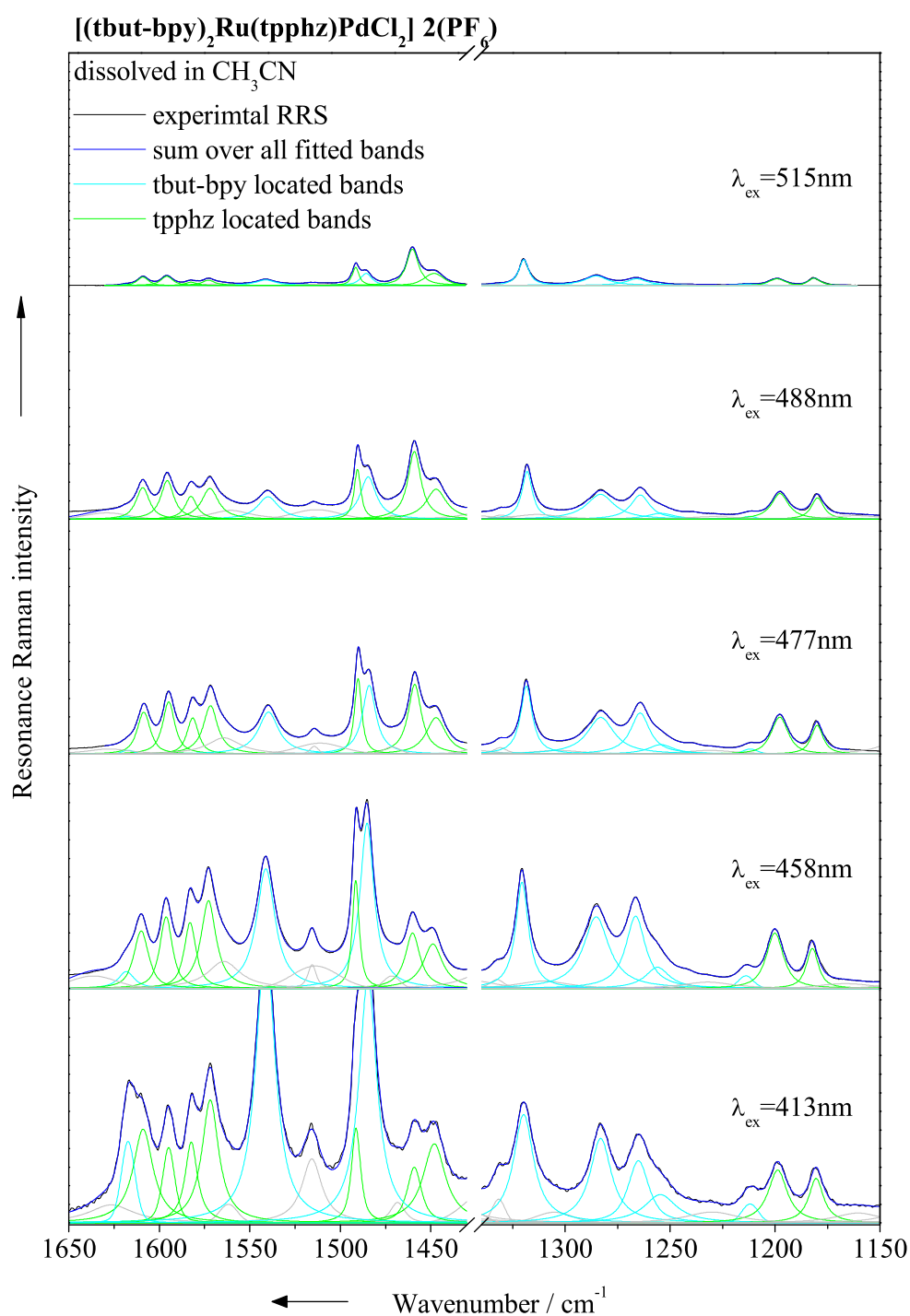


Figure 5.6: Deconvolution of experimental resonance Raman spectra of $[\text{RuPd}]^{2+}$ dissolved in acetonitrile, excited at 515, 488, 477, 458, 413 nm (top down). Black graphs: experimental RRS; green and pale blue pseudo-Voigt-profiles: tp-phz and tbut-bpy assigned modes; dark blue graphs: sums over all respective pseudo-Voigt-profiles.

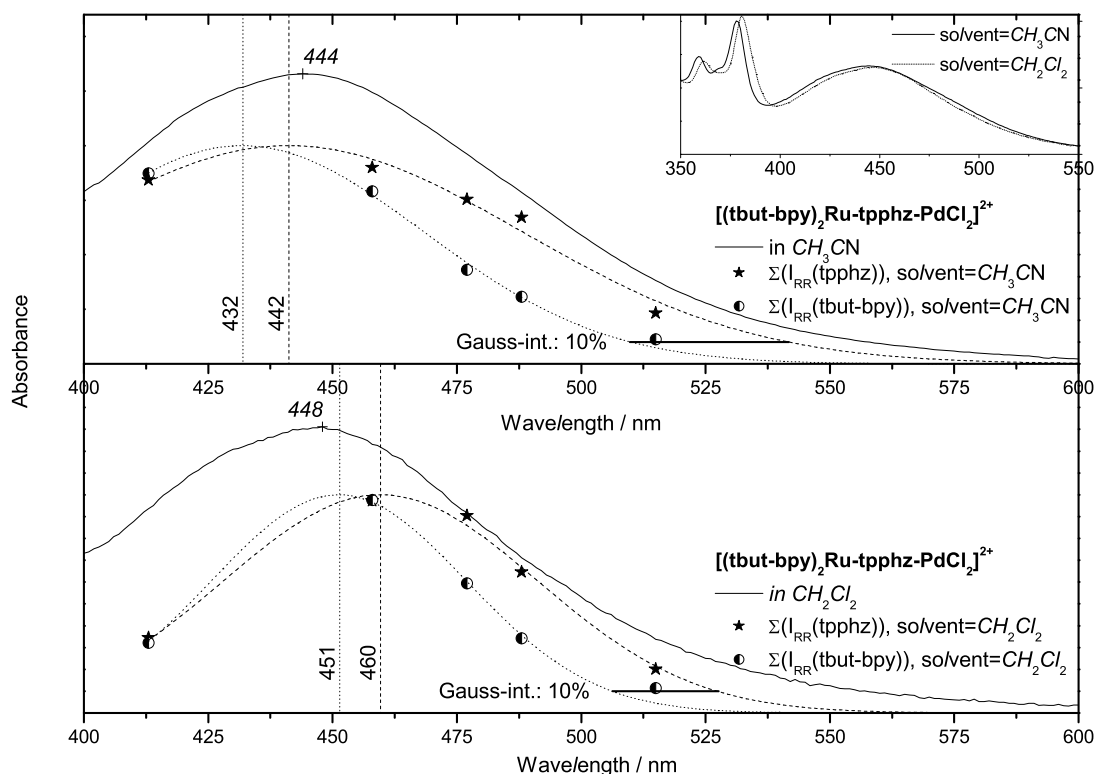


Figure 5.7: MLCT-absorption band of $[\text{RuPd}]^{2+}$; dots: normalized sums of ν^4 -corrected RR-intensities, star-shaped dots: tpphz-assigned RR-bands, circle dots: tbut-bpy-assigned RR-bands, dotted and dashed lines: Gauss-fits; upper graph: solvent = CH_3CN , lower graph: solvent = CH_2Cl_2 ; inset: normalized UV-vis spectra of $[\text{RuPd}]^{2+}$ dissolved in CH_3CN (solid line) and CH_2Cl_2 (dotted line). Horizontal lines: $^1\text{MLCT}$ shifts at 10% absorption.

applied solvents, the $\sum I_{RR}(\text{tpphz})$ -maximum is red-shifted against the $\sum I_{RR}(\text{tbut-bpy})$ -maximum. Since the $(\text{tpphz})\leftarrow\text{Ru}^{2+}$ $^1\text{MLCT}$ possesses a lower energy than the $(\text{tbut-bpy})\leftarrow\text{Ru}^{2+}$ $^1\text{MLCT}$, a targeted charge transfer to tpphz can be realized by excitation at the low-energetic edge of the $^1\text{MLCT}$ absorption band.

The energy levels of the ligand assigned $^1\text{MLCT}$ s are determined from the low-energy wavelength-values at 10% of the maximal intensities of the fitted Gauss-profiles, since these values are assumed to approximate the energies of electronic 0-0-transitions.^e The shifts at 10% intensity are illustrated by horizontal lines in figure 5.7. As figure 5.8 re-

^e0-0-transition: from the electronic and vibrational ($\nu=0$) groundstate to the vibrational groundstate ($\nu=0$) of the electronic excited state

veals, the energy difference between the ligand assigned $^1\text{MLCT}$ states is smaller for the CH_2Cl_2 solution than for the CH_3CN solution, even if the distances between the maxima of the ligand-assigned $^1\text{MLCT}$ s are minor differing between both solvents. In contrast, the maximum of the $^1\text{MLCT}$ absorption band of $[\text{RuPd}]^{2+}$ dissolved in dichloromethane is red-shifted of only about 4 nm against the corresponding maximum of the acetonitrile solution. This discrepancy between the solvent dependent maxima-shifts of the particular ligand-located $^1\text{MLCT}$ s and the respective superimposed absorption bands in the UV-vis spectra might be explained by different intensity ratios of the underlying ligand-assigned $^1\text{MLCT}$ bands. Therefore, it is assumed that in the case of the CH_2Cl_2 solution the $^1\text{MLCT}$ ending up at tbut-bpy is more pronounced than the one ending up at tpphz, while this difference in the CH_3CN solution is supposed to be smaller. Hence, one can conclude that a transition to tpphz compared to tbut-bpy is of higher probability in the CH_3CN solution than in the respective CH_2Cl_2 solution. This fact is supposed to contribute to the different hydrogen-yields between CH_3CN - and CH_2Cl_2 -solutions of $[\text{RuPd}]^{2+}$.

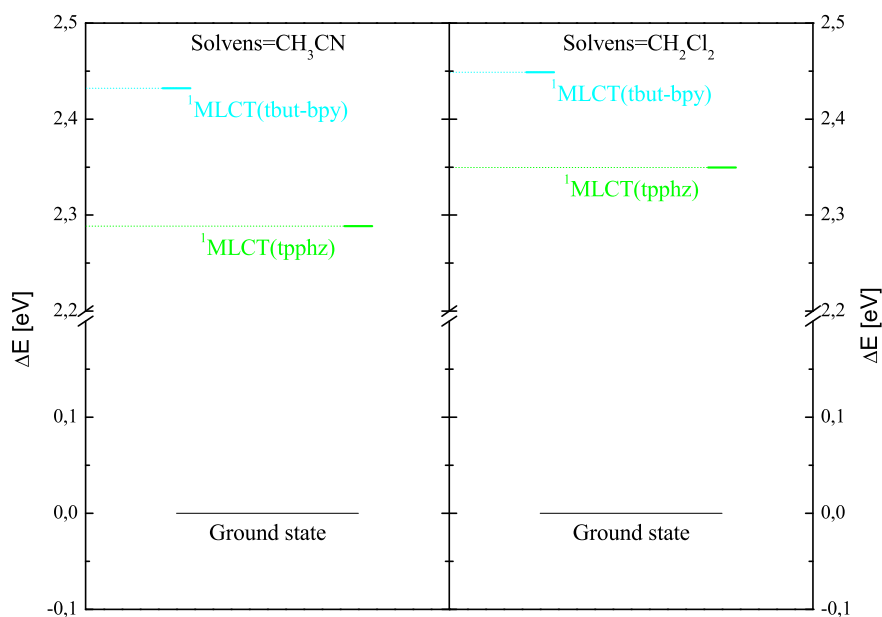


Figure 5.8: $^1\text{MLCT}$ energy differences ΔE referring to the groundstate energy (set zero). ΔE -values are estimated at 10% of the maximal amplitude of the Gauss profiles. Left: solvent = CH_3CN , right: solvent = CH_2Cl_2

6 Summary - Zusammenfassung

6.1 Summary

The major aim of the present work is the correlation of electron density investigations with vibrational spectroscopic studies. In particular, Raman spectroscopy was applied to qualitatively approve DFT-calculated changes in the electron density distribution induced by structural modifications. Moreover, a method was derived to predict properties of the electron density distribution quantitatively via combinations of vibrational spectroscopic and NMR spectroscopic data. Furthermore, the initial changes in the electron density distribution upon photoexcitation and related changes in the molecular structure were investigated via resonance Raman spectroscopy. The results of all these studies are shortly summarized in the following.

After the impact and the limitations of electron density studies are outlined in the "Introduction" (chapter 1), the basic tools to calculate and analyze the electron density distribution $\rho(\mathbf{r})$ are summarized in chapter 2 "Theoretical details". In section 4.1 an illustrative example of $\rho(\mathbf{r})$ -studies in the life sciences was discussed in detail. This example is related to an investigation of Schirmeister and Luger, who studied the selectivity of an inhibition reaction of an aziridine derivative functioning as a protease inhibitor. For that purpose they determined the electron densities at the carbon atoms within the aziridine ring via high resolution x-ray measurements of an aziridine single crystal and via DFT-calculations of an isolated aziridine molecule. Continuing the work of Schirmeister and Luger the influences of neighboring molecules on $\rho(\mathbf{r})$ and therewith on the electrophilicity of the aziridine carbons were studied to shed light on the impact of intermolecular interactions on the electron density distribution $\rho(\mathbf{r})$. It turned out that NHN-hydrogen bridges and intermolecular interactions between dimethylmalonate moieties exhibit opposite influences on the aziridine ring. In particular, an electrophilic attack to a protease enzyme would occur at C2 if hydrogen bridges at the aziridine-N are ruling. In contrast, C1 would be more electrophilic than C2 if intermolecular interactions of the dimethylmalonate group are dominating. The results and the study of an aziridine in a simulated aqueous environment support the assumption of Schirmeister and Luger, who supposed the electrophilic attack occurs via C1.

The electron density distribution $\rho(\mathbf{r})$ can only be determined of substances in the single crystalline state. Consequently, for the experimental investigation of $\rho(\mathbf{r})$ -properties of non-crystalline substances an alternative approach is necessary. In section 4.2 a method to study $\rho(\mathbf{r})$ via spectroscopic techniques is introduced. It could be demonstrated, that vibrational spectroscopy, especially Raman spectroscopy in cause of application to physiological aqueous samples, and NMR spectroscopy are well suited to determine specific $\rho(\mathbf{r})$ -characteristics. In particular, it could be shown that vibrational wavenumber values and $^1\text{H-NMR}$ shifts are important quantities to predict electron densities, respective laplacians and ellipticities in bond critical points of CH-bonds in benzene derivatives via linear functions.^a Since usual normal modes are not local and might involve for example substituent motions, they are not suited for correlations with local particular electron density properties. To solve this problem, the stretching vibration of the CD-bond in mono-deuterated analoges of the benzene derivatives were chosen for correlation with the respective electron density properties, since these vibrations are inherently localized. In doing so, it is possible to predict properties of the electron density distribution by means of experimental universal accessible spectroscopic measures for the first time. A further improvement of the method might be achieved by introducing normal mode partitioning schemes to yield vibrational spectroscopic data of particular internal coordinates. This would be a promising approach to find more general relations between the herein studied spectroscopic quantities and $\rho(\mathbf{r})$ -features.

In section 4.3 quantum mechanical $\rho(\mathbf{r})$ -studies in combination with Raman spectroscopy were applied to characterize tpy-ph-R ligands and related Ru(II) and Zn(II) complexes. In particular, the extension of the π -electron system was studied via the ellipticity in the bond critical point of the py-ph bond and related geometrical and vibrational spectroscopic measures. In doing so, the influences of complexation and substitutions at phenylene on the tpy-ph π -system were quantified and guided the way to actuate the respective π -delocalization. In conjunction with the data from section 4.2 target structures possessing a defined conjugation of the π -system can be derived. Exemplarily, it was demonstrated how to increase the π -character of the py-ph bond maximal. Surprisingly, additional NH_2 -substituents in *ortho*-positions to the inter-annular bond are even enhanc-

^aIn the studies presented in the section 4.2 the $\rho(\mathbf{r})$ -properties were determined separately for each of the five CH-positions. In subsequent investigations functions were derived which are able to describe all five CH-positions together but depend only on particular spectroscopic measures. Those functions are of the type $f = A + B(Cx^2 + De^{-x^2})$ or $f = A + B(Cx^2 + Dx^4)$. The parameter A, B, C, D are derived due to fit-procedures and are subsequently expressed via spectroscopic properties. These functions are possessing a good prediction performance which is nevertheless not as excellent as the prediction performance of the functions presented in section 4.2. Since these studies are not finished yet, they are not included in the present manuscript.

ing electron delocalization between py and ph, even if the corresponding dihedral angle is enlarged. Consequently, the electronic influence of *ortho*-NH₂-groups exceeds corresponding steric effect. Furthermore, *ortho*-substituents are expected to significantly affect the geometry of electronically excited states. In particular, the planarization of the py-ph unit is supposed to be avoided due to *ortho*-substituents. Since this planarization is responsible for decreased lifetimes of the ³MLCT state in Ru(II) complexes as compared to non-aromatic but unsaturated substituents, the *ortho*-substituted structures suggested in section 4.3.3 are expected to exhibit a prolonged lifetime of the charge separated ³MLCT state. In conclusion, the results of the systematic QTAIM study facilitates the derivation of new tpy-related structures with improved properties.

In chapter 5 the metal to ligand charge transfer (¹MLCT) in Ru(II)-(tpy-ph) complexes is investigated via resonance Raman spectroscopy. Since the ¹MLCT is the initial step at photoexcitation, it determines all following processes. It could be shown that the ¹MLCT involves not only the tpy moiety but also the ph moiety. In contrast, the *para*-ph substituents are not involved in the ¹MLCT since no corresponding resonantly enhanced Raman modes could be detected.

Furthermore, the relative energies of the ¹MLCTs in the hydrogen generating photocatalyzer [(tbut-bpy)₂Ru(tpphz)PdCl₂]²⁺ were estimated via resonance Raman spectroscopy. Due to the differently pronounced resonance enhancements of tbut-bpy- and tpphz-related Raman bands which depend on the excitation energies, the (tpphz)←Ru²⁺ transition was determined to be red shifted compared to the (tbut-bpy)←Ru²⁺ transition. This result is valid for the Ru(II) complex dissolved in CH₃CN and in CH₂Cl₂. Comparison of the shifts between the (tpphz)←Ru²⁺ and the (tbut-bpy)←Ru²⁺ transition reveals the energy difference of these transitions being significantly higher for the CH₃CN solution than for the CH₂Cl₂ solution. This finding supports an explanation for the different hydrogen yields of the CH₃CN and the CH₂Cl₂ solution.

Finally, one can summarize that Raman spectroscopy was successfully applied to investigate structure-property relations qualitatively as shown in section 4.3. Furthermore, due to the combination of Raman spectroscopy with other spectroscopic techniques a method was derived allowing for a quantitatively prediction of electron density features by means of easily accessible spectroscopic measures (see section 4.2). Moreover, it was outlined how this method might be further improved. In context of the investigation of the electron density properties of terpyridine derivatives and their transition metal complexes surprising results were obtained concerning the influence on the electron delocalization of NH₂-substituents *ortho* to the py-ph bond. In particular, the results of the AIM-analysis revealed that the electronic influences of *ortho*-NH₂-groups overcompensate the corresponding steric effects. Consequently, a roughly total delocalization between the

π -systems of terpyridine and phenylene is expected, despite the torsion between pyridine and phenylene. The next important step is the synthesis and the photophysical characterization of the suggested structures to approve the effects of the *ortho*-substituents and the related supposed changes in the photophysical properties.

6.2 Zusammenfassung

Ein Ziel der vorliegenden Arbeit war die Verknüpfung von Elektronendichte-Analysen mit schwingungsspektroskopischen Studien. Insbesondere die Raman-Spektroskopie wurde eingesetzt, um Zusammenhänge zwischen Strukturvariationen und damit verbundenen Änderungen der mittels DFT berechneten Elektronendichteverteilungen qualitativ zu bestätigen. Darüber hinaus wurde aufgezeigt, wie Schlüsseigenschaften der Elektronendichteverteilung über Kombinationen verschiedener spektroskopischer Methoden quantitativ bestimmt werden können. Weiterhin wurden die initialen Änderungen der Elektronendichte bei Photoanregung und die damit verbundenen Geometrieänderungen mittels Resonanz-Raman-Spektroskopie untersucht. Im Folgenden werden die Ergebnisse dieser Studien kurz zusammengefasst.

Nachdem einleitend der Nutzen und die Limitierungen von Elektronendichtestudien dargelegt wurden, folgte im Kapitel 2 "Theoretical details" ein kurzer Überblick über die Berechnung und Analyse von Elektronendichteverteilungen $\rho(r)$. In Abschnitt 4.1 wird eine Anwendung von $\rho(r)$ -Studien in den Lebenswissenschaften diskutiert. Es handelt sich dabei um eine Untersuchung aus den Arbeitsgruppen Schirmeister und Luger, bei der die Selektivität der Hemmreaktion eines Proteaseinhibitors (Aziridin-Derivat) anhand des Unterschieds der Elektronendichte der Kohlenstoffatome im Aziridin-Ring studiert wird. Aufbauend auf den am Einkristall experimentell und vom isolierten Molekül theoretisch bestimmten $\rho(r)$ -Daten wurde in dieser Arbeit der Einfluss von Nachbarmolekülen auf $\rho(r)$ und insbesondere auf die Elektrophilie der beiden Schlüssel-C-Atome untersucht. Es wurde festgestellt, dass intermolekulare Wechselwirkungen über die Aziridin-NHN Wasserstoffbrückenbindungen und über die Malonsäureestergruppen das Verhältnis der Elektrophilie der beiden Aziridin-Kohlenstoffatome gegensätzlich beeinflussen. Die kovalente Bindung zum Enzym wird über C2 erfolgen, wenn der Aziridin Ring während der Hemmreaktion über eine Wasserstoffbrückenbindung mit der Proteinhülle des Enzyms oder mit Solvensmolekülen verbunden ist. Falls eine solche H-Brückenbindung nicht ausgeprägt ist und stattdessen die Malonsäureesterfunktion eine dominante Wechselwirkung mit dem Enzym eingeht, wäre C1 elektrophiler. Die Betrachtung aller untersuchten Dimere und eine Studie des einzelnen Aziridin Derivates mit simulierter Wasserumgebung stützen die Hypothese von Schirmeister und Luger, dass die Ringöffnungsreaktion, die zur Deak-

tivierung der Protease führt, bevorzugt durch einen elektrophilen Angriff an C1 initiiert wird.

Die Untersuchungen zur Reaktivität des Proteaseinhibitors sind vorwiegend theoretischer Natur, da die Elektronendichteverteilung selbst nur am Einkristall und nicht in wässrigen oder komplexen physiologischen Umgebungen experimentell bestimmt werden kann. Als Alternative wird in Abschnitt 4.2 eine Methode vorgeschlagen, die es ermöglicht Aussagen über wesentliche Eigenschaften der Elektronendichteverteilung mittels spektroskopischer Methoden zu treffen. Diese Methode ist auf alle denkbaren Aggregatzustände und Umgebungen anwendbar. Es konnte gezeigt werden, dass Schwingungs- und NMR-spektroskopische Messgrößen mit der Elektronendichte, den entsprechenden Laplace-Werten und der Elliptizität in bindungskritischen Punkten von CH-Bindungen in einer Reihe von monosubstituierten Aromaten linear korrelieren. Aufwendige Validierungsprozeduren weisen insbesondere schwingungsspektroskopische Wellenzahlwerte und $^1\text{H-NMR}$ -Verschiebungen als wichtige Größen in den erarbeiteten Fit-Funktionen aus. Allerdings sind im Allgemeinen Normalmoden nicht lokal, sondern beziehen z.B. Schwingungen des Substituenten mit ein. Demzufolge eignen sie sich nicht um einzelne lokale Bindungen oder andere lokale Strukturen quantitativ zu beschreiben. Aus diesem Grund wurden einfach deuterierte Benzenderivate untersucht, da die CD-Schwingungen bei einfacher Deuterierung auf die CD-Bindung lokalisiert sind. Damit ist es zum ersten Mal möglich Vorhersagen von Elektronendichteigenschaften anhand spektroskopischer Messgrößen zu treffen.^b Eine weitere Verallgemeinerung der vorgestellten Methode kann die Verwendung von Partitionierungsschemata bieten. Diese weisen analog der natürlichen Lokalisierung der CD-Streckschwingungen jedem internen Freiheitsgrad spezifische Schwingungsparameter zu.

In Abschnitt 4.3 werden mit Hilfe von ρ -Analysen (QTAIM und $\Delta\rho$ -plots) und Raman Spektroskopie die Einflüsse von Komplexierung der tpy-Einheit und von Substitutionen am Phenylen-Ring von 4'(phenyl)-2,2':6',2''-terpyridin (tpy-ph) auf die π -Elektronendelokalisierung zwischen tpy und ph untersucht und quantifiziert. Die gewonnenen Erkennt-

^bVorerst wurden besagte Studien für jede CH-Position am Aromaten separat durchgeführt. Um den Nutzen solcher Vorhersagen zu steigern wurden Funktionen untersucht, die die Elektronendichteigenschaften aller fünf CH-Bindungen eines Benzenderivates beschreiben können und dennoch nur von wenigen ausgewählten spektroskopischen Größen (die sich beispielsweise nur auf die *ortho*-Positionen beziehen) abhängen. Solche Funktionen haben die Form $f = A + B(Cx^2 + De^{-x^2})$ oder $f = A + B(Cx^2 + Dx^4)$. Die Parameter A, B, C, D werden mittels Fit-Prozeduren ermittelt und anschließend über spektroskopische Größen ausgedrückt. Diese Funktionen zeigen eine akzeptable Vorhersagegenauigkeit, erreichen aber nicht die Präzession der in Abschnitt 4.2 vorgestellten linearen Funktionen. Da die Arbeiten zu dieser Studie noch nicht ganz abgeschlossen sind, wurden sie in dem vorliegenden Manuskript nicht berücksichtigt.

nisse über die Wirkung der *ph*-R-Substituenten und der Komplexierung ermöglichen das zielgerichtete Design von Strukturen mit definiertem π -Delokalisierungsgrad. Es konnte beispielhaft gezeigt werden, wie man einen maximalen π -Charakter der *py-ph*-Bindung und damit eine maximale Delokalisierung des π -Systems von *tpy-ph* erreichen kann. Die Einführung von NH_2 -Substituenten in *ortho*-Position zur *py-ph*-Bindung führt zwar zu einer Erhöhung des entsprechenden Diederwinkels, bewirkt aber überraschenderweise dennoch eine Erhöhung der Elliptizität der *py-ph*-Bindung. Demzufolge wird der sterische Effekt von *ortho*- NH_2 -Gruppen durch ihren elektronischen Einfluss überkompensiert. Außerdem sollte die *ortho*-Substitution einen deutlichen Einfluss auf Geometrien elektronisch angeregter Zustände haben. Insbesondere die von Hanan beschriebene Planarisierung zweier benachbarter Aromaten im elektronisch angeregten Zustand,⁵⁸ die zu einer kürzeren Lebenszeit des ³MLCT-Zustandes führt, ist für *ortho*-substituierte Derivate unwahrscheinlich. Demzufolge sind die Ergebnisse der systematischen QTAIM-Analysen für die Suche nach neuen Zielstrukturen mit definierten Eigenschaften nützlich. Dies wurde beispielhaft für Strukturen mit maximalem π -Charakter in der *py-ph* Bindung demonstriert.

In Abschnitt 5.1 wird der Übergang vom elektronischen Grundzustand in den ¹MLCT Zustand von Ru(II)-(tpy-ph)-Komplexen mittels Resonanz-Raman-Spektroskopie untersucht. Da der Übergang zum ¹MLCT-Zustand der initiale Schritt in allen photophysikalischen Reaktionen ist, hängen von ihm alle folgenden Prozesse ab. Es konnte gezeigt werden, dass dieser Übergang am Franck-Condon-Punkt nicht ausschließlich die tpy-Einheit einbezieht, sondern die von Ru(II) weiter entfernte Phenylen-Gruppe instantan involviert ist. Eine direkte Beeinflussung der *para-ph*-Substituenten kann allerdings ausgeschlossen werden, da keine entsprechenden Resonanz-Raman-Signale detektiert wurden.

Weiterhin wurden mittels Resonanz-Raman-Spektroskopie die relativen energetischen Lagen der ¹MLCT-Zustände in dem H_2 -erzeugenden Photokatalysator $[\text{RuPd}]^{2+}$ bestimmt.^c Über die Abhängigkeiten der Intensitäten der tbut-bpy- und tppez-Resonanz-Raman-Banden von den Anregungswellenlängen wurde der (tppez) \leftarrow Ru²⁺-Übergang als rot-verschoben gegenüber dem (tbut-bpy) \leftarrow Ru²⁺-Übergang ermittelt. Dies gilt sowohl für CH_2Cl_2 als auch für CH_3CN als Lösemittel. Bei dem Vergleich der Wellenlängen der energetisch niedrigen Flanken der Resonanz-Raman-Profile von tppez und tbut-bpy für beide Lösemittel zeigt sich, dass die Energiedifferenz zwischen dem (tppez) \leftarrow Ru²⁺- und dem (tbut-bpy) \leftarrow Ru²⁺-Übergang in Acetonitril deutlich größer ist als in Methylenchlorid. Diese Erkenntnis trägt zur Erklärung der unterschiedlichen Effizienzen des Ru(II)-Photokatalysators in CH_2Cl_2 und CH_3CN bei.

Abschließend kann man festhalten, dass die Raman-Spektroskopie zum einen für qualitative Untersuchungen von Struktur-Eigenschafts-Beziehungen erfolgreich eingesetzt

^c $[\text{RuPd}]^{2+} = [(\text{tbut-bpy})_2\text{Ru}(\text{tppez})\text{PdCl}_2]^{2+}$

wurde (siehe Abschnitt 4.3). Zum anderen konnte durch die Kombination der Raman-Spektroskopie mit weiteren spektroskopischen Techniken eine Methode zur quantitativen Bestimmung von Elektronendichte-Eigenschaften entwickelt werden (siehe Abschnitt 4.2). Außerdem wurden Möglichkeiten zur Erweiterung dieser Methode aufgezeigt. Im Rahmen der Untersuchungen zur Elektronendichteverteilung in Terpyridin-Systemen lieferten AIM-Analysen überraschende Ergebnisse hinsichtlich Substitutionen *ortho*-ständig zu einer Pyridin-Phenylen-Bindung. Es stellte sich heraus, dass der elektronische Einfluss von NH₂-Gruppen den sterischen Einfluss in der *ortho*-Position überkompensiert und dadurch trotz der Torsion zwischen Pyridin und Phenylen eine nahezu vollständige Elektronendelokalisierung zwischen beiden aromatischen Ringen zu erwarten ist. In naher Zukunft ist die Synthese und photophysikalische Charakterisierung solcher Verbindungen von höchstem Interesse, um die vorhergesagten Eigenschaften zu bestätigen.

A Supporting vibrational data

A.1 Vibrational assignment of the Raman spectrum of $[\text{Zn}(\text{L4})_2]^{2+}$

Table A.1: Vibrational assignment of the DFT-calculated Raman spectrum of $[\text{Zn}(\text{L4})_2]^{2+}$

Mode	$\tilde{\nu}$ [cm ⁻¹]	RA [$\frac{4}{\text{amu}}$]	Assignment
1	12,7	4,6	$\delta\text{N27ZnN14}$
2	13,3	3,8	$\delta\text{N8ZnN34}$
3	29,5	20,6	$\delta\text{N14ZnN34}$
4	38,8	4,2	δtpyN8 (butterfly mode)
5	40,4	5,1	δtpyN27 (butterfly mode)
6	44,3	5,2	$\delta\text{tpy}(\text{N27} + \text{N8 (butterfly mode)}) + \delta_{oop}\text{ph-CCH}$
7	45,6	2,4	$\delta^{tors}\text{tpy}$ (torsaxis N4N14/N34N40) + $\delta_{oop}\text{ph-CCH}$
8	53,6	8,7	$\delta\text{C30C45C76} + \delta\text{N8ZnN34}$
9	54,4	13,1	$\delta^{tors}\text{phC20}$ (torsaxis C11C20)
10	55,2	13,8	$\delta^{tors}\text{phC45}$ (torsaxis C45C30)
11	55,8	11,5	$\delta\text{C11C20C21} + \delta\text{N14ZnN27}$
12	72,4	0,1	$\delta^{tors}\text{tpy}$ (torsaxis N4N14/N34N40)
13	76,6	1,3	$\nu_{sym}\text{N8ZnN27}$
14	78,7	13,9	$\delta^{tors}\text{tpy}$ (torsaxis N4N14/N34N40) + $\delta_{oop}(\text{tpy} + \text{ph-CCH})$
15	79,9	7,7	$\delta^{tors}\text{tpy}$ (torsaxis N4N14/N34N40) + $\delta_{oop}(\text{tpy} + \text{ph-CCH})$
16	88,6	5,6	$\delta^{tors}\text{tpy}$ (torsaxis N4N14/N34N40) + $\delta_{oop}\text{tpy}$
17	99,2	3,6	$\delta_{ip}\text{tpy} + \nu_{sym}(\text{N4ZnN14, N34ZnN40}) + \text{ligand movem. } 180^\circ \text{ p.s.}$
18	108	4,9	$\delta_{ip}\text{tpy} + \nu_{sym}\text{NznN} + \text{ligand movem. i.p.}$
19	112,7	1,4	$\delta^{tors}\text{tpy}$ (torsaxis C11C20/C30C45) + $\delta_{oop}\text{tpy}$
20	116,2	0,1	$\delta^{tors}\text{tpy}$ (torsaxis C11C20/C30C45) + $\delta_{oop}\text{tpy}$
21	116,5	0,1	$\delta^{tors}\text{tpy}$ (torsaxis C11C20/C30C45) + $\delta_{oop}\text{tpy}$
22	133,5	5,5	$\delta\text{ph-CCH} + \nu(\text{N4ZnN14} + \text{N40ZnN34})$
23	138,5	48,3	$\delta^{tors}\text{tpy}$ (torsaxis C11C20/C30C45) + $\delta_{oop}\text{tpy}$
24	145	5,1	$\delta_{ip}\text{phCC(H)}$
25	149,9	4,8	$\delta_{ip}\text{phCC(H)} + \nu\text{N4ZnN14}$
26	158,3	0,2	$\delta_{ip}\text{phCC(H)} + \text{w. } \nu\text{N4ZnN14}$
27	178,2	0,9	$\delta_{asym}\text{N4ZnN14} + \delta_{oop}(\text{tpy} + \text{ph-CCH})$
28	179	3,1	$\nu_{asym}\text{N34ZnN40} + \delta_{oop}(\text{tpy} + \text{ph-CCH})$
29	197,5	0,3	$\nu_{asym}\text{N8ZnN27} + \text{w. } \delta_{ip}(\text{tpy} + \text{ph})$
30	215,9	0,1	$\delta^{tors}\text{py}_c$ (torsaxis C11C20/C30C45) + w. $\delta_{oop}\text{tpy}$
31	220,3	57,8	$\delta^{tors}\text{py}_c$ (torsaxis C11C20/C30C45) + w. $\delta_{oop}\text{tpy}$
32	225,9	0,1	$\delta_{oop}\text{ph-CCH} + \delta_{ip}\text{tpy}$
33	226,8	3,7	$\delta_{oop}\text{ph-CCH} + \delta_{ip}\text{tpy}$
34	227,5	19,2	$\delta^{tors}\text{py}_c$ (torsaxis C11C20/C30C45) + w. $\delta_{oop}\text{ph-CCH}$

continued on next page

Vibrational assignment of the DFT-calculated RS of $[\text{Zn}(\text{L4})_2]^{2+}$

Mode	$\tilde{\nu}$ [cm ⁻¹]	RA [$\frac{4}{\text{amu}}$]	Assignment
35	240,6	2,6	$\delta^{twist}\text{N14ZnN8} + + \delta\text{N27ZnN4}$
36	241,4	2,9	$\delta\text{N27ZnN8} + \text{w. } \delta_{oop}\text{tpy}$
37	242,2	2	$\nu_{asym}\text{N27ZnN8} + \text{w. } \delta_{ip}\text{tpy}$
38	269	2,3	$\delta_{oop}(\text{py}_c + \text{ph} + \text{CCH})$
39	274,5	0,4	$\delta_{oop}(\text{py}_c + \text{ph} + \text{CCH})$
40	299,3	0	$\delta_{ip}\text{tpy}$
41	303,2	1	$\delta_{ip}\text{tpy}$
42	306,8	22,7	$\delta_{ip}\text{tpy} + \nu\text{ZnN} + \text{tpy movem. i.p.}$
43	316,3	0,6	$\delta_{ip}\text{tpy} + \nu\text{ZnN} + \text{tpy movem. } 180^\circ \text{ p.s.}$
44	378,1	1,6	$\delta_{oop}\text{py}_c\text{-ph-CCH}$
45	378,5	8,3	$\delta_{oop}\text{py}_c\text{-ph-CCH}$
46	399,2	44,9	$\delta_{oop}\text{ph (W.No. 16a)}$
47	399,8	57,2	$\delta_{oop}\text{ph (W.No. 16a)}$
48	402,5	0	$\delta_{oop}(\text{py} + \text{w. ph})$
49	408,1	0,4	$\delta_{oop}\text{py}_p$ (comp. W.No. 16a)
50	409,4	0,8	$\delta_{oop}\text{py}_p$ (comp. W.No. 16a)
51	415,4	9,7	$\delta_{oop}\text{py}_p$ (comp. W.No. 16a)
52	436,4	50	$\delta_{ip}(\text{tpy} + \text{w. ph}) + \nu\text{ZnN} + \text{tpy movem. i.p.}$
53	436,7	8,3	$\delta_{oop}\text{ph-CCH}$
54	437,4	2,7	$\delta_{oop}\text{ph-CCH}$
55	442,3	0,4	$\delta_{ip}(\text{tpy} + \text{w. ph}) + \nu\text{ZnN} + \text{tpy movem. } 180^\circ \text{ p.s.}$
56	448	18,5	$\delta_{oop}\text{tpy}$
57	449,2	0,1	$\delta_{oop}\text{tpy}$
58	481,5	0,9	$\delta_{oop}\text{tpy}$
59	481,7	3,1	$\delta_{oop}\text{tpy}$
60	522,6	2,1	$\delta_{ip}\text{phCC(H)}$
61	522,7	6,9	$\delta_{ip}\text{phCC(H)}$
62	529,9	103,3	$\nu\text{ZnN} + \delta_{ip}(\text{py}_c + \text{ph}) + \text{py}_c \text{ movem. i.p.}$
63	533	0,6	$\nu\text{ZnN} + \delta_{ip}(\text{py}_c + \text{ph}) + \text{py}_c \text{ movem. } 180^\circ \text{ p.s.}$
64	539,4	0,9	$\delta_{oop}\text{ph} + \text{ph movem. i.p.}$
65	539,6	5,1	$\delta_{oop}\text{ph} + \text{ph movem. } 180^\circ \text{ p.s.}$
66	576,5	2,1	$\delta_{oop}\text{ph} + \delta_{ip}\text{PY}_c$
67	576,7	3,8	$\delta_{oop}\text{ph} + \delta_{ip}\text{PY}_c$
68	620,9	1,3	$\delta_{oop}(\text{ph} + \text{py}_c + \text{w. py}_p) + \delta_{ip}\text{ph}$
69	621,3	1,4	$\delta_{oop}(\text{ph} + \text{py}_c + \text{w. py}_p) + \delta_{ip}\text{ph}$
70	629,5	8,6	$\delta_{ip}\text{PY}_p$
71	631,4	1	$\delta_{ip}\text{PY}_p$
72	631,5	1,4	$\delta_{ip}\text{PY}_p$
73	632,6	8,6	$\delta_{ip}\text{PY}_p + \delta_{oop}\text{PY}_c$
74	632,9	1,3	$\delta_{ip}\text{PY}_p + \delta_{oop}\text{PY}_c$
75	634,3	4,9	$\delta_{ip}\text{PY}_p + \delta_{oop}\text{PY}_c$
76	639,5	1,2	$\delta_{ip}\text{ph (W.No. 6b)} + \delta_{oop}\text{PY}_c$
77	639,9	6,2	$\delta_{ip}\text{ph (W.No. 6b)} + \delta_{oop}\text{PY}_c$
78	652,1	0,3	$\delta_{ip}\text{py (W.No. 6b)}$
79	652,1	0	$\delta_{ip}\text{py (W.No. 6b)}$
80	661,7	24,9	$\delta_{oop}(\text{ph})\text{CCH}$
81	663,1	22,3	$\delta_{oop}(\text{ph})\text{CCH}$
82	665,1	1,7	$\delta_{ip}(\text{ph})\text{CCH}$
83	666,8	3,5	$\delta_{ip}(\text{ph})\text{CCH}$
84	679,1	6,2	$\delta_{ip}\text{py (W.No. 6b)}$
85	681,6	0,3	$\delta_{ip}\text{py (W.No. 6b)}$

continued on next page

Vibrational assignment of the DFT-calculated RS of $[\text{Zn}(\text{L4})_2]^{2+}$

Mode	$\tilde{\nu}$ [cm ⁻¹]	RA [$\frac{4}{\text{amu}}$]	Assignment
86	723,7	0,2	δ_{oop} (tpy: py_p i.p., py_c 180° p.s.)
87	723,8	0,4	δ_{oop} (tpy: py_p i.p., py_c 180° p.s.)
88	734	1,9	$\delta_{oop}\text{ph}$ (W.No. 4) + w. on tpy
89	734,2	6,4	$\delta_{oop}\text{ph}$ (W.No. 4) + w. on tpy
90	739,2	0	δ_{oop} (W.No. 11, py_c 180° p.s.)
91	742,2	2,6	δ_{oop} (W.No. 11, py_c 180° p.s.)
92	744,7	0,9	δ_{oop} (W.No. 11, tpy i.p.) + w. $\delta_{oop}\text{ph}$ (W.No. 4)
93	745,1	0,9	δ_{oop} (W.No. 11, tpy i.p.) + w. $\delta_{oop}\text{ph}$ (W.No. 4)
94	752,8	3,6	$\delta_{ip}(\text{ph} + \text{py}_c)$
95	753,1	43,5	$\delta_{ip}(\text{ph} + \text{py}_c)$
96	794	4,2	δ_{oop} (W.No. 11, $\text{pyN14} + \text{pyN34} + \text{w. on } (\text{py}_c\text{N8} + \text{py}_c\text{27})$)
97	794,3	2	δ_{oop} (W.No. 11, py i.p.)
98	794,6	3,6	δ_{oop} (W.No. 11, $\text{pyN4} + \text{pyN40} + \text{w. on } (\text{py}_c\text{N8} + \text{py}_c\text{N27})$)
99	795,8	14	δ_{oop} (W.No. 11, py_p 180° p.s.)
100	813,3	30,4	δ_{oop} (W.No. 10a)
101	814,4	31,3	δ_{oop} (W.No. 10a)
102	830,1	3,9	δ_{oop} (comp. W.No. 11) + w. δ_{ip} tpy
103	830,7	4,2	δ_{oop} (comp. W.No. 11) + w. δ_{ip} tpy
104	832,5	93,3	$\delta_{ip}(\text{py}_c + \text{ph}) + \nu\text{ZnN}(\text{py}_c)$
105	832,8	454,2	$\delta_{ip}(\text{py}_c + \text{ph}) + \nu\text{ZnN}(\text{py}_c)$
106	841,4	15,5	$\delta_{ip}\text{tpy}$ (py_c comp. W.No. 6b) + $\delta_{oop}\text{ph}$ (comp. W.No. 11)
107	841,7	14,6	$\delta_{ip}\text{tpy}$ (py_c comp. W.No. 6b) + $\delta_{oop}\text{ph}$ (comp. W.No. 11)
108	875	17,6	δ_{ooptpy} (str.: CH on py_c , 180° p.s.)
109	875,8	58	δ_{ooptpy} (str.: CH on py_c , 180° p.s.)
110	878,2	1,4	δ_{ooptpy} (str.: CH on py_c , i.p.) + w. $\delta_{oop}\text{ph}$ (comp. W.No. 11)
111	878,2	3,5	δ_{ooptpy} (str.: CH on py_c , i.p.) + w. $\delta_{oop}\text{ph}$ (comp. W.No. 11)
112	885,2	1	$\delta_{ooptpy}(\text{CH})$
113	885,6	0,6	$\delta_{ooptpy}(\text{CH})$
114	888,4	44	$\delta_{ooptpy}(\text{CH})$
115	889,2	4,4	$\delta_{ooptpy}(\text{CH})$
116	944,2	1,5	$\delta_{oop}\text{ph}$ (W.No. 17a)
117	945,2	1,3	$\delta_{oop}\text{ph}$ (W.No. 17a)
118	948	0,5	$\delta_{oop}\text{ph}$ (W.No. 17b)
119	948,7	0,5	$\delta_{oop}\text{ph}$ (W.No. 17b)
120	957,7	0,1	$\delta_{oop}\text{py}_p\text{N34}$ (comp. W.No. 17b)
121	957,8	0,1	$\delta_{oop}\text{py}_p\text{N14}$ (comp. W.No. 17b)
122	957,8	0,1	$\delta_{oop}\text{py}_p\text{N40}$ (comp. W.No. 17b)
123	958	0,1	$\delta_{oop}\text{py}_p\text{N4}$ (comp. W.No. 17b)
124	994,2	4,4	$\delta_{oop}\text{py}_p\text{N40}$ (comp. W.No. 17a)
125	994,4	9,8	$\delta_{oop}\text{py}_p\text{N14}$ (comp. W.No. 17a)
126	994,6	0,4	$\delta_{oop}\text{py}_p\text{N4}$ (comp. W.No. 17a)
127	994,8	1,2	$\delta_{oop}\text{py}_p\text{N34}$ (comp. W.No. 17a)
128	995,3	208,6	$\nu_{trb}^N + \delta_{ip}\text{py}$ (all py_p i.p., py_c 180° p.s. to py_p) + $\delta_{ip}\text{ph}$ (W.No. 18a)
129	995,5	29,6	$\nu_{trb}^N + \delta_{ip}\text{py}$ (py_p i.p., tpy 180° p.s.) + $\delta_{ip}\text{ph}$ (W.No. 18a)
130	999,6	49,5	$\nu_{trb}^N + \delta_{ip}\text{py}$ ($\text{py}_p\text{N40/N4}$ and $\text{py}_p\text{N34/14}$ i.p.)
131	999,6	49,6	$\nu_{trb}^N + \delta_{ip}\text{py}$ ($\text{py}_p\text{N34/N4}$ and $\text{py}_p\text{N40/14}$ i.p.)
132	1001	168,7	$\delta_{ip}\text{ph}$ (W.No. 18a)
133	1001,2	278,4	$\delta_{ip}\text{ph}$ (W.No. 18a)
134	1007	73,4	$\delta_{ip}\text{py}_c$ (ν_{trb}^N , 180° p.s.)
135	1009,7	2290,3	$\delta_{ip}\text{py}$ (ν_{trb}^N , all i.p.)
136	1032,8	15,5	$\delta_{ip}\text{tpy}$ (ν_{trb}^N) + $\delta_{ip}\text{py}$ (comp. W.No.18a) + lig. movem. 180° p.s.

continued on next page

Vibrational assignment of the DFT-calculated RS of $[\text{Zn}(\text{L4})_2]^{2+}$

Mode	$\tilde{\nu}$ [cm ⁻¹]	RA [$\frac{4}{\text{amu}}$]	Assignment
137	1034,5	627,9	$\delta_{ip}tpy$ ($\nu_{trb}C$) + $\delta_{ip}py$ (comp. W.No.18a) + lig. movem. i.p.
138	1050,8	2	$\delta_{ip}py_p$ (W.No. 18b, py_p 180° p.s.)
139	1050,9	1,9	$\delta_{ip}py_p$ (W.No. 18b, py_p 180° p.s.)
140	1061,4	14,4	$\delta_{ip}py_p$ (W.No. 18b, all py_p i.p.)
141	1063	8,5	$\delta_{ip}py_p$ (W.No. 18b, py_p i.p.) + lig. movem. 180° p.s.
142	1073,9	1,1	$\delta_{ip}py_cN8$ (W.No. 18a)
143	1074,3	3,1	$\delta_{ip}py_cN27$ (W.No. 18a)
144	1094,9	0	$\delta_{ip}tpy$ (W.No. 9b, py_p 180° p.s.)
145	1095,2	0	$\delta_{ip}tpy$ (W.No. 9b, py_p 180° p.s.)
146	1109,1	46,5	$\delta_{ip}tpy$ (W.No. 9b, all py i.p.)
147	1110,6	5,3	$\delta_{ip}tpy$ (W.No. 9b) + lig. movem. 180° p.s.
148	1114,5	1,6	$\delta_{ip}ph$ (W.No. 18b)
149	1114,9	1,8	$\delta_{ip}ph$ (W.No. 18b)
150	1157	5	$\delta_{ip}tpy$ (W.No.15 on py_p , 180° p.s.)
151	1157,5	5	$\delta_{ip}tpy$ (W.No.15 on py_p , 180° p.s.)
152	1162,2	25,8	$\delta_{ip}tpy$ (W.No.15 on py_p , i.p.)
153	1162,6	211,8	$\delta_{ip}tpy$ (W.No.15 on py_p , i.p.)
154	1165,6	2,6	$\delta_{ip}tpy$ (str. on C1H67, C17H58 comp. W.No.15 on py_p , 180° p.s.)
155	1165,9	0,2	$\delta_{ip}tpy$ (str. on C37H46, C43H47 comp. W.No.15 on py_p , 180° p.s.)
156	1173,2	2,1	$\delta_{ip}ph$ (W.No.9a, ph 180° p.s.)
157	1173,5	1733,4	$\delta_{ip}ph$ (W.No.9a, ph i.p.)
158	1214,6	121,5	$\nu C23C26$ (PhC(CH)) + $\delta_{ip}ph$ (str. on C21H60, C25H62, C22C23C24)
159	1214,8	148,6	$\nu C74C81$ (PhC(CH)) + $\delta_{ip}ph$ (str. on C72H77, C76H80, C73C74C75)
160	1232,4	345,3	$\nu(C11C20 + C30C45) + \delta_{ip}(ph + py_c) + \text{lig. movem. i.p.}$
161	1232,6	137,5	$\nu(C11C20 + C30C45) + \delta_{ip}(ph + py_c) + \text{lig. movem. 180° p.s.}$
162	1241	310,1	$\nu(C3C7 + C9C15) + \delta_{ip}py_c(C10H64, C12H65)$
163	1241,7	314,1	$\nu(C28C33 + C32C39) + \delta_{ip}py_c(C29H52, C31H51)$
164	1277,3	8,3	$\delta_{ip}py_p$ (W.No. 3, str.: py_pN4 , medium: $py_pN34/N40/N14$) + w. $\nu CN(py_p)$
165	1278	12,3	$\delta_{ip}py_p$ (W.No. 3, str.: py_pN14 , medium: $py_pN34/N40/N14$) + w. $\nu CN(py_p)$
166	1278,3	15	δ_{ip} (W.No. 3, $py_pN34/N40 + phC45$)
167	1281,3	47,3	δ_{ip} (W.No. 3, py_p all i.p. + w. ph)
168	1281,6	3,7	δ_{ip} (W.No. 3, $phC45 + tpyN27/N34/N40$)
169	1281,7	4,4	δ_{ip} (W.No. 3, $phC45 + tpyN4/N8/N14$)
170	1296,7	6,2	$\nu_{asym}C73C74C75 + \delta_{ip}phC45 + \nu CC/CN(tpyN27/N34/N40)$
171	1296,8	6,9	$\nu_{asym}C22C23C24 + \delta_{ip}phC20 + \nu CC/CN(tpyN4/N8/N14)$
172	1299,4	409,5	$\nu/\delta_{ip}py_p$ (W.No. 14) + $\delta_{ip}py_c$ + lig. movem. i.p.
173	1300,1	82,7	$\nu/\delta_{ip}py_p$ (W.No. 14) + $\delta_{ip}py_c$ + lig. movem. 180° p.s.
174	1309,2	11,8	ν/δ_{ip} (W.No. 14, $ph + py_p$ 180° p.s.)
175	1309,3	14,2	ν/δ_{ip} (W.No. 14, $ph + py_p$ 180° p.s.)
176	1329,4	9,7	ν/δ_{ip} (W.No. 14, $ph + py_c$)
177	1329,7	10,8	ν/δ_{ip} (W.No. 14, $ph + py_c$)
178	1349,4	242,6	$\nu_{trb}Cpy_c + \nu CC(2*3 py_c-R) + w. d_{ip}(py_p + ph) + \text{lig. movem. 180° p.s.}$
179	1351,4	6170,7	$\nu_{trb}Cpy_c + \nu CC(2*3 py_c-R) + w. d_{ip}(py_p + ph) + \text{lig. movem. i.p.}$
180	1401,8	347,5	δ_{ip} (W.No. 19a, $tpy + ph$) + lig. movem. i.p.
181	1403,4	19,5	δ_{ip} (W.No. 19a, $tpy + ph$) + lig. movem. 180° p.s.
182	1406,6	49	δ_{ip} (W.No. 19b, $py_c + ph$ i.p.)
183	1407,4	51,2	δ_{ip} (W.No. 19b, $py_c + ph$ i.p.)
184	1417,9	173,5	δ_{ip} (W.No. 19b, $py_c + ph$ 180° p.s.)
185	1418,9	167,5	δ_{ip} (W.No. 19b, $py_c + ph$ 180° p.s.)
186	1431,5	0	$\delta_{ip}py_p$ (W.No. 19a, py_p 180° p.s.) + w. $\delta_{ip}py_c$ (W.No. 19b)
187	1431,7	0,1	$\delta_{ip}py_p$ (W.No. 19a, py_p 180° p.s.) + w. $\delta_{ip}py_c$ (W.No. 19b)

continued on next page

Vibrational assignment of the DFT-calculated RS of $[\text{Zn}(\text{L4})_2]^{2+}$

Mode	$\tilde{\nu}$ [cm ⁻¹]	RA [$\frac{4}{\text{amu}}$]	Assignment
188	1449	62,4	$\nu_{\text{sym}}\text{CNC}(\text{py}_c) + \delta_{ip}(\text{W.No. 19a, tpy} + \text{ph}) + \text{lig. movem. } 180^\circ \text{ p.s.}$
189	1450,1	1287,9	$\nu_{\text{sym}}\text{CNC}(\text{py}_c) + \delta_{ip}(\text{W.No. 19a, tpy} + \text{ph}) + \text{lig. movem. i.p.}$
190	1461,3	75,6	$\delta_{ip}\text{py}_p(\text{W.No. 19b, py}_p \text{ i.p.}) + \text{lig. movem. } 180^\circ \text{ p.s.}$
191	1462,1	2401,3	$\delta_{ip}\text{py}_p(\text{W.No. 19b, py}_p \text{ i.p.}) + \text{lig. movem. i.p.}$
192	1471,9	515,3	$\delta_{ip}\text{tpy}(\text{W.No. 19b}) + \nu_{\text{a}_{\text{sym}}}(\text{C3C7C12, C10C9C15})$
193	1472,1	519,1	$\delta_{ip}\text{tpy}(\text{W.No. 19b}) + \nu_{\text{a}_{\text{sym}}}(\text{C29C28C33, C31C32C39})$
194	1494,9	102,6	$\delta_{ip}\text{ph}(\text{W.No. 19a, } \nu\text{C45C30})$
195	1495,1	175,5	$\delta_{ip}\text{ph}(\text{W.No. 19a, } \nu\text{C20C11})$
196	1511	497,2	$\delta_{ip}(\text{W.No.8b, py}_c + \text{ph i.p.})$
197	1511,4	507,3	$\delta_{ip}(\text{W.No.8b, py}_c + \text{ph i.p.})$
198	1535,2	102,3	$\delta_{ip}(\text{W.No.8b, py}_c + \text{ph } 180^\circ \text{ p.s.})$
199	1535,4	100,5	$\delta_{ip}(\text{W.No.8b, py}_c + \text{ph } 180^\circ \text{ p.s.})$
200	1567,4	480,2	$\delta_{ip}(\text{W.No.8b, py}_p\text{N34} + \text{w. on py}_p\text{N4/N14})$
201	1567,5	483,2	$\delta_{ip}(\text{W.No.8b, py}_p\text{N40} + \text{w. on py}_p\text{N4/N14})$
202	1567,7	82,3	$\delta_{ip}(\text{W.No.8b, py}_p\text{N4} + \text{py}_p\text{N14 } 180^\circ \text{ p.s.} + \text{w. py}_p\text{N40/N34}) + \text{w. on } \delta_{ip}\text{py}_c\text{N8}$
203	1567,9	51,9	$\delta_{ip}(\text{W.No.8b, py}_p\text{N4} + \text{py}_p\text{N14 i.p.} + \text{w. py}_p\text{N40/N34}) + \delta_{ip}\text{py}_c\text{N8}(\text{W.No.8a})$
204	1575,1	992,9	$\delta_{ip}(\text{W.No.8a, py}_c\text{N8} + \text{phC20 i.p.} + \text{w. py}_c\text{N27} + \text{phC45}) + \text{w. } \delta_{ip}\text{py}_p(\text{W.No.8b})$
205	1576	4450	$\delta_{ip}(\text{W.No.8a, py}_c\text{N27} + \text{phC45 i.p.} + \text{w. py}_c\text{N8} + \text{phC20}) + \text{w. } \delta_{ip}\text{py}_p(\text{W.No.8b})$
206	1588,5	245,9	$\delta_{ip}(\text{W.No.8a, py}_p\text{N34/N40 } 180^\circ \text{ p.s.})$
207	1588,6	252,1	$\delta_{ip}(\text{W.No.8a, py}_p\text{N4/N14 } 180^\circ \text{ p.s.})$
208	1590,7	68,6	$\delta_{ip}(\text{W.No.8a, py}_p\text{N4/N14 i.p.} + \text{ph}) + \text{lig. movem. } 180^\circ \text{ p.s.}$
209	1591,6	5182,3	$\delta_{ip}(\text{W.No.8a, py}_p\text{N4/N14 i.p.} + \text{ph}) + \text{lig. movem. i.p.}$
210	1603,3	731,2	$\delta_{ip}(\text{W.No.8a, py}_c\text{N8} + \text{phC20 } 180^\circ \text{ p.s.})$
211	1604,2	1837,1	$\delta_{ip}(\text{W.No.8a, py}_c\text{N27} + \text{phC45 } 180^\circ \text{ p.s.})$
212	2143,2	8670,8	νC81C82
213	2143,6	15316	νC26C70
214	3103,5	62,6	$\nu\text{py}(\text{C19H56} + \text{w. on C18H57, C5H69})$
215	3103,8	182,3	$\nu\text{py}(\text{C5H69} + \text{w. on C6H68, C19H56})$
216	3104,2	104,2	$\nu\text{py}(\text{C35H48} + \text{w. on C36H49, C41H54})$
217	3105,7	123,2	$\nu\text{py}(\text{C41H54} + \text{w. on C42H55, C35H48})$
218	3106,3	51,9	$\nu\text{ph}(\text{C72H77} + \text{w. on C73H78, C76H80})$
219	3107,4	59,5	$\nu\text{ph}(\text{C76H80} + \text{w. on C72H77, C75H79})$
220	3107,5	56,4	$\nu\text{ph}(\text{C21H60} + \text{w. on C22H61, C25H62})$
221	3109,4	58,8	$\nu\text{ph}(\text{C25H62} + \text{w. on C24H63, C21H60})$
222	3125,4	88,9	$\nu\text{py}(\text{C17H58 } 180^\circ \text{ p.s. to C18H57, C16H59})$
223	3125,8	61,3	$\nu\text{py}(\text{C37H46, C42H55, C44H53 } 180^\circ \text{ p.s. to C36H49, C38H50, C43H47})$
224	3125,8	122,2	$\nu\text{py}(\text{C37H46, C43H47 } 180^\circ \text{ p.s. to C36H49, C38H50, C42H55, C44H53})$
225	3125,9	115,1	$\nu\text{py}(\text{C1H67 } 180^\circ \text{ p.s. to C2H66, C6H68, C5H69})$
226	3134,4	99	$\nu\text{ph}(\text{C75H79, C76H80 } 180^\circ \text{ p.s. to C73H78})$
227	3135,8	140	$\nu\text{ph}(\text{C75H79} + \text{w. on C76H80, C73H78, C72H77 all i.p.})$
228	3135,9	91,2	$\nu\text{ph}(\text{C22H61, C21H60 } 180^\circ \text{ p.s. to C24H63, C25H62})$
229	3136,8	156,8	$\nu\text{ph}(\text{C22H61} + \text{w. on C21H60, C24H63, C25H62 all i.p.})$
230	3138,6	47,7	$\nu\text{py}(\text{C18H57, C10H64 } 180^\circ \text{ p.s. to C17H58, C16H59})$
231	3138,9	44,8	$\nu\text{py}(\text{C6H68, C12H65 } 180^\circ \text{ p.s. to C1H67C2H66})$
232	3139,9	48,5	$\nu\text{py}(\text{C42H55, C31H51 } 180^\circ \text{ p.s. to C44H53, C43H47})$
233	3140,2	85,4	$\nu\text{py}(\text{C36H49, C29H52 } 180^\circ \text{ p.s. to C38H50})$
234	3143,8	202,6	$\nu\text{py}(\text{CH on py}_p\text{N14 } 180^\circ \text{ p.s. to C10H64 on py}_c\text{N8})$
235	3144	135,5	$\nu\text{py}(\text{CH on py}_p\text{N34 } 180^\circ \text{ p.s. to C29H52 on py}_c\text{N27})$
236	3144,2	222,4	$\nu\text{py}(\text{CH on py}_p\text{N4 } 180^\circ \text{ p.s. to C12H65 on py}_c\text{N8})$
237	3144,4	234,9	$\nu\text{py}(\text{CH on py}_p\text{N40 } 180^\circ \text{ p.s. to C31H51 on py}_c\text{N27})$
238	3150,5	69,9	$\nu\text{py}(\text{C10H64, C16H59 i.p.})$

continued on next page

Vibrational assignment of the DFT-calculated RS of $[\text{Zn}(\text{L4})_2]^{2+}$			
Mode	$\tilde{\nu}$ [cm^{-1}]	RA [$\frac{4}{\text{amu}}$]	Assignment
239	3150,6	134,5	$\nu_{\text{py}}(\text{C12H65}, \text{C2H66} \text{ i.p.})$
240	3151,4	129,7	$\nu_{\text{py}}(\text{C29H52}, \text{C38H50} \text{ i.p.})$
241	3152,1	139,3	$\nu_{\text{py}}(\text{C31H51}, \text{C44H53} \text{ i.p.})$
242	3385,7	1,4	$\nu_{\text{CH}} (\text{C70H71}, \text{C82H83} \text{ } 180^\circ \text{ p.s.})$
243	3386,2	5,7	$\nu_{\text{CH}} (\text{C70H71}, \text{C82H83} \text{ i.p.})$

Numbering of atoms is according to figure ??.

A.2 Raman spectra of $[(\text{tbut-bpy})_2\text{Ru}(\text{tpphz})\text{PdCl}_2]^{2+}$, $[(\text{tbut-bpy})_2\text{Ru}(\text{tpphz})]^{2+}$ and $[(\text{tbut-bpy})_2\text{Ru}(\text{dppz})(\text{Br})_2]^{2+}$

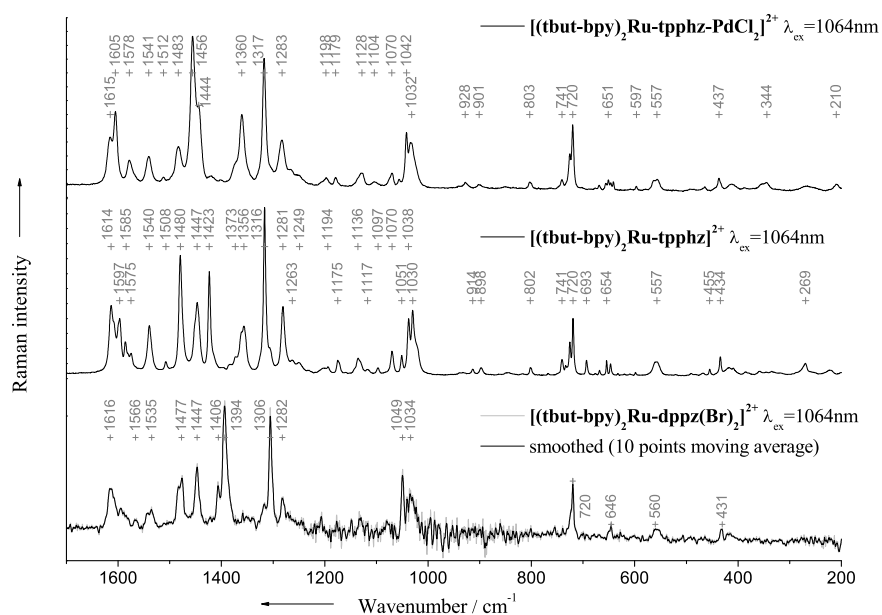


Figure A.1: Comparison of the Raman spectra of $[\text{RuPd}]^{2+}$, $[(\text{tbut-bpy})_2\text{Ru}(\text{tpphz})]^{2+}$ and $[(\text{tbut-bpy})_2\text{Ru}(\text{dppz})(\text{Br})_2]^{2+}$ detected in the solid state.

The non-resonant Raman spectra were recorded with a Bruker FT Raman spectrometer (RFS 100/S) and excited at 1064 nm by means of a Nd:YAG laser. A liquid nitrogen cooled Ge-detector was used to collect the Raman scattered light. The resolution of the Raman spectra is about 0.24 cm^{-1} .

Bibliography

- [1] Hohenberg, P.; Kohn, W. *Physical Reviews B: Solid State* **1964**, *136*, 864.
- [2] Luger, P. *Organic and Biomolecular Chemistry* **2007**, *5*, 2529–2540.
- [3] Henn, J.; Leusser, D.; Stalke, D. *Journal of Computational Chemistry* **2007**, *28*(14), 2317–2324.
- [4] Henn, J.; Ilge, D.; Leusser, D.; Stalke, D.; Engels, B. *Journal of Physical Chemistry A* **2004**, *108*, 9442–9452.
- [5] Messerschmidt, M.; Scheins, S.; Grubert, L.; Pätzelt, M.; Szeimies, G.; Paulmann, C.; Luger, P. *Angewandte Chemie, International Edition* **2005**, *44*, 3925–3928.
- [6] Eickerling, G.; Mastalerz, R.; Herz, V.; Scherer, W.; Himmel, H.-J.; Reiher, M. *Journal of Chemical Theory and Computation* **2007**, *3*, 2182–2197.
- [7] Hebben, N.; Himmel, H.-J.; Eickerling, G.; Herrmann, C.; Reiher, M.; Herz, V.; Presnitz, M.; Scherer, W. *Chemistry - A European Journal* **2007**, *13*, 10078–10087.
- [8] Grabowsky, S.; Pfeuffer, T.; Checinska, L.; Weber, M.; Morgenroth, W.; Luger, P.; Schirmeister, T. *European Journal of Organic Chemistry* **2007**, pages 2759–2768.
- [9] Flaig, R.; Koritsanszky, T.; Soyka, R.; Häming, L.; Luger, P. *Angewandte Chemie-International Edition* **2001**, *40*(2), 355–359.
- [10] Hibbs, D. E.; Austin-Woods, C. J.; Platts, J. A.; Overgaard, J.; Turner, P. *Chemistry-A European Journal* **2003**, *9*(5), 1075–1083.
- [11] Jelsch, C.; Pichon-Pesme, V.; Lecomte, C.; Aubry, A. *Acta crystallographica. Section D, Biological crystallography* **1998**, *D54*, 1306–1318.
- [12] Housset, D.; Benabicha, F.; Pichon-Pesme, V.; Jelsch, C.; Maierhofer, A.; David, S.; Fontecilla-Camps, J. C.; Lecomte, C. *Acta crystallographica. Section D, Biological crystallography* **2000**, *D56*, 151–160.

- [13] Dittrich, B.; Koritsanszky, T.; Luger, P. *Angewandte Chemie-International Edition* **2004**, *43*, 2718–2721.
- [14] Pichon-Pesme, V.; Jelsch, C.; Guillot, B.; Lecomte, C. *Acta crystallographica. Section A, Foundations of Crystallography* **2004**, *A60*, 204–208.
- [15] Volkov, A.; Li, X.; Koritsanszky, T.; Coppens, P. *Journal of Physical Chemistry A* **2004**, *108*, 4283–4300.
- [16] Pichon-Pesme, V.; Lecomte, C.; Lachekar, H. *Journal Of Physical Chemistry* **1995**, *99*(16), 6242–6250.
- [17] Matta, C. F.; Bader, R. F. *PROTEINS: Structure, Function, and Genetics* **2000**, *40*, 310–329.
- [18] Matta, C. F.; Bader, R. F. *PROTEINS: Structure, Function, and Genetics* **2002**, *40*, 310–329.
- [19] Matta, C. F.; Bader, R. F. *PROTEINS: Structure, Function, and Genetics* **2003**, *52*, 360–399.
- [20] Mebs, S.; Messerschmidt, M.; Luger, P. *Zeitschrift für Kristallographie* **2006**, *221*, 656–664.
- [21] Gatti, C.; Bianchi, R.; Destro, R.; Merati, F. *Theochem* **1992**, *87*, 409–33.
- [22] Volkov, A.; Abramov, Y.; Coppens, P.; Gatti, C. *Acta Crystallographica, Section A: Foundations of Crystallography* **2000**, *A56*(4), 332–339.
- [23] Hammett, L. P. *Physical Organic Chemistry* **1940**, *59*, 96–103.
- [24] Jaffe, H. H. *Chemical Reviews* **1953**, *53*(191), 191–261.
- [25] Suschtschinskij, M. M. *Ramanspektren von Molekülen und Kristallen*; Heyden and Son GmbH, Rheine, 1974.
- [26] Hansch, C.; Leo, A.; Taft, R. W. *Chemical Reviews* **1991**, *91*, 165–195.
- [27] Roth, S. *One-Dimensional Metals*; VCH: Weinheim, 1995.
- [28] Katz, H. E.; Lovinger, A. J.; Johnson, J.; Kloc, C.; Siegrist, T.; Li, W.; Lin, Y.-Y.; Dodabalapur, A. *Nature* **2000**, *404*, 478 – 481.
- [29] Mecher, E.; Gallego-Gomez, F.; Tillmann, H.; Hörhold, H.-H.; Hummelen, J. C.; Meerholz, K. *Nature* **2002**, *418*, 959.

- [30] Prins, M. W. J.; Welters, W. J. J.; Weekamp, J. W. *Science* **2001**, *291*, 277.
- [31] Hayes, R. A.; Feenstra, B. J. *Nature* **2003**, *425*, 383.
- [32] Müllen, K.; Scherf, U. *Organic Light Emitting Devices*; Wiley-VCH: Weinheim, 2006.
- [33] Yersin, H. *Highly Efficient OLEDs with Phosphorescent Materials*; Wiley-VCH: Weinheim, 2008.
- [34] Chiu, C.-W.; Chow, T. J.; Chuen, C.-H.; Lin, H.-M.; Tao, Y.-T. *Chemistry of Materials* **2003**, *15*, 4527–4532.
- [35] Zaumseil, J.; Sirringhaus, H. *Chemical Reviews* **2007**, *107*, 1296–1323.
- [36] Stutzmann, N.; Friend, R. H.; Sirringhaus, H. *Science* **2003**, *299*, 1881–1884.
- [37] Gamota, D. R.; Brazis, P.; Kalyanasundaram, K.; Zhang, J. *Printed Organic and Molecular Electronics*; Kluwer Academic Publishers: New York, 2004.
- [38] Xu, M. J. *Synthetic Metals* **2000**, *115*, 1.
- [39] Singh, T.; Sariciftci, N. S. *Annual Review of Materials Research* **2006**, *36*, 199.
- [40] Sirringhaus, H.; Kawase, T.; Friend, R. H.; Shimoda, T.; Inbasekaran, M.; Wu, W.; Woo, E. P. *Science* **2000**, *290*, 2123–2126.
- [41] Bao, Z. *Advanced Materials* **2000**, *12*(3), 227–230.
- [42] Crone, B.; Dodabalapur, A.; Lin, Y.-Y.; Filas, R. W.; Bao, Z.; LaDuca, A.; Sarpeshkar, R.; Katz, H. E.; Li, W. *Nature* **2000**, *403*, 521–523.
- [43] Hoppe, H.; Sariciftci, N. S. *Polymer Solar Cells*, Vol. 214 of *Advances in Polymer Science*; Springer: Heidelberg, Berlin, 2008.
- [44] Brabec, C. J.; Sariciftci, N. S.; Hummelen, J. C. *Advanced Functional Materials* **2001**, *11*, 15–26.
- [45] Rogers, J.; Bao, Z. *Journal of Polymer Science A* **2002**, *40*, 3327.
- [46] Friend, R. H.; Gymer, R. W.; Holmes, A. B.; Burroughes, J. H.; Marks, R. N.; Taliani, C.; Bradley, D. D. C.; Dos Santos, D. A.; Bredas, J. L.; Lögdlund, M.; Salaneck, W. R. *Nature* **1999**, *397*, 121–128.

- [47] Huebler, A.; Doetz, F.; Kempa, H.; Katz, H.; Bartzsch, M.; Brandt, N.; Hennig, I.; Fuegmann, U.; Vaidyanathan, S.; Granstrom, J.; Liu, S.; Sydorenko, A.; Zillger, T.; Schmidt, G.; Preissler, K.; Reichmanis, E.; Eckerle, P.; Richter, F.; Fischer, T.; Hahn, U. *Organic Electronics* **2007**, *8*, 480–486.
- [48] Gates, B. D.; Xu, Q.; Stewart, M.; Ryan, D.; Willson, C. G.; Whitesides, G. M. *Chemical Reviews* **2005**, *105*, 1171–1196.
- [49] Sirringhaus, H.; Tessler, N.; Friend, R. H. *Science* **1998**, *280*, 1741.
- [50] Chiang, C. K.; Fincher, C. R., J.; Park, Y. W.; Heeger, A. J.; Shirakawa, H.; Louis, E. J.; Gau, S. C.; MacDiarmid, A. G. *Physical Review Letters* **1977**, *39*(17), 1098.
- [51] Chiang, C. K.; Druy, M. A.; Gau, S. C.; Heeger, A. J.; Louis, E. J.; MacDiarmid, A. G.; Park, Y. W.; Shirakawa, H. *Journal of the American Chemical Society* **1978**, *100*, 1013.
- [52] Shirakawa, H.; Louis, E. J.; MacDiarmid, A. G.; Chiang, C. K.; Heeger, A. J. *Journal of the Chemical Society, Chemical Communications* **1977**, page 579.
- [53] Winter, A.; Friebe, C.; Chiper, M.; Schubert, U. S.; Presselt, M.; Dietzek, B.; Schmitt, M.; Popp, J. *ChemPhysChem* **2009**, *10*, 787–798.
- [54] Beenken, W. J. D.; Lischka, H. *The Journal of Chemical Physics* **2005**, *123*(14), 144311/1–144311/9.
- [55] Westenhoff, S.; Beenken, W. J. D.; Friend, R. H.; Greenham, N. C.; Yartsev, A.; Sundström, V. *Physical Review Letters* **2006**, *97*(16), 166804/1–166804/4.
- [56] Westenhoff, S.; Beenken, W. J. D.; Yartsev, A.; Greenham, N. C. *Journal of Chemical Physics* **2006**, *125*(15), 154903/1–154903/7.
- [57] Winter, A.; Hummel, J.; Risch, N. *Journal of Organic Chemistry* **2006**, *71*, 4862–4871.
- [58] Medlycott, E. A.; Hanan, G. S. *Chemical Society Reviews* **2005**, *34*, 133–142.
- [59] Flamigni, L.; Barigelletti, F.; Armaroli, N.; Collin, J.-P.; Dixon, I. M.; Sauvage, J.-P.; Williams, G. J. *Coordination Chemistry Reviews* **1999**, *190-192*, 671–682.
- [60] Balzani, V.; Juris, A.; Venturi, M.; Campagna, S.; Serroni, S. *Chemical Reviews* **1996**, *96*, 759–833.
- [61] Andres, P. R.; Schubert, U. S. *Advanced Materials* **2004**, *16*(13), 1043–1068.

- [62] Watson, M. D.; Fechtenkötter, A.; Müllen, K. *Chemical Reviews* **2001**, *101*, 1267–1300.
- [63] Bader, R. F. W. *Atoms in Molecules: A Quantum Theory*; Oxford University Press: New York, 1990.
- [64] Schäfer, B.; Görls, H.; Presselt, M.; Schmitt, M.; Popp, J.; Henry, W.; Vos, J. G.; Rau, S. *Dalton Transactions* **2006**, *18*(2225-2231).
- [65] Rau, S.; Schäfer, B.; Schebesta, S.; Grüssing, A.; Poppitz, W.; Walther, D.; Duati, M.; Browne, W. R.; Vos, J. G. *European Journal Of Inorganic Chemistry* **2003**, (8), 1503–1506.
- [66] Rau, S.; Walther, D.; Vos, J. G. *Dalton Transactions* **2007**, (9), 915–919.
- [67] Schwalbe, M.; Schäfer, B.; Görls, H.; Rau, S.; Tschierlei, S.; Schmitt, M.; Popp, J.; Vaughan, G.; Henry, W.; Vos, J. G. *European Journal Of Inorganic Chemistry* **2008**, (21), 3310–3319.
- [68] Dietzek, B.; Kiefer, W.; Blumhoff, J.; Böttcher, L.; Rau, S.; Walther, D.; Schmitt, M.; Popp, J. *Chemistry - A European Journal* **2006**, *12*(19), 5105–5115.
- [69] Dietzek, B.; Akimov, D.; Kiefer, W.; Rau, S.; Popp, J.; Schmitt, M. *Laser Physics Letters* **2007**, *4*(2), 121–125.
- [70] Juris, A.; Balzani, V.; Barigelletti, F.; Campagna, S.; Belser, P.; von Zelewsky, A. *Coordination Chemistry Reviews* **1988**, *84*, 85–277.
- [71] Sauvage, J.-P.; Collin, J.-P.; Chambron, J.-C.; Guillerez, S.; Coudret, C.; Balzani, V.; Barigelletti, F.; De Cola, L.; Flamigni, L. *Chemical Reviews* **1994**, *94*, 993–1019.
- [72] Constable, E. C.; Housecroft, C. E.; Schofield, E. R.; Encinas, S.; Armaroli, N.; Barigelletti, F.; Flamigni, L.; Figgemeier, E.; Vos, J. G. *Chemical Communications* **1999**, (10), 869–870.
- [73] Harriman, A.; Mayeux, A.; De Nicola, A.; Ziessel, R. *Physical Chemistry Chemical Physics* **2002**, *4*(11), 2229–2235.
- [74] Hjelm, J.; Constable, E. C.; Figgemeier, E.; Hagfeldt, A.; Handel, R.; Housecroft, C. E.; Mukhtar, E.; Schofield, E. *Chemical Communications* **2002**, (3), 284–285.
- [75] Laine, P.; Bedioui, F.; Amouyal, E.; Albin, V.; Berruyer-Penaud, F. *Chemistry-A European Journal* **2002**, *8*(14), 3162–3176.

- [76] Maestri, M.; Armaroli, N.; Balzani, V.; Constable, E. C.; Thompson, A. *Inorganic Chemistry* **1995**, *34*(10), 2759–2767.
- [77] Hecker, C. R.; Gushurst, A. K. I.; McMillin, D. R. *Inorganic Chemistry* **1991**, *30*(3), 538–541.
- [78] Herrmann, C.; Neugebauer, J.; Presselt, M.; Uhlemann, U.; Schmitt, M.; Rau, S.; Popp, J.; Reiher, M. *Journal of Physical Chemistry B* **2007**, *111*(21), 6078–6087.
- [79] Szeghalmi, A. V.; Erdmann, M.; Engel, V.; Schmitt, M.; Amthor, S.; Kriegisch, V.; Nöll, G.; Stahl, R.; Lambert, C.; Leusser, D.; Stalke, D.; Zabel, M.; Popp, J. *Journal of the American Chemical Society* **2004**, *126*, 7834–7845.
- [80] Schrader, B. *Infrared and Raman Spectroscopy*; VCH, 1995.
- [81] Rau, S.; Schäfer, B.; Gleich, D.; Anders, E.; Rudolph, M.; Friedrich, M.; Görls, H.; Henry, W.; Vos, J. G. *Angewandte Chemie, International Edition* **2006**, *45*(37), 6215–6218.
- [82] Pauling, L. *Journal Of Chemical Education* **1988**, *65*(4), 375–375.
- [83] Foundation, T. N. http://nobelprize.org/nobel_prizes/chemistry/laureates/.
- [84] Mulliken, R. S. *Journal of Chemical Physics* **1934**, *2*, 782.
- [85] Allred, A. L.; Rochow, E. G. *Journal of Inorganic Nuclear Chemistry* **1958**, *5*, 264–268.
- [86] Allred, A. L. *Journal of Inorganic Nuclear Chemistry* **1961**, *17*, 215–221.
- [87] Mulliken, R. S. *The Journal of Chemical Physics* **1955**, *23*(12), 2343–2346.
- [88] Mulliken, R. S. *The Journal of Chemical Physics* **1955**, *23*(12), 2338–2342.
- [89] Mulliken, R. S. *The Journal of Chemical Physics* **1955**, *23*(10), 1841–1846.
- [90] Mulliken, R. S. *The Journal of Chemical Physics* **1955**, *23*(10), 1833–1840.
- [91] Meister, J.; Schwarz, W. H. E. *Journal of Physical Chemistry* **1994**, *98*, 8245–8252.
- [92] Reiher, M.; Brehm, G.; Schneider, S. *Journal of Physical Chemistry A* **2004**, *108*, 734–742.
- [93] Szabo, A.; Ostlund, N. S. *Modern Quantum Chemistry: Introduction to Advanced Electronic Structure Theory*; Dover Publications, Inc.: Mineola, 1996.

- [94] Neugebauer, J.; Reiher, M.; Kind, C.; Hess, B. A. *Journal of Computational Chemistry* **2002**, *23*, 895–910.
- [95] Foster, J. P.; Weinhold, F. *Journal of the American Chemical Society* **1980**, *102*, 7211–7218.
- [96] Reed, A. E.; Curtiss, L. A.; Weinhold, F. *Chemical Reviews* **1988**, *88*, 899–926.
- [97] Reed, A. E.; Weinhold, F. *Journal of Chemical Physics* **1983**, *78*(6), 4066–4073.
- [98] Reed, A. E.; Weinhold, F. *Journal of Chemical Physics* **1985**, *83*, 1736.
- [99] Reed, A. E.; Weinstock, R. B.; Weinhold, F. *Journal of Chemical Physics* **1985**, *83*(2), 735–746.
- [100] Weinhold, F. *Natural Bond Orbital Methods*, Vol. 3 of *Encyclopedia of Computational Chemistry*; John Wiley and Sons: Chichester, UK, 1998.
- [101] Bader, R. F. W.; Chang, C. *Journal of Physical Chemistry* **1989**, *93*, 2946–2956.
- [102] Bader, R. F. W.; MacDougall, P. J. *Journal of the American Chemical Society* **1985**, *107*, 6788–6795.
- [103] Hernandez-Trujillo, J.; Bader, R. F. W. *Journal of Physical Chemistry A* **2000**, *104*, 1779–1794.
- [104] Messerschmidt, M.; Wagner, A.; Wong, M. W.; Luger, P. *Journal of the American Chemical Society* **2002**, *124*(5), 732–733.
- [105] Herrmann, C.; Reiher, M.; Hess, B. A. *Journal of Chemical Physics* **2005**, *122*.
- [106] Gomes, T. C. F.; Viãsozo da Silva Jr., J. A.; Vidal, L. N.; Vazquez, P. A. M.; Bruns, R. E. *Theoretical Chemistry Accounts* **2008**.
- [107] Reinhold, J. *Quantentheorie der Moleküle - Eine Einführung*, Vol. 2. Auflage; B. G. Teubner: Stuttgart, Leipzig, Wiesbaden, 2004.
- [108] Scherz, U. *Quantenmechanik - Eine kompakte Einführung*, Vol. 1. Auflage; B. G. Teubner: Stuttgart, Leipzig, Wiesbaden, 2005.
- [109] Parr, R. G.; Yang, W. *Density Functional Theory of Atoms and Molecules*, Vol. 16 of *International Series of Monographs on Chemistry*; Oxford University Press: Oxford, New York, 1989.
- [110] Henn, J. *The electron density: A bridge between exact quantum mechanics and fuzzy chemical concepts* Dissertation, Julius-Maximilians-Universität, **2004**.

- [111] Putrino, A. *Ab-initio Raman spectra of anharmonic and disordered systems* Dissertation, Universität Stuttgart, **2000**.
- [112] Szeghalmi, A. V. *The Ground and Excited State Molecular Structure of Model Systems Undergoing Photochemical Processes and the Characterization of Active Agents by means of Vibrational Spectroscopy and Theoretical Calculations* Dissertation, Iulius-Maximilians-Universität, **2004**.
- [113] Jahn, B. *Allene und Heteroallene als Substrate biomimetischer Additionsreaktionen durch Zink-Komplexe* Dissertation, Friedrich-Schiller-Universität Jena, **2009**.
- [114] Eger, W. *Aktivierung von Heterokumulenen in Theorie und Experiment: Sind Isothiocyanate geeignete Substrate für Carboanhydrase-Modelle?* Dissertation, Friedrich-Schiller-Universität Jena, **2008**.
- [115] Stephens, P. J.; Devlin, F. J.; Chabalowski, C. F.; Frisch, M. J. *Journal of Physical Chemistry* **1994**, *98*, 11623–11627.
- [116] Szilagyai, R.; Frenking, G. *Organometallics* **1997**, *16*, 4807–4815.
- [117] Sousa, S.; Fernandes, P.; Ramos, M. *Journal of Physical Chemistry A* **2007**, *111*, 10439–10452.
- [118] Alcamí, M.; Mo, O.; Yanez, M.; Cooper, I. L. *Journal of Chemical Physics* **2000**, *112*, 6131–6140.
- [119] Zhao, Y.; Truhlar, D. G. *Accounts of Chemical Research* **2008**, *41*, 157–167.
- [120] Lee, C.; Yang, W.; Parr, R. G. *Physical Reviews B* **1988**, *37*, 785–789.
- [121] Becke, A. D. *Physical Review A* **1988**, *38*, 3098–3100.
- [122] Becke, A. D. *Journal of Chemical Physics* **1993**, *98*, 5648–5652.
- [123] *TURBOMOLE - Program Package for ab initio Electronic Structure Calculations: USER'S MANUAL*, Vol. Version 5; 2004.
- [124] Perdew, J. P. *Physical Review B* **1986**, *33*, 8822–8824.
- [125] Furche, F.; Perdew, J. P. *Journal of Chemical Physics* **2006**, *124*, 44103.
- [126] Ahlrichs, R.; Furche, F.; Grimme, S. *Chemical Physics Letters* **2000**, *325*(1-3), 317–321.
- [127] Rappe, A. K.; Casewit, C. J.; Colwell, K. S.; Goddard III, W. A.; Skiff, W. M. *Journal of the American Chemical Society* **1992**, *114*, 10024.

-
- [128] von Arnim, M.; Ahlrichs, R. *The Journal of Chemical Physics* **1999**, *111*, 9183–9190.
- [129] Pulay, P.; Fogarasi, G.; Pang, F.; Boggs, J. E. *Journal of the American Chemical Society* **1979**, *101*, 2550.
- [130] Roothaan, C. C. J. *Reviews in Modern Physics* **1960**, *32*, 179.
- [131] Sierka, M.; Hogekamp, A.; Ahlrichs, R. *Journal of Chemical Physics* **2003**, *118*, 9136–9148.
- [132] Dunlap, B. I.; Connolly, J. W. D.; Sabin, J. R. *Journal Of Chemical Physics* **1979**, *71*(8), 3396–3402.
- [133] Dunlap, B. I.; Connolly, J. W. D.; Sabin, J. R. *Journal Of Chemical Physics* **1979**, *71*(12), 4993–4999.
- [134] Baerends, E. J.; Ellis, D. E.; Ros, P. *Chemical Physics* **1973**, *2*(1), 41–51.
- [135] Baerends, E. J.; Ros, P. *Chemical Physics* **1973**, *2*(1), 52–59.
- [136] Møller, C.; Plesset, M. S. *Physical Review* **1934**, *46*, 618.
- [137] Clark, T.; Chandrasekhar, J.; Spitznagel, G. W.; Schleyer, P. v. R. *Journal of Computational Chemistry* **1983**, *4*, 294.
- [138] Krishnan, R.; Binkley, J. S.; Seeger, R.; Pople, J. A. *Journal of Chemical Physics* **1980**, *72*, 650.
- [139] McLean, A. D.; Chandler, G. S. *Journal of Chemical Physics* **1980**, *72*, 5639.
- [140] Binning Jr., R. C.; Curtiss, L. A. *Journal of Computational Chemistry* **1990**, *11*, 1206.
- [141] Curtiss, L. A.; McGrath, M. P.; Blaudeau, J.-P.; Davis, N. E.; Binning Jr., R. C.; Radom, L. *Journal of Chemical Physics* **1995**, *103*, 6104.
- [142] McGrath, M. P.; Radom, L. *Journal of Chemical Physics* **1991**, *94*, 511.
- [143] *Gaussian 98 Users Referenz Second Edition*; 1999.
- [144] Schäfer, A.; Horn, H.; Ahlrichs, R. *Journal of Chemical Physics* **1992**, *97*(4), 2571–2577.
- [145] Schäfer, A.; Huber, C.; Ahlrichs, R. *Journal of Chemical Physics* **1994**, *100*(8), 5829–5835.

- [146] Ahlrichs, R.; Bär, M.; Häser, M.; Horn, H.; Kölmel, C. *Chemical Physics Letters* **1989**, *162*, 165–169.
- [147] Gaussian03. Frisch, M. J.; Trucks, G. W.; Schlegel, H. B.; Scuseria, G. E.; Robb, M. A.; Cheeseman, J. R.; J. A. Montgomery, Jr., J. A.; Vreven, T.; Kudin, K. N.; Burant, J. C.; Millam, J. M.; Iyengar, S. S.; Tomasi, J.; Barone, V.; Mennucci, B.; Cossi, M.; Scalmani, G.; Rega, N.; Petersson, G. A.; Nakatsuji, H.; Hada, M.; Ehara, M.; Toyota, K.; Fukuda, R.; Hasegawa, J.; Ishida, M.; Nakajima, T.; Honda, Y.; Kitao, O.; Nakai, H.; Klene, M.; Li, X.; Knox, J. E.; Hratchian, H. P.; Cross, J. B.; Adamo, C.; Jaramillo, J.; Gomperts, R.; Stratmann, R. E.; Yazyev, O.; Austin, A. J.; Cammi, R.; Pomelli, C.; Ochterski, J. W.; Ayala, P. Y.; Morokuma, K.; Voth, G. A.; Salvador, P.; Dannenberg, J. J.; Zakrzewski, V. G.; Dapprich, S.; Daniels, A. D.; Strain, M. C.; Farkas, O.; Malick, D. K.; Rabuck, A. D.; Raghavachari, K.; Foresman, J. B.; Ortiz, J. V.; Cui, Q.; Baboul, A. G.; Clifford, S.; Cioslowski, J.; Stefanov, B. B.; Liu, G.; Liashenko, A.; Piskorz, P.; Komaromi, I.; Martin, R. L.; Fox, D. J.; Keith, T.; Al-Laham, M. A.; Peng, C. Y.; Nanayakkara, A.; Challacombe, M.; Gill, P. M. W.; Johnson, B.; Chen, W.; Wong, M. W.; Gonzalez, C.; Pople, J. A. **2004**.
- [148] Vibrational analysis in gaussian. Ochterski, J. **1999**.
- [149] Asher, S.; Asunskis, D. J.; Atkinson, G. H.; Bain, C. D.; Beattie, D. A.; Benner, R. E.; Bermejo, D.; Bertie, J. E.; Besemann, D.; Birch, J.; Brimmer, P. J.; Buffeteau, T.; Buijs, H.; Carrabba, M. M.; Chalmers, J. M.; Chase, B.; Chesters, M. A.; Choquette, S. J.; Clarke, F. J. J.; Condon, N.; Denton, M. B.; DeThomas, F. A.; DeVerse, R. A.; Duewer, D. L.; Dukor, R. K.; Eilert, A. J.; Everall, N. J.; Fateley, W. G.; Ford, M.; Freedman, T. B.; George, M. W.; Ghosh, A. K.; Griffiths, P. R.; Grills, D. C.; Guelachvili, G.; Hamaguchi, H.; Hammaker, R. M.; Hanssen, L. M.; Hashimoto, M.; Hipps, K. W.; Homes, C.; Hug, W.; Ikeda, R.; Iwata, T.; Iwata, K.; Jackson, R. S.; Kato, C.; Keresztury, G.; Koenig, J. L.; Kruezelecky, R. V.; Lomonosov, M. V.; Manning, C. J.; Mantz, A. W.; Masutani, K.; Mazur, U.; McClure, W. F.; McCreery, R. L.; McHale, J. L.; McNaughton, D.; Meyer, K.; Miller, C. E.; Miller, G. P.; Murdoch, K.; Nafie, L. A.; Osawa, M.; Owen, H.; Palmer, R. A.; Pan, M.-W.; Parker, S. F.; Pelletier, M. J.; Pzolet, M.; Picqu, N.; Polavarapu, P. L.; Pommier, C. J. S.; Ridder, T. D.; Rodger, C.; Rödig, C.; Rosenthal, T. C.; Schatz, G. C.; Sheppard, N.; Siebert, F.; Smith, L. M.; Smith, G. D.; Smith, W. E.; Springsteen, A. W.; Stanfield, D. L.; Stark, E. W.; Steele, D.; Sweat, J. A.; Theocharous, T.; Travis, J. C.; Turner, J. J.; Ujj, L.; Van Duyne, R. P.; Vidrine, D. W.; Wagner, D. R.; Walton, L. K.; Weber, A.; Wetzal, D. L.;

- Wilks, P. A.; others. *Theory and Instrumentation*, Vol. 1 of *Handbook of vibrational spectroscopy*; John Wiley and Sons Ltd, 2001.
- [150] Raman, C. V.; Krishnan, K. S. *Nature* **1928**, *121*, 501.
- [151] Landsberg, G. S. *Isd. AN SSSR* **1958**, pages 101–110.
- [152] Mandelstam, L. I. *Isd. AN SSSR* **1947**, *1*, 293, 305.
- [153] Lommel, E. *Pogg. Ann.* **1871**, *143*, 26.
- [154] Smekal, A. *Naturwissenschaften* **1923**, *11*, 873.
- [155] Schmitt, M.; Popp, J. *Journal Of Raman Spectroscopy* **2006**, *37*(1-3), 20–28.
- [156] Vol. 1-5 of *Handbook of vibrational spectroscopy*; John Wiley and Sons Ltd, 1996.
- [157] Harz, M.; Kiehntopf, M.; Stöckel, S.; Rösch, P.; Deufel, T.; Popp, J. *Analyst* **2008**, *133*(10), 1416–1423.
- [158] Krause, M.; Rösch, P.; Radt, B.; Popp, J. *Analytical Chemistry* **2008**, *80*(22), 8568–8575.
- [159] Petry, R.; Schmitt, M.; Popp, J. *Chemphyschem* **2003**, *4*(1), 14–30.
- [160] Rösch, P.; Schmitt, M.; Kiefer, W.; Popp, J. *Journal Of Molecular Structure* **2003**, *661*, 363–369.
- [161] Cialla, D.; Rösch, P.; Moller, R.; Popp, J. *Biophotonics 2007: Optics In Life Science* **2007**, *6633*, U6331–U6331.
- [162] Cinta-Pinzaru, S.; Peica, N.; Küstner, B.; Schlücker, S.; Schmitt, M.; Frosch, T.; Faber, J. H.; Bringmann, G.; Popp, J. *Journal Of Raman Spectroscopy* **2006**, *37*(1-3), 326–334.
- [163] Dörfer, T.; Schmitt, M.; Popp, J. *Journal Of Raman Spectroscopy* **2007**, *38*, 1379–1382.
- [164] Hering, K.; Cialla, D.; Ackermann, K.; Dörfer, T.; Moller, R.; Schneidewind, H.; Mattheis, R.; Fritzsche, W.; Rösch, P.; Popp, J. *Analytical And Bioanalytical Chemistry* **2008**, *390*(1), 113–124.
- [165] Schmuck, C.; Wich, P.; Küstner, B.; Kiefer, W.; Schlücker, S. *Angewandte Chemie-International Edition* **2007**, *46*(25), 4786–4789.

- [166] Frosch, T.; Schmitt, M.; Popp, J. *Journal Of Physical Chemistry B* **2007**, *111*(16), 4171–4177.
- [167] Harz, A.; Rösch, P.; Popp, J. *Cytometry Part A* **2009**, *75A*(2), 104–113.
- [168] Harz, M.; Claus, R. A.; Bockmeyer, C. L.; Baum, M.; Rösch, P.; Kentouche, K.; Deigner, H. P.; Popp, J. *Biopolymers* **2006**, *82*(4), 317–324.
- [169] Harz, M.; Krause, M.; Bartels, T.; Cramer, K.; Rösch, P.; Popp, J. *Analytical Chemistry* **2008**, *80*(4), 1080–1086.
- [170] Küstner, B.; Schmuck, C.; Wich, P.; Jehn, C.; Srivastava, S. K.; Schlücker, S. *Physical Chemistry Chemical Physics* **2007**, *9*(32), 4598–4603.
- [171] Szeghalmi, A. V.; Engel, V.; Zgierski, M. Z.; Popp, J.; Schmitt, M. *Journal Of Raman Spectroscopy* **2006**, *37*(1-3), 148–160.
- [172] Lecture: Chemistry 21b: The physical description of chemical systems: Spectroscopy / statistical thermodynamics. Blake, G. A.
- [173] Claus, R.; Merten, L.; Brandmüller, J. *Light Scattering by Phonon-Polaritons*; Springer-Verlag, 1975.
- [174] Poulet, H.; Mathieu, J. *vibration spectra and symmetry of crystals*; Gordon and Breach: New York, London, Paris, 1976.
- [175] Spiess, D. H. H. W. *Spektroskopie amorpher und kristalliner Festkörper*; Steinkopff Verlag, 1995.
- [176] Engelke, F. *Aufbau der Moleküle*; Teubner: Stuttgart, 1996.
- [177] Kagiya, T.; Sumida, Y.; Inoue, T. *Bulletin of the Chemical Society of Japan* **1968**, *41*(4), 767–73.
- [178] Emsley, J. W. *Journal of the Chemical Society [Section] A: Inorganic, Physical, Theoretical* **1968**, (8), 2018–22.
- [179] Tino, J.; Klimo, V. *Journal of Molecular Structure* **1977**, *39*(1), 139–44.
- [180] Dailey, B. P.; Gawer, A.; Neikam, W. C. *Discussions of the Faraday Society* **1962**, No. 34, 18–24.
- [181] Kanekar, C. R.; Govil, G.; Khetrupal, C. L. Vol. 65, page 353, 1967.
- [182] Brownlee, R. T. C.; Katritzky, A. R.; Topsom, R. D. *Journal of the American Chemical Society* **1965**, *87*, 3260.

- [183] Brownlee, R. T. C.; Katritzky, A. R.; Topsom, R. D. *Journal of the American Chemical Society* **1966**, *88*(7), 1413.
- [184] Brownlee, R. T. C.; Hutchinson, R. E. J.; Katritzky, A. R.; Tidwell, T. T.; Topsom, R. D. *Journal of the American Chemical Society* **1968**, *90*(7), 1757–1767.
- [185] Brownlee, R. T. C.; Katritzky, A. R.; Sinnott, M. V.; Szafran, M.; Yakhontov, L. N.; Topsom, R. D. *Tetrahedron Letters* **1968**, *9*(55), 5773–5776.
- [186] Schmid, E. D. *Spectrochimica Acta* **1966**, *22*, 1659–1675.
- [187] Schmid, E. D.; Hoffmann, V. *Spectrochimica Acta* **1966**, *22*, 1633–1643.
- [188] Schmid, E. D.; Hoffmann, V.; Joeckle, R.; Langenbucher, F. *Spectrochimica Acta* **1966**, *22*, 1615–1619.
- [189] Schmid, E. D.; Joeckle, R. *Spectrochimica Acta* **1966**, *22*, 1645–1658.
- [190] Schmid, E. D.; Langenbucher, F. *Spectrochimica Acta* **1966**, *22*, 1621–1632.
- [191] Taft, R. W. J. *Steric Effects in Organic Chemistry*; John Wiley and Sons: New York, 1956.
- [192] Palat, Karel, J.; Waisser, K.; Exner, O. *Journal of Physical Organic Chemistry* **2001**, *14*(10), 677–683.
- [193] Bobovich, J. S. *Optika i Spektroskopija* **1965**, *19*(279), 886.
- [194] Bobovich, J. S.; Beljajewskaja, N. M. *Optika i Spektroskopija* **1965**, *19*, 198.
- [195] Bobovich, J. S. *Optika i Spektroskopija* **1966**, *20*, 252.
- [196] Bobovich, J. S. *Optika i Spektroskopija* **1966**, *20*, 68.
- [197] Presselt, M. *Spektroskopische Untersuchungen von 5,5'-Di(Phenylethynyl)-2,2'-Bipyridyl unter Ausschluß von Aggregation durch Verwendung von Zeolith-L als Wirt* Diploma thesis, Friedrich-Schiller-Universität Jena, **2004**.
- [198] Hogue, R. *Fresenius' Journal of Analytical Chemistry* **1991**, *339*, 68–69.
- [199] Kühnert, M. *Raman-spektroskopische Charakterisierung der Struktureigenschaften von Protease-Inhibitoren und Übergangsmetall-Borylen-Komplexen im Festkörper und in Lösung* Diploma thesis, Friedrich-Schiller-Universität Jena, **2007**.

- [200] Uhlemann, U. *Aufklärung von StrukturEigenschaften und StrukturDynamikbeziehungen von Metallkomplexen und metallaktivierten Reaktionen durch schwingungsspektroskopische Methoden in Kombination mit quantenchemischen Rechnungen* Dissertation, Friedrich-Schiller-Universität Jena, **2008**.
- [201] Frosch, T.; Meyer, T.; Schmitt, M.; Popp, J. *Analytical Chemistry* **2007**, *79*, 6159–6166.
- [202] Schrader, B. *Raman/Infrared Atlas of Organic Compounds*; VCH Verlagsgesellschaft: Weinheim, 1989.
- [203] Bronstein, I.; Semendjajew, K.; Musiol, G.; Mühlig, H. *Taschenbuch der Mathematik*; Verlag Harri Deutsch: Thun und Frankfurt, 2001.
- [204] Schirmeister, T. *Liebigs Annalen / Recueil* **1997**, pages 1895–1899.
- [205] Mathematica. Wolfram-Research. **2005**.
- [206] Biegler-König.; Schönbohm.; Bayles. *Journal of Computational Chemistry* **2001**, *22*(5), 545–559.
- [207] Aim2000. Biegler-König, F.; Schönbohm, J. **2002**.
- [208] Rode, J. E.; Dobrowolski, J. C. *Chemical Physics Letters* **2007**, *449*, 240–245.
- [209] Lopez, C. S.; Faza, O. N.; Cossio, F. P.; York, D. M.; de Lera, A. R. *Chemistry* **2005**, *11*, 1734–1738.
- [210] Presselt, M.; Schnedermann, C.; Schmitt, M.; Popp, J. *Journal of Physical Chemistry A* **2009**, *113*(13), 3210–3222.
- [211] Klöckner, H. W.; Finsterholzl, H.; Srinivasan, K.; Schrötter, H. W. *Applied Spectroscopy* **1978**, *32*(4), 401–402.
- [212] London, F. *Journal de Physique et Le Radium* **1937**, *8*, 397.
- [213] McWeeny, R. *Physical Reviews* **1962**, *126*, 1028.
- [214] Ditchfield, R. *Molecular Physics* **1974**, *27*, 789.
- [215] Dodds, J. L.; McWeeny, R.; Sadlej, A. J. *Molecular Physics* **1980**, *41*, 1419.
- [216] Wolinski, K.; Hilton, J. F.; Pulay, P. *Journal of the American Chemical Society* **1990**, *112*, 8251.

- [217] Gutmann, T.; Schweitzer, A.; Wächtler, M.; Breitzke, H.; Buchholz, A.; Plass, W.; Buntkowsky, G. *Zeitschrift Für Physikalische Chemie* **2008**, *222*, 1389–1406.
- [218] Schweitzer, A.; Gutmann, T.; Wächtler, M.; Breitzke, H.; Buchholz, A.; Plass, W.; Buntkowsky, G. *Solid State Nuclear Magnetic Resonance* **2008**, *34*, 52–67.
- [219] Danzer, K.; Hobert, H.; Fischbacher, C.; Jagemann, K.-U. *Chemometrik - Grundlagen und Anwendungen*; Springer: Berlin, 2001.
- [220] Ivanovski, V.; Mayerhöfer, T.; Popp, J. *Vibrational Spectroscopy* **2008**, *47*, 91–98.
- [221] Presselt, M.; Dietzek, B.; Schmitt, M.; Winter, A.; Chipper, M.; Friebe, C.; Schubert, U. S.; Popp, J. *Journal of Physical Chemistry C* **2008**, *112*(47), 1865118660.
- [222] Presselt, M.; Dietzek, B.; Schmitt, M.; Winter, A.; Schubert, U. S.; Rau, S.; Popp, J. *in preparation* **2009**.
- [223] Lehn, J. M. *Supramolecular Chemistry, Concepts and Perspectives*; VCH: Weinheim, 1995.
- [224] Schubert, U. S.; Hofmeier, H.; Newkome, G. R. *Modern Terpyridine Chemistry*; Wiley-VCH: Weinheim, 2006.
- [225] Hofmeier, H.; Schubert, U. S. *Chemical Society Reviews* **2004**, *33*(6), 373–399.
- [226] Yu, S. C.; Kwok, C. C.; Chan, W. K.; Che, C. M. *Advanced Materials* **2003**, *15*(19), 1643–1647.
- [227] Chen, Y.-Y.; Tao, Y.-T.; Lin, H.-C. *Macromolecules* **2006**, *39*, 8559–8566.
- [228] Chou, P.-T.; Chi, Y. *Chemistry-A European Journal* **2007**, *13*, 380–395.
- [229] Wang, X.-Y.; Del Guerso, A.; Schmehl, R. H. *Chemical Communications* **2002**, pages 2344–2345.
- [230] Goodall, W.; Williams, G. J. A. *Chemical Communications* **2001**, pages 2514–2515.
- [231] Hwang, S.-H.; Moorefield, C. N.; Wang, P.; Kim, J.-Y.; Lee, S.-W.; Newkome, G. R. *Inorganica Chimica Acta* **2007**, *360*, 1780–1784.
- [232] Ziegler, M.; Monney, V.; Stoeckli-Evans, H.; Von Zelewsky, A.; Sasaki, I.; Dupic, G.; Daran, J.-C.; Balavoine, G. G. A. *Journal of the Chemical Society, Dalton Transactions: Inorganic Chemistry* **1999**, *5*, 667–676.
- [233] Eichkorn, K.; Treutler, O.; Öhm, H.; Häser, M.; Ahlrichs, R. *Chemical Physics Letters* **1995**, *240*, 283–290.

- [234] Eichkorn, K.; Weigend, F.; Treutler, O.; Ahlrichs, R. *Theoretical Chemistry Accounts* **1997**, *97*, 119–124.
- [235] Dollish, F. R. *Characteristic Raman Frequencies of Organic Compounds*; John Wiley and Sons Inc., 1973.
- [236] Deepa, P.; Kolandaivel, P.; Senthilkumar, K. *Biophysical chemistry* **2008**, *136*(1), 50–8.
- [237] Hensen, C.; Hermann Johannes, C.; Nam, K.; Ma, S.; Gao, J.; Holtje, H.-D. *Journal of medicinal chemistry* **2004**, *47*(27), 6673–80.
- [238] Absar, I.; VanWazer, J. R. *Angewandte Chemie, International Edition* **1978**, *17*, 80–88.
- [239] Gao, J.; Xia, X. *Science* **1992**, *258*(5082), 631–635.
- [240] McRee, D. E.; Redford, S. M.; Getzoff, E. D.; Lepock, J. R.; Hallewell, R. A.; Tainer, J. A. *The Journal of biological chemistry* **1990**, *265*(24), 14234–41.
- [241] Monteilhet, C.; Blow, D. M. *Journal of Molecular Biology* **1978**, *122*(4), 407–17.
- [242] Grier, D. L.; Streitwieser, A. *Journal of the American Chemical Society* **1982**, *104*, 3556–3564.
- [243] Schäfer, B. *Polypyridophenazin-Komplexe als artifizielle Modelle für photosynthetische Reaktionszentren* Dissertation, Friedrich-Schiller-Universität Jena, **2006**.

Selbstständigkeitserklärung

Ich erkläre, dass ich die vorliegende Arbeit selbstständig und unter Verwendung der angegebenen Hilfsmittel, persönlichen Mitteilungen und Quellen angefertigt habe.

Jena, den 8. Mai 2009

Martin Presselt

Acknowledgement - Danksagung

An erster Stelle möchte ich Prof. Jürgen Popp für die Möglichkeit danken die hier vorgestellten Themen zu bearbeiten, für seine Unterstützung, Motivation und die mir gelassenen Gestaltungsfreiheiten sowie für die Ermöglichung verschiedener dienstlicher Reisen.

Ein besonderer Dank gilt PD Dr. Michael Schmitt, der vielfältige Anregungen lieferte, mit dem stets ein ungezwungener Gedankenaustausch möglich war und der immer ein offenes Ohr für allerlei Problemstellungen hatte.

Ein weiteres herzliches Dankeschön an: meine Freunde und Kollegen Burkhard Jahn und Dr. Wilhelm Eger für zahlreiche Hilfestellungen bei Computerfragen und für die mit ihnen verbrachte Zeit; Dr. Benjamin Dietzek, Dr. Torsten Frosch, Thomas Bocklitz, Dr. Ute Uhlemann, Mario Krause, Dr. Michaela Harz, Christian Kuhnt und Stefan Zahn für fachliche Diskussionen und Benjamin besonders für das akribische Korregieren einiger Manuskripte. Tobias Meyer, Dr. Nicolae Tarcea, Dr. Claudio Dem und Dr. Petra Rösch möchte ich für die freundliche Unterstützung bei apparativen und sonstigen Problemen danken.

Für die gute Zusammenarbeit danke ich Prof. Oehme, Prof. Schubert, Dr. Andreas Winter, Prof. Sven Rau, Dr. Bernhard Schäfer, Dr. Matthias Schwalbe, Sebastian Losse, Dr. Dieter Gleich, Dr. Helmar Görls, Gunter Bührdel, Dr. Uwe Köhn, Dr. Fischer, Prof. Plass und Dr. Axel Buchholz, Prof. Buntkowsky, Torsten Gutmann und Dr. Hergen Breitzke, Daniel Escuerdo, Michael Kuschke und besonders Christoph Schnedermann, der mich bei den aufwändigen Fit-Prozeduren unterstützt hat.

Weiterhin möchte ich Prof. Kiefer, Dr. Bernd Küstner, PD Dr. Sebastian Schlücker und Belinda Böhm für den Gastaufenthalt und die freundliche Aufnahme in Würzburg danken sowie Prof. Schirmeister, Thomas Pfeuffer, PD Dr. Carsten Strohmann und Dr. Dominik Auer, Prof. Braunschweig, Dr. Michael Burzler und Simon Grabowsky für die erfolgreiche Kooperation danken.

Ein besonderer Dank gilt auch der Institutswerkstatt, allen voran Herr Fähndrich, dem Institutnetzwerkadministrator Dr. Dirk Bender sowie Gisela Persch, Rita Sieler und Erika Kielmann für ihre freundliche Unterstützung im Labor und bei der Praktikumsbe-

treuung.

Weiterhin möchte ich mich bei Steffi und Micha bedanken.

Großes Glück hatte ich bei meiner Büro-Gesellschaft und möchte mich bei Dr. Michaela Harz, Mario Krause, Angela Walter, Anne März, Anna Keese, Susanne Kuhri, Anja Boßecker, Tobias Meyer, Stephan Stöckel, Dana Cialla, Sebastian Reitzenstein und Katharina Gauss für die angenehme Zeit bedanken.

Vielen Dank auch an die übrige AG Popp, insbesondere Thomas S., Bob, Christian K. und Thomas B. für die gemeinsame Stressbewältigung im "Sandkasten" und für die unglaublichen Erlebnisse beim Winterseminar (insbesondere Thomas B., Christian und Rene).

Ein besonderer Dank gilt natürlich meinen lieben Eltern, da sie mir immer den Rücken gestärkt haben sowie meiner ganzen Familie und Freunden. Matthias Gaipf und meiner Frau möchte ich zusätzlich für das Korrekturlesen der Arbeit danken.

Alles aufzuzählen, wofür ich meiner lieben Frau Katja danke, würde den Rahmen der Arbeit sprengen, daher: vielen Dank für Alles!

Vita

Personal information

Address	Martin Presselt Dornburger Str. 32 07743 Jena Germany
Date and place of birth	19.12.1979 in Jena, Germany
Family status	Married with Katja Presselt

Education

1986-1991	Primary education Grundschule Kahla
1991-1998	High school: Staatliches Gymnasium Kahla, Abitur: 1,8
1998-1999	German Red Cross aidman in Kahla (civilian service)
1999-2004	Study of Chemistry at Friedrich-Schiller-University (FSU) Jena, Final mark of diploma: 1,8 Diplomathesis in the research group of Prof. Grummt (Institute of physical chemistry, FSU Jena): "Spectroscopic investigation of 5,5-Di(Phenylethynyl)-2,2-Bipyridyl incorporated in Zeolith-L to avoid aggregation"
Since 2005	PhD Thesis in the research group of Prof. Popp (Institute of physical chemistry, FSU Jena): "Describing and predicting molecular properties via vibrational spectroscopy in combination with electron density analysis"

Services to the Community

2002 - 2003	Proxy of a "Konzil" of the FSU Jena
2007	Member of a calling committee for a chair in theoretical chemistry
Since 2007	Member of the German chemical society DFG

Trainings

2003 Berlin	Genomics seminar (Applied Biosystems)
2006 Jena	Academy for foundation management
2008 Jena	Statistical data analysis using SAS Enterprise Guide
2008 Jena	Introduction in the statistic software SPSS

Employment

09 - 10 / 2000	INNOVENT e.V., work focus: lacquer and photo initiators
09 - 12 / 2002	Scientific assistant of Prof. Grummt (FSU Jena), work focus: Introduction of the MD-program "Gromacs"
01.2005 - 03.2009	Scientific staff at the institute of physical chemistry, FSU Jena
Since 04.2009	Scientific staff at the institute of experimental physics, TU Ilmenau

Experience in Guidance and Teaching

2005 - 2008	Guidance of a research scholar, a trainee, research and diploma students
-------------	--

Poster and Talks

2005 Jena	Conference of the Collaborative Research Centre SFB 436 <i>Poster</i> (M. Schmitt, B. Dietzek, M. Presselt, U. Uhlemann, J. Blumhoff, L. Böttcher, B. Schäfer, S. Rau, D. Walther, J. Popp): "Time- and Frequency-resolved Investigations of the Excited States in Various homo- and heteronuclear Ru-complexes" <i>Talk</i> (U. Uhlemann, M. Schmitt, A. Walter, M. Presselt, J. Popp; Speaker: Prof. Popp): "Aufklärung von Struktur-Eigenschafts-Beziehungen von Metallo-Komplexen und Metallaktiverter Reaktionen durch schwingungs-spektroskopische Methoden in Kombination mit Ab-initio-Simulationen"
-----------	---

-
- 2006 Hamburg DFG Priority Program SPP 1178: First report colloquium at DESY Hasylab
- Talk* (M. Presselt, M. Schmitt, J. Popp; Speaker: Dr. Schmitt): "Raman spectroscopy filling the gap between single crystal and liquid phase investigations to determine electron density related molecular characteristics - Raman studies to derive reactivity concepts"
- 2006 Yokohama International Conference of Raman Spectroscopy
- Japan
- Poster 1* (M. Presselt, M. Schmitt, D. Auer, C. Strohmann, D. Stalke, J. Popp): "Raman spectroscopic investigations to describe exceptional chemical bonds - correlations between Raman spectra of solutions and single crystals"
- Poster 2* (S. Tschierlei, M. Presselt, M. Schmitt, B. Schäfer, M. Meier, M. Schwalbe, M. Auth, S. Rau, J. Popp): "Resonance Raman spectroscopic investigations of artificial light harvesting antennas"
- 2006 Erlangen 105. Bunsentagung: Katalyse
- Poster 1* (M. Presselt, D. Auer, S. Dilsky, M. Schmitt, J. Popp, C. Strohmann): "Structure / reactivity studies of -lithiated benzylianes"
- Poster 2* (M. Schmitt, B. Dietzek, M. Presselt, U. Uhlemann, S. Tschierlei, L. Böttcher, M. Meier, S. Rau, D. Walther, J. Popp): "Time- and Frequency-resolved Investigations of the excited states in various homo- and heteronuclear Ru-complexes"
- 2006 Potsdam IV European Charge Density Meeting
- Poster* (M. Presselt, D. Auer, S. Dilsky, M. Schmitt, J. Popp, C. Strohmann): "Structure / reactivity studies of -lithiated benzylianes"
- 2007 Bad Honnef 393. WE-Heraeus-Seminar: "Trends in Molecular Biophysical Spectroscopy"

- Poster* (S. Tschierlei, M. Presselt, B. Dietzek, M. Karnahl, S. Rau, M. Schmitt, J. Popp): "Resonance Raman and Femto-second-Time-Resolved Studies on Artificial Light Harvesting Systems Based on Ruthenium Polypyridine Complexes"
- 2007 Kloster Banz DFG SPP 1178: 2nd Proposal Colloquium
- Talk* (M. Presselt, M. Schmitt, J. Popp; Speaker: Dr. Schmitt): "Raman spectroscopy filling the gap between single crystal and liquid phase investigations to determine electron density related molecular characteristics - Raman studies to derive reactivity concepts"
- 2007 Graz 106. Bunsentagung: Heterogene Neuartige Kohlenstoff-strukturen
Austria
- Poster* (M. Presselt, M. Kühnert, M. Schmitt, T. Pfeuffer, T. Schirmeister, J. Popp): "Raman spectroscopy filling the gap between single crystal and liquid phase investigations to determine electron density related molecular characteristics"

Publications

- 1) B. Schäfer, H. Görls, M. Presselt, M. Schmitt, J. Popp, W. Henry, J. G. Vos, S. Rau; "Derivatives of dipyrido[3,2-a:2',3'-c]phenazine and its ruthenium complexes, influence of aryl substitution on photophysical properties."
Dalton Transactions **2006**, 18, 2225-2231.
- 2) C. Herrmann, J. Neugebauer, M. Presselt, U. Uhlemann, M. Schmitt, S. Rau, J. Popp, M. Reiher; "The First Photoexcitation Step of Ruthenium-Based Models for Artificial Photosynthesis Highlighted by Resonance Raman Spectroscopy."
Journal of Physical Chemistry B **2007**, 111, (21), 6078-6087.
- 3) M. Presselt, B. Dietzek, M. Schmitt, A. Winter, M. Chipper, C. Friebe, U. S. Schubert, J. Popp; "The Influence of Zinc(II) in a bis-Terpyridine-Phenylene Complex on the pi-Conjugation between the Terpyridine and the Phenylene Moiety."
Journal of Physical Chemistry C **2008**, 112, (47), 18651-18660.
- 4) M. Presselt, C. Schnedermann, M. Schmitt, J. Popp; "Prediction of electron densities, the respective laplacians and ellipticities in bond-critical points of phenyl-CH-bonds via linear relations to parameters of inherently localized CD stretching vibrations and ¹H-NMR-shifts."
Journal of Physical Chemistry A **2009**, 113, (13), 3210-3222.

-
- 5) A. Winter, C. Friebe, M. Chiper, U. S. Schubert, M. Presselt, B. Dietzek, M. Schmitt, J. Popp; "Synthesis, Characterization and Electrooptical Properties of Zn(II) Complexes with p-Conjugated Terpyridines as Ligands."
ChemPhysChem **2009**, 10, 787-798.
 - 6) M. Jäger, M. Auth, H. Görls, G. Vaughan, R. Beckert, M. Presselt, M. Schmitt, J. Popp, W. Henry, J. G. Vos, S. Rau; "Synthesis and Characterisation of Photoredoxactive Building Blocks for Organometallic Coupling Reactions."
in preparation **2009**.
 - 7) M. Presselt, B. Dietzek, M. Schmitt, S. Rau, U. S. Schubert, J. Popp; "QTAIM analysis of the electron density distribution in tpy-ph compounds as a tool to design new structures with delocalized π -systems."
to be submitted **2009**.
 - 8) M. Presselt, S. Losse, M. Jäger, M. Schmitt, S. Rau, J. Popp; "Expansion of the initial excited state in Ruthenium(II)-4'-Phenylene-Terpyridine revealed by Resonance Raman Spectroscopy."
in preparation **2009**.
 - 9) B. Schäfer, J. Schöffel, S. Losse, H. Görls, W. Henry, J. G. Vos, M. Presselt, M. Schmitt, J. Popp, S. Rau; "Synthesis and properties of ruthenium complexes containing tetraalkyne substituted 1,10-phenanthrolines."
in preparation **2009**.
 - 10) S. Tschierlei, M. Presselt, C. Kuhnt, A. Yartsev, T. Pascher, V. Sundsröm, M. Karnahl, M. Schwalbe, B. Schäfer, S. Rau, M. Schmitt, B. Dietzek, J. Popp; "Photophysics of the intramolecular hydrogen evolving photocatalyst Ru-tpphz-Pd."
Chemistry **2009**, accepted.
 - 11) M. Presselt, C. Schnedermann, M. Schmitt, J. Popp; "Derivation of functions able to predict bond-properties of all phenyl-CH-bonds dependent on vibrational and H-NMR spectroscopic quantities."
to be submitted **2009**.